# ELECTRO-OPTIC MICRODISK RF-WIRELESS RECEIVER

by

Mani Hossein-Zadeh

---

A Dissertation Presented to the
FACULTY OF THE GRADUATE SCHOOL
UNIVERSITY OF SOUTHERN CALIFORNIA
In Partial Fulfillment of the
Requirements for the Degree
DOCTOR OF PHILOSOPHY
(ELECTRICAL ENGINEERING)

December 2004

# Dedication

To

My parents

Maman and Papa

# Acknowledgements

First and foremost, I would like to express my deepest gratitude to my parents Jamileh and Mahmoud and to Iliga for their unconditional love, encouragement, and the many sacrifices they have made for me. Their patience, love and support always created a warm and safe atmosphere, conducive to a happy life, and to studies in particular. They raised me to work hard towards realizing my dreams, and yet to be content with what I have; to be honest with those around me and myself; to never sacrifice my values for success. I will never find words adequate enough to express my gratitude, deep respect, and endless love for them.

I would also like to thank my aunts, uncles, and cousins in Los Angeles, without whom I would not have been able to adapt to my new life. My acknowledgements would be endless if I were to name them all. Needless to say, their love and encouragement during my studies supported me through the financial and emotional adjustments I faced when I first arrived. I could not have survived without them then, and they continue to be a great source of strength for me now.

I would like to thank my dissertation advisor Professor A. F. J. Levi for offering me the opportunity to work on this exciting project within his research group. His constructive criticism and original ideas were my main drive to becoming a professional researcher. I have learnt much from him and hold him in great respect.

I would like to thank Dr. David Cohen to whom I owe most of the Lab management and technical skills I learned. He patiently explained to me everything from basic measurement to advanced techniques. His presence as a friend and teacher transformed the learning process into a truly enjoyable experience.

I would like to thank my colleague Fernando Harriague. Not only was he a great Lab mate, but a wonderful friend, a true brother. I always enjoyed our conversations that spanned topics as diverse as physics, politics, and social issues.

I would like to thank Kim L. Reid for taking care of all the administrative tasks during the project. More importantly she was always there as a caring friend and gave me the feeling of having a sister by my side.

I would like to thank my friend and Lab mate Ioan Georma who did most of the work for antenna design and fabrication. I particularly appreciate his help with CST (a commercial EM simulation software). He was a true friend and knowledgeable colleague.

I would like to thank Dr. Bindu Madhavan. A friend and colleague from whom I learned subjects as diverse as integrated circuits and spiritual development. His great suggestions always helped me make the best decisions at the most crucial times.

I would like to thank Dr. John D. O'Brien and Stephan Haas for graciously agreeing to serve on my dissertation committee.

I would like to thank past members of my research group for their useful comments and suggestions: Dr Sumesh Thiyagarajan, Dr Barath Raghvavan, Dr Panduka Wijetunga, Yuliang Du, Alex Tarasyuk, Jeff Sondeen, Ashirvad Bahukhandi, Kundan Patidar and Karan Gupta. I would especially like to thank Kundan for helping me make the PCB board for the photoreceiver, and Karan for assistance in video transmission and the video editing software.

To all those who have supported me in various ways and whom I love, thank you.

# Table of Contents

## 2 $LiNbO_3$ microdisk modulator



## 3 Microdisk modulator in RF-optical link

## 4 Optical down-conversion



## 5 Conclusion and future work

# List of Tables

# List of Figures

# Abbreviations

| | |
|---|---|
| BW | Bandwidth |
| CW | Continuous wave |
| DC | Constant power |
| DD | Direct detection |
| DSC | Double sidebands suppressed carrier RF modulation format |
| FBG | Fiber Bragg grating |
| FP | Fabry-Perot |
| IF | intermediate frequency |
| MZ | Mach-Zehnder optical modulator |
| NRZ | Non-return-to-zero |
| PRBS | Pseudo-random beat stream |
| PM | Polarization maintaining |
| RoF | RF over fiber |
| RF | Radio frequency |
| WG | Whispering Gallery |

# Abstract

A self-homodyne photonic receiver for transmitted carrier wireless links is demonstrated. The key innovations in this photonic RF-receiver are the design and implementation of a resonant $LiNbO_3$ microdisk electro-optic modulator and novel RF down-conversion techniques that exploit the sensitivity of the microdisk for efficient RF down-conversion in the optical domain. By careful RF and optical design, simultaneous photonic and RF resonance is achieved in a $LiNbO_3$ microdisk modulator resulting in a sensitivity of -80 dBm at 14.6 GHz.

Two photonic RF down-conversion techniques are proposed to extract the baseband information from a RF signal that has a transmitted carrier modulation format. In the first approach we use an optical filter to modify the optical output spectrum of the microdisk modulator. Photodetection of the subsequent optical signal generates the baseband photocurrent. In the second technique the RF carrier and sidebands are mixed through *nonlinear* optical modulation in the microdisk and the down-converted signal is detected using a photodetector. In both cases the bandwidth of the photodetector and electronic circuitry are limited to that of the baseband signal.

Receiver operation is demonstrated by demodulating up to 100 Mb/s digital data from a 14.6 GHz RF carrier frequency. Power efficiency, small volume, light weight and elimination of high-speed electronic components are the main specifications of the photonic RF-receiver that make it useful for applications like wireless LANs, fiber-feed backbone networks or video distribution systems.

# Chapter 1
# Introduction

## 1.1 Motivation

### 1.1.1 Photonic RF signal processing

Microwave links are essential parts of today's radio communication and radar systems. A factor limiting use of mm-wave carrier frequencies in these links is the high attenuation of RF signals in microwave cables and low efficiency of conventional electronic devices. The design complexity and cost of fabricating solid-state electronics based signal processing devices and circuits increases significantly at mm-wave frequencies. RF-photonic technology is an alternate approach that employs an optical carrier in hybrid microwave-photonic links to transmit and distribute RF-signals as well as performing some signal processing functions photonically [1-10]. The primary task in a RF-photonic system is up-conversion from RF to optical frequencies or optical modulation. Direct modulation of laser sources becomes highly inefficient at mm-wave frequencies and external optical modulators, especially conventional $LiNbO_3$ Mach-Zehnder (MZ) modulators, are the best alternative. Recently the bandwidth, efficiency and size of MZ-type modulators have been dramatically improved by better RF design and employing semiconductor electro-optic materials [15,20]. In RF subcarrier optical links information is carried within a limited bandwidth around a high-frequency RF-

carrier. This is an opportunity to employ the high sensitivity offered by resonant optical modulators. Resonant modulators use either optical or electrical resonance to enhance the interaction length or modulating voltage at the expense of loosing bandwidth [55-80]. These modulators can only modulate within a limited bandwidth around discrete frequencies separated by RF or optical free-spectral-range of the resonator. Resonant modulators are typically smaller than regular MZ modulators and by careful design their sensitivity can be maintained up to mm-wave frequencies where MZ modulators face significant RF-optical phase mismatch.

Processing microwave and mm-wave signals in the optical domain has been the subject of research for the past few years [1-3]. One of the most interesting applications of photonic RF processing is RF frequency conversion. RF frequency conversion in the optical domain has many advantages such as optical isolation from environmental RF noise and signals, independence from carrier frequency and elimination of high-speed electronic circuitry. Frequency conversion in the optical domain is mainly achieved through optical filtering and nonlinear modulation.

Photonic generation of pure RF and mm-wave signals is another attractive application of RF-photonics [3,4]. Mixing infrared lasers in a high-speed photodiode is a powerful technique to generate a RF signal. Tunability over a wide range of frequencies, simplicity of the design, small volume, purity of the RF spectrum are among the most promising features of photonic RF generators. The high-frequency limit of these generators is mainly imposed by the photodiode response. Recently the advent of the uni-traveling carrier photodiode has noticeably increased the

operational frequency of the photonic generators. The state-of-the art UTC-PD based photonic mm-wave source can generate a 90 GHz signal by mixing two DFB lasers [4]. The power and phase stability of these devices is determined by the relative phase fluctuations of the laser sources. An accurate and stable phase locking mechanism is a crucial requirement for a reliable RF or mm-wave source.

A resonant $LiNbO_3$ microdisk modulator uses simultaneous electrical and optical resonance and hence benefits from both voltage-gain and enhanced electro-optic interaction length. This feature increases the sensitivity of a microdisk modulator compared to other types of modulators, and makes it a good candidate for a RF-photonic receiver. In this thesis it will be shown that $LiNbO_3$ microdisk modulators can be used in an all-optical receiver design that exploits their sensitivity in combination with optical signal processing techniques to receive and down-convert the data from an RF signal.

### 1.1.2 RF subcarrier links in wireless LANs and fiber-feed backbone networks

A wireless local area network (LAN) is a data communication system implemented as either an extension to, or as an alternative to a conventional wired LAN. The majority of wireless LAN systems use Radio Frequency (RF) transmission technology. Wireless LANs are typically fed through the wired LAN. The radio

access point consists of a bridge and a base station, and acts as the interface between the wired LAN and the wireless LAN. The requirement of high data rates and cell isolation push the carrier frequencies into mm-wave.

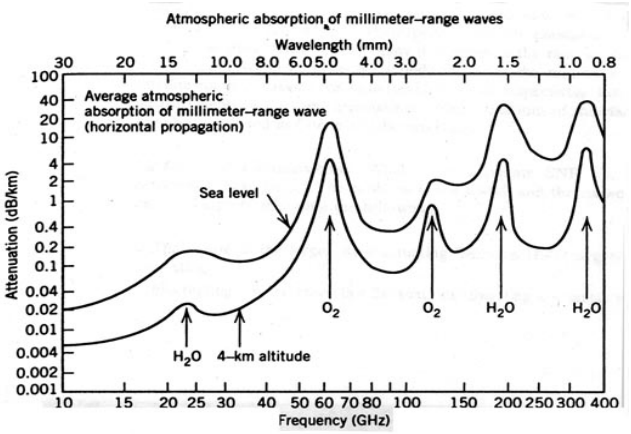


(a)

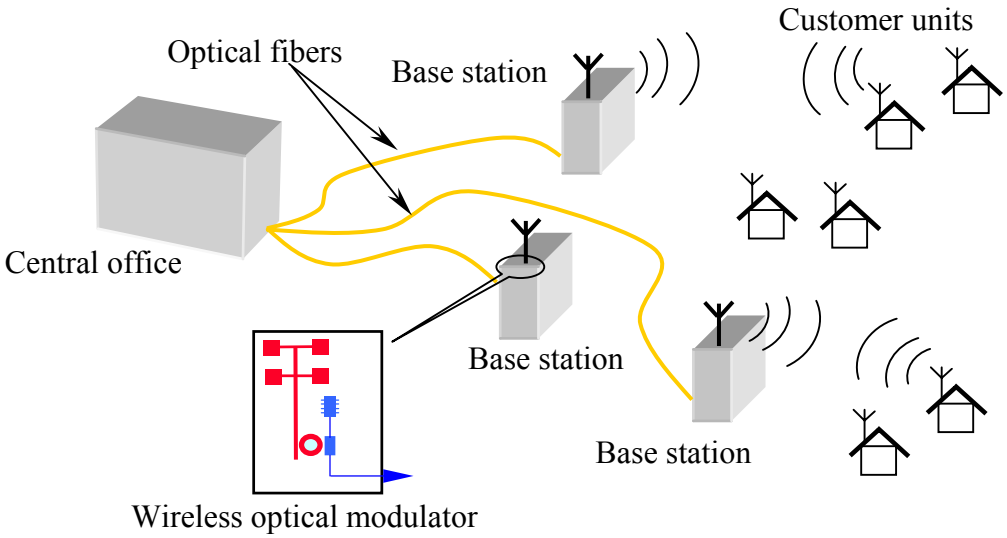


(b)

**Figure 1.1** (a) Shows the propagation loss of the electromagnetic waves in air as a function of frequency. Two absorption peaks are observed at 23 and 60 GHz (Source: phased array-based systems and applications, Nicholas Fourikis, pp. 27-28, John Wiley & Sons, 1997). (b) A schematic diagram showing the concept of fiber-feed backbone networks and the function of wireless-optical modulator in the network.

The propagation loss is high at mm-wave frequencies (Fig. 1.1(a)) so each base station will have a smaller coverage radius (5-10 km for micro-cellular and 1 km for pico-cellular). Adjacent cell interference is minimized and the network has a high degree of frequency reuse.

However, having small radio cells also means that numerous radio access points (or base stations) are required to cover a large area. Also, broadband wireless networks require a high capacity feeder network. The deployment and maintenance of such a system using today's copper based wired LANs is economically unattractive. An alternative is they are replaced by a high capacity optical fiber infrastructures [5-8]. RF over fiber (RoF) is the best candidate for this purpose (Fig. 1.1(b)). An important component in RoF systems is a low-power wireless optical modulator that can efficiently modulate the optical carrier using the weak RF power received by the antenna (typically 1-10 μW). Microdisk modulators can be made sensitive enough to operate at very small RF-powers (SNR of 10 dB at -70 dBm RF power is demonstrated in this thesis), which makes it a useful component in these types of links.

### 1.1.3 Indoor wireless

A video transmission system is an example of a simple millimeter-wave application because it is a one-way redistribution system for received terrestrial or satellite broadcast video signal, and it is the first common millimeter-wave application in house-hold use [10].

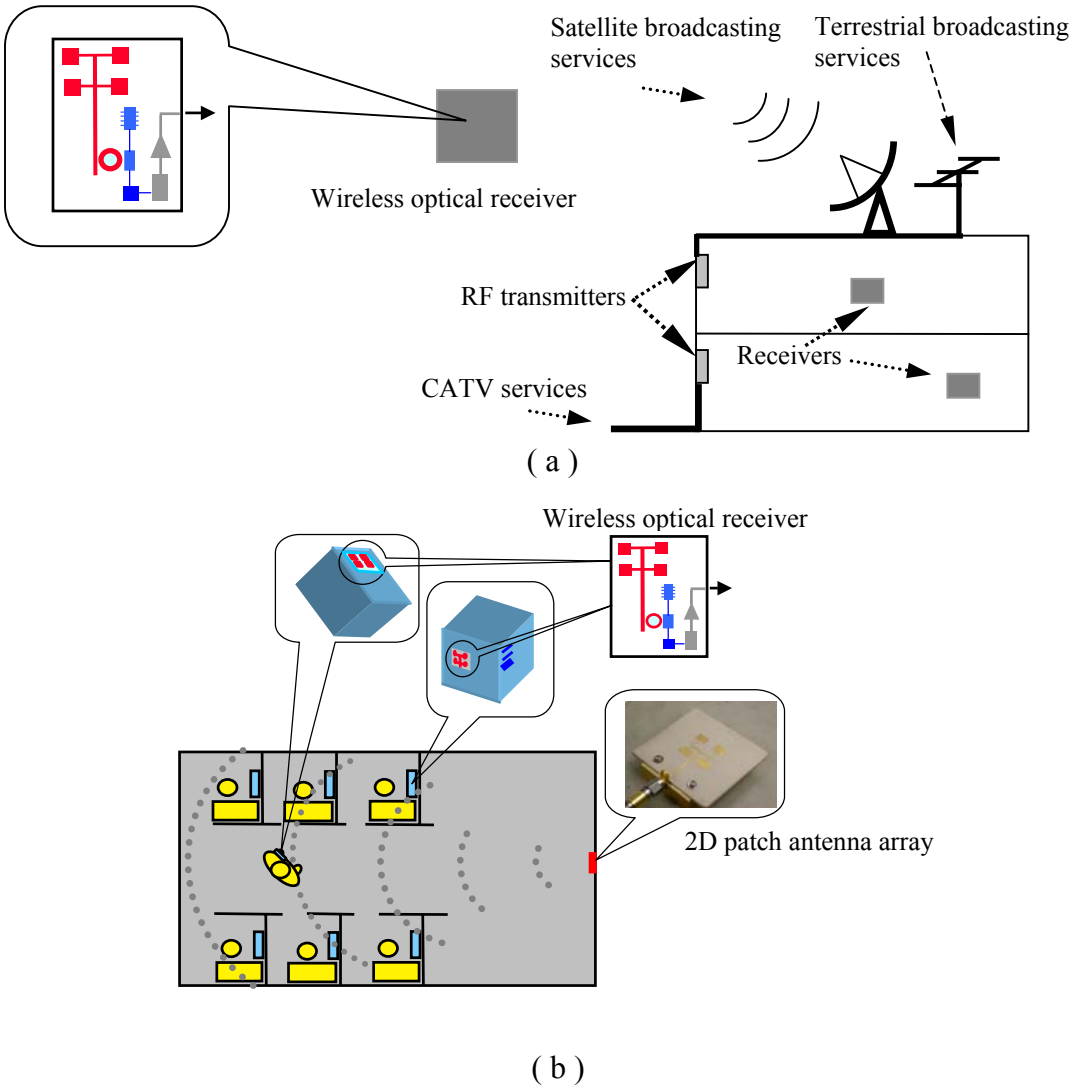


**Figure 1.2** (a) Video redistribution for households based on RF-photonic receiver system. (b) Application of RF-photonic receiver in an indoor wireless LAN.

Fig. 1.2(a) illustrates the concept of a mm-wave video transmission system for household use. Terrestrial, satellite-broadcast and/or cable television (CATV) signals are redistributed through the house by using mm-waves and optics [10]. A small low power RF-photonic receiver can be connected to each display device to receive the modulated carrier and recover the video signal.

An indoor wireless data distribution system is another potential candidate for employing a RF-photonic receiver. Fig. 1.2(b) shows an example where a data modulated RF-carrier is transmitted by a directional antenna that broadcasts to all users. A small RF-photonic receiver is attached to each computer to receive the RF-signal and send the down-converted data to the computer.

## 1.2 Brief survey of the related topics

$LiNbO_3$ microdisk optical modulator employs principles, techniques and physical concepts that have been the subject of research for many years. Consequently, a brief survey of the most important related research is useful.

Fig. 1.3 shows four major concepts and technologies that are combined in a $LiNbO_3$ microdisk resonant modulator. In this section the main aspects of these subjects are discussed.

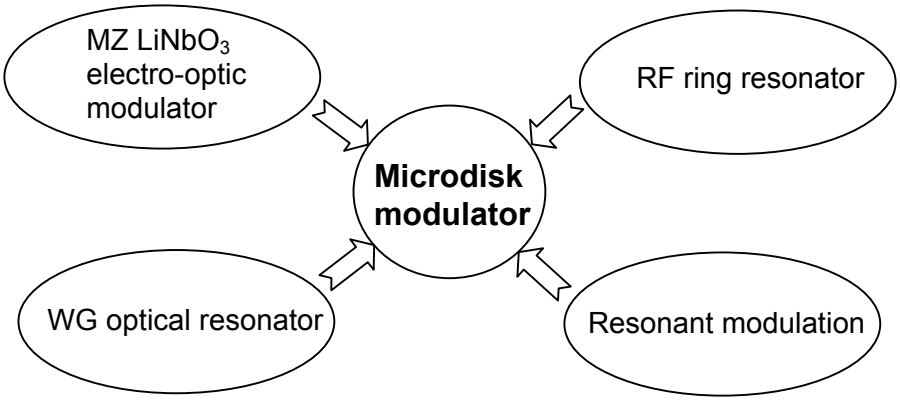


**Figure 1.3** Convergence of four principal technologies in microdisk optical modulator.

### 1.2.1 Mach-Zehnder modulator

Traveling wave Mach-Zehnder (MZ) amplitude modulators are widely used in high-speed optical communication systems. Conventional MZ interferometric modulators rely on two physical effects to vary the light intensity. The effects are voltage dependence of light velocity in electro-optic materials (known as Pockels effect) and optical interference. Such modulators are typically composed of two Ti-diffused optical wave-guide arms fabricated in a $LiNbO_3$ wafer. The waveguides are typically 8×6 $\mu m^2$ in cross section with a loss of 0.1 dB/cm (the optical mode is 7×4 $\mu m^2$ located about 2 μm below the surface) [9]. The electric field is applied with CPW [(1)] or CPS [(2)] structures. Performance is characterized by bandwidth, drive voltage ($V_\pi$), optical insertion loss and chirp. One of the main challenges for increasing the sensitivity at high frequencies is to maintain RF-optical phase

matching for a long distance. The effective optical and RF refractive index of $LiNbO_3$ are different so there is an inherent mismatch between the optical and microwave velocities. As a result, the maximum achievable drive frequency decreases as the modulator length is increased. Conversely, to lower the drive voltage and power, a long device length is required. Thus a performance tradeoff is made between maximum drive frequency and required drive power. A large amount of effort has been dedicated to solve this problem resulting in lower drive voltages (factor of 5) during the past 10 years [11-15]. Fig. 1.4(a) shows the picture of a $LiNbO_3$ MZ modulator with a $V_\pi$ of 0.9 V at 40 Gb/s, which has been developed using a new design concept featuring a wide-gap and a long CPW electrode [15].

On the other hand these devices are relatively big and bulky (1cm×1cm×10cm) and hard to integrate with microphotonic devices. Integration with planar antennas is another issue, which makes using a conventional MZ modulator for certain wireless applications questionable. MZ modulators have been also fabricated using III-V compound semiconductor materials [18-20]. These modulators are typically smaller than $LiNbO_3$ and they can be monolithically integrated with other microphotonic devices such as lasers and photodetectors. Heterostructures for electro-optic phase modulation are typically made of AlGaAs or InGaAsP compounds. A detail explanation of the electro-optic effects in III-V structures is presented in Chapter 5.

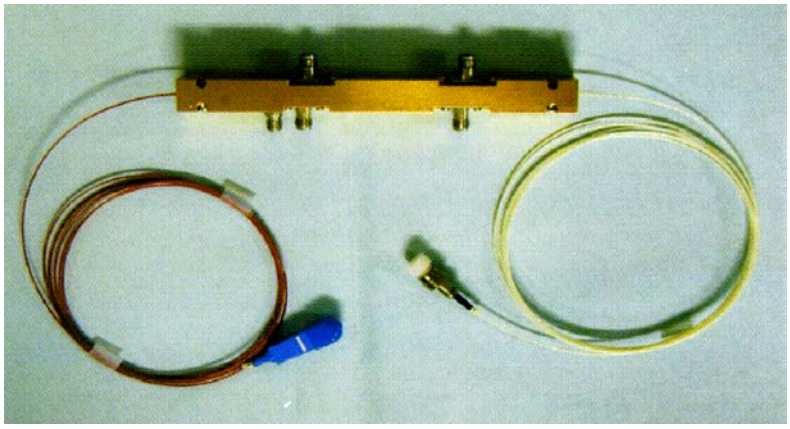

( a )

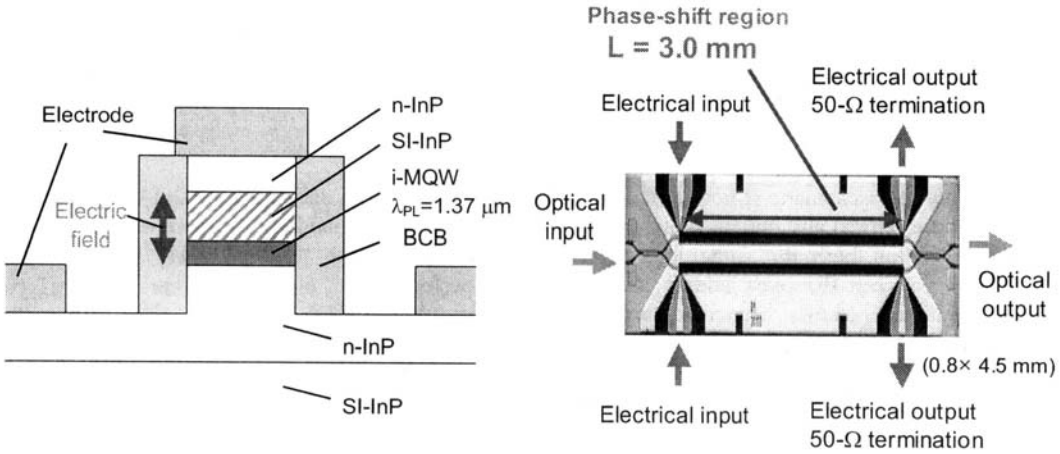


( b )

**Figure 1.4** (a) Photograph of a state-of–the-art low-drive voltage ($V_\pi$ = 0.9 Volt) 40 Gb/s $LiNbO_3$ MZ modulator [15]. (b) A semiconductor MZ modulator fabricated on a SI-InP substrate. Cross-sectional geometry of the n-i-n InP waveguide (left) and a photograph of the fabricated chip (right) [20].

Recently an InP-based Mach-Zehnder has been introduced with a bandwidth larger than 40 Gb/s and a $V_\pi$ of 2.2 V [20]. The length of the active arm in this modulator is about 3 mm. Fig 1.4(b) shows the cross-sectional geometry of the active waveguide and a photograph of the MZ modulator chip (0.8 mm × 4.5 mm).

### 1.2.2 Microsphere optical resonator

Microsphere resonators are very small (25 μm to 4 mm radius) optical resonators usually made of fused silica. They are interesting because of the ability to support confined high-$Q$ Whispering–Gallery (WG) modes. Quality factors exceeding $Q = 10^{10}$ have been reported for these microresonators [21]. The long photon lifetime inside the microsphere is the key feature that makes it very attractive for various optical and opto-electronical applications.

Challenges that must be overcome for practical applications are fabrication and optical coupling to Whispering-Gallery modes. Basic understanding of the ultimate $Q$ of optical resonators and mode analysis has been investigated since mid 1990's [21-23]. Different schemes have been used to couple light into and out of resonators, such as prism coupling, tapered-fiber coupling [26,27], angle polished fiber coupler [25] and planar single mode waveguide coupler [24]. Among them the tapered-fiber coupling seems to be the most promising due to high coupling efficiency (98%) and geometrical compatibility with photonic circuit and filter designs. Fig. 1.5(a) is the photograph of a microsphere coupled to two angle polished fiber couplers and Fig. 1.5(b) shows a microsphere resonator coupled to two tapered-fiber couplers in an add-drop filter configuration. Experimental results indicate that optical coupling loss of less than -3 dB is routinely achievable with this method [26]. Microspheres suffer from coupling stability and geometrical incompatibility with planar structures that will keep them from being commercially feasible.

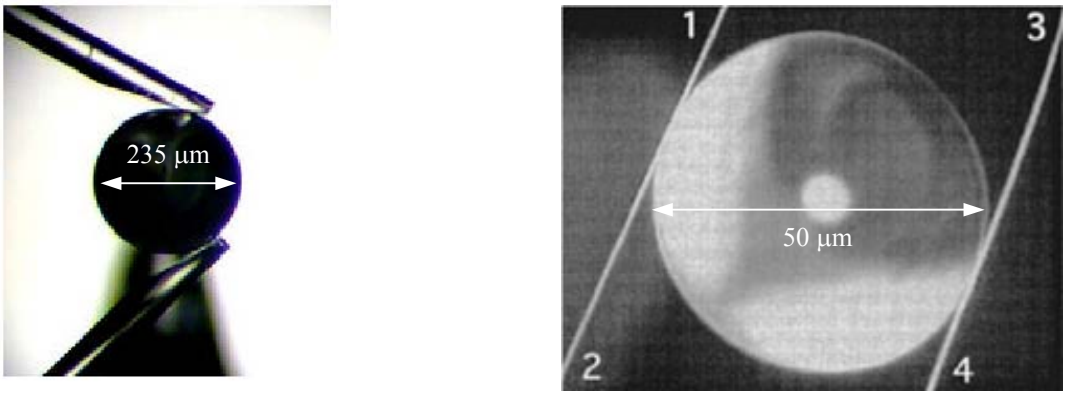


( a ) ( b )

**Figure 1.5** (a) Photograph of a 235 μm radius silica microsphere photonic resonator showing angle polished-fiber couplers [25]. (b) Photograph of a silica microsphere coupled to tapered-fibers as an add-drop filter. Over coupling of this device results in low loaded optical-$Q$ of $4\times10^4$ for broadband applications [26].

### 1.2.3 Microdisk and microring optical resonator

Microdisk optical resonators are disk shaped Whispering-Gallery optical resonators. Medium size disks (1-10 mm diameter, 0.1-1 mm thickness) can be made from bulk material using special grinding and polishing techniques. Small size resonators (10-200 μm diameter and 10-50 μm thickness) can be made using standard lithographic patterning and etching techniques. The principle advantage of the small disks is that they can be integrated with other monolithic microphotonic deices. But since most electro-optic crystals cannot be deposited and also the etching techniques do not provide the desired surface roughness quality to achieve very high optical-$Q$, currently for certain applications medium size disks are the only candidates. Prism

coupling and etch eroded half-block coupling are the main methods for coupling to medium size disks. Fig. 1.6(a) is a photograph of a $LiNbO_3$ microdisk with a diameter of 1 mm and a thickness of 0.2 mm.

Small size InP microdisk optical resonators have been fabricated using optical lithography and wafer bonding techniques [33,35]. The diameter of these devices is typically between 4 to 12 μm and they can be vertically (Fig. 1.6(b)) or laterally (Fig. 1.6(c)) coupled to ridge waveguides fabricated on the same substrate and work as add-drop filters or switches [61,62]. The quality factor of these disks is around 6000 and is limited by surface roughness of the etching process used in fabrication. Semiconductor microdisks can be used as active switches since their refractive index and loss can be changed by free carrier injection; consequently the optical $Q$-factor and the resonant wavelengths may be controlled by current flow [61]. Due to high index contrast, the air-guided structures (the waveguide and the microring are surrounded by air) are not always favorable in terms of optical losses and coupling efficiencies. Recently a buried InP/InGaAs microring resonator with a $Q$ of $10^5$ has been demonstrated. Fig. 1.6(d) is the SEM cross-sectional view of the buried InP microring resonator [35]. Multi-quantum well microdisk lasers employ the WG optical-modes of a microdisk [36-38]. Fig. 1.6(e) shows a microdisk laser with radius $R = 0.8\ \mu m$ and lasing wavelength of $\lambda \approx 1.5\ \mu m$. Detailed studies and modeling of these active optical devices have revealed much of the physics governing device operation.

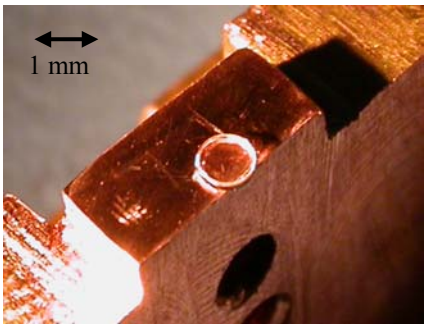


( a )

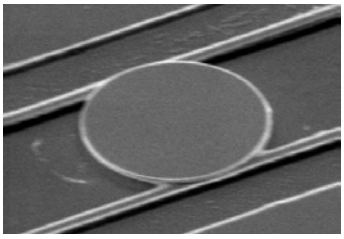

( b )

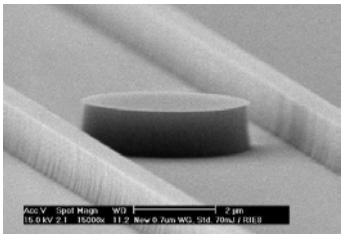

( c )

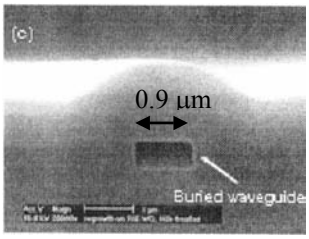


( d )

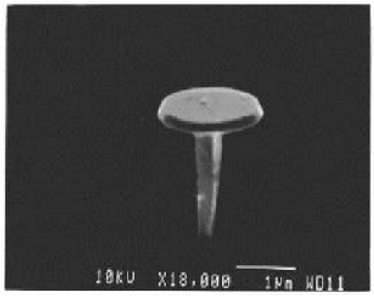


( e )

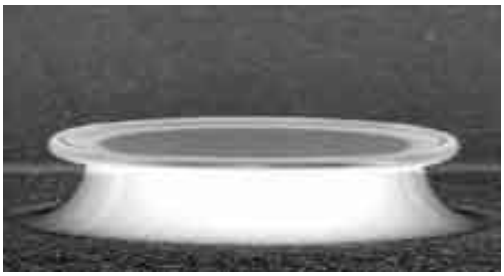

( f )

**Figure 1.6**

(a) Photograph of $LiNbO_3$ microdisk ($D$ = 1 mm).

(b) Photograph of an InP microdisk vertically coupled to parallel waveguides ($D$ = 30 μm)[34].

(c) Photograph of an InP microdisk laterally coupled to parallel waveguides ($D$ = 4 μm)[34].

(d) An SEM cross-sectional view of a buried microring resonator [35].

(e) Photograph of a microdisk laser ($D$ = 1.6 μm) [37].

(f) Photograph of an ultra-high-$Q$ ($10^8$) toroidal silica microdisk.($D$ = 150 μm) [31].

The CW room-temperature operation of optically pumped InGaAs/InGaP microdisk lasers has been reported [38]. Monolithic microring and microdisk resonators have

been also fabricated based on Si-$SiO_2$ [28-30]. The diameter of these ring resonators is typically 8-50 μm and their *Q*-factor strongly depends on the fabrication techniques. Recently a $SiO_2$ toroidal microdisk has been reported with a *Q* of $10^8$ (Fig. 1.6(f)) [31]. These resonators have been mostly used for add-drop optical filter design [29,30,31]. Ring resonators with a *Q*-factor of about $10^5$ have been also fabricated based on polymer materials [32]. The diameter of these rings is between 50 and 500 μm and they are vertically coupled to polymer waveguides. Since they are made of electro-optic polymers, they can be used as modulators (section 1.4.2)

### 1.2.4 RF microring resonator

RF ring resonators are ring shaped microstrip structures used as resonant elements in RF filter design [39]. Previously, most of the research in this subject has been on resonant frequency, *Q*-factor estimation and excitation methods for ring based RF filter design [39-43]. Several schemes have been developed to couple RF power into and out of the ring resonators. Of these, magnetic side coupling and capacitive gap coupling are the most commonly used methods. Ring resonators are also used in electro-optic devices. G. K. Gopalakrishnan *et al.* have investigated the microwave optoelectronic interactions in a microstrip ring resonator by monolithically integrating a Schottky diode photodetector into a microstrip ring resonator [45].

The semi-ring resonator [44] hasn't been used as much as the ring resonator for filter design. However, since its resonant frequency can be easily tuned (by trimming the length), it has been used in initial designs of the microdisk modulator where RF-optical frequency matching is an important issue [74,75,79,80]. Fig. 1.7(a) shows a photograph of microstrip ring resonators side coupled to a microstrip line on a printed circuit board (PCB). Fig. 1.7(b) shows a ring resonator on top of a $LiNbO_3$ microdisk that is side-coupled to microstrip line fabricated on a PCB. The typical $Q$-factor of these ring resonators is between 50-150, depending on the surface roughness of the ring, ring size and properties of the substrate material. The geometrical compatibility and relatively high-$Q$ makes these resonators a good choice to provide voltage gain (through resonance) in a microdisk modulator.

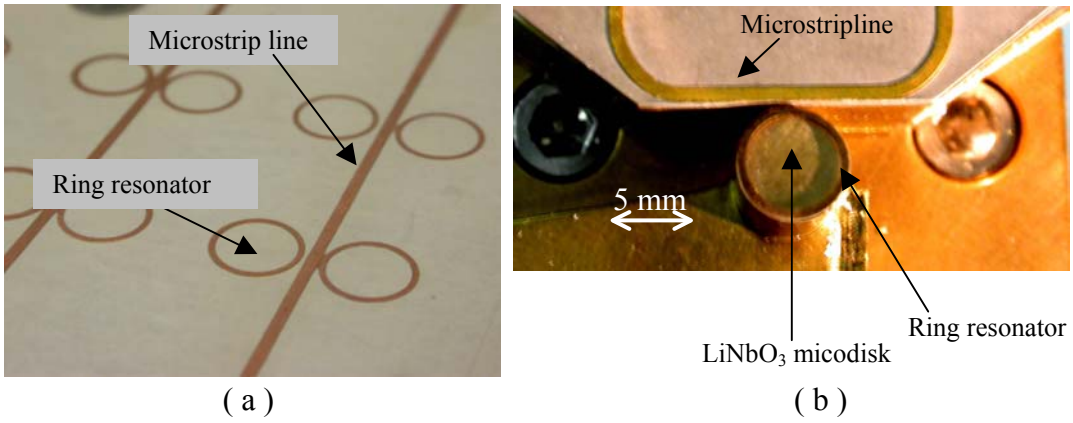


**Figure 1.7** (a) Photograph of microstrip ring resonators side-coupled to a microstrip line on a printed circuit board (PCB). (b) A ring resonator on top of a $LiNbO_3$ disk ($D$ = 5.8 mm), side coupled to a microstrip line on a PCB.

### 1.2.5 Wireless receivers

A well-designed radio receiver must satisfy the following requirements [47]:

(A) High gain (~100 dB) to restore the low power of the received signal to a level near its original baseband value. (B) Frequency selectivity, in order to receive the desired signal while rejecting adjacent channels, image frequencies, and interference. (C) Down-conversion from the received RF frequency to an IF frequency for processing. (D) Detection of the received analog or digital information. (E) Isolation from the transmitter to avoid saturation.

Because the typical power level from the receive antenna may be as low as –100 to –120 dBm, the receiver may be required to provide power gain as high as 100 to 120 dB. The global system for mobile communication (GSM) standard [(3)] requires a minimum sensitivity of -102 dBm and a dynamic range of 62 dB [(4)]. This much gain should be spread over RF, IF and baseband stages to avoid instabilities and possible oscillation. It is generally good practice to avoid more than about 50-60 dB of gain at any one frequency band. The fact that amplifier cost generally increases with frequency is a further reason to spread gain over different frequency stages. Here we present an overview of some of the most important types of RF wireless receiver architectures:

*Direct conversion receiver*: The direct conversion receiver, shown in Fig. 1.8(a), uses a mixer and local oscillator to perform frequency down-conversion with zero IF frequency. The local oscillator is set to the same frequency as the desired RF signal,

which is then converted directly to baseband. The direct conversion receiver is sometimes called a *homodyne* receiver. For AM reception the received baseband signal would not require any further detection.

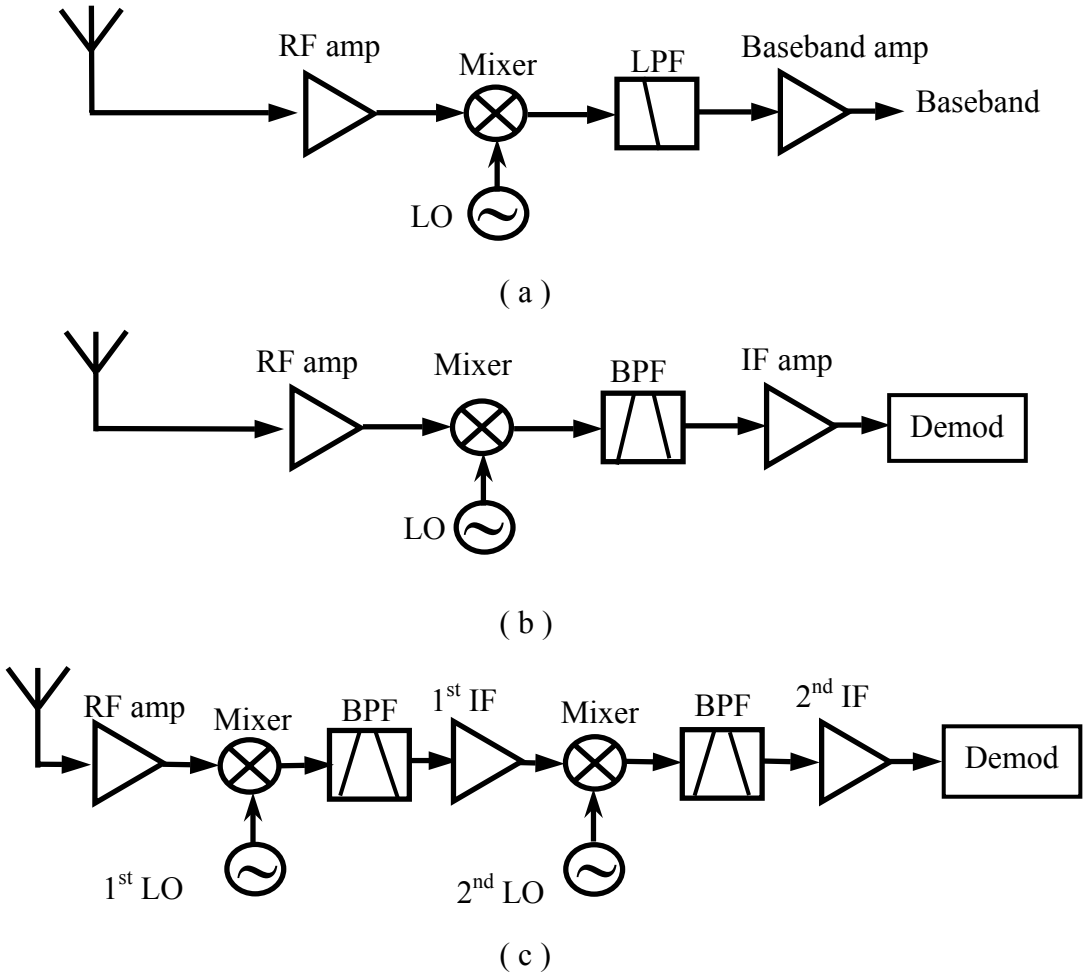


**Figure 1.8** Block diagrams of wireless receiver architectures. (a) Direct conversion (homodyne) receiver. (b) Super heterodyne receiver. (c) Dual conversion superheterodyne receiver.

*Superheterodyne Receiver*: By far the most popular type of receiver used today is the superheterodyne architecture shown in Fig. 1.8(b). In this design the intermediate frequency (IF) is not zero. A midrange IF allows the use of an IF amplifier. Tuning is conveniently accomplished by varying the frequency of the

local oscillator so that the IF frequency remains constant. At microwave and mm-wave frequencies it is often necessary to use two stages of down-conversion to avoid problems due to LO stability. The dual-conversion superheterodyne receiver of Fig. 1.8(c) employs two local oscillators and mixers to achieve down-conversion to baseband with two IF frequencies.

*Self-heterodyne Receiver*: Recently a novel receiver design has been proposed for mm-wave indoor wireless video distribution [48,49]. In this architecture the local oscillator is transmitted along with the signal. The signal is down-converted to IF frequencies by mixing the received local oscillator and the signal in a self-mixer. So the high-frequency local oscillator is eliminated. The term *self-heterodyne* implies a heterodyne receiver that relies on self-mixing rather than mixing with a local oscillator. In Chapter 4 we will show that by eliminating the IF stage the self-mixing technique may be employed in a self-homodyne photonic receiver that down-coverts the baseband information in optical domain.

Currently one of the main challenges in wireless receiver design is to increase the carrier frequency and design efficient wireless links at mm-wave frequencies [50-54]. Recently a 24 GHz CMOS front-end has been demonstrated in a 0.18μm process that consist of a low-noise amplifier (LNA) and a mixer that down-converts an RF input of 24 GHz to an IF of 5 GHz [53]. Today's frequency performance limitations of CMOS technology has led to use of alternative material systems for 60 GHz applications. Preliminary studies and experiments show a 60 GHz transceiver circuit based on SiGe bipolar technology is achievable [54].

The NEC group has developed a 60 GHz transmit/receive electronic analog RF front-end module using 0.15 μm gate-length AlGaAs/InGaAs heterojunction FETs with $f_{max}$ > 220 GHz for electronic circuitry and a $Ba(Mg,Ta)O_3$ dielectric resonator to stabilize a fixed frequency, low phase-noise, local oscillator (LO). The packaged device occupies a volume of $900mm^3$ and consumes 400mW power [51].

Operation at carrier frequencies above 60 GHz is an opportunity for new system design as well as a change in device technology because the conventional electronic devices lose their efficiency to a level that cannot easily be compensated for by novel system designs.

Processing the received RF/mm-wave signal in the optical domain is a promising alternative to conventional electronic with the potential benefit of reduced power consumption as well as reduced device volume. In this thesis we investigate some of the possibilities of employing photonic technology in wireless receiver design.

## 1.3 Resonant optical modulator

### 1.3.1 Optical resonance

In an optical resonator energy is confined in a small volume by means of multi-reflections at low loss and high reflectivity interfaces. The photons are trapped in the resonator for a relatively long period of time (compared to the time for a single pass

through the resonator). The resonance boundary conditions impose a constraint on the frequency of the resonant photons thus only photons within a limited bandwidth around certain frequencies can resonate in the cavity. Spatial confinement, long photon lifetime and frequency selectivity are the main traits of the optical resonance that can be used in many photonic devices.

The average amount of time that a photon stays in the resonator is called photon life time ($\tau_p$) and can be estimated as $\tau_p = Q/\omega$, where $Q$ is the quality factor of the resonance and $\omega$ is the photon frequency. The number of photons inside the resonator can be written as [65]:

$$N(t) = N_0 e^{-(\omega/Q)t} \tag{1.1}$$

where $N$ is the number of photons in the resonator at time $t$, $N_0$ is the initial number of photons in the cavity. So at time $t = \tau_p$ the number of photons in the cavity (initially $N_0$) reduces to $(1/e)N_0$. The photon lifetime ($\tau_p$) can also be written as [65]:

$$\tau_p = \frac{\tau_{RT}}{1 - S} \tag{1.2}$$

where $\tau_{RT}$ is the photon roundtrip time and $S$ is the survival factor or the number of photons surviving in a roundtrip. Evidently a long photon life time or high-$Q$ requires a low-loss resonator.

For a resonator with an effective refractive index $n$, $\tau_p$ can be translated to an effective length $L_{eff} = \tau_p c/n$ that is the characteristic length a photon travels before escaping from the resonator. In electro-optic applications, the long photon lifetime can be used to enhance the interaction between the electro-optic medium and the photon in a very small volume.

A well-known optical resonator is the Fabry-Perot (FP) resonator. It is a linear resonator with two reflecting boundaries. The spectrum of the transmitted optical power through a Fabry-Perot resonator is a series of equally spaced peaks. The frequency interval between the peaks is called the free-spectral-range (FSR). The full-width-half-maximum (FWHM) of each peak is $\Delta\nu_{FWHM} = Q/\nu_{res}$ where $\nu_{res}$ is the resonant frequency. The FSR and the $Q$ of a Fabry-Perot resonator are determined by the mirror reflections, and the length of the resonator. Fig. 1.9(a) shows the geometry of a Fabry-Perot resonator.

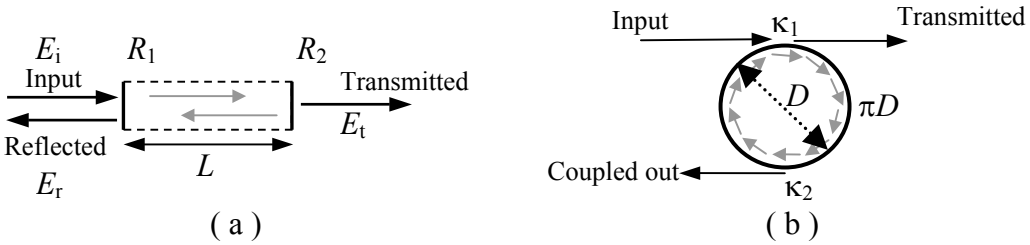


**Figure. 1.9** (a) Geometry of a Fabry-Perot standing wave resonator. Input electric field is $E_i$, reflected field is $E_r$ and transmitted field is $E_t$. The cavity is of length $L$ and the reflectivity of the two mirrors is $R_1$ and $R_2$. (b) Geometry of a circular traveling wave resonator.

The input optical power is coupled to the resonator through a mirror of reflectivity $R_1$. The reflected and transmitted power spectrum can be calculated in terms of the resonator length, loss factor inside the resonator, and mirror reflections. Table 1.1 summarizes the main parameters of a Fabry-Perot resonator and their relations.

Ring resonators are another important category of optical resonator. The main difference between a ring resonator and a Fabry-Perot resonator is the fact that the electromagnetic field in a Fabry-Perot resonator has a standing wave distribution but in a ring resonator it can be a traveling wave. In a ring resonator the reflecting

surfaces are distributed around the periphery of the resonator and the traveling wave is continuously reflected while it travels around the resonator. If the ring resonator has a spherical geometry the lowest order fundamental traveling resonance is WG mode.

Coupling into and out of a ring resonator can be achieved by means of evanescent coupling from a media that has a larger refractive index than the resonator

**Table 1.1** Summary of Fabry-Perot formulas

| Quantity | Relation with other parameters |
|---|---|
| Round-trip phase shift (RTPS) | $\theta = \frac{n\omega L}{c}$ |
| Transmitted power $T = \frac{\lvert E_t \rvert^2}{\lvert E_i \rvert^2}$ | $T = \frac{(1-R_1)(1-R_2)}{(1-\sqrt{R_1R_2})^2 + 4\sqrt{R_1R_2}\sin^2\theta}$ |
| Reflected power $R = \frac{\lvert E_r \rvert^2}{\lvert E_i \rvert^2}$ | $R = \frac{(\sqrt{R_1}-\sqrt{R_2})^2 + 4\sqrt{R_1R_2}\sin^2\theta}{(1-\sqrt{R_1R_2})^2 + 4\sqrt{R_1R_2}\sin^2\theta}$ |
| Quality factor $Q = \frac{\nu_0}{\Delta\nu_{FWHM}}$ | $Q = \frac{2\pi nL}{\lambda_0} = \frac{(R_1R_2)^{1/4}}{1-(R_1R_2)^{1/2}}$ |
| Finesse $F = \frac{\nu_{FSR}}{\Delta\nu_{FWHM}}$ | $F = \frac{c/2nL}{\Delta\nu_{FWHM}} = \frac{\pi(R_1R_2)^{1/4}}{1-(R_1R_2)^{1/2}}$ |
| Free spectral range (FSR) | $\Delta\nu_{FSR} = \frac{c}{2nL}$ |

Thus the input/output coupling mirrors in a Fabry-Perot resonator ($R_1$ and $R_2$) are replaced by the couplers ($\kappa_1$ and $\kappa_2$). Fig. 1.9(b) shows the basic geometry of a ring resonator. By carefully replacing the reflectivity ($R_i$) with coupling factor ($\kappa_i$) and the length ($L$) with circumference ($2\pi R$) most formulas from Table 1.1 can be used for a ring resonator. Notice that the optical power coupled out from the second

coupler in a ring resonator is equivalent to the reflected optical power in the Fabry-Perot resonator.

The FSR of a ring resonator can be written as: $\Delta\nu_{FSR} = \frac{c}{2nL}$ , where $R$ is the ring radius. Fig. 1.10(a) shows the FSR against the disk diameter for an average size ring resonator made of $LiNbO_3$ ($n$ = 2.14).

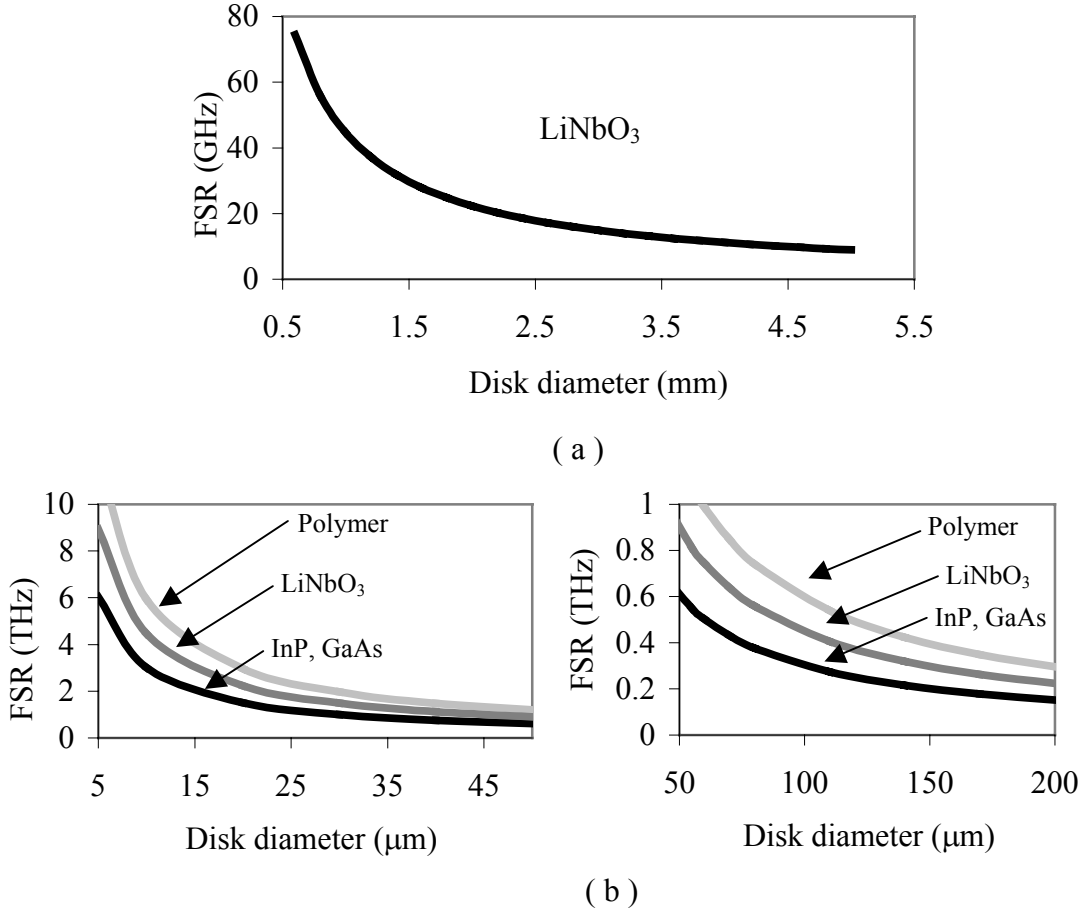


**Figure 1.10** (a) FSR of a $LiNbO_3$ average size microdisk optical resonator against its diameter. (b) FSR of polymer, $LiNbO_3$ and semiconductor microdisk optical resonators against their diameter.

Fig. 1.10(b) shows the FSR of a microring resonator made of polymer ($n$ = 1.5), $LiNbO_3$ and semiconductor ($n$ = 3.4) against their diameter.

### 1.3.2 Electrical resonance

An electrical resonator is the equivalent of an optical resonator at relatively low frequencies (MHz-GHz). The main difference is that in most electric resonators the wavelength is similar in value to the resonator dimensions or larger ($\lambda/L \geq 1$), while in most optical resonators the wavelength is much smaller than the resonator dimensions ($\lambda/L << 1$). So even in RF resonators with ring geometry the resonances are standing waves. Due to this difference the behavior of RF resonator is better understood as the energy exchange between electric and magnetic field oscillations rather than a traveling wave.

The operation of most electronic resonators can be explained in terms of lumped-element resonators of circuit theory. The most basic resonant circuits are series and parallel *RLC* resonant circuits.

Fig. 1.11(a) and (b) show series and parallel *RLC* resonators respectively. Table 1.2 summarizes the relation among the key parameters of series and parallel *RLC* resonators. For opto-electronic applications the most commonly used resonator structures are microstripline based.

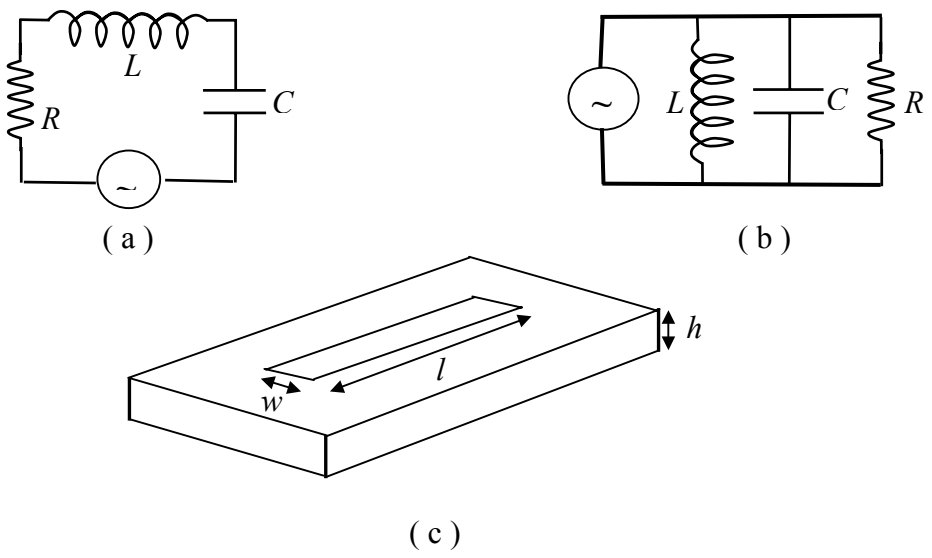


**Figure 1.11** (a) Series resonant circuit. (b) Parallel resonant circuit. (c) Open ended microstrip resonant circuit

The simplest microstripline resonator is an open ended rectangular patch on a dielectric substrate (Fig. 1.11(c)). Because of its application in RF filter design, various aspects of this resonator have been the subject of research for a long time [66,67]. The properties of the microstrip resonator are determined by its geometry and permittivity and the loss tangent of the dielectric substrate. In a resonant electro-optic modulator, we intent to use these resonators to control and amplify the *E*-field in certain regions.

Using the relations in Table 1.2, one can easily derive the voltage across the capacitor in a series *RLC* circuit at resonance ($\omega = \omega_0$):

$$|V_c| = |V_{in}| \sqrt{\frac{Q}{C|Z_{in}|\omega_o}} \tag{1.3}$$

This equation shows that a series *RLC* resonant circuit can amplify the voltage with a factor proportional to $\sqrt{Q}$. So any distributed element circuit whose equivalent

circuit may be simplified as a series lumped element resonant circuit, in principle, will have the same voltage amplification factor ($\propto\sqrt{Q}$). It is evident that $C$, $R$ and $L$ should be derived in terms of the geometrical and dielectric properties of the distributed element resonant circuit.

**Table 1.2** Summary of main formulas of series and parallel resonant circuits

| Quantity | Series *RLC* resonator | Parallel *RLC* resonator |
|---|---|---|
| Average magnetic energy stored in the inductor ($W_m$) | $W_m = \frac{1}{4}\lvert I\rvert^2 L$ | $W_m = \frac{1}{4}\lvert V\rvert^2 \frac{1}{\omega^2 L}$ |
| Average electric energy stored in the capacitor ($W_e$) | $W_e = \frac{1}{4}\lvert V_c\rvert^2 C$ | $W_e = \frac{1}{4}\lvert V_c\rvert^2 C$ |
| Power loss | $P_{loss} = \frac{1}{2}\lvert I\rvert^2 R$ | $P_{loss} = \frac{1}{2}\frac{\lvert V\rvert^2}{R}$ |
| Unloaded quality factor ($Q_{RF,U}$) | $Q_{RF,U} = \omega\frac{W_e + W_m}{P_{loss}} = 1/\omega_0 RC$ | $Q_{RF,U} = \omega\frac{W_e + W_m}{P_{loss}} = 1/\omega_0 RC$ |
| Resonant frequency ($\omega_0$) | $\frac{1}{\sqrt{LC}}$ | $\frac{1}{\sqrt{LC}}$ |
| Input impedance ($Z_{in}$) | $Z_{in} = R + j\omega L - j\frac{1}{\omega C}$ | $Z_{in} = \left(\frac{1}{R} + \frac{1}{j\omega L} + j\omega C\right)^{-1}$ |

### 1.3.3 Resonant electro-optic modulation

Resonant optical modulators use resonance to enhance the electro-optical interaction through amplified *E*-field and/or longer interaction length. These modulators can be divided into three main categories depending on the nature of the resonance that is employed in their design: electrical, optical or both. Electric resonance increases the

*E*-field intensity and optical resonance increases the interaction length, in both cases frequency bandwidth is sacrificed for modulation efficiency. Resonant modulators can only perform efficient modulation within limited bandwidth around discrete RF center frequencies defined by integer multiples of optical free spectral range or RF resonant frequencies. Operation in simultaneous electrical and optical resonance operation requires a resonant RF equal to the optical FSR or an integer multiple of the FSR. The modulation bandwidth is limited by the highest quality factor (which in most cases we will consider is the optical *Q*).

The concept of resonant modulation has been investigated since 1962 [58] and many resonant modulators have been developed using different types of electrical and optical resonators [55-80]. Although MZ modulators with bandwidth in excess of 40 GHz have been demonstrated [15], such devices exhibit only modest RF conversion efficiency. Wireless communication typically doesn't require MZ's broadband response. For example Personal Communication Systems (PCS) standards require only 60 MHz bandwidth around the center frequency of 1.9 GHz, allowing great potential for optimization of modulation efficiency through resonant enhancement.

Fig. 1.12(a) shows the schematic diagram of an electrically resonant modulator. In this configuration the RF-resonance is achieved by introducing impedance discontinuities at RF input and output ports of the electrode in an MZ modulator. RF resonance occurs at 540 MHz with a bandwidth of 92 MHz. 10 dB enhancement over a regular impedance matched traveling wave modulator has been reported [70].

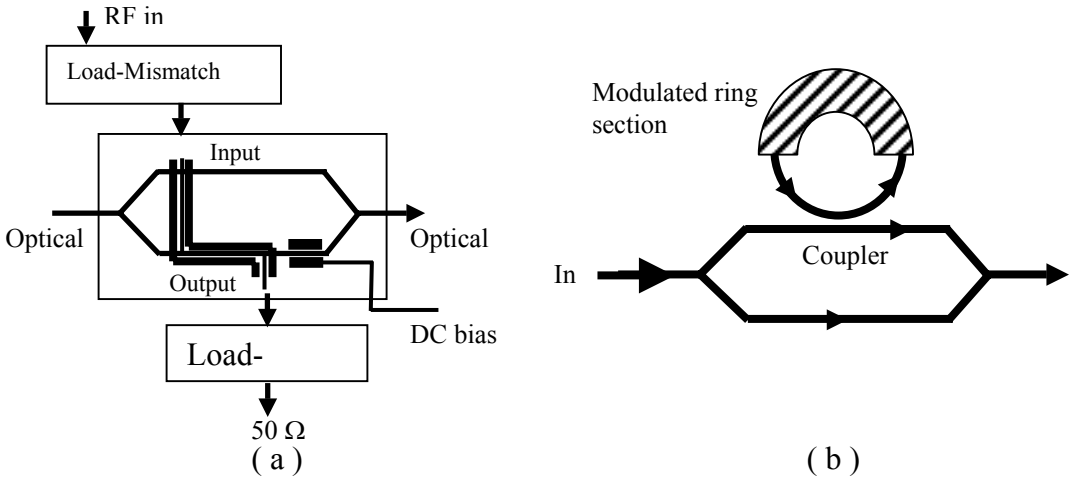


**Figure 1.12** (a) An electrically resonant MZ-modulator. 10 dB enhancement through electrical resonance has been achieved [70]. (b) An optically resonant modulator. 5 dB enhancement compared to a straight waveguide of length equal to the ring has been reported [60].

Fig 1.12(b) shows an optically resonant modulator where a ring resonator is side-coupled to one arm of a MZ modulator.

The ring is made of 25 InGaAsP/InP quantum-wells and its refractive index is sensitive to applied *E*-field across the ring. A semi-ring metal electrode that is placed on top of the ring provides the modulating *E*-field.

The ring effectively increases the electro-optic interaction length in the active arm and enhances the sensitivity of the device. The optical-*Q* of the resonator is 4500 and 5 dB enhancement compared to a straight waveguide of length equal to the ring has been reported [60].

It is important to mention that in optically resonant modulators (unlike MZ modulators) $V_\pi$ is not a well-defined quantity since the device does not work based on MZ interference principle. Instead there is a Lorentzian transfer function whose

resonant wavelength changes as a function of applied electric field. In this case the voltage $V_{FWHM}$ required to shift the resonance by $\Delta\nu_{FWHM}$ (where $\Delta\nu_{FWHM} = Q/\nu_{res}$, $\nu_{res}$: optical resonant frequency) may be used to quantify the modulator performance. Another definition used as a measure of modulator sensitivity is the variation of the optical intensity with respect to voltage at the half-transmission point: $\left.\frac{dP_{o,out}}{dV}\right|_{1/2}$.

For a MZ modulator this quantity is related to $V_\pi$ by: $V_\pi = \frac{\pi}{2}\left(\left.\frac{dP_{o,out}}{dV}\right|_{1/2}\right)^{-1}$ [59]. This relation can be used to define an equivalent $V_\pi^{eq}$ for a resonant modulator. If one uses the bandwidth/voltage ratio ($f_{3dB}/V_\pi^{eq}$) as the figure of merit for an electro-optic modulator, traveling wave MZ modulators outperform resonant modulators [59]. Although using $f_{3dB}/V_\pi^{eq}$ as a figure of merit is a reasonable choice for broadband optical communication applications, it is not a suitable choice for RF-subcarrier optical links where a limited bandwidth around a high-frequency carrier is usually required.

**Modulation bandwidth limitation imposed by optical resonance**

The modulation bandwidth of an optically resonant modulator is limited by spectral linewidth and the free spectral range. Using the optical transmission spectrum of the modulator, the modulation spectrum can be qualitatively explained as follows:

The optical transmission spectrum of the modulator is a series of equally spaced Lorentzians with linewidths of $\Delta\nu_{FWHM}$ ($\Delta\nu_{FWHM} = Q/\nu_{res}$) separated by $\Delta\nu_{FSR}$ as shown in Fig. 1.13 ($\Delta\nu_{FSR} = c/2\pi Rn_e = 1/\tau_{rt}$. $\tau_{rt}$ = optical roundtrip time of the

resonator). Through the modulation process optical power is coupled out from $\nu_{laser}$ (optical carrier frequency) into optical sidebands $\nu_{laser} \pm f_{RF.}$ All of these frequencies ($\nu_{laser} \pm f_{RF}$, $\nu_{laser}$) have to be resonant inside the microdisk so that optical energy cannot be pumped into them. The optical transmission spectrum can be used as a filter that modifies the optical spectrum of the modulated signal. Assuming the laser frequency is tuned to $\nu_m$- $\Delta\nu_{FWHM}$ /2 (middle of the slope), when $f_{RF} \leq \Delta\nu_{FWHM}$ /2 both sidebands would be inside the *m*-th resonance so the output will be modulated (Fig. 1.13(a)).

Now as we increase $f_{RF}$ the optical power in the sidebands decreases until they are completely filtered out (Fig. 1.13(b)). So low frequency modulation is allowed with a bandwidth of about $\Delta\nu_{FWHM} / 2$. If we continue increasing $f_{RF}$, at $f_{RF} \approx \Delta\nu_{FSR}$ again the sidebands become resonant (Fig. 1.13(c)). It is obvious that since the spectral linewidth is $\Delta\nu_{FWHM}$, the modulation bandwidth around $\Delta\nu_{FSR}$ is $\Delta\nu_{FWHM}$. The same situation is periodically repeated around $f_{RF} = m \times \Delta\nu_{FSR}$ (*m* is an integer).

We may conclude that only RF frequencies less than $\Delta\nu_{FWHM}/2$ and within a $\Delta\nu_{FWHM}$ bandwidth centered around integral multiples of the optical FSR can modulate the optical mode. We refer to the low frequency modulation as *linewidth* modulation and the modulation at $m \times \Delta\nu_{FSR}$ ($m \neq 0$) as FSR modulation.

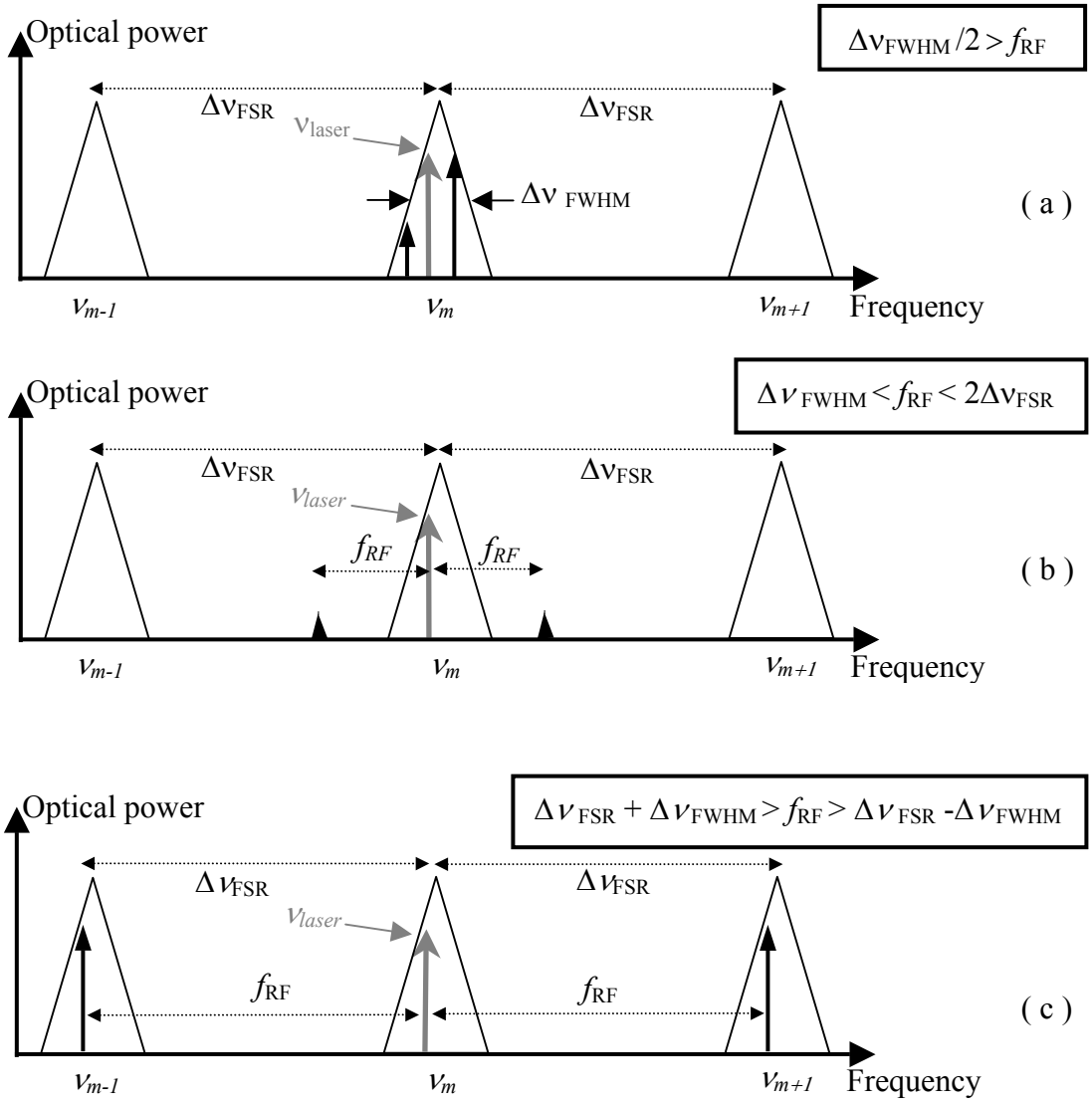


**Figure 1.13** Qualitative behavior of the frequency response based. (a) Linewidth modulation: the RF carrier frequency is smaller than $\Delta\nu_{FWHM}/2$. Polymer and semiconductor microring and microring resonators work in this regime. (b) No modulation: the RF frequency is larger than optical bandwidth but smaller than the optical free-spectral-range so the RF-optical sidebands are filtered out by the optical transfer function. (c) FSR modulation: The RF-optical sidebands are within the adjacent resonances. $LiNbO_3$ microdisk modulator works in this regime.

Fig. 1.14(a) shows the ideal frequency response of a resonant optical modulator (solid line) and a traveling wave optical modulator (dashed line).

In both cases we assume the RF and optical waves are phase matched and the high frequency response of the modulator is limited by electrical losses. We should point out that here we want to have a qualitative estimation of the modulation and the details strongly depend on the specific modulator design. As may be seen at high-frequencies where the sensitivity of the traveling wave modulator is reduced we expect better sensitivity from the resonant modulator, even though within a small bandwidth around $m \times \Delta\nu_{FSR.}$. The bandwidth limitation imposed by $\Delta\nu_{FWHM}$ and $\Delta\nu_{FSR}$ may challenge the usefulness of employing high-$Q$ resonant modulators for broadband optical communications where data rates as high as 40 Gb/s are currently achieved by traveling wave modulators.

However in most RF-subcarrier links and also wireless communications broadband is unnecessary. In such circumstances resonant microdisk modulators offering efficient modulation around a high frequency carrier may represent a competitive technology. Since the center frequencies ($m \times \Delta\nu_{FSR}$) are determined by the refractive index and the diameter of the disk, the RF carrier frequency imposes limitation on the disk size and the electro-optic material. For example Fig. 1.10(b) shows that for current wireless applications, where the carrier frequency is between 1 GHz 1 and 60 GHz, the small size polymer and semiconductor microdisks cannot be used for FSR modulation because their FSR is in THz regime. In contrast, the FSR of the average size $LiNbO_3$ microdisks is about 5 to 50 GHz and so is suitable for many wireless applications.

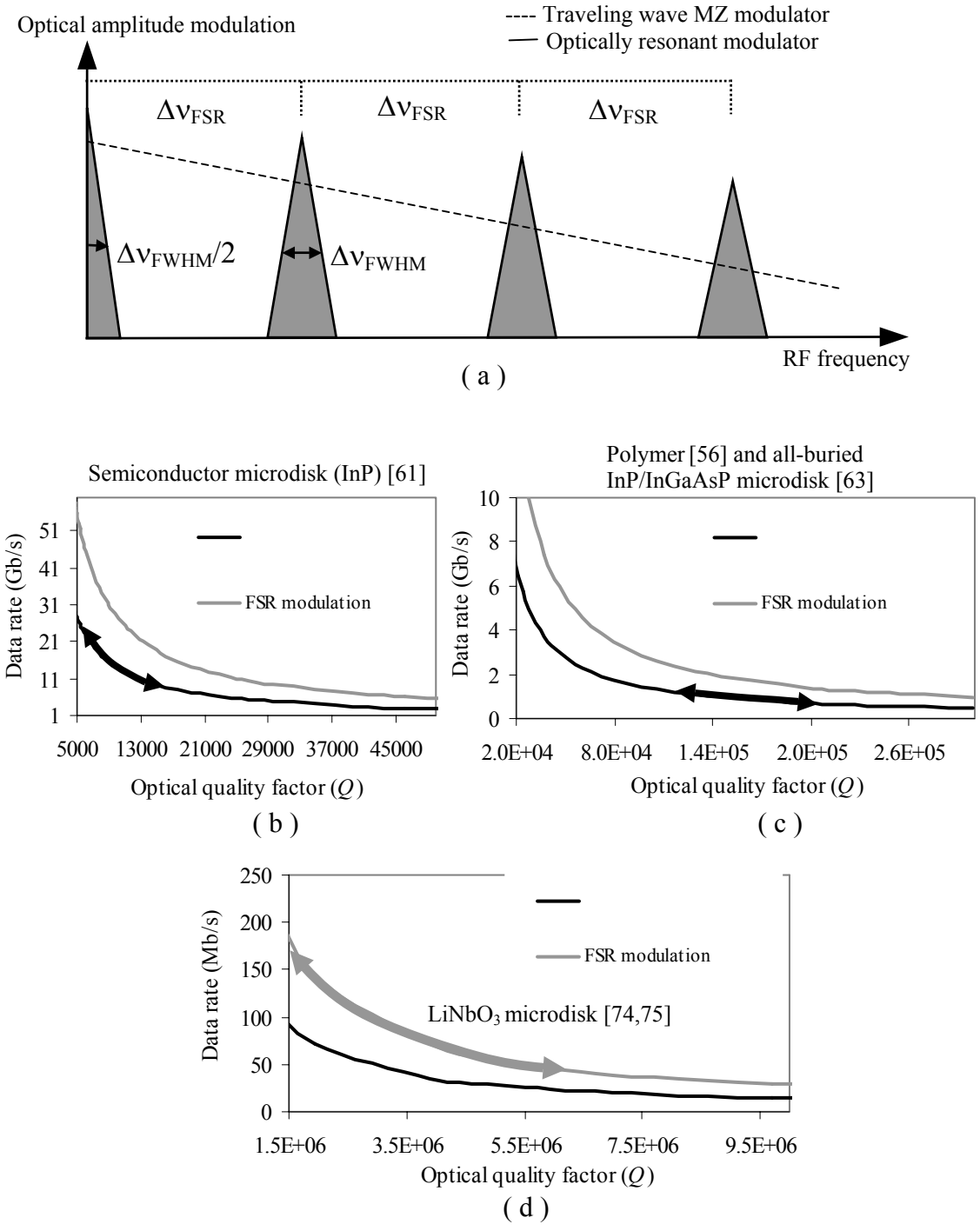


**Figure 1.14** (a) Ideal frequency response of a resonant optical modulator (solid line) and a traveling wave optical modulator (dashed line). (b), (c) and (d) Digital modulation bandwidth of microdisk modulator against optical quality factor in baseband and FSR modulation regimes.

Fig 1.14 (a), (b) and (c) show the digital modulation bandwidth of baseband and FSR modulation as a function of optical-$Q$ for microdisk modulator technology we have developed. The digital modulation bandwidth (data rate) is estimated knowing that if the analog bandwidth is about 70% of digital bandwidth an acceptable BER (below $10^{-9}$) can be achieved. As may be seen semiconductor microdisk modulators can provide a bandwidth of about 20 Gb/s using baseband modulation (assuming the electronic properties do not limit the modulation speed). High-$Q$ polymer modulators have a modulation bandwidth of about 3 Gb/s again in the baseband modulation regime [56]. Low-$Q$ polymer modulators may have bandwidths as high as 15 GHz [64] but their sensitivity is too low for practical applications. Due to its high quality factor, $LiNbO_3$ microdisk modulator has a bandwidth of about 100 Mb/s using FSR modulation.

## 1.4 Microdisk and microring optical modulators

The microdisk modulator is a traveling–wave optical resonator made of electro-optic material with an electrode structure that provides the modulating $E$-field in the optical mode region. Because of the high quality factor of whispering-gallery (WG) modes inside the microdisk ($10^6$ - $10^7$) the photon lifetime is large and therefore efficient electro-optic interaction becomes possible in a small volume. If the electrode is also designed as a RF-resonator with a fundamental resonant frequency

equal to the optical free spectral range of the microdisk, simultaneous RF-optical resonance can be achieved, which makes the modulator more sensitive.

### 1.4.1 $LiNbO_3$ microdisk modulator

The first microdisk modulator reported was fabricated in $LiNbO_3$ [74,75] and to our knowledge it is the only modulator that is both optically and electrically resonant. It consists of a microdisk optical resonator, a RF resonator and coupling structures for optical and RF coupling to these resonators.

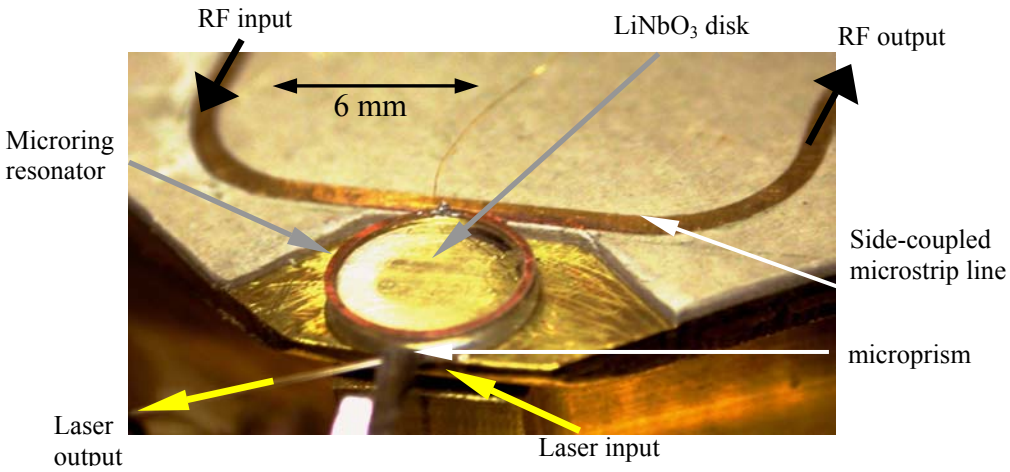


**Figure 1.15** Photograph of a $LiNbO_3$ microdisk modulator ($D$ = 5.8 mm) with RF-ring resonator and single-prism optical coupling.

The optical resonator is fabricated from a disk shaped $z$-cut $LiNbO_3$. Fig. 1.15 shows the photograph of a $LiNbO_3$ microdisk modulator.

The basic geometry of the $LiNbO_3$ resonator is a disk of radius $R$, and thickness $h$. The sidewalls of the disk are optically polished with a radius of curvature $R_s$, which is typically equal to the radius of the disk (since the disk is usually made by thinning a sphere down to the desired thickness). The RF resonator is a full-ring or half-ring copper electrode placed on top of the disk with a radius equal to the radius of the disk. Light is coupled into and out of the disk by using a single or double prism coupling method. RF power is coupled to the half-ring (or ring) by side coupling to a microstrip line that can be open or 50 Ω terminated. TE polarized ($E$-field parallel to $c$-axis) optical WG modes inside the microdisk are exited with a single mode DFB laser ($\lambda$ = 1550 nm) and detected with a cleaved (or lensed) fiber. The fundamental resonant frequency of the standing wave RF-resonator is equal to the FSR of the disk. Therefore, by feeding the microstrip line at $f_{RF} = \Delta\nu_{FSR}$, simultaneous electrical and optical resonance is achieved. It has been shown that, unlike the Mach–Zehnder modulator, the microdisk can perform efficient optical modulation without use of a reference arm to convert phase to amplitude modulation [80].

### 1.4.2 Polymer microring modulator

Polymer microring modulators have been recently developed based on similar principles as $LiNbO_3$ microdisk modulator [56,64] but they use electro-optic polymers instead of $LiNbO_3$ as their active media. These materials have been

previously used for making regular MZ modulators [16,17]. Fig. 1.16 shows the layout and the cross section of the fabricated device. A micro-ring waveguide made of electro-optic polymer material (M1) is vertically coupled to the input and output ridge-waveguides made of a different material (M2). The space between the waveguides and the microring resonator is filed with a third material (M3) that has a lower refractive index than M1 and M2. A gold-ring on top of the device provides the modulating *E*-field around the ring.

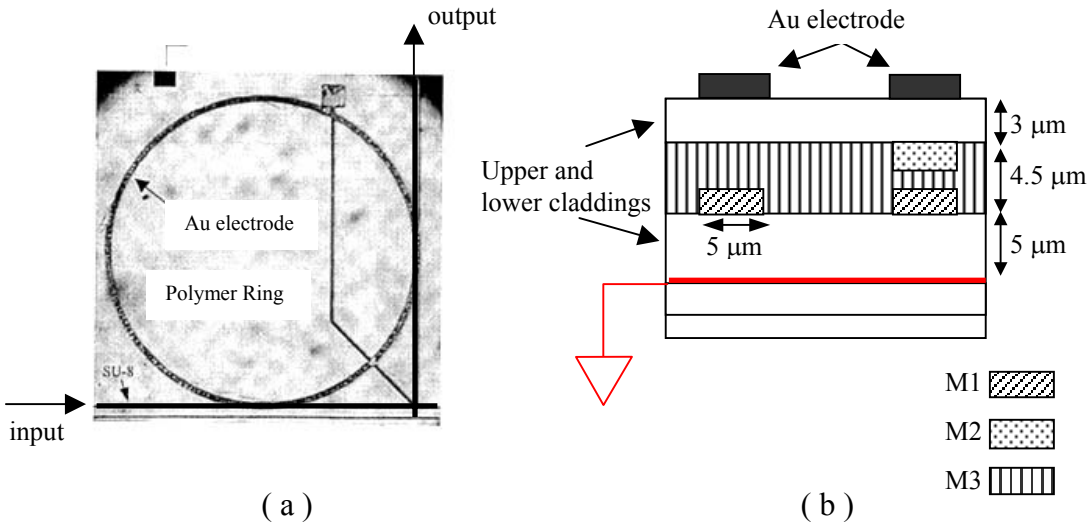


**Figure 1.16** (a) Layout photograph of the fabricated device showing polymer microring waveguide ($D$ = 500 μm) vertically coupled to perpendicular straight waveguides. (b) Schematic diagram of the device cross-section showing the material system and dimensions.

It is important to notice that in this case the ring is not an RF-resonator because it is much smaller than the microwave wavelength and its high-speed behavior is mainly capacitive [64]. So the polymer microring resonators are optically resonant modulators similar to the MZ modulator in Fig. 1.12(b).

The FSR and optical-$Q$ of the ring as well as coupling efficiency between the wave guide and the resonator are determined by refractive index contrast (M2-M3 and M1-M2), size and spacing. Maximum possible refractive index contrast using polymer materials is about 0.3.

The typical $Q$ of these devices is about 5-8×$10^4$. The $Q$ and hence the sensitivity of polymer microdisk modulators depends of the device diameter, optical mode polarization (TE or TM) and the resonant wavelength. At $\lambda_{res}$ = 1300 nm a polymer microdisk with a 1.5 mm diameter has a $Q$ of 6.2×$10^4$ for TE polarized modes ($E$-field perpendicular to the disk surface) and a $Q$ of 7.6×$10^4$ for TM polarized modes [56]. These $Q$s correspond to bandwidths of 3 GHz and 4 GHz respectively. The FWHM-shift-voltage ($V_{FWHM}$) is about 4.86 Volt for this device. At $\lambda_{res}$ = 1550 nm the $Q$ drops to almost half of its value at 1300 nm and the $V_{FWHM}$ is about 16 V. Reducing the microdisk diameter increases the bending loss and therefore decreases the $Q$. A 3 mm diameter polymer microdisk has a $Q$ of 4.7×$10^4$ for TE polarized modes ($E$-field perpendicular to the disk surface) and a $Q$ of 5.8×$10^4$ for TM polarized modes [56].

### 1.4.3 Semiconductor microdisk modulator

Microdisk optical modulators have been also fabricated based on III-V semiconductor materials. One of the first examples is an InP microdisk resonator

vertically coupled to two parallel waveguides [62] similar to the one shown in Fig.1.6(b). The microdisk has a radius of 10 μm, an optical-$Q$ of about 5500 ($\Delta\nu_{FWHM}$ 0.27 nm), and a FSR of 10 nm. The change in effective refractive index in this microdisk is achieved by free carrier injection (FCI). It is also possible to incorporate quantum wells with emission wavelength near 1550 nm to define a gain region that can controls optical loss in the WG cavity.

The measured response of the FCI device shows a modal index change of $-2\times10^{-3}$ /mA. The maximum tuning range is limited by the cavity heating. Increasing the drive current in a microdisk with active QW region near the bandgap decreases the loss in the cavity and increases the $Q$. At around 10 mA injected current the device acts as an amplifier and increases the optical power in the drop channel. Applying a reverse bias on the active microdisk, shifts the absorption edge towards longer wavelengths by a slope of about 0.06 nm/V corresponding to an index change of about $4\times10^{-4}$. Any of these changes may be used for switching or modulating the coupled optical power to the drop or transmission channel.

When free carrier injection is used to change the refractive index, the modulation bandwidth is limited by the minority carrier lifetime. So achieving a large modulation bandwidth requires use of other electro-optic mechanisms in the semiconductor. An externally applied electric field can change the refractive index of a p-n junction by changing the depletion. Recently a semiconductor microdisk modulator has been demonstrated that uses this mechanism for electro-optic modulation [63]. The active microdisk is made of a InGaAsP p-n junction and has a

$Q$ of about 8500 ($\Delta\nu_{FWHM}$ = 0.18 nm). Using this device a modulation bandwidth of about 8 GHz has been achieved at a modulation voltage of less than 1 V.

## 1.5 Microdisk photonic RF receiver

In a photonic RF-receiver, the intent is to replace all the electronic components of a conventional RF receiver with photonic elements that, in principle, they are smaller and consume less power. Processing RF and mm-wave signals in the optical domain reduces the design and performance issues associated with high-frequency electronics. In a photonic receiver, the carrier frequency may be extended from a few GHz to mm-wave frequencies without any major change in system architecture since eventually the signal is processed in the optical domain. The photonic RF receiver also benefits from optical isolation wherever protection from interference with environmental and unwanted signals is required.

The 60 GHz transmit/receive electronic analog RF front-end module developed by NEC [51] consumes 1.2 W of which 0.4 W is used for the receiver with a digital bandwidth of 10 Mb/s, sensitivity of 10 μW and a volume of 900 $mm^3$. We will show that a photonic receiver can provide the same sensitivity and bandwidth in a smaller volume and less power consumption.

In the photonic RF-wireless receiver shown in Fig. 1.17, the electromagnetic radiation detected by the receiving antenna modulates a laser beam. Through signal

processing in the optical domain using optical filtering, optical mixing, and photodetection, the electrical baseband information signal is extracted from the received RF/mm-wave signal.

Three mechanisms may be used to extract the baseband information in the optical domain:

1) The intensity of the optical carrier (laser) is linearly modulated by the received RF/mm-wave signal and is then detected with a *nonlinear* photodetector that generates a photocurrent proportional to the *square* of the optical power. Through nonlinear photodetection the up-converted carrier and sidebands are mixed resulting in a baseband modulated photocurrent. In this approach a very sensitive optical intensity modulator and a high-speed photodetector are required. The photodetector should operate in a strong nonlinear regime that may require a modified photodetector design.

2) The intensity of the optical carrier (laser) is linearly modulated by the received RF/mm-wave signal and is then fed to an optical filter that filters out the optical carrier and the higher frequency sideband. When this modified optical signal is fed to a photodiode, the baseband photocurrent is generated. In this approach a very sensitive optical amplitude modulator and optical filter with proper role-off and a low-speed detector are required. Since the photodetection is linear, a conventional photodetector can be used.

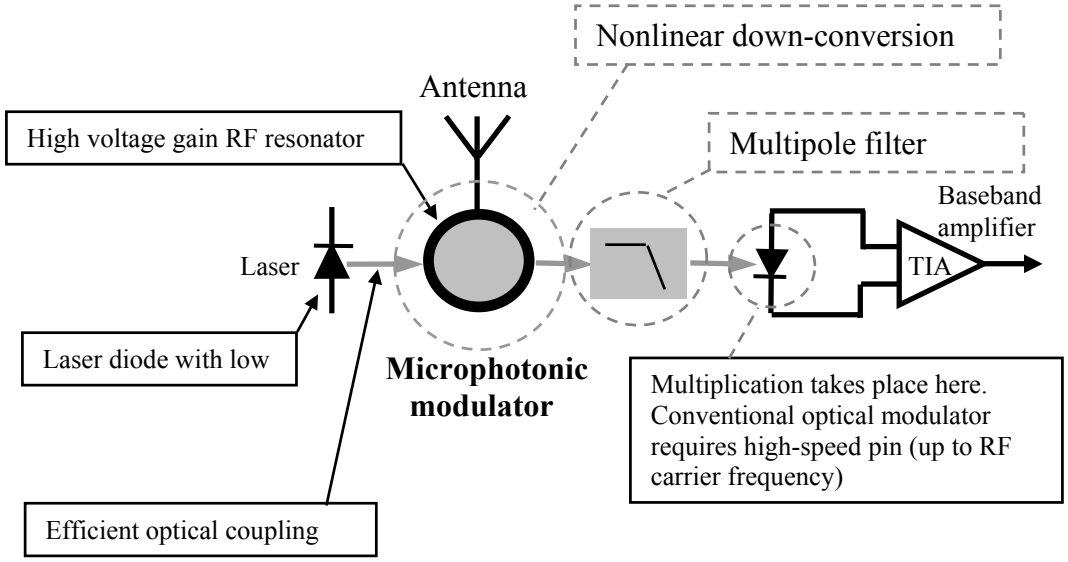


**Figure 1.17** The schematic diagram of a photonic RF-wireless receiver .

3) The intensity of the optical carrier (laser) is nonlinearly modulated by the received RF/mm-wave signal. Due to nonlinear modulation the output intensity will be baseband modulated and the baseband photocurrent is generated in a low-speed photodetector. In this approach optical filters are not required but they can be used to improve the noise performance of the receiver.

In such photonic receiver designs employing a transmitted carrier RF modulation format there is no need for a local oscillator. The mixing occurs in the optical domain and the baseband current is generated by a photodetector. In the 2$^{nd}$ and 3$^{rd}$ approach the bandwidth of the photodetector is limited to that of the baseband and no high-speed electronic components are required.

A sensitive modulator that can convert a weak detected RF-power from the antenna (μW regime) to optical modulation is a key component in all of these architectures.

The high sensitivity due to simultaneous optical and electrical resonance, small size, operation in the RF carrier frequency range of 5 GHz to 60 GHz makes the $LiNbO_3$ microdisk modulator a suitable candidate for this task.

It is useful to describe gain in the photonic RF-wireless receiver in the context of a conventional electronic RF-wireless receiver architecture. The gain in the photonic receiver is mainly provided by the RF-to-optical conversion in the modulator and optical-to-electrical baseband conversion in the photoreceiver. So basically the total gain is a combination of the modulator and photoreceiver sensitivity. For every photonic down-conversion method we can define a RF-to-baseband optical gain as:

$$G_{RF,OB} = \frac{\text{Baseband modulated optical power}}{\text{Received RF power}} \tag{1.4}$$

This gain is directly proportional to modulator sensitivity and also the chosen mechanism for down-conversion. The detector sensitivity is normally quantified as responsivity ($R$) that is the ratio between the photocurrent and the input optical power. So if we define the gain of the wireless receiver as the ratio between the down-converted baseband power and the received RF power, the overall gain of the photonic wireless receiver can be written as:

$$G_{total} = \frac{P_b}{P_{RF}} = G_{RF,OB}^2 \times R^2 \times Z_L \times P_{RF} \tag{1.5}$$

where $Z_L$ is the load impedance and $P_b$ is the down-converted baseband power.

One of the most important parameters of a wireless receiver is sensitivity. Sensitivity is defined as the minimum detectable RF power at the receiver input such that there is a sufficient signal-to-noise ratio (SNR) at the output of the receiver for a given application. So each wireless standard may require a different sensitivity.

Current wireless links are mainly digital, so the minimum SNR is translated to the maximum bit error ratio (BER) that is required in the link. In a digital photonic receiver it is convenient to use a digital photoreceiver to detect the data modulated optical power because it contains all the digital electronic circuitry integrated with the photodiode. The sensitivity ($S_d$) of a digital photoreceiver is defined as the minimum data modulated optical power required to have certain BER ($10^{-9}$) in the output. So assuming that the maximum BER required in the wireless link is the same as the BER at which $S_d$ is measured, the sensitivity of the photonic wireless receiver can be written as:

$$\text{Receiver sensitivity} = \frac{S_d}{G_{RF,OB}} \tag{1.6}$$

## 1.6 Summary

A combination of wireless system design methodologies, optical modulation and optical signal processing techniques, can result in a novel RF/mm-wave photonic wireless receiver design with reduced volume, low power consumption and no sophisticated electronic devices and circuitry. Such a photonic receiver potentially can be used in wireless LAN's, fiber-feed backbone networks and indoor wireless data/video distribution systems. We have proposed three different approaches to photonic baseband down-conversion from a RF/mm-wave signal. All of these

methods require efficient optical intensity modulation around a high-frequency carrier. Resonant optical modulators are among the best candidates for this task.

To our knowledge the $LiNbO_3$ microdisk optical modulator is the most sensitive resonant optical modulator. In this thesis we explore various aspects of employing a $LiNbO_3$ microdisk modulator in an all-optical wireless receiver.

The design and implementation of a sensitive $LiNbO_3$ microdisk modulator is explained in Chapter 2. Chapter 3 presents the experimental results of $LiNbO_3$ microdisk modulator performance in a RF-optical link. In Chapter 4 we explore the various methods for all-optical down-conversion through theory and experimental results. Finally, Chapter 5 summarizes the potential improvements that may define the road to a practical monolithic photonic RF receiver. We will also address the future challenges toward an all-optical wireless link.

## 1.7 References


RF-photonic (links and signal processing)

[1] B. Vidal, V. Polo, J. L. Corral, and J. Marti, "Efficient architecture for WDM photonic microwave filters," *IEEE Photon. Technol. Lett.*, vol. 16, pp. 257-259, Jan. 2004.

[2] P. O. Hedekvist, B.-E. Olsson, and A. Wiberg, "Microwave harmonic frequency generation utilizing the properties of an optical phase modulator," *J. of Lightwave Technol*., vol. 22, pp. 882-886, March 2004.

[3] A. Hirata, M. Harada, and T. Nagatsuma, "120-GHz wireless link using photonic techniques for generation, modulation, and emission of millimeter-wave signals," *J. of Lightwave Technol*., vol. 21, pp. 2145-2153, Oct 2003.

[4] H. Ito, T. Ito, Y. Muramoto, T. Furuta, and T. Ishibashi, "Rectangular waveguide output unitraveling-carrier module for high-power photonic millimeter-wave generation in the F-band," *J. of Lightwave Technol*., vol. 21, no. 12, pp. 3456-3462, Dec 2003.

[5] G. H. Smith, D. Novak, C. Lim, "A millimeter-wave full-duplex WDM/SCM fiber-radio access network," *OFC* technical digest, pp. 18.

[6] H. Ogava, D. Polifko, and S. Banba, "Milimeter-wave fiber optic systems for personal radio communication," *IEEE Trans. on microwave theory and techniques*, vol. 40, no. 12, pp. 2285-2293, Dec 1992.

[7] D. Novak, G. H. smith, C. Lim, H. F. Liu, R. B. Waterhouse, "Optically fed millimeter-wave wireless communication," *OFC* '98 technical digest, pp. 14.

[8] M. Hossein-Zadeh, and A. F. J. Levi, "Mb/s data transmission over a RF fiber-Optic link using a $LiNbO_3$ microdisk optical modulator", *Solid-State Electronics*, vol. 46, pp 2173-2178, 2002.

[9] "RF photonic technology in optical fiber links", Edited by William S. C. Chang. Cambridge university press, 2002.

[10] J. Oreilly and P. Lane, "Remote delivery of video services using mm-waves and optics," *IEEE J. of Lightwave Technol*., vol 12, no 2, pp. 369-375, Feb 1994.

Mach-Zhender modulator


[11] E. L. Wooten, K. M. Kissa, A. Y.-Yan, E. J. Murphy, D. A. Lafaw, P. F. Hallemeir, D. Mack, D. V. Attanasio, D. J. Fritz, G. J. McBrien, and D. E. Bossi, "A review of Lithium Niobate modulators for fiber-optic communications systems," *IEEE J. of Selected Topics in Quant. Electron.*, vol. 6, no. 1, pp. 69-82, Jan-Feb 2000.

[12] T. Nakazawa, "Low drive voltage and broad-band $LiNbO_3$ modulator", *Microwave photonics*, international conference, pp. 45-48, 2002.

[13] K. Noguchi, O. Mitomi, and H. Miyazawa, "Millimeter-wave Ti:$LiNbO_3$ optical modulators," *J. of Lightwave Technol.*, vol. 16, no. 4, pp. 615-619, April 1998.

[14] O. Mitomi, K. Noguchi, and H. Miyazawa, "Broadband and low driving-voltage $LiNbO_3$ optical modulators," *IEE Proc.-Optoelectron*., vol. 145, no. 6, pp. 360-364, Dec 1998.

[15] M. Sugiyama, M. Doi, S. Taniguchi, T. Nakazawa, and H. Onaka, "Low-drive voltage $LiNbO_3$ 40-Gb/s modulator," *IEEE LEOS news letter*, vol. 17, no. 1, pp. 12-13, Feb 2003.

[16] D. Chen, D. Bhattacharya, A. Udupa, B. Tsap, H. R. Fetterman, A. Chen, S. Lee, J. Chen, W. H. Steier, F. Wang, L. R. Dalton, "High-frequency polymer modulators with integrated finline transitions and low $V_{\pi,}$" *IEEE Photonics Lett.*, vol. 11, no. 1, pp.54-56, Jan 1999.

[17] S.-S. Lee, S. M. Garner, V. Chuyanov, H. Zhang, W. H. Steier, F. Wang, L. Dalton, A. H. Udupa, and H. R. Fetterman, "Optical intensity modulator based on a novel electro-optic polymer incorporating a high $\mu\beta$ chromophore," *IEEE J. of Quant. Electro.*, vol. 36, no. 5, pp. 527-532, May 2000.

[18] R. G. Walker, "High-speed III-V semiconductor intensity modulators," *IEEE J. of Quantum Electron.*, vol. 27, no. 3, March 91.

[19] M. Fetterman, C-P. Chao, and S. R. Forrest, "Fabrication and analysis of high-contrast InGaAsP-InP Mach-Zehnder modulators for use at 1.55-μm wavelength," *IEEE Photonics Technology Lett.*, vol. 8, no. 1, Jan 1996.

[20] K. Tsuzuki, T. Ishibashi, T. Ito, S. Oku, Y. Shibata, R. Iga, Y. Kondo, and Y. Tohmori, "40 Gb/s *n-i-n* InP Mach-Zehnder modulator with a $\pi$ voltage of 2.2 V," *Electron. Lett*., vol. 39, no. 20, pp. 1464-1466, Oct 2003.

[21] M. L. Gorodetsky, A. A. Savchenkov, and V. S. Ilchenko, "Ultimate *Q* of optical microsphere resonators," *Optics Lett.*, vol. 21, no. 7, pp 453-455, April 1996.

[22] M. L. Gorodetsky and V. S. Ilchenco, "Optical microsphere resonators: optimal coupling to high-*Q* Whispering-Gallery modes," *J. of Opt. Soc. Am. B*, vol. 16, no. 1, pp 147-154, Jan. 1999.

[23] B. E. Little, J. P. Laine, and H. Haus, "Analytic theory of coupling from tapered fibers and half-blocks into microsphere resonators," *IEEE J. Lightwave Tech*., no. 17, pp. 704-715, 1999.

[24] B. E. Little, J. P. Laine, D. R. Lim, H. A. Haus, L. C. Kimerling, and S. T. Chu, "Pedestal anitresonant reglecting waveguides for robust coupling to microsphere resonators and for microphotonic circuits," *Optics Letters*, vol. 25, no. 1, pp. 152-153, 2000.

[25] V. S. Ilchenko, X. S. Yao, and L. Maleki, "Pigtailing the high-*Q* microsphere cavity: a simple fiber coupler for optical whispering-gallery modes," *Opt. Lett*., vol. 24, pp. 723-725, 1999.

[26] M. Cai; G. Hunziker, and K. Vahala, "Fiber-optic add-drop device based on a silica microsphere-whispering gallery mode system," *IEEE Photon. Tech. Lett.*, vol. 11, pp. 686-687, 1999.

[27] M. Cai, P. O. Hedekvist, A. Bhardwaj, and K. Vahala, "5-Gbit/s BER performance on an all fiber-optic add/drop device based on a taper–resonator–taper structure," *IEEE Photon. Tech. Lett.*,vol. 12, no. 9, pp. 1177-1187, 2000.

[28] B. E. Little, J. S. Foresi, G. Steinmeyer, E. R. Thoen, S. T. Chu, H. A. Haus, E. P. Ippen, L. C. Kimerling, and W. Greene, "Ultra-compact Si-$SiO_2$ microring resonator optical channel droppingfilters," *IEEE photonics technol. Lett*., vol. 10, no. 4, pp.549-551, April 1998.

[29] J. V. Hryniewicz, P. P Absil, B. E. Little, R. A. Wilson, and P. –T. Ho, "Higher order filter response in coupled microring resonators," *IEEE photonics technol. Lett*., vol. 12, no. 3, pp. 320-322, March 2000.

[30] B. E. Little, S. T. Chu, H. A. Haus, J. Foresi, and J. –P. Lain, "Microring resonator channel droping filters," *IEEE J. Lightwave Tech.*, vol. 15, no. 6,pp. 998-1005, June 1997.

[31] D. K. Armani, T. J. Kippenberg, S. M. Spillane, and K. J. Vahala, "Ultra-high-*Q* microcavity on a chip," *Nature*, vol. 421, pp. 925-928, Feb 2003.

[32] P. Rabiei, W. H. Steier, C. Zhang, and L. R. Dalton, "Polymer micro-ring filters and modulators," *IEEE J. of Lightwave Technol*., vol. 20, no. 11, pp 1968-1974, Nov 2002.

[33] K. Djordjev, S.J. Choi, S. J. Choi, and P. D. Dapkus, "High-*Q* vertically-coupled InP microdisk resonators," *IEEE Photonics Technology Letters*, vol.14, no.3, March 2002, pp.331-333.

[34] www.csl.usc.edu (Compound semiconductor lab. University of Southern California).

[35] S. J. Choi, Q. Yang, Z. Peng, S. J. Choi, and P. D. Dapkus, "High-*Q* buried heterostructure microring resonator," *IEEE/LEOS, summer topical meetings*, 2004, CTHF1.

*Semiconductor microdisk lasers*

[36] S.L. McCall, A. F. J. Levi, R. E. Slusher, S. J. Pearton, and R. A. Logan, "Whispering mode microdisk lasers," *Appl. Phys. Lett.,* vol. 60, pp. 289-291, 1992.

[37] A. F. J. Levi, S. L. McCall, S. J. Pearton, and R. A. Logan, "Room temperature operation of submicrometre radius disk laser," *Electron. Lett*., vol. 29, pp. 1666-1667, 1993.

[38] S. M. K. Thiyagarajan, A. F. J. Levi, C. K. Lin, I. Kim, P. D. Dapkus, and S. J. Pearton, "Continuous room-temperature operation of optically pumped InGaAs/InGaAsP microdisk lasers," *Electron. Lett.,* vol. 34, pp. 2333-2334, 1998

RF ring resonator

[39] K. Chang, "Microwave ring circuits and antennas," Wiley series in microwave and optical engineering, John Wiely & Sons Inc, 1996.

[40] S.-L. Lu, and A. M. Ferendeci, "Coupling modes of a ring side coupled to a microstrip line," *Electtron. Lett.*, vol. 30, no. 16, pp 1314-1315, August 1994.

[41] Y. S. Wu, and F. J. Rosenbaum, "Mode chart for microstrip ring resonators," *IEEE trans. on microwave theory and techniques*, vol. MTT-21, pp 487-489, July 1973.

[42] G. K. Gopalakrishnan, and K. Chang, "Novel excitation schemes for the microstrip ring resonator with low insertion loss," *Electron Lett*., vol. 30, no 2, pp 148-149, Jan 1994.

[43] K. Chang, S. Martin, F. Wang, and J. L. Klein, "On the study of microstrip ring and varactor-tuned ring circuits," *IEEE trans. on microwave theory and techniques*, vol. MTT-35, no 12, pp 1288-1295, Dec 1987.

[44] I. Wolf, and V. Tripathi, "The microstrip open-ring resonator," *IEEE trans. on microwave theory and techniques*, vol. MTT-32, no. 1, pp 102-107, Jan 1984.

[45] G. K. Gopalakrishnan,B. W. Fairchild, C. L. Yeh, C.-S. Park, K. Chang, M. H. Weichold, and H. F. Taylor, "Experimental investigation of microwave-optoelectronic interactions in a microstrip ring resonator," *IEEE trans. on microwave theory and techniques*, vol. MTT-39, no 12, pp 2052-2060, Dec 1991.

[46] P. A. Bernard, andJ. M. Gautray, "Measurment of dielectric constant using a microstrip ring resonator," *IEEE trans. on microwave theory and techniques*, vol. MTT-39, no 3, pp 592-594, March 1991.

Wireless receiver

[47] D. M. Pozar, "Microwave and RF design of wireless systems," John Wiley & Sons, Inc., 2001.

[48] J. Park, Y. Wang, and T. Itoh, "A microwave communication link with self-heterodyne direct down-conversion and system predistortion," *IEEE Trans. On Microwave Theory and Tech*, vol. 50, no. 12, pp. 3059-3063. Dec 2002.

[49] Y. Shoji, K. Hamaguchi, and H. Ogawa, "Millimeter-wave remote self-heterodyne system for extremely stable and low-cost broad-band signal transmission," *IEEE Trans. on Microwave Theory and Tech.,* vol. 50, no. 6, June 2002.

[50] K. Kojucharow, H. Kaluzni, and W. Nowak, "A wireless LAN at 60 GHz-novel system design and transmission experiments," *Microwave symposium digest*, *IEEE MTT-S international*, vol. 3, pp. 1513-1516, 1998.

[51] K. Ohata, T. Inoue, M. Funabashi, A. Inoue, Y. Takimoto, T. Kuwabara, S. Shinozaki, K. Maryhashi, K. Hosaya, and H. Nagai, "Sixty-GHz-Band ultra-miniature monolithic T/R modules for multimedia wireless communication systems," *IEEE Trans. on Microwave Theory and Tech.*, vol. 11, no. 12, pp. 2354-2360, Dec 1996.

[52] S. K. Reynolds, B. Floyd, T. beukema, T. Zwick, U. Pfeiffer, and H. Ainspan, "A direct-conversion receiver IC for WCDMA mobile systems," *IEEE J. Solid-State Circuits*, vol.38, pp. 1555-1560, Sept 2003.

[53] X. Guan, A. Hajimiri, "A 24-GHz CMOS Front-End," *IEEE J. Solid-State Circuits*, vol.39, pp. 368-373, Feb 2004.

[54] S. Reynolds, B. Floyd, U. Pfeiffer, T. Zwick, "60 GHz transceiver circuits in SiGe bipolar technology," *ISSCC* 2004, session 24, pp. 442.

Resonant modulators (optical resonance)

[55] J. J. Huang, T. Chung, M. Lerttamrab, S. L. Chuang, and M. Feng, "1.55-μm asymmetric Fabry-Perot modulator (AFPM) for high-speed applications," *IEEE Photon. Technol*., vol. 14, no. 12, pp. 1689-1691, Dec 2002.

[56] P. Rabiei, W. H. Steier, C. Zhang, and L. R. Dalton, "Polymer micro-ring filters and modulators," *J. of Lightwave Technol.*, vol. 20, no. 11, Nov 2002

[57] N. Shaw, W. J. Stewart, J. Heaton, and D. R. Whight, "Optical slow-wave resonant modulation in electro-optic GaAs/AlGaAs modulators," *Electron. Lett*., vol. 35, no. 18, pp 1557-1558, Sept. 1987.

[58] E. I. Gordon and J. D. Rigden, "The Fabry-Perot electo-optic modulator," The *Bell system technical journal*, pp. 155-179, Jan. 1963.

[59] I. L. Gheorma and R. M. Osgood, Jr., "The fundamental limitations of optical resonator based high-speed EO modulators," *IEEE Photon. Technol.*, vol. 14, no. 14, pp. 795-797, June 2002.

[60] M. H. Kwakernaak, A. N. Leopre, H. Mohseni, H. An, Z. A. Shellenbarger, J. H. Abeles, J. –O, S. L. Rommel, and I. Adesida, "Eletrco-refractive low loss MMI-coupled ring resonators," *CLEO 2003* technical digest.

[61] Kostadin Djordjev; Seung June Choi, Sang Jun Choi, and P. Daniel Dapkus, "Active semiconductor microdisk devices," *IEEE J.l of Lightwave Technology*, vol.20, no.1, pp. 105-113, Jan 2002.

[62] K. Djordjev, S. S. Choi, S. J. Choi, P. D. Dapkus, "Novel active switching components," *28th European Conference on Optical Communication* (ECOC 2002), September 2002, Monday - paper 2.3.5

[63] T. Sadagopan, S. J. Choi, S. J. Choi, and P. D. Dapkus, "High-speed, low-voltage modulation in circular WGM microresonator," *IEEE/LEOS, summer topical meetings*, 2004, MC2-3.

[64] P. Rabbiei, W. Steier, C. Zhang, C.-g. Wang, H. J. Lee, E. H. Turner, and P. J. Maloney, "Polymer micro-ring modulator with 1 THz FSR," *CLEO 2002* technical digest.

[65] J. Verdein, "Laser electronics," *Prentice Hall* , 1995.

Resonant modulators (electrical resonance)

[66] T. Itoh, "Analysis of microstrip resonators," *IEEE trans. on microwave theory and techniques*, vol. 22, no. 11, pp. 946-952, 1974.

[67] A. Gopinath, "Maximum Q-factor of microstrip resonators," *IEEE trans. on microwave theory and techniques*, vol. 29, no. 2, pp. 946-952, 1981.

[68] R. Krahenbuhl, and M. M. Howerton, "Investigations on short-path-length high-speed optical modulators in $LiNbO_3$ with resonant-type electrodes," *J. Lightwave Technol.*, vol. 19, no. 9, pp. 1287-1297, Sep 2001.

[69] T. Kawanishi, S. Oikawa, K. Higuma, Y. Matsuo, and M. Izutsu, "$LiNbO_3$ resonant-type optical modulator with double-stub structure," *Electron. Lett.*, vol. 37, no. 20, pp. 1244-1246, Sep 2001.

[70] Y. S. Visagathilagar, A. Mitchel, and R. B. Waterhouse, "Fabry-Perot type resonantly enhanced Mach-Zehnder modulator," *Microwave Photonics*, MWP '99. International Topical Meeting on, vol. 1, pp. 17-20, 1999.

[71] G. K. Gopalakrishnan, and W. K. Burns, "Performance and modeling of resonantly enhanced $LiNbO_3$ modulators for low-loss analog fiber-optic links," *IEEE Trans. on Microwave Theory and Techniques*, vol. 42, no. 12, pp. 2650-2656, 1994.

Resonant modulator (electro-optical resonance)

[72] T. Kawanishi, S. Oikawa, K. Higuma, Y. Matsuo, and M. Izutsu, "Low-driving-voltage band-operation $LiNbO_3$ modulator with lightwave reflection and double-stub structure," *Electron. Lett.*, vol. 38, no. 20, pp. 1204-1205, Sept 2002.

[73] J. H. Abeles, "Resonant enhanced modulator development," *DARPA/MTO R-FLICs program: Kickoff meeting*, Aug 2000.

[74] D. A. Cohen, M. Hossein-Zadeh, and A. F. J. Levi, "High-*Q* microphotonic electro-optic modulator," *Solid-State Electron.*, vol. 45, pp. 1577-1589, 2000.

[75] D. A. Cohen, M. Hossein-Zadeh, and A. F. J. Levi, "Microphotonic modulator for microwave receiver," *Electron. Lett.*, Vol. 37, no.5, pp 300-301, 2001.

[76] M. Hossein-Zadeh, and A. F. J. Levi, "A new electrode design for microdisk optical modulator," *CLEO* 2003 technical digest.

[77] T. F. Gallagher, N. H. Tran, and J. P. Watjen, "Principles of a resonant cavity optical modulator," *Appl. Optics Lett.*, vol. 25, no. 4, pp 510-514, Feb 1986.

[78] L. Maleki, A. Savchenkov, V. Ilchencho, T. Handley, and A. Matsko, "Novel photonic filter and receiver based on Whispering Gallery mode," Microwave-photonics conf .

[79] V. S. Ilchenko, A. A. Savchenkov, A. B. Matsko, and L. Maleki, "Sub-microwatt photonic microwave receiver," *IEEE photonics technol.*, vol 14, no. 11, Nov 2002.

[80] D. A. Cohen, "Lithium Niobate microdisk modulators," PhD dissertation, USC 2001, (www.usc.edu/alevi)

---

## Technical notes

(1) CPW: coplanar waveguide structure where as opposed to the microstripline structure the ground planes are located on both sides of the signal line and on the same plane.

(2) CPS: coplanar stripline.

(3) The GSM (Global system for mobile communication) was developed by European standard committee. The European GSM is currently being developed in the United States in the 1900 MHz band is named PCS1900. (kabuki.eecs.berkeley.edu/~weldon/ papers/spec/**gsm**s6.pdf)

(4) The sensitivity is defined as the minimum detectable signal power (typically specified in units of dBm) at the receiver input such that there is a sufficient signal to noise ratio at the output of the receiver for a given application.
(kabuki.eecs.berkeley.edu/~weldon/ papers/spec/**gsm**s6.pdf)

# Chapter 2

# $LiNbO_3$ microdisk modulator

## 2.1 Introduction

This chapter describes the design and operation of a $LiNbO_3$ microdisk modulator. The physics behind the operation and interaction of the RF and optical elements are explored using both simulation and experiment. We start with the $LiNbO_3$ microdisk physical properties and their importance in the modulation process. A brief explanation of the microdisk resonator optical modes and coupling from a fiber-launched electromagnetic field is followed by the experimental results of prism coupling to different disks and a discussion of novel coupling schemes. Electro-optical interaction in the microdisk is introduced by studying the DC shift of an optical resonance. Bistable behavior is demonstrated as an example of the slow-speed electro-optic response of a microdisk optical resonator. The RF-resonator is the second element of the microdisk modulator that is considered. RF-resonator design strongly influences modulation efficiency. After a brief review of the different electrode structures that have been tested in the preliminary experiments, a ring resonator is introduced. Resonant frequencies, RF coupling, voltage gain, *E*-field distribution, even and odd harmonics are among the most important aspects of the ring resonator operation that are addressed in this section. Experimental results

are presented to support the simulation and analytical studies. The physics of resonant electro-optic modulation and its application to the microdisk modulator is the next topic covered in this chapter. A simple model for the behavior of the modulator based on DC-shift is described. This model is very helpful for evaluating the role of the different parameters in modulation efficiency. In chapter three and four the same model is used to analyze the noise performance of the microdisk based RF-photonic link and the concept of direct RF down-conversion by nonlinear optical modulation. Finally the results of linear and harmonic optical modulation experiments using a $LiNbO_3$ microdisk modulator are described.

## 2.2 Microdisk optical resonator

### 2.2.1 Physical, electronic and optical properties of $LiNbO_3$

Crystalline Lithium Niobate ($LiNbO_3$) is a commonly used electro-optic material in optical modulators. Its optical, electrical and mechanical characteristics such as low loss at RF and optical frequencies, high electro-optic coefficient, mechanical robustness and stable crystal structure at room temperature make it an excellent candidate in many electro-optical devices including microdisk modulators. At room temperature, well below its ferroelectrics curie temperature (~1210°C), $LiNbO_3$ is a

negative uni-axial crystal with crystal symmetry of the trigonal 3m point group and R3C space group [1]. Fig.2.1 shows the $LiNbO_3$ crystal structure.

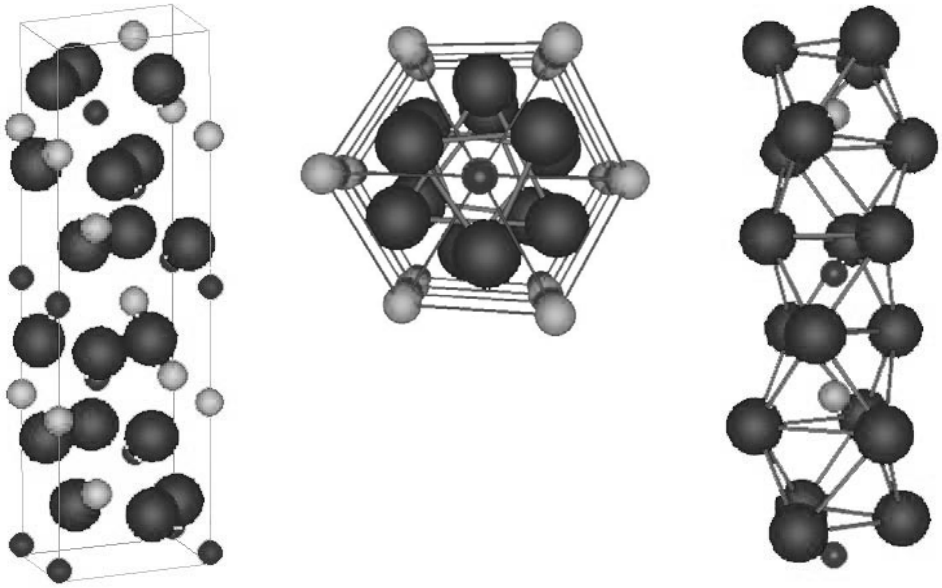

( a ) ( b ) ( c )

**Figure 2.1** $LiNbO_3$ molecular structure. Niobium atoms are represented as dark gray small spheres, Lithium as light gray small spheres and Oxygen as large spheres. (a) Vertical view of the $LiNbO_3$ conventional hexagonal unit cell. (b) View along *c* (or *z*) axis. (c) Octahedral oxygen structure of $LiNbO_3$ [5].

$LiNbO_3$ is birefrigent and therefore sensitive to the polarization of an electromagnetic wave propagating through the material. Its optical index of refraction at wavelength $\lambda$ = 1550 nm along the extraordinary axis is $n_e$ = 2.138 and $n_o$ = 2.21. along the ordinary axis. $LiNbO_3$ is an insulating crystal that is essentially transparent to wavelengths from approximately 400 nm to 5000 nm. The RF permittivity of $LiNbO_3$ is high compared to materials such as optical polymers, III-V semiconductors, and common microwave substrates such as alumina.

**Table.2.1** Bulk properties of $LiNbO_3$

| Property | Value | Notes |
|---|---|---|
| Optical index of refraction ($O^*$) | 2.223 | $\lambda$ = 1550 nm |
| Optical index of refraction (E*) | 2.143 | $\lambda$ = 1550 nm |
| RF permitivity (O) | 42.5 - 43 | 100 MHz - 140 GHz |
| RF permitivity (E) | 26-28 | 100 MHz - 140 GHz |
| Electrical conductivity | $1\times10^{8}$ $(\Omega\text{-cm})^{-1}$ | DC |
| Thermal conductivity | 5.6 W/m.K | |
| Thermal expansion coefficient (O) | $14\times10^{-6}$ $K^{-1}$ | |
| Thermal expansion coefficient (E) | $4\times10^{-6}$ $K^{-1}$ | |
| Thermal effect on index (O) | $1.85\times10^{-6}$ $K^{-1}$ | $1/n_o(dn_o/dT)$ |
| Thermal effect on index (E) | $1.6\times10^{-6}$ $K^{-1}$ | $1/n_e(dn_e/dT)$ |
| Electro-optic coefficients | $r_{33}$ = 30.8 pm/V | |
| | $r_{22}$ = 3.4 pm/V | |
| | $r_{13}$ = 8.6 pm/V | |
| | $r_{51}$ = 28.0 pm/V | |
| Nonlinear-optic coefficients | $d_{31}$ = 11.6 $d_{22}$ = 5.60 | |
| | $d_{33}$ = 8.60 | |
| Piezoelectric coefficient | $d_{15}$ = 69.20 pm/V | Defined as $d_{ij}/d_{36}$ |
| | $d_{31}$ = -0.85 pm/V | |
| | $d_{22}$ = 20.80 pm/V | |
| | $d_{33}$ = 6.00 pm/V | |
| Pyroelectric coefficient | $-4\times10^{-5}$ $(C/K\text{-}m^2)$ | |
| Dielectric loss tangent along *c*-axis | 0.004 | |

* E: e-wave where *E*-field is polarized along *c*-axis

* O: o-wave where *E*-field is polarized perpendicular to *c*-axis

However it is low compared to some other electro-optic materials such as Strontium Barium Niobate (SBN). SBN60 has a $r_{33}$ of 235pm/V and an RF permittivity of 880 along *c*-axis.

The bulk $LiNbO_3$ crystal properties are summarized in Table. 2.1 [1-8].

The measured value of the dielectric loss tangent for $LiNbO_3$ is small enough ($\approx$ 0.004 in the range DC – 100 GHz) that this is a minor source of loss compared to conductor loss [8]. For electro-optic applications mechanical stress in $LiNbO_3$ is an important parameter that must be kept low enough to avoid changes in the modulator bias point through the acousto-optic effect (stress couples to refractive index). Refractive index change caused by high optical power density can also be a problem for such modulators, because it also causes changes in the bias point. This mechanism is wavelength dependent, for a regular Ti-diffused $LiNbO_3$ wave guide (optical mode dimension $\approx 7 \times 4$ μm), less than one mW (power density of $3.5\times10^3$ W/cm$^2$) at 632 nm wavelength can cause significant index change, while at 1320 nm wavelength the waveguide can be stable at up to optical power of 400 mW power (power density of $1.4\times10^6$ W/cm$^2$) [3,8]. $LiNbO_3$ exhibits pyroelectric response (generation of an electric field due to temperature change) along the *c*-axis. When the temperature on one surface of the crystal is changed, a large potential difference between *z*-surfaces of the crystal can cause rapid changes in the bias point of a modulator. For $LiNbO_3$, the induced electric field magnitude is about $1.73\times10^5$ V/m.K.

### 2.2.2 $LiNbO_3$ microdisk

A core element of the microdisk modulator is a $LiNbO_3$ microdisk optical resonator that supports very high-$Q$ Whispering-Gallery (WG) optical resonances. The microdisk resonator is fabricated from a $z$-cut $LiNbO_3$ cylinder. As shown in Fig. 2.2(a), the basic geometry is a disk of diameter $D$, and thickness $h$. For devices presently under test, 0.1 mm < $h$ < 1 mm and 1 mm < ($D$ = 2$R$) < 6 mm. The sidewall of the disk is optically polished with a radius of curvature $R$, typically equal to the radius of the disk. In addition, the equator of the disk's sidewall should be accurately maintained at height $h$/2. Polishing curved sidewalls to an optical finish in $LiNbO_3$ is not a standard practice and it is very difficult to achieve the surface quality needed for high-$Q$ operation. Fig. 2.2(b) shows a 3D picture of the sidewall surface roughness for a typical microdisk. ($h$ = 0.4 mm, $D$ = 3 mm). The peak-to-peak value [4] ($S_y$) of roughness is about 5.1 nm and the rms value [4] ($S_q$) is about 0.846 nm. With this surface quality, loaded optical-$Q$s up to $3\times10^6$ (unloaded optical $Q$ of about $7\times10^7$) have been achieved. This corresponds to a distributed loss of 0.0075 $cm^{-1}$ or 0.03 dB/cm.

If an electric field of magnitude $E_c$ is applied along the c-axis, the optical refractive indices change according to:

$$\Delta n_{zz} = n_{eo}^3 \, r_{33} E_c/2 \qquad \Delta n_{xy} = n_{oo}^3 \, r_{13} E_c/2$$

where, from Table 1 $r_{33} \approx 30.8 \times 10^{-12}$ m/V and $r_{13} \approx 8.6 \times 10^{-12}$ m/V.

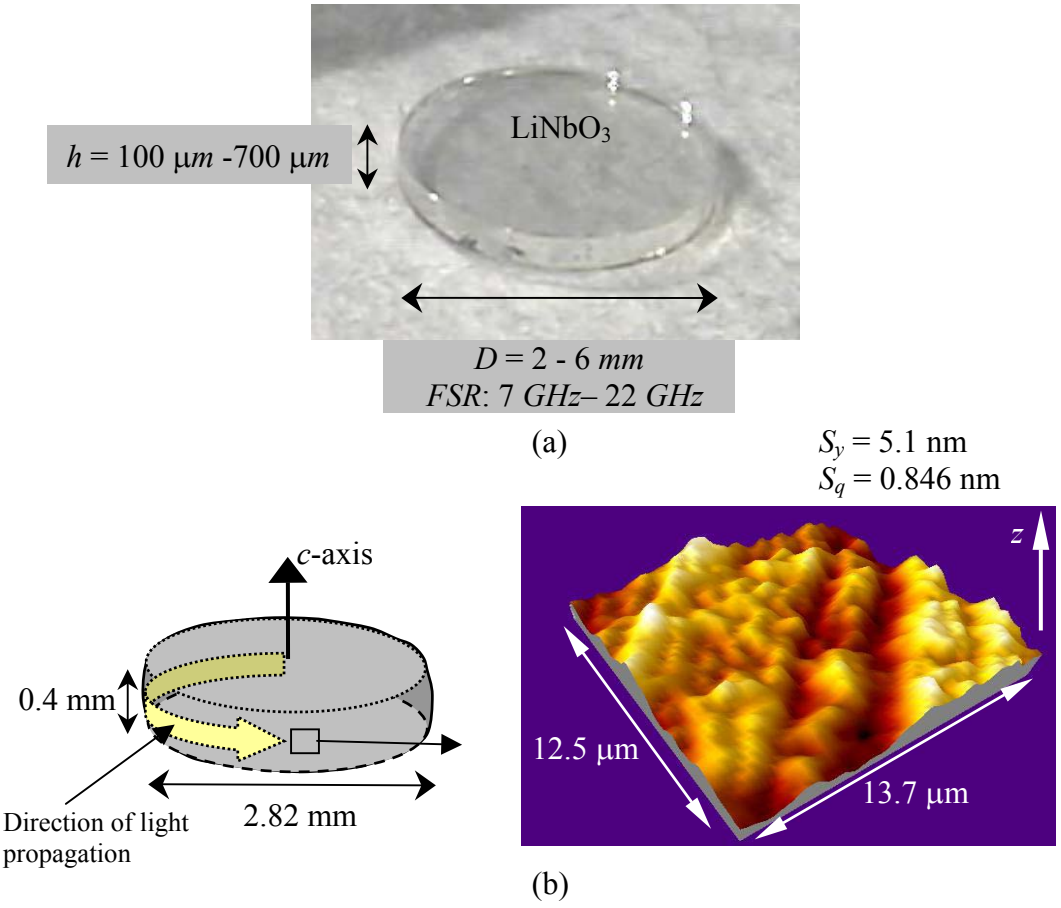


**Figure 2.2** (a) Photograph of a $LiNbO_3$ disk with optically polished sidewalls. (b) 3D picture of the disk sidewall surface taken by interferometric surface profilometer [4]. nm scale scratch marks due to mechanical polishing are clearly visible.

## 2.3 Optical coupling

Efficient optical coupling to optical modes of a microdisk resonator is essential for successful device operation. Modulation can only be efficient if energy coupling to WG modes occurs without introducing large coupling losses that decrease the optical

*Q*. In this section the WG resonance structure in the microdisk resonator and a method for evanescent coupling to them are described

### 2.3.1 Whispering Gallery (WG) resonances

**WG resonance structure**

A dielectric sphere is an open cavity supporting tunneling leaky waves. In the presence of high dielectric contrast (between the sphere and surrounding medium), we can neglect the radiation part and focus only on the bound portion of the field and find the resonant modes of the sphere. Assuming that the direction of the polarization is constant along a fixed set of spherical coordinates, the Helmholtz equation can be separated for high-order confined modes in the following way [14]:

$$\psi_{qlm}(r,\theta,\varphi) = N_s \psi_r(r)\psi_\theta(\theta)\psi_\varphi(\varphi) \tag{2.1}$$

$$\psi_\varphi(\varphi) = \exp[\pm jm\varphi] \qquad m >> 1 >> \theta \tag{2.2-a}$$

$$\psi_\theta(\theta) = \exp\left[-\frac{m}{2}\theta^2\right] H_N\left(\sqrt{m}\theta\right) \tag{2.2-b}$$

$$\psi_r(r) = \begin{cases} j_l(kn\ r) & r \le R \\ j_l(knR)\exp[-\alpha_s(r-R)] & r > R \end{cases} \tag{2.2-c}$$

where:

$$N_s = \left\{\sqrt{\frac{\pi}{m}} 2^{N-1} N! R^2 \left[\left(1+\frac{1}{\alpha_s R}\right) j_l^2(kn_s R) - j_{l-1}(kn_s R) j_{l+1}(kn_s R)\right]\right\}^{\frac{-1}{2}} \tag{2.3}$$

$$\alpha_s = \sqrt{\beta_l^2 - k^2 n_0^2}, \beta_l = \frac{\sqrt{l(l+1)}}{R}, N = l - m, k = \frac{2\pi}{\lambda} \tag{2.4}$$

$\psi_{qlm}$ represents either the $E_\theta$ or $H_\theta$, corresponding to TE and TM polarized modes respectively.

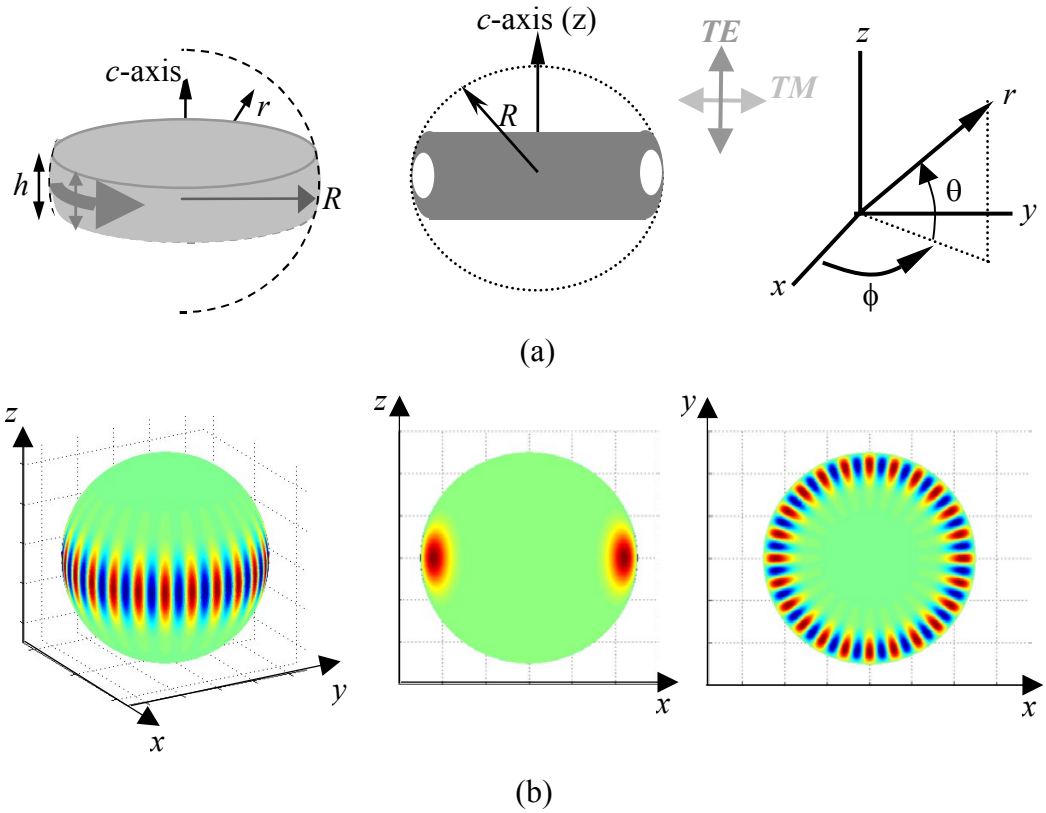


**Figure 2.3** (a) Geometry of the microdisk resonator and definition of the coordinate system used (notice that θ is measured relative to the equatorial plane unlike the conventional definition where it is measured relative to the *z*-axis. This new definition has been chosen because it is more convenient for WG resonances that are confined around the equator). Also shown is the definition of the TE and TM polarized resonances. (b) Normalized modal distribution for $l = m = 24$ that is the projection of spherical harmonic $Y_{24,24}$ on a unit sphere (longitudinal and equatorial cross section).

The *E*-field vector of a TE resonance is polarized along **θ** (for equatorial propagation this is the same as the **z** direction) and the *E*-field vector of a TM resonance is polarized in the *xy* plane. The $H_N$ is the Nth order Hermite polynomial.

The electromagnetic solutions to the disk resonator are found from those of a sphere by simply defining the disk to be a sphere with part of the top and bottom

hemispheres removed (the geometry of this resonator is shown in Fig. 2.3(a)). A sphere's mode is described in terms of three integers $l$, $m$ and $q$. The value of $q$ counts the number of field maximum in the radial direction and $l$-$m$ +1 ($|m| \leq l$) is the number of field maxima in the polar direction, perpendicular to equatorial plane and between the two poles. The resonant wavelength is determined by $q$ and $l$. The mode has a propagation constant $\beta_l$ and its projection on the equator is commonly referred to as the "propagation constant" because it is the wave vector in the net direction of propagation. Note that an ideal microsphere (microdisk) is a traveling wave optical resonator (when $\lambda << R$ that is almost always true). Whispering-Gallery (WG) modes are solutions with large values of $l$ and $m$ and small values of $l$-$m$ and $q$ ($q << l$), this means that they are highly confined in r and θ directions very close to the equator and the sidewall while their propagation is described by a function of $\phi$. For these modes $\beta_l = \beta_m = m/R$ ($R$ is the sphere radius and m is a positive integer). This condition can be used to calculate the approximate resonant frequency of the WG modes. $m$ essentially corresponds to the number of optical wavelengths that fit into the microdisk's circumference. The mode labeled by $l = m$ and $q = 1$ is called the fundamental mode and it only has one maximum in each direction (it is Guassian in nature). Fig. 2.3(b) shows the modal distribution for $l = m = 24$. While this is helpful to visualize the fundamental mode, in practice an average size disk (2 mm < $2R$ < 6mm) has a value of $l$ that is usually greater than 5000. Using equation (2) we can approximately calculate the mode size for the fundamental and low order ($l$-$m$ < 10) WG modes inside the sphere. Fig. 2.4 shows

the definition of the fundamental mode profile parameters and their values for three $LiNbO_3$ disks with different sizes commonly used in our experiments [47]. $\delta r_{FWHM}$ is the full-width-half-maximum of the power distribution along the radial direction and $\delta\theta_{FWHM}$ is the full width half maximum along the polar direction.

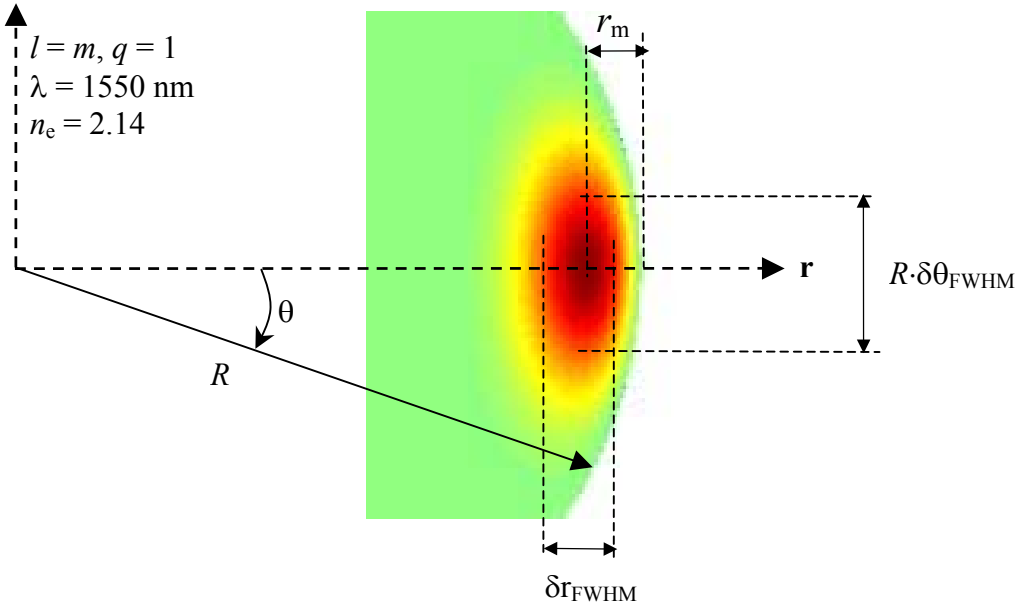


| 2R (mm) | $R\cdot\delta\theta_{FWHM}$ (μm) | $\delta r_{FWHM}$ (μm) | $r_m$(μm) | $l$ (= $m$) |
|---|---|---|---|---|
| 2 | 17.8 | 4.06 | 3.31 | 8660 |
| 3.5 | 24 | 4.99 | 4.00 | 15120 |
| 5.84 | 30 | 5.80 | 4.58 | 25260 |

**Figure 2.4** WGM power distribution in *xz* plane, for microdisks with different diameters.

For microdisk modulator applications, we are interested in WG modes with TE polarization (*E*-field parallel to *z*-axis) because the elecro-optic coefficient of $LiNbO_3$ is larger along the *c*-axis. The resonance frequencies of TE WG modes in a sphere with a refractive radius $R$ ($R>>\lambda$) and a refractive index $n$ surrounded by air ($n = 1$) can be obtained from [24]:

$$\frac{2\pi Rn}{c}\nu_{lq} = l + \frac{1}{2} - a_q\left(\frac{l+0.5}{2}\right)^{\frac{1}{3}} - \frac{n}{\sqrt{n^2-1}} + \frac{3a_q^2}{2^{\frac{1}{3}}10(l+0.5)^{\frac{1}{3}}} + \frac{n^3 a_q}{3\sqrt[3]{2}\left(n^2-1\right)^{\frac{3}{2}}(l+0.5)^{\frac{2}{3}}} \quad (2.5)$$

where $a_q$ denotes the $q$-th zero of Airy function, c is the speed of light, and $\nu_{lq}$ is the frequency of the mode. For the fundamental and low order modes we can use the approximation: $m(\lambda/n) = \pi D \qquad (l = m)$ (2.6)

and calculate the free spectral range frequency $\Delta\nu_{FSR}$ using:

$$\Delta\nu_{FSR} = c/(\pi nD) \quad (2.7)$$

**Losses and quality factor**

The optical loss mechanisms in the $LiNbO_3$ microdisk resonator (or any spherical optical resonator) are: Rayleigh scattering, surface scattering and material loss. It has been shown that even for small spheres the Rayleigh scattering is suppressed for WG modes [20]. For medium size disks since ($R >> \lambda$) loss due to finite curvature becomes small, since the resonator dimension is significantly greater than the optical resonant wavelength. Hence for optical wavelengths near $\lambda$ = 1550 nm, the unloaded (intrinsic) quality factor of optical dielectric resonators with a diameter greater than 10 μm is typically limited by attenuation due to scattering from surface imperfections and material loss. The distributed optical loss for WG modes can be derived from the photon lifetime in the resonator. Assuming the number of photons present in a WG mode decays exponentially in time (due to intrinsic optical losses) we can express the unloaded optical quality factor of that mode as $Q_u = \omega\tau_p$ where $\tau_p$ is the 1/e photon lifetime and $\omega = 2\pi\nu_{lq.}$ We can also define a distributed loss constant per unit length $\alpha = n/c\tau_p$ (c: is the speed of light and $n$ is the effective

optical refractive index for the corresponding optical mode). So $Q_u$ and the distributed loss are related as:

$$\alpha = n\omega/cQ_u \tag{2.8}$$

The loaded optical quality factor $Q$ of an optical mode can be calculated based on the measured full-width half maximum of the spectral peak at the resonant optical frequency $\nu_{res} = \nu_{lq}$, $Q = \nu_{res}/\Delta\nu_{FWHM}$ (or $Q = \lambda_{res}/\Delta\lambda_{FWHM}$). The typical loaded $Q$-factor values that we observe for optically polished $LiNbO_3$ micodisks is between $2\times10^6$ and $7\times10^6$ (see section 2.3.3). Experimentally we measure the loaded $Q$ and if we insert the measured $Q$ in equation 2.8 to calculate $\alpha$, the optical coupling loss will be included in the distributed loss. In section 2.3.4 we will show that the loaded quality factor of a critically coupled WG mode can be used to calculate the intrinsic distributed loss in the microdisk resonator. The high quality of the optical modes reveals the small magnitude of the surface roughness of the sidewalls -- a fact confirmed by surface profilometer measurements (2.2.2). The high quality of sidewall surface is not only important for high-$Q$ optical resonance but also to guarantee the traveling-wave nature of the WG modes. It is well known that surface roughness can generate back-scattered optical-waves that couple energy into modes with negative wave-vectors (effectively increasing the VSWR) [21]. In a microdisk modulator the energy coupled to modes circulating in the opposite direction do not contribute to the optical modulation process.

### 2.3.2 Evanescent optical coupling

Light must be coupled to the WG modes without disturbing their propagation around the disk or reducing their high-$Q$. In principle it is not possible to couple energy into any resonator without coupling some energy out; hence there is always a certain amount of loss associated with coupling. The objective here is to reduce the coupling loss and more importantly, to avoid as much as possible any physical perturbation. Evanescent coupling in which an exterior field tunnels into the sphere, appears to be the most promising approach. The excitation of whispering gallery modes is achieved via evanescent fields. The mechanism for this type of coupling is that of frustrated total internal reflection. As may be seen in Fig. 2.5(a) light in medium 1 (refractive index = $n_1$) incident on the interface of medium 1 and 2 (where $n_1 > n_2$) is totally reflected if θ (angle with respect to normal) is greater than the critical angle. But an evanescent field will exist beyond the interface (in medium 3) with a skin depth of δ given by:

$$\delta = \frac{\lambda}{\sqrt{4\pi^2\left(\frac{n_1^{\,2}}{n_2^{\,2}}\sin^2\theta - 1\right)}} \tag{2.9}$$

If a third medium is present within a distance $g_o$ from medium 1 where $g_o \leq \delta$, then light will couple to the third medium with an angle ϕ where ϕ and θ follow the regular Snell's law meaning: $n_1\sin(\theta) = n_3\sin(\phi)$. This phenomenon is called

'frustrated total internal reflection' and can be used to couple light to WG modes inside the disk.

Fig. 2.5(b) shows how an equilateral prism with a refractive index $n_1 > n_3$ and angle $\theta_c$ (where $\theta_c$ is the critical angle for the $n_1$ and $n_3$ interface) placed in the vicinity of medium 3 ($g_o \leq \delta$), can couple light into (and out of) optical waves propagating parallel to the interface. Since the wave vector of WG modes is almost tangential to the microdisk surface, a prism that has a higher refractive index than $LiNbO_3$ can be used for coupling light from free space to these modes. There are numerous other methods for evanescent coupling of light into guided modes [9,10,11,15,16,17], but because of the large refractive index of $LiNbO_3$, the prism coupling approach is the most convenient.

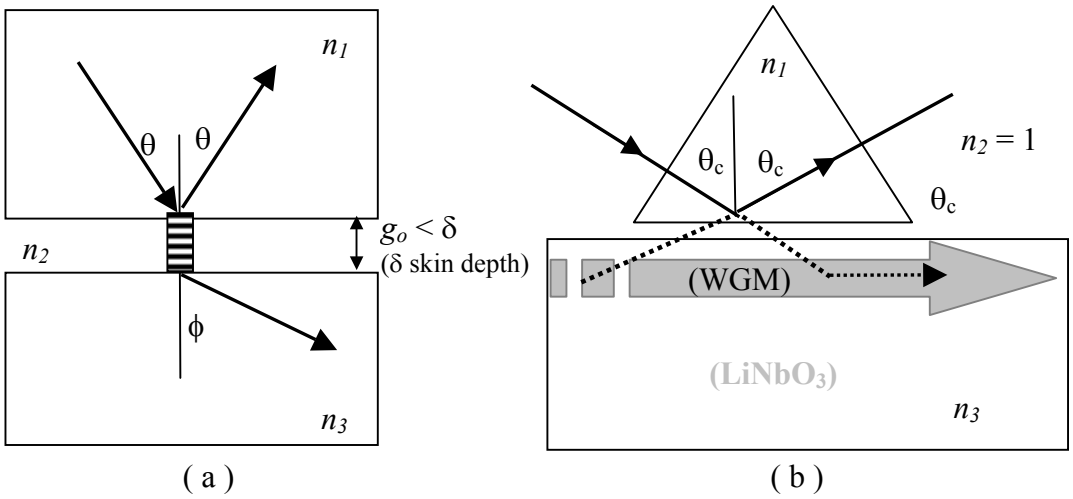


**Figure 2.5** (a) Frustrated total internal reflection. (b) Evanescent prism coupling to surface waves

### 2.3.3 Prism coupling to WG modes

In our experiments we use small diamond prisms with the dimensions shown in Fig. 2.6(a). The refractive index of diamonds is near 2.4 and is thus larger than the refractive index of $LiNbO_3$ for both TE and TM modes ($n_e$ = 2.14, $n_o$ = 2.23). The use of diamond microprisms to couple to WG modes inside a $LiNbO_3$ disk, is equivalent to setting $n_3$ = 2.14 and $n_1$ = 2.4 in Fig. 2.5(b). The skin depth ($\delta$) for a diamond-air interface excited by $\lambda$ = 1550 nm radiation is about 135 nm. It is possible to use a single prism to couple light into and out of the microdisk (Fig. 2.6(b)) or to use one prism to couple in and another one to couple out (Fig. 2.6(c)). The detection of coupled WG peaks using two prisms is easier since the reflected part of the input that is not coupled and coupled light do not interfere. However, since two prisms are in contact with the microdisk, the $Q$ is smaller due to the larger coupling loss, and the portion of the optical WGM power that is coupled out through the first prism does not contribute to the modulated signal. In a one-prism coupling scheme this problem does not exist but experimental results show that the WGM cone coupled out of the disk and the totally reflected beam cone have spatial overlap (Fig. 6(c)), therefore, depending on the location of the collecting fiber the detected output spectrum can be WGM peaks, transmission dips or just the reflected beam. This effect adds to the complexity of the alignment of the output port. Also experimental results show that two-prism coupling generally results in a cleaner mode structure. In chapter 4 we will demonstrate that using transmission dips in a

one-prism coupling scheme is a better choice for nonlinear modulation and optical down-conversion due to reduced DC optical power at resonance.

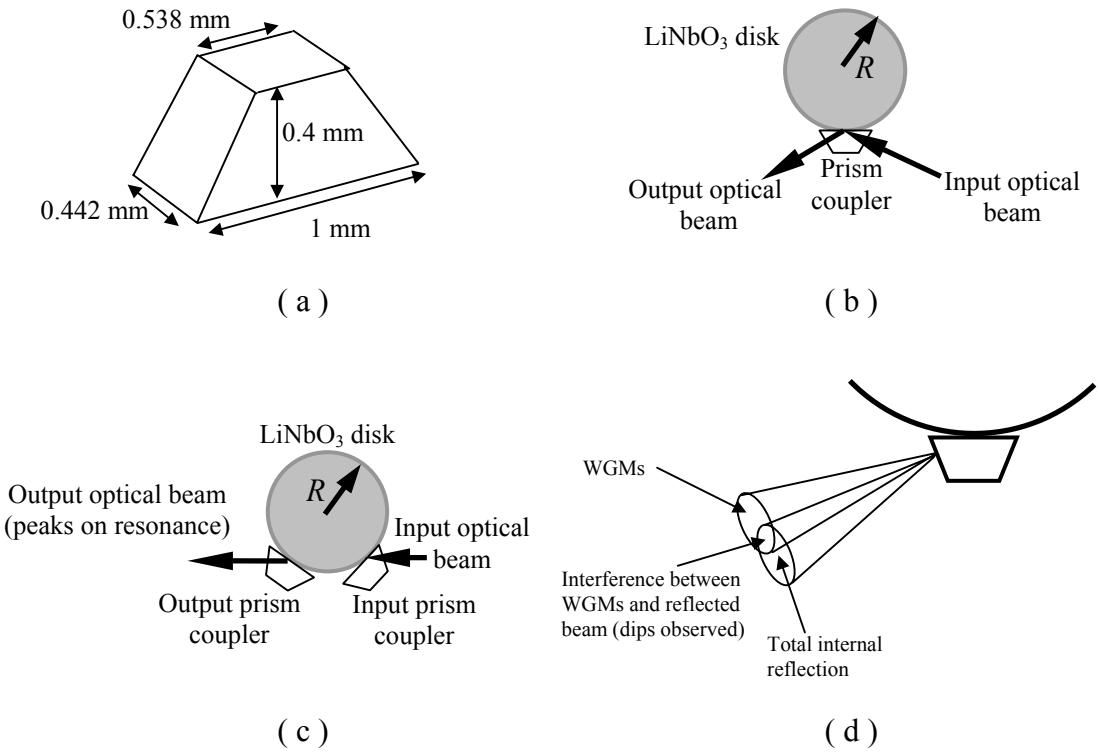


**Figure 2.6** (a) Diamond microprism dimensions. (b) Single-prism coupling. (c) Double-prism coupling. (d) Interference effect in single-prism coupling.

Fig. 2.7 depicts the schematic diagram of the typical experimental arrangement used for optical coupling and mode structure characterization. The laser light is generated using a DFB laser (line width = 3 MHz). After passing through an optical isolator and a polarizer, the light is coupled to a lens system through a cleaved end. We use the polarizer to selectively excite the TE modes (*E*-field parallel to c-axis, which is normal to the top surface of a *z*-cut microdisk). As mentioned previously, this

polarization is preferred because of the large magnitude of the $LiNbO_3$ electro-optic coefficient along the *c*-axis.

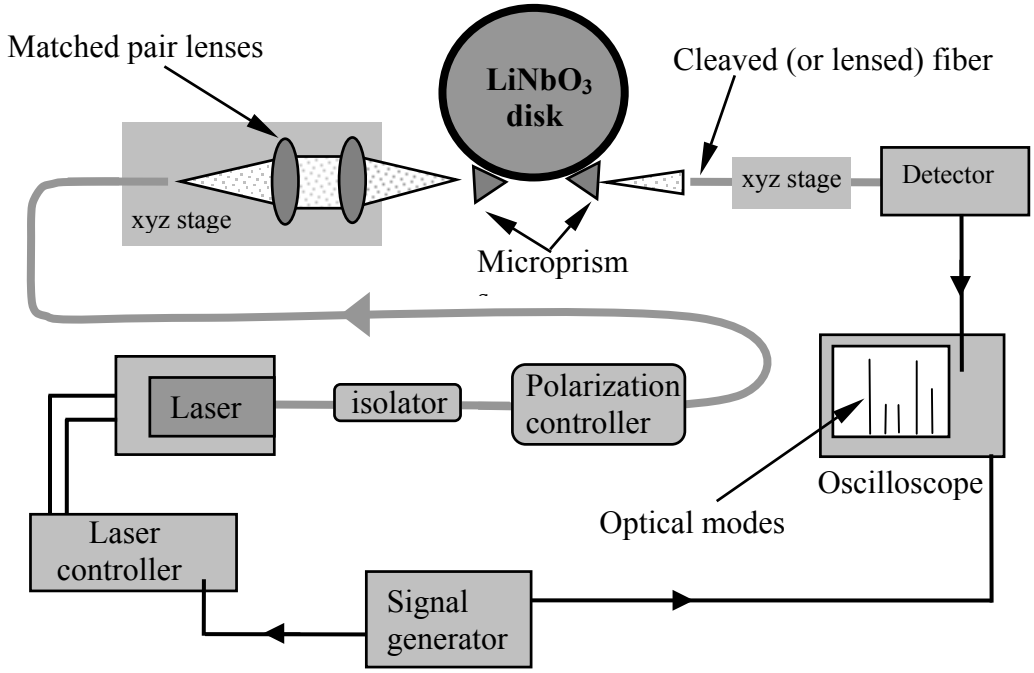


**Figure 2.7** Schematic diagram of the experimental arrangement used for optical coupling measurement.

The lens system is an IR coated matched pair with a focal length of 11 mm (we have also tried 6 mm) mounted on a *xyz* stage. The laser beam is focused on the input prism and evanescently couples to the WG modes inside the disk. The modes are coupled out through the second prism and collected with a cleaved fiber (or lensed fiber) that is also mounted on a *xyz* stage. In a one-prism coupling scheme, the same prism is used for coupling into and out of the disk. Finally the output goes to a detector and is monitored with an oscilloscope.

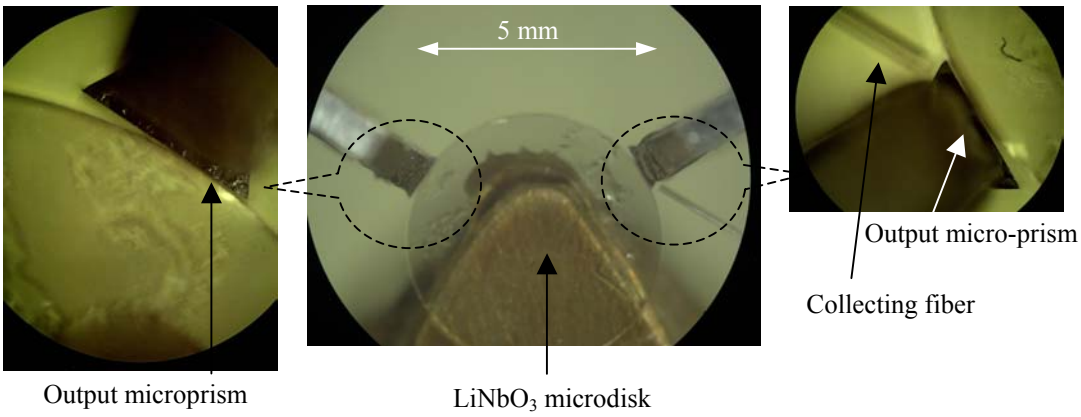


(a)

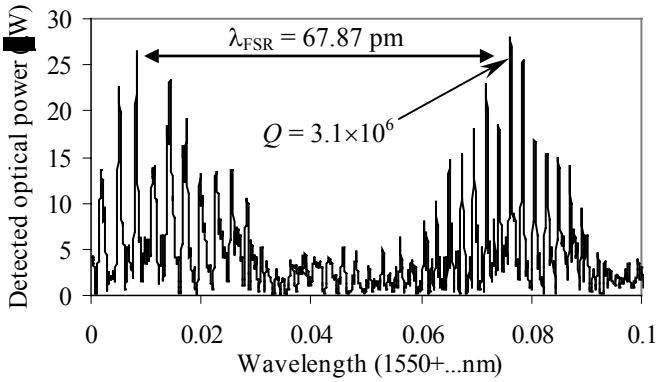


(b)

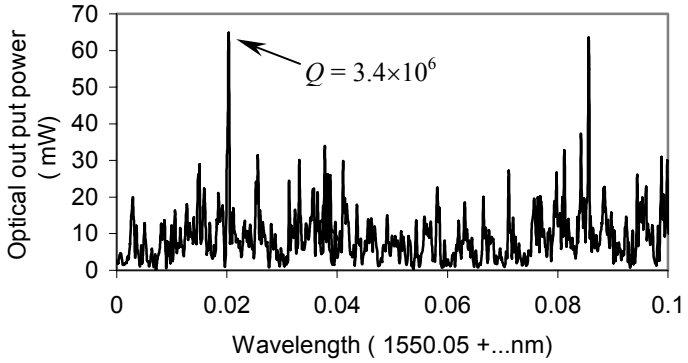


(c)

**Figure 2.8** (a) Top view photograph of a 5.13 mm diameter $LiNbO_3$ microdisk in contact with two microprisms. (b) The detected TE WG optical spectrum. (c) High coupling efficiency (> %15) and a clean TE spectrum obtained with the same set up after accurate alignment (optical input power in both cases is about 1200 μW)

To sweep the laser wavelength, a triangular voltage signal is fed to the laser power supply that modulates the current and consequently the laser wavelength (the power is also modulated but we can normalize it). By triggering the oscilloscope with the same signal we can observe the frequency spectrum on the oscilloscope.

After careful alignment and finding the desired spectrum, we change the light source to a high-resolution tunable laser (line width < 0.5 MHz, wavelength resolution < 0.1 pm) and scan a small part of the spectrum to measure details of the mode structure.

Fig. 2.8(a) shows a photograph of a $LiNbO_3$ microdisk ($D$ = 5.13 mm and $h$ = 400 μm) in contact with two microprisms. Fig. 2.8(b) shows a typical TE WG mode spectrum. The measured FSR is in very good agreement with the calculated value using equation 2.7, assuming $n_e$ = 2.14, for a 5.13 mm diameter disk the measured value is 67.87 pm and the calculated value 69.24 pm. This is consistent with the effective refractive index of the TE WG modes being almost the same as the bulk extraordinary refractive index ($E$-field along $c$-axis). Fig. 2.8(c) shows another TE mode spectrum for the same disk. As may be seen the maximum optical power is 2 times greater and the spectrum has fewer features. Achieving such a good coupling requires a very accurate alignment of all optical elements with pico-motor drivers [(1)]. In both cases (Fig. 2.8(b) and(c)), the input optical power is about 1200 μW, By taking into account the losses through the system, specially reflection from prism surfaces and power lost in the first coupler, one may estimate optical coupling efficiency of 15%. Note that in all cases we define the coupling efficiency (ρ) as the ratio of the maximum optical power detected and the total power injected into the

input prism. The same experimental arrangement can be used to demonstrate one prism coupling by removing one prism and moving the other to the middle of the microdisk. Fig. 2.9 shows the TE mode spectrum obtained with the one-prism coupling scheme.

As expected, the measured optical $Q$ in both cases is larger than observed when using a two prism coupling scheme and also more modes have been coupled out resulting in a complex spectrum. The laser input power is about 1400 μW in both cases but the maximum coupled power in the second case.

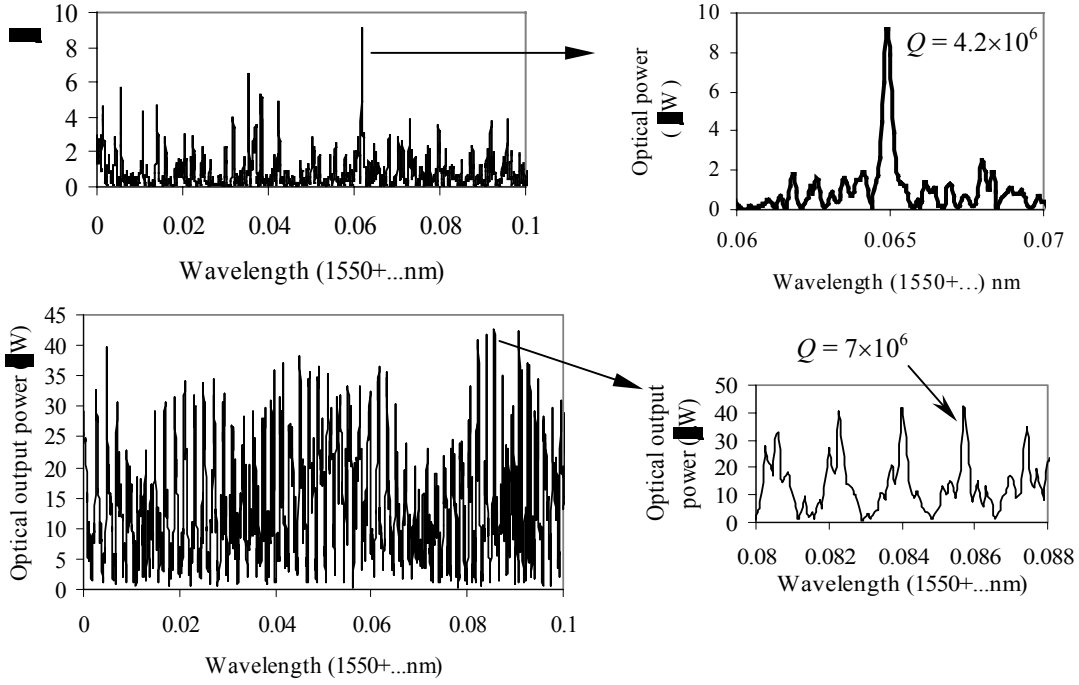


**Figure 2.9** TE mode spectrum obtained using a single prism for coupling light in and out of the microdisk. The quality factor of the second measurement (bottom) is the highest $Q$ observed.

One may see that when we try to couple more light into one mode, many other modes are excited and hence there is a trade-off between a clean spectrum and the maximum coupled optical power to a certain mode (with the exception of some special cases that are mostly unrepeatable).

We have also studied optical coupling to a toroidal (the side wall curvature is smaller than the disk radius *R*) $LiNbO_3$ miocrodisk.

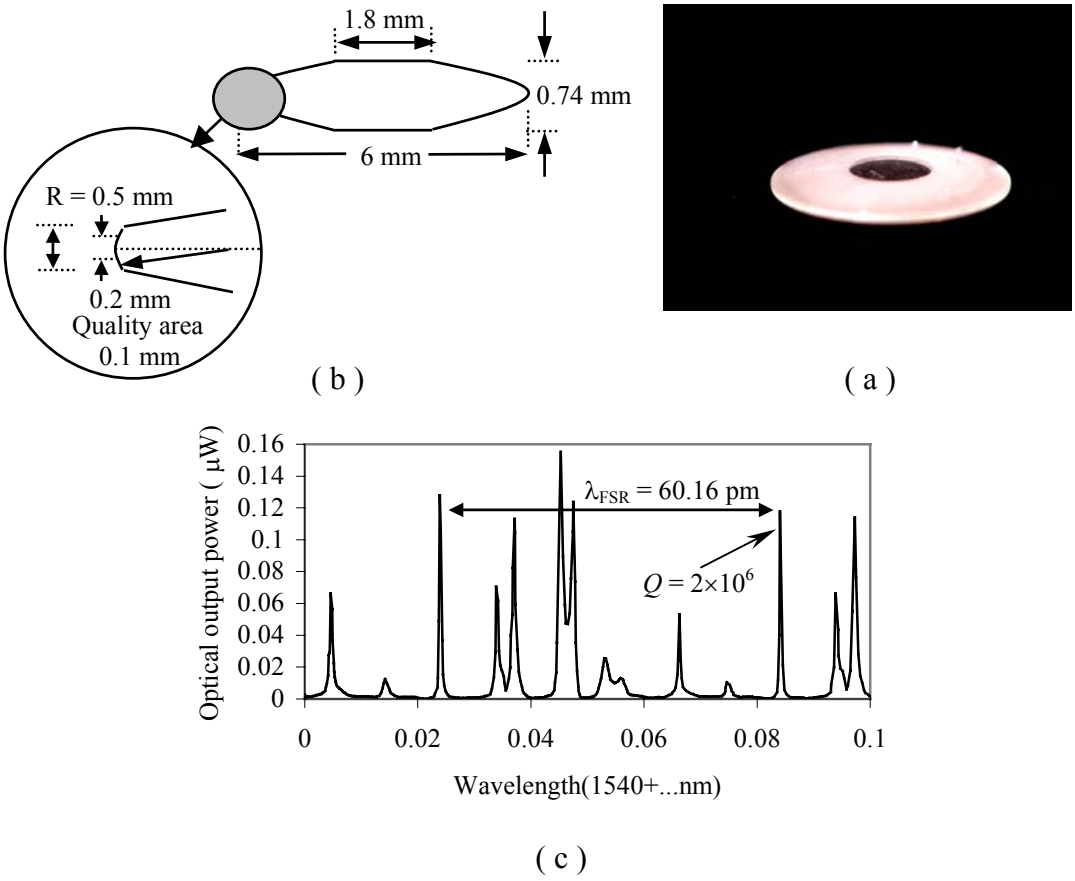


**Figure 2.10** (a) Photograph of the toroidal $LiNbO_3$ microdisk. (b) The microdisk dimensions and the sidewall profile. (c) TE mode spectrum obtained using a two prism coupling scheme. Although the spectrum is very clean the coupling efficiency is low (≈%3).

Fig. 2.10(a) shows the photograph of the microdisk and Fig. 2.10(b) is a schematic diagram showing the details and dimensions of the sidewall.

The sidewall curvature is about 10 times smaller than the disk radius, resulting in strong confinement along $\theta$. This should result in a cleaner spectrum due to the absence of extra transverse modes (different values of $m$) that could resonate in a regular microdisk. Fig. 2.10(c) shows a TE mode spectrum obtained by the two prism coupling method. Although the mode structure is cleaner the coupling efficiency is very low (~ %3).

The low coupling efficiency is a result of mode mismatch between the incident beam that has a Gaussian profile and the small cross section area of the WG mode. Decreasing the waist size in a Gaussian beam does not improve the efficiency because it simultaneously increases the beam divergence.

As mentioned previously, using a single prism coupling scheme, the optical spectrum of the collected output power can be a series of transmission dips or peaks depending on the position of the output fiber.

Fig. 2.11 shows the spectrum of the TE optical output power from a single prism coupled $LiNbO_3$ microdisk ($D$ = 3 mm, $h$ = 0.4 mm). In Fig. 2.11 (a) the output fiber is located at the overlap of the WG cone and the totally reflected cone (Fig. 2.6(d)) while in Fig. 2.11(b) it only collects the WG optical power.

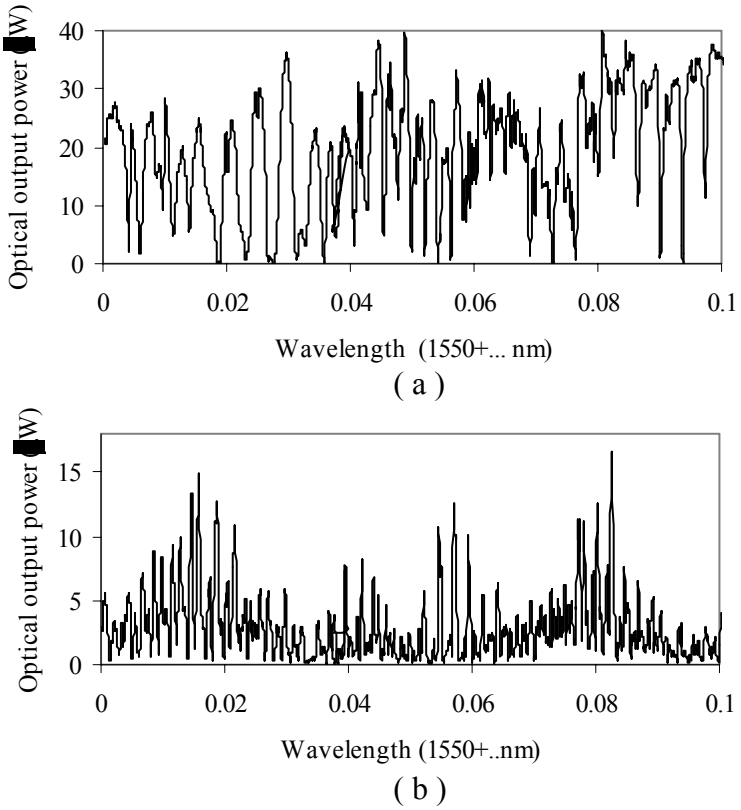


**Figure 2.11** Optical output power spectrum of a single prism coupled $LiNbO_3$ microdisk ($D$ = 3 mm, $h$ = 0.4 mm). (a) Detected transmission dips when the output fiber is tuned to the overlap region of the WG cone and the total reflection cone. (b) Detected WG peaks when the output fiber only collects optical power from the WG cone.

Fig. 2.12 shows photographs of visible (red) scattered light from WG modes inside a 6 mm diameter ($h$ = 700 μm) excited by a He-Ne laser ( $\lambda$ = 623.2 nm). A single prism is used to both couple in and out the laser light from a 30 mW He-Ne laser. The laser is focused on the prism using an 11 mm focal length matched pair lens.

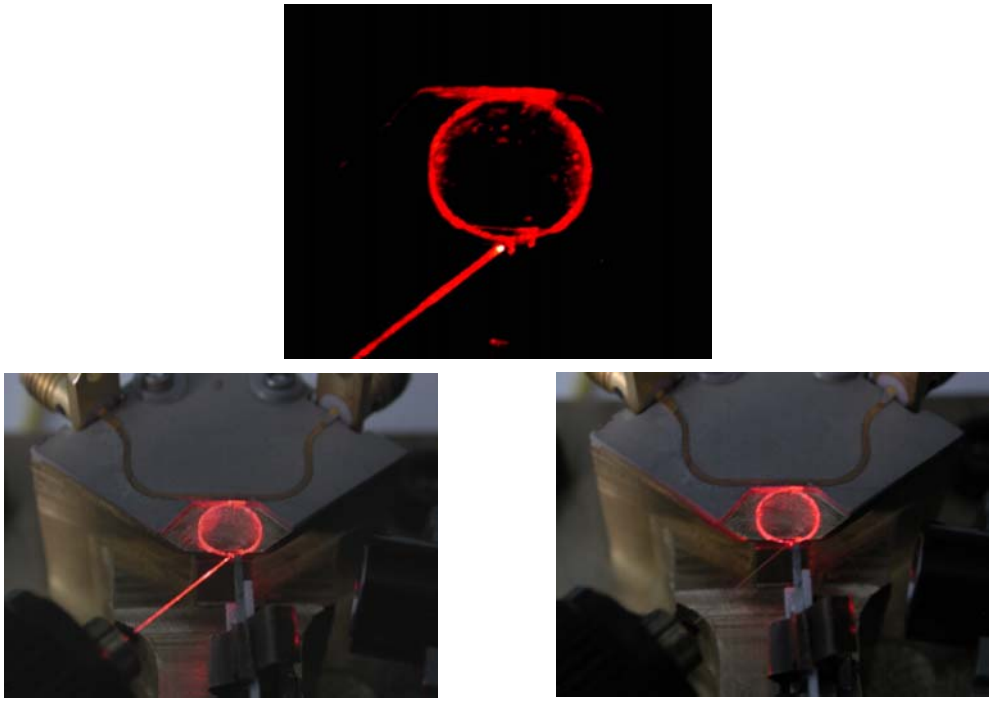

**Figure 2.12** Observation of WG modes inside the $LiNbO_3$ disk ($h$ = 700 μm, $D$ = 5.85 mm) using He-Ne laser.

In the photograph we can also see the scattered light from the collecting (output) fiber that shows the WG modes are coupled to the fiber. In the bottom-right picture of Fig. 2.11 the output fiber is decoupled (moved slightly up) and only WG modes inside the disk are observable.

### 2.3.4 Critical coupling and intrinsic loss

When the output fiber is tuned to the interference region where transmission dips are observed, the single-prism coupled microdisk can be, treated as an effective optical

ring resonator side coupled to a waveguide. The generic description of this system is schematically shown in Fig. 2.13(a). The corresponding optical transfer function may be calculated using the general relation for coupling between an optical resonator and a dielectric waveguide [12]. The transmitted optical power ratio ($T = P_{ot}/P_{o,in} = |E_t|^2/|E_{in}|^2$) is written as:

$$T = \frac{a^2 + |t|^2 - 2a|t|\cos(\pi kD)}{1 + a^2|t|^2 - 2a|t|\cos(\pi kD)} \tag{2.10}$$

where $D$ is the microdisk diameter, $k$ is the wave vector of the WG optical resonance, $a = exp(-\alpha\pi D)$ is the inner circulation loss factor ($E_a = a \times e^{i\theta} \times E_b$, $\theta = \pi D n_e/\lambda_{res}$) and $\boldsymbol{t}$ is the transmission coefficient ($\boldsymbol{t} = E_t/E_{in}$). $\alpha$ is the total distributed loss factor that combines the scattering losses and absorption. If the coupling mechanism is lossless the optical coupling factor ($\kappa$) may be expressed as $(1 - \boldsymbol{tt}^*)^{1/2}$.

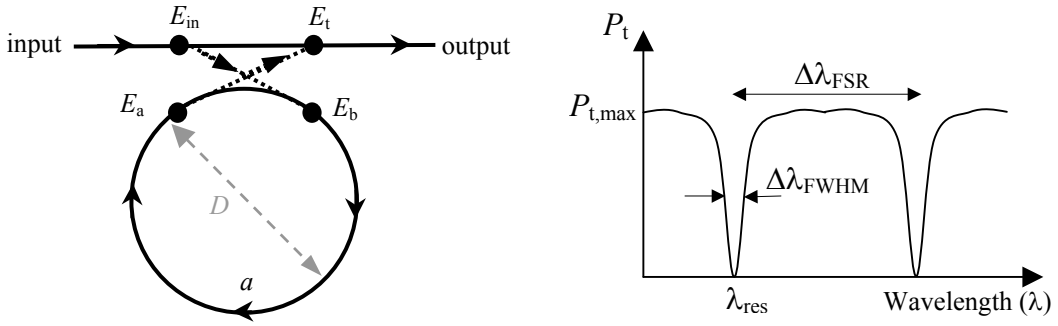


**Figure 2.13** (a) Generic description of a single waveguide coupled ring resonator. (b) Typical transfer function of a waveguide-resonator system.

It is important to notice that all parameters except $D$ are different for different WG resonances. The optical transfer function (equation 2.10) defines a series of resonant transmission dips that are equally spaced by the optical free spectral range of the

microdisk resonator ($\Delta\nu_{FSR} = c/\pi nD$) as shown schematically in Fig. 2.13(b). Each resonance has a Lorentzian shape with full-width-half-maximum wavelength $\Delta\lambda_{FWHM}$ around its resonant wavelength $\lambda_{res}$ and a loaded optical $Q = \lambda_{res}/\Delta\lambda_{FWHM}$ limited by $\kappa$ and $\alpha$. Loaded $Q$ can be estimated using the general relation derived for Fabry-Perot (FP) resonators [19] and by changing the factor $R_1R_2$ to $ta$:

$$Q = \frac{\pi^2 n\ D\sqrt{ta}}{(1-ta)\lambda_{res}} \tag{2.11}$$

$n$ is the refractive index of the optical resonator along the optical mode polarization.

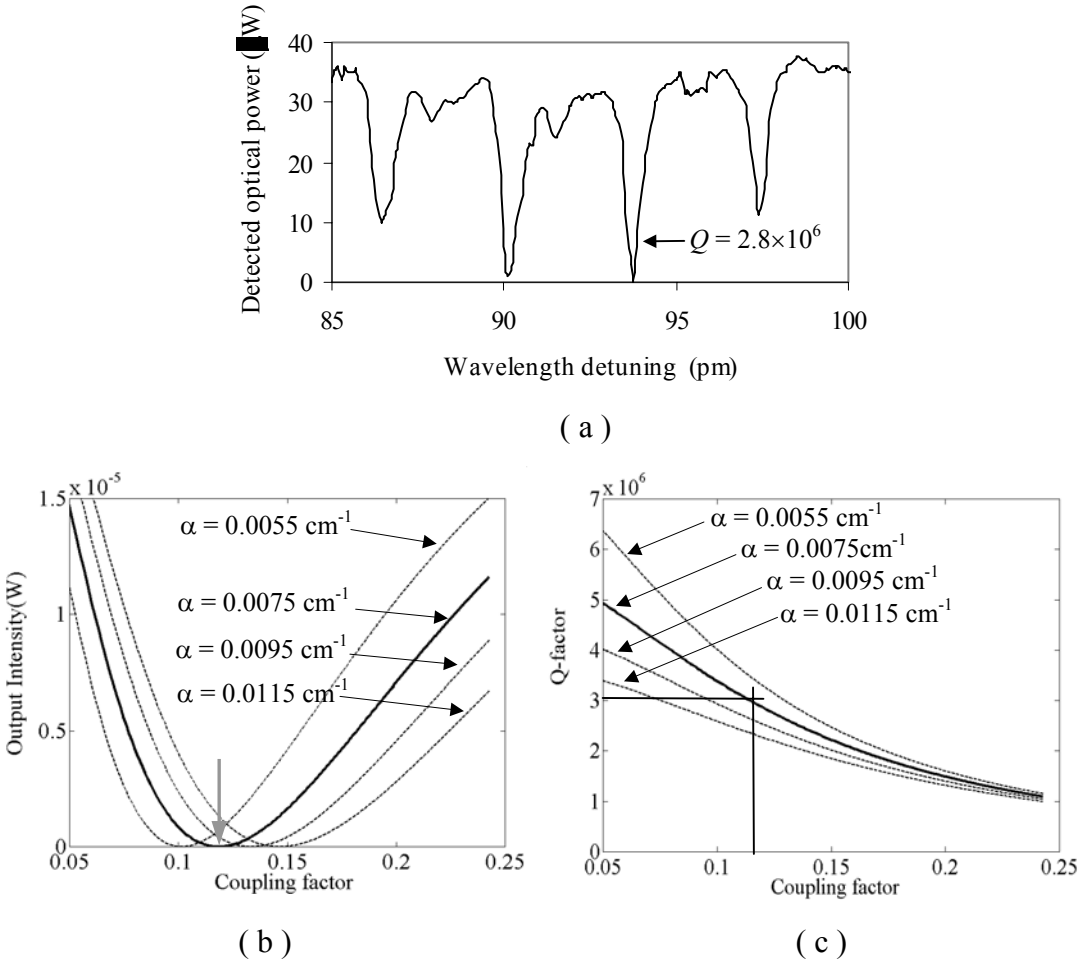


**Figure 2.14** (a) Transmitted optical power spectrum of 3 mm diameter and 0.4 mm thick microdisk optical resonator. (b) Simulated optical output power against coupling factor for different values of distributed loss factor. (c) Simulated optical quality factor against coupling factor for different values of distribute loss factor.

Fig. 2.14(a) shows part of the transmission spectrum for a single-prism coupled $LiNbO_3$ microdisk with a diameter $D$ = 3 mm and a thickness $h$ = 0.4 mm. For a TE mode of the $LiNbO_3$ microdisk resonator, $n$ should be replaced by $n_e$ that is the unperturbed value of the extraordinary refractive index $n_e$ ~2.14. As may be seen, at the resonant wavelength of the third mode, the transmitted optical power is zero so that one may infer the mode is critically coupled. The measured transmitted optical power and loaded $Q$ may be used to calculate the intrinsic distributed loss of a resonant mode. For example the critically coupled mode in Fig. 2.14(a) has a $Q$ of $2.8\times10^6$. Now if we use equations (2.10) and (2.11) to plot the transmitted optical power and the loaded $Q$ versus the optical coupling factor ($\kappa$) for different values of distributed loss factor ($\alpha$), we see that there is a unique value of $\alpha$ which results in critical coupling and a certain value of loaded $Q$ for the same coupling factor. Fig. 2.14(b) and 2.14(c) show the simulated transmitted optical power and loaded $Q$ for the same microdisk and different values of $\alpha$. As may be seen, the mode is critically coupled at $\alpha$ = 0.0075 $cm^{-1}$ and has a loaded $Q$ of about $2.8\times10^6$ at $\kappa$ = 0.12. So, using simulation results and the measured $Q$ value of the critically coupled mode, we have simultaneously estimated the value of $\kappa$ and $\alpha$ for the mode.

We can calculate the unloaded quality factor ($Q_u$) of an optical mode using the estimated value of $\alpha$ and equation (2.8). The critically coupled mode in Fig. 2.14(a) has a $Q_u$ of about $1.2\times10^7$.

### 2.3.5 Other optical coupling methods

Coupling methods such as tapered fiber [9], etch-eroded fiber coupler [11] and waveguide coupler [16] that have been successfully used for coupling light into silica microspheres, do not work for $LiNbO_3$ microdisks because of its high refractive index. These techniques are based on evanescent-coupling and as mentioned before (2.3.2) the incident light should enter the resonator from a medium with a higher refractive index (compared to the resonator). It may be possible to use a Ti-diffused waveguide on $LiNbO_3$ that is pigtailed to single mode fibers. By accurately designing the waveguide dimensions and tuning the propagation constant, it is possible to achieve high efficiency coupling to WG modes in an average-size $LiNbO_3$ microdisk. Another possibility is to improve the efficiency of the prism coupling by tailoring the gap between the prism and microdisk's sidewall. It has been shown that using cylindrically shaped prisms the coupling to planar waveguides can be improved up to 92% [10,17,18]. Notice that as opposed to prism coupling to slab-waveguides, the coupling-gap is already tapered in the microdisk case. Assuming that the prism is in contact with the disk and knowing the skin depth for a diamond prism (≈135 nm at $\lambda$ = 1550 nm), we can easily calculate the coupling length (about 30 μm for $D$ = 2.9 mm). By shaping the base of the prism we can tune this length to achieve optimum coupling efficiency. Since it is difficult to polish diamond prisms, ZnSe crystal may be a good candidate for this task. ZnSe has a zinc blend structure and a refractive index of 2.435. ZnSe is transparent in a wide

wavelength window from 500 nm to 22 μm. Plano-convex ZnSe lenses (spherical or cylindrical) are commercially available and so, for these and other reasons it might be possible to use them instead of prisms and take advantage of the fact that they can also be used to focus the beam. Fig 2.15 shows a possible configuration where a plano-convex ZnSe lens might be used to focus a free space collimated beam and couple it to WG modes inside the microdisk. The collimated beam is easily generated using a pigtailed collimator.

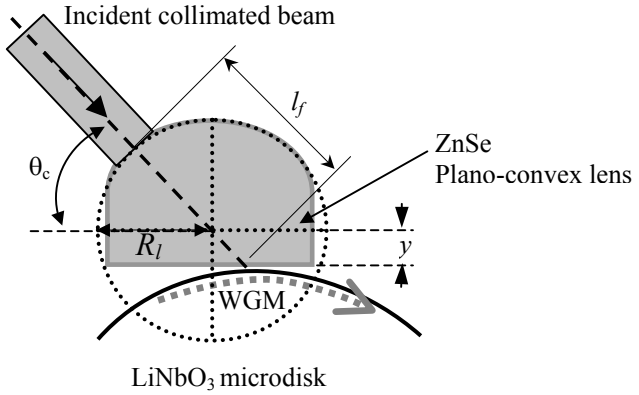


**Figure 2.15** Geometry of direct coupling to WG modes through a plano-convex ZnSe lens.

The main parameters of this design that have to be optimized are the lens radius ($R_l$) and the center offset ($y$). Using a basic wave tracing matrix for a spherical air-ZnSe interface and the ABCD law for guassian beams one may calculate the proper value of $R_l$ and $y$ for generating a guassian beam with a waist size of $w$ at the contact point of the microdisk and plano-convex lens. The value of the beam waist size ($w$) has to be chosen according to the WG mode profile. Consider that the beam axis is passing through the center of the lens, and therefore, there is no deviation due to refraction at

the air-ZnSe interface. The beam should enter the interface with an incident angle equal to the ZnSe-$LiNbO_3$ critical angle ($\theta_c = 60°$), so knowing this angle and $l_f$ we can easily calculate $y$.

The last possibility that we describe here uses a $LiNbO_3$ half-disk to couple to a full-disk. Coupling non-resonant WG modes of a half-disk from free space using a cleaved fiber or a cylindrically shaped fiber is easy and very efficient. Since the wave vectors of the WG mode inside the half-disk and the WG mode in the full-disk are similar, if both disks are in contact the touching point should act as a directional coupler in analogy with regular fiber couplers and splitters.

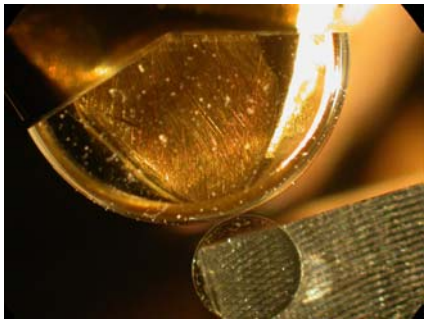

( a )

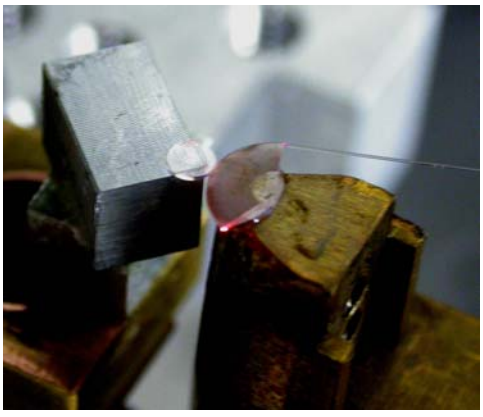

( b )

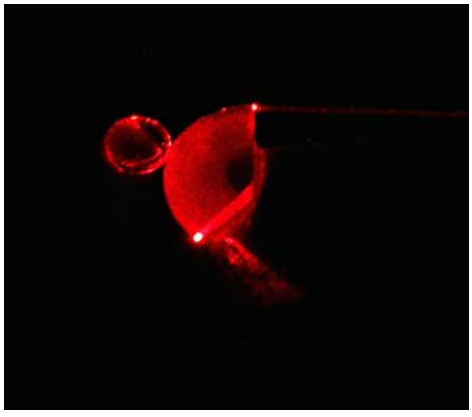

( c )

**Figure 2.16** (a) Photograph of the experimental arrangement used for testing a half-disk coupler. (b) The toroidal half-disk ($D$ = 6 mm) coupled to a microdisk ($D$ = 2 mm). (c) He-Ne laser light coupled to the WG resonance of the 2 mm microdisk through a toroidal half-disk coupler.

We have done some preliminary work on this scheme but the measured coupling is very weak due to mode mismatch (we didn't have two identical disks).

Fig. 2.16(a) shows a photograph of the first experimental arrangement used for investigating the half-disk coupling scheme. The half-disk and the microdisk have diameters of 6 mm and 2 mm respectively. Fig. 2.16(b) shows another arrangement where a toroidal half-disk (made by grinding the microdisk shown in Fig. 2.10) is coupled to the 2 mm microdisk. Fig. 2.16(c) shows He-Ne laser (red light, $\lambda = 623.2$ nm) coupled to the microdisk through the toroidal half-disk.

## 2.4 DC response

Study of DC electrical-optic response of the WG modes in the microdisk is useful since it provides information regarding the strength of the electro-optic interaction inside the disk without the complication of the microwave design issues of a RF modulator. This section covers the low-speed electro-optic response in a $LiNbO_3$ microdisk optical resonator.

### 2.4.1 DC shift

If we place a conductive ring on top of a microdisk (of the same radius) mounted on a ground plane, a DC voltage on the ring will generate an *E*-field (mainly along *z*-

direction) around the disk where the WG modes are propagating. Since $LiNbO_3$ is an electro-optic material, the *E*-field changes its refractive index and consequently the resonant wavelengths of WG modes. Using equation (2.6) (Sec. 2.3.1) we can estimate this change for TE WG modes:

$$\lambda_m = \pi D n_e/m \Rightarrow \Delta\lambda_m = \pi D \Delta n_e/m \Rightarrow \Delta\lambda_m = \lambda_m(\Delta n_e/ n_e) \quad (2.12)$$

We have used $n_e$ because we are interested in large $r_{33}$ and hence modes that are TE polarized. Since in most telecom applications the laser wavelength is around 1550 nm usually $\lambda_m = \lambda_o = 1550$ nm. The refractive index change may be estimated using $\Delta n_e = n_e^3\, r_{33} E_{eff}/2$ ($r_{33} \approx 30.8 \times 10^{-12}$ m/V) so:

$$\Delta\lambda_m = \lambda_m\, n_e^2\, r_{33} E_{eff}/2 \quad (2.13)$$

$E_{eff}$ is the magnitude of the *E*-field along the *z*-axis in the equatorial plane of the microdisk where the WG mode is traveling. Ideally, in the absence of fringing and other perturbing factors the *E*-field intensity in the middle of the disk should be equal to *V/h* (*V* is the applied voltage). But due to a fringing field effect, the *E*-field in the vicinity of the sidewall has a component along **r** ($E_r$). The magnitude of $E_r$ varies along the *z*-axis and is zero at the equatorial plane. Simulation shows that for a 400 μm thick $LiNbO_3$ disk, $E_r$ is about 8 times smaller than $E_z$ at $z \sim \pm 100$ μm from the equatorial plane. The air gap between the ring and the microdisk surface will also reduce the *E*-field intensity inside $LiNbO_3$. We summarize all these effects and the overlap integral between optical mode and the *E*-field in a correction factor called the optical-mode-electric-field overlap correction factor $\beta_{EO}$ so:

$$E_{eff} = \beta_{EO}(V/h) \quad (2.14)$$

When $V$ = 1 V $\Delta\lambda_m$ is called the DC shift or $\Delta\lambda_{DC}$. This DC shift is an important parameter in a microdisk modulator because it quantifies the electro-optic response of the modulator and is helpful for calculating the RF modulation response. The measured value of the DC shift for a WG resonance of a microdisk can be used to estimate the corresponding $\beta_{EO}$. The desired value of $\beta_{EO}$ should be close to 1 but in most cases it is less than 0.5. $\beta_{EO}$ is determined by many parameters and it also varies slightly for different WG resonances. It is possible to improve $\beta_{EO}$ by using a geometry that forces the *E*-fields to better overlap the optical mode region. For example in our latest design we mount the microdisk on a cylindrical ground plain with the same radius as the disk and we observe a slightly larger DC shift.

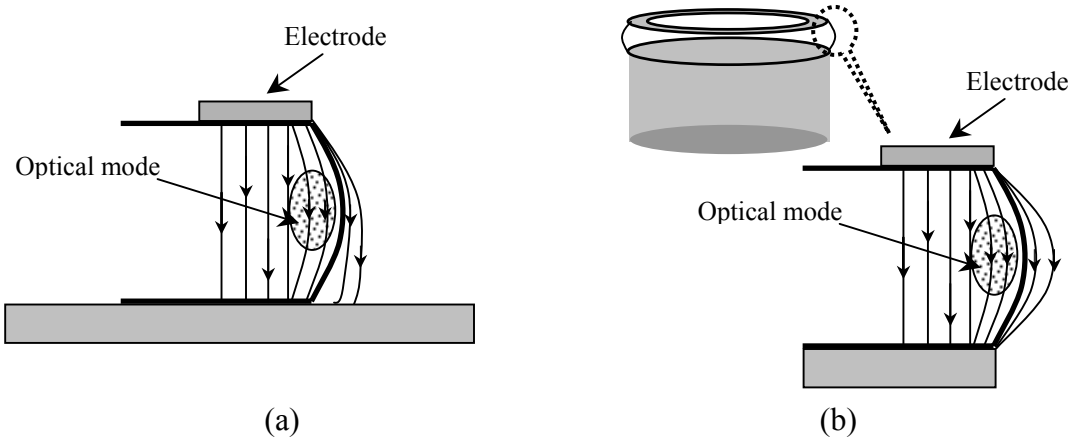


**Figure 2.17** (a) Schematic diagram showing the *E*-field lines in the vicinity of the microdisk sidewall (the curvature and fringing effect have been exaggerated). (b) The modified design where the microdisk is mounted on a cylindrical ground plane.

Fig. 2.17(a) shows the old design where the microdisk was mounted on a large ground plane and Fig. 2.17(b) shows the modified design. Table 2.2 shows the results of the DC shift measurements for the microdisk modulators tested in our lab.

The last microdisk was mounted on our modified design and has the largest $\beta_{EO}$. Fig. 2.18(a) shows a photograph of the microdisk resonator ($D$ = 3 mm, $h$ = 0.4 mm) mounted on a cylindrical ground plane.

**Table 2.2** DC-shift and $\beta_{EO}$ for different disks

| $D = 2R$ (mm) | $h$(mm) | $\Delta\lambda$ (pm/V) (measured) | $\Delta\lambda$ (pm/V) (calculated) | $\beta_{EO}$ |
|---|---|---|---|---|
| 5.13 | 0.4 | 0.09 | 0.27 | 0.33 |
| 5.84 | 0.74 | 0.06 | 0.15 | 0.4 |
| 2.9 | 0.4 | 0.05 | 0.27 | 0.18 |
| 2.95 | 0.4 | 1.3 | 0.27 | 0.48 |

Fig. 2.18(b) shows the measured optical output spectrum of the microdisk in Fig. 2.18(a) at 0 V and 5 V DC bias. The resonator is coupled through a single prism and the output fiber is tuned to the WG cone to detect WG peaks.

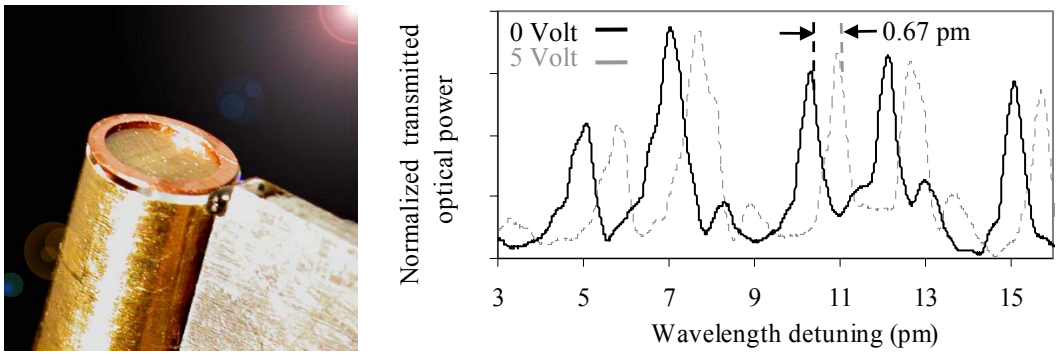


( a ) ( b )

**Figure 2. 18** (a) Photograph of the microdisk resonator mounted on a cylindrical ground plane. (b) Measured optical output spectrum at 0 V and 5 V DC bias voltages.

We can also simulate the DC shift ($\Delta\lambda_{DC}$) using equation (2.10) and the voltage dependent $k$-vector:

$$k(V) = \frac{2\pi n_e(V)}{\lambda} = \frac{2\pi[n_e + \Delta n_e(V)]}{\lambda} \tag{2.15}$$

Fig. 2.19 shows the simulated WG resonant wavelength shift for a microdisk resonator with following parameters: $\kappa = 0.0999$, $\alpha = 0.0075$ cm$^{-1}$, $P_{o,in} = 50$ μW, $\beta_{EO} = 0.5$, $h = 0.4$ mm. When the electric field is applied $\lambda_m \rightarrow \lambda_m \pm \Delta\lambda_m$ (the sign depends on the relative direction of the *E*-field and *c*-axis). The simulated values are in good agreement with values obtained from equation (2.13). In section 2.6 we will use the same approach to calculate the optical modulation amplitude in a microdisk modulator.

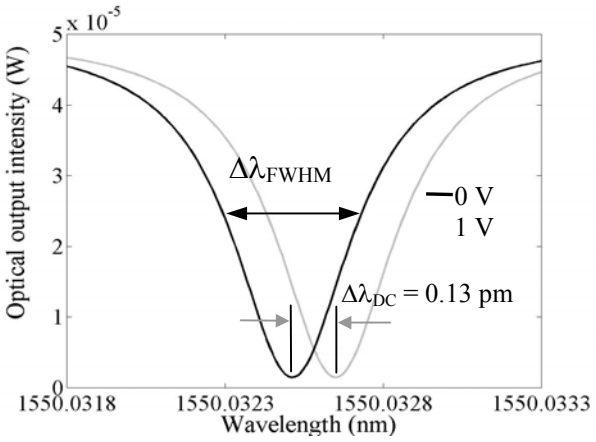


**Figure 2.19** (a) simulated resonant shift of the transmission dip for a microdisk resonator with: $\kappa = 0.0999$, $\alpha = 0.0075$ cm$^{-1}$, $P_{o,in} = 50$ μW, $\beta_{EO} = 0.5$, $h = 0.4$ mm.

To simulate a double-prism coupled microdisk resonator or a single-prism coupled resonator with an output alignment for detecting WG peaks, we have to use a different transfer function that corresponds to a microdisk coupled to two waveguides. This is because the output beam is not propagating in the same direction as the reflected beam so they do not interfere.

The corresponding transfer function may be written as:

$$C = \frac{a^2(1-|t|^2)^2}{1+a^2|t|^4 - 2a|t|^2\cos(\pi kD)} \tag{2.16}$$

The parameters in this equation are the same as in equation (2.10). The optical spectrum represented by equation (2.16) is a series of peaks rather than dips.

### 2.4.2 Optical bistability

Bistable optical devices are of great interest for their possible applications to all-optical signal processing for optical computing, optical thresholding and memory. The most common intrinsic bistable optical devices consist of a Fabry-Perot (FP) resonator containing nonlinear media. To date optical bistability has been observed in different types of nonlinear resonators using materials with various nonlinearity mechanisms [27-32]. Here we demonstrate the bistable behavior of the $LiNbO_3$ microdisk resonator when configured as part of an electrical feedback loop. This differs from the FP case in that we are using a traveling wave resonator. The reason for our interest is that the high-$Q$ should, in principle, make a sensitive device. However, there will be a trade off between speed of response and sensitivity.

Fig. 2.20 (a) is a photograph of the microdisk modulator used in our experiment. The microdisk resonator has a diameter of 5.8 mm and a thickness of 0.74 mm. The measured DC shift for this configuration is about 0.09 pm/V (Table 2.2). The experimental arrangement to measure electro-optic non-linearity is shown in Fig.

2.20(b). The voltage applied to the electrode is a function of resonator optical output power. Optical input power to the resonator is, provided by a frequency-stabilized laser diode whose output is intensity modulated to create a 500 Hz triangle wave. Optical output power is detected using a photodiode. To study electro-optic bistability, amplified detector output voltage is fed back to the disk electrode.

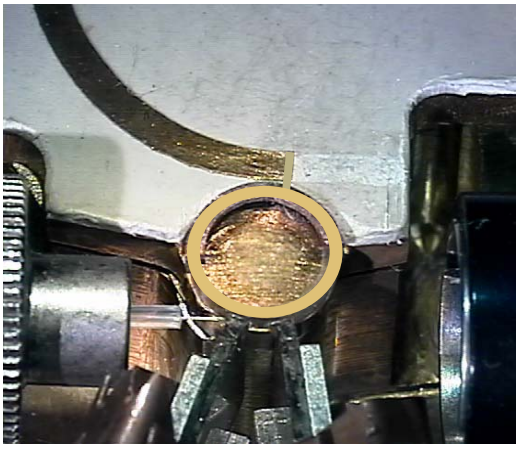

( a )

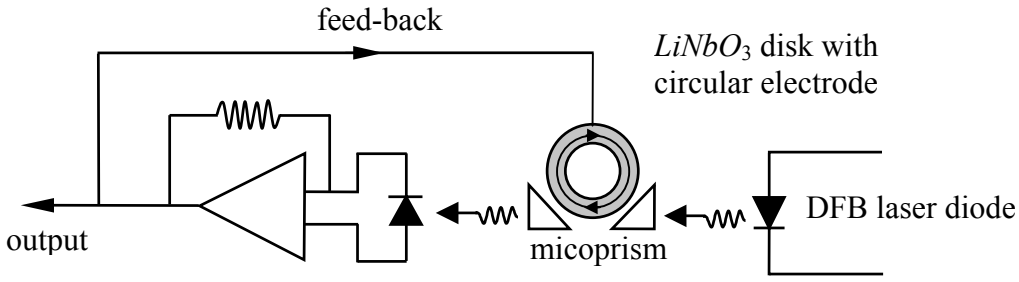


( b )

**Figure 2.20** (a) Photograph of the $LiNbO_3$ microdisk modulator. (b) Experimental arrangement used for demonstrating the bistable behavior of the microdisk optical resonator with a feed-back loop.

Fig. 2.21(a) shows the measured optical output-power as a function of optical input-power for the indicated values of peak-to-peak voltage feed-back ($V_{fb}$) and optical $Q$-factor. The electro-optic system shows a slight non-linearity when $V_{fb}$ = 1.5 V, using

an optical mode with $Q = 7.5\times10^5$, and significant bistability and hysteresis behavior when $V_{fb}$ = 3.0 V, using an optical mode with $Q = 10^6$. The arrows indicate the sense of the hysteresis loop. Fig. 2.21(b) shows results of simulation for the ideal case where just one set of modes has been excited inside the disk. The simulation shows a behavior similar to the experimental results of Fig. 2.21(a).

Since two-prism coupling technique is employed used in this experiment, equation (2.16) is used to calculate the optical output power as a function of optical input power. The optical output power can be written as $C\times P_{o,in}$ where $C$ is a function of $P_{o,in}$ because $k$ is proportional to $V_{fb}$ and $V_{fb}$ is proportional to the optical output power. $V_{fb}$ creates an electric field along the z-direction equal to $E_z = V_{fb} / h$ which changes the refractive index at incident optical wavelength $\lambda_0$ = 1550 nm from $n_e$= 2.138 to $n_e = n_e - n_e^3 r_{33} E_z / 2$. Consequently the WG wave vector $k$ ($=2\pi n_e/\lambda_0$) depends on $V_{fb}$. Hence, with feed-back, the transfer function ($C$) becomes a function of optical output power as well as wavelength. The optical output power $P_{out}(\lambda)$ of the system is calculated by applying a discretized triangular input signal and solving the equation $P_{out}(\lambda) = C(\lambda,P_{out})\times P_{o,in}(\omega)$ iteratively. The laser wavelength is set to be $\lambda_{res}$-$\Delta\lambda_{FWHM}/2$ where $\lambda_{res}$ is one of the resonant wavelengths of the microdisk resonator, and $\Delta\lambda_{FWHM}/2$ is the spectral line width of the optical resonance.

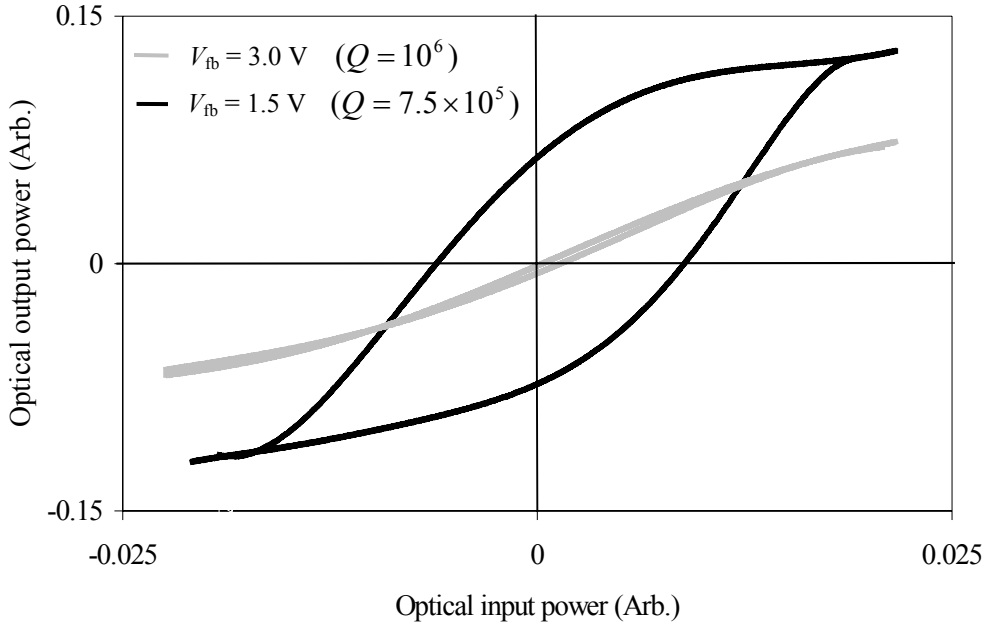


( a )

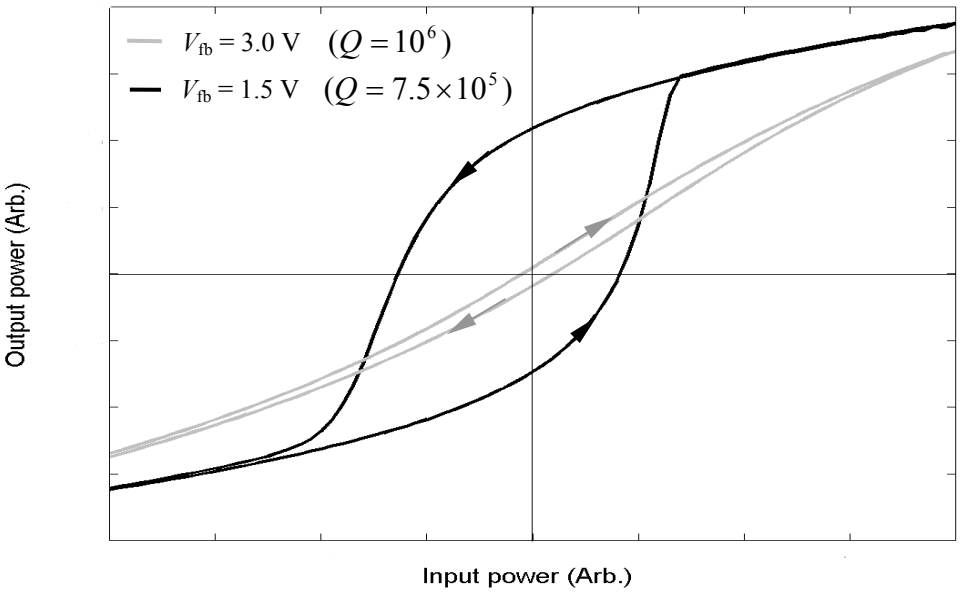


( b )

**Figure 2.21** (a) Measure optical output-power as a function of optical input-power for indicated values of peak-to-peak voltage feedback ($V_{fb}$) and optical $Q$-factor. (b) Results of simulation for the ideal case where just one set of modes has been excited inside the disk

## 2.5 RF resonator

The key characteristics of the modulating *E*-field for an efficient electro-optic interaction with WG optical modes inside the disk may be summarized as:

1) Proper RF *E*-field spatial distribution.
2) RF oscillation frequency equal to $m_o \times \Delta\nu_{FSR}$ ($m_o$: integer).
3) Large interaction length.
4) Large magnitude.
5) Good overlap with the optical mode (large $\beta_{EO}$).

The role of a good RF resonator is to generate an *E*-field that satisfies all these requirements. We show that the microstrip ring resonator can fulfill all requirements with minimal complexity. It is very important to note that in a conventional MZ modulator both optical and electrical waves are traveling along an open linear trajectory and they are velocity matched for broadband operation. In contrast, in a microdisk modulator, the optical wave is a resonant traveling wave that circulates around the microdisk. Given the large difference between the RF resonant wavelength, $\lambda_{RF} = c/(n_{RF,e}\,\Delta\nu_{FSR})$, and resonant optical wavelength, $\lambda_{res} = c/(n_e \nu_{res})$, it is not easy to create a traveling wave RF resonance around the disk. In our microdisk modulator the RF field is a standing wave and the phase matching between the optical and RF waves is achieved by frequency matching ($f_{RF} = m_o \times \Delta\nu_{FSR}$) and appropriate spatial distribution of the *E*-field.

### 2.5.1 Linear and half-ring RF resonator

Fig. 2.22 shows the linear standing-wave resonator design, which was been used for the first demonstration of optical modulation with simultaneous electrical and optical resonance in a microdisk [47]. The RF power is fed to the central open-ended microstrip and gradually couples to two linear resonators.

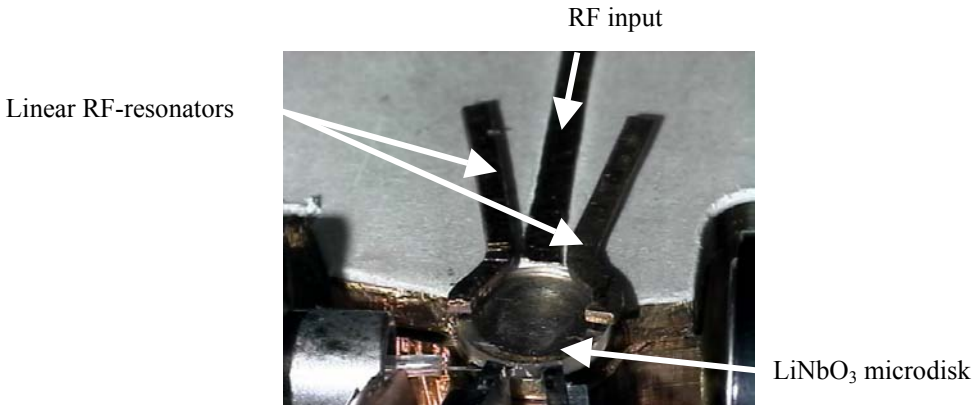


**Figure 2.22** Photograph of the first RF-resonator (linear) used for modulating the WG modes inside the $LiINbO_3$ disk.

About 2/3 of each resonator's length is on the PCB board ($\varepsilon_r$ = 2.94, thickness = 0.508 mm). The remaining length (1/3) is curved with a radius *R* (equal to the microdisk radius) and covers about 2/5 of the disk. The frequencies of both resonators are tuned to $\Delta\nu_{FSR}$. Although we observed optical modulation using this configuration, their low efficiency (and complexity of RF tuning) caused us to replace the linear resonators with a semi-ring resonator.

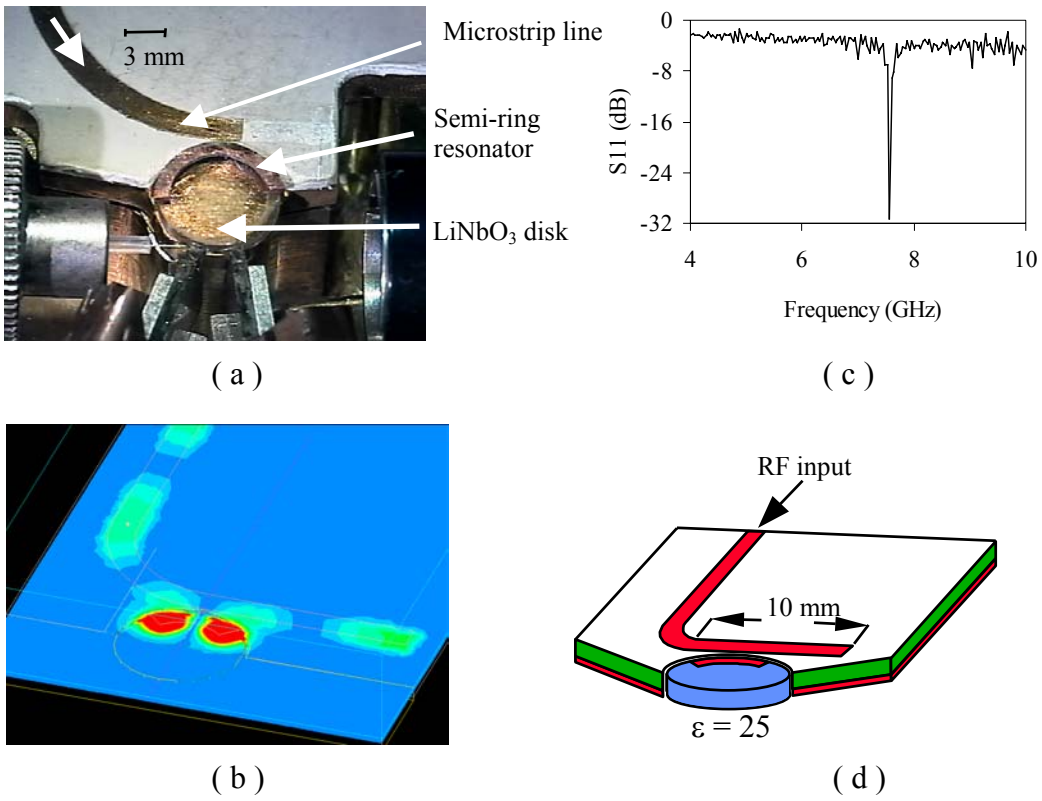


**Figure 2.23** (a) Photograph of the microdisk modulator designed based on side coupled semi-ring RF resonator. (b) The measured $S_{11}$ spectrum for the open-ended microstripline side-coupled to the semi-ring. (c) The result of simulating the resonant *E*-field (magnitude) distribution on a cut-plane located in the middle of the disk. (d) The structure used in the simulation. Dielectric substrate thickness = 0.508 mm, dielectric constant = 2.94, microstrip linewidth = 1.2 mm, disk thickness = 0.7 mm, semi-ring resonator width = 1.2 mm, resonator angle = 90 degree.

Fig. 2.23(a) shows the photograph of a microdisk modulator that uses a semi-ring as the RF-resonator. The resonator is placed on the $LiNbO_3$ microdisk while the side-coupled open terminated microstrip line is fabricated on a PCB board ($\varepsilon_r$ = 2.94, thickness = 0.508 mm). The outer radius of the semi-ring ($R_o$) is equal to the microdisk radius in order to maximize the overlap between the *E*-field and the optical mode. The length of the semi-ring is chosen such that its fundamental resonant frequency ($f_{RF}$) is equal to the optical free spectral range frequency ($\Delta\nu_{FSR}$)

that is 7.6 GHz for this disk. Experimentally it has been found that this length is very close to half of the disk circumference. Fig. 2.23(c) shows a diagram of the configuration used for simulating the *E*-field distribution on the RF-resonator. The dimensions are slightly different than those of the actual experimental arrangement, but qualitatively the predicted behavior matches the experimental results. We used Ansoft HFSS software [(3)] for this simulation. As may be seen, when the ring is fed at its fundamental resonant frequency, the magnitude of the *E*-field in the disk is larger than the magnitude of the *E*-field underneath the line. The *E*-field magnitude is plotted on a cut-plane that passes through the middle of the disk. This proves that the resonance in the ring amplifies the *E*-field. The amplification depends on the intrinsic quality-factor of the ring and the coupling efficiency to the microstrip line. To measure the resonant frequencies of the semi-ring and estimate the *Q*-factor we use the standard RF reflection measurement ($S_{11}$) with a RF network analyzer. Fig. 2.23(b) shows a typical $S_{11}$ spectrum obtained for the semi-ring shown in Fig. 2.23(a). Fig. 2.24 shows a schematic diagram of the voltage distribution around the semi-ring. The *E*-field is a standing wave and, due to the open boundary condition, its maxima are located at open ends of the semi-ring (points A and B). Similar to an open circuit length of transmission line, the semi-ring resonator behaves as a parallel *RLC* resonant circuit (see section 1.3.1).

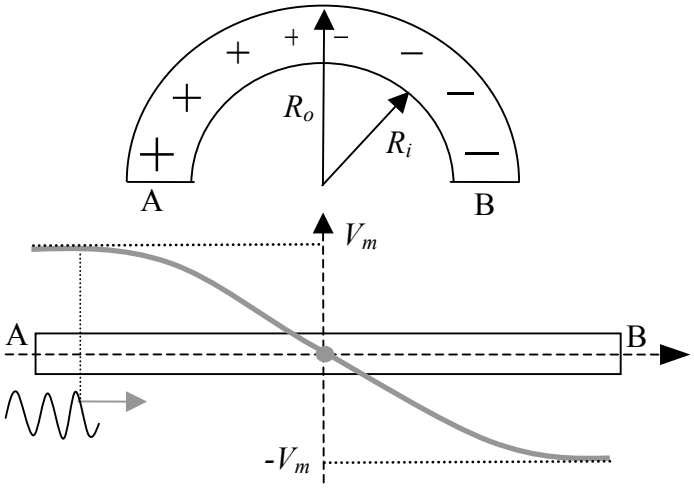


**Figure 2.24** Schematic diagram showing the voltage distribution around the semi-ring RF resonator

Unlike a Mach-Zehnder modulator it is not possible to lock the optical phase to the maximum of the *E*-field. However, by choosing $f_{RF} = \Delta\nu_{FSR}$, the photon roundtrip time ($\tau_{RT}$) would be equal to the RF period ($T_{RF}$) and therefore the electro-optic phase accumulation per roundtrip is maximized. The fundamental resonant frequency of a semi-ring (with a length equal to $\pi R'$) may be written as:

$$f_{RF,1} = c/2\pi R' n_{RF} \tag{2.17}$$

where $R' = (R_o + R_i)/2$ is the half-ring mean radius and $n_{RF}$ is the effective RF refractive index. Since the extraordinary RF refractive index of $LiNbO_3$ ($n_{RF,e} = 5.1$) is larger than the optical ($n_e = 2.14$), matching optical FSR and RF resonant frequency of a semi-ring is a difficult task but if we relax the limitation on ring length it is possible to tune the frequency by tuning the length. In practice by reducing the half-ring length by about 5-10 %, we were able to match the frequencies. Because of this relatively easy tuning technique, the semi-ring

resonator was the first resonator successfully employed in the microdisk modulator design [47,48]. More details about the physics of resonance in side coupled ring/half ring resonators are discussed in the next section. The main disadvantages of the semi-ring as a RF-resonator are a reduced quality factor due to electromagnetic radiation from the open ends, poor coupling efficiency at high frequencies, and the fact that only half of the full photon roundtrip is used for electro-optic interaction. A ring resonator solves the latter two problems by closed loop operation and interacting over the full photon roundtrip.

### 2.5.2 Ring resonator

Microstrip ring resonators are widely utilized in measurement applications as well as filter, oscillator and antenna design [41,42,44,45]. Compact size, low radiation loss, high quality factor and geometrical compatibility make the ring resonator a perfect candidate for disk and ring shaped optoelectronic devices. A ring resonator with the same diameter as the microdisk can generate the modulating *E*-field around the full photon path length. Several methods have been developed for coupling RF power to ring resonators [36,38,44]. In our design the metal ring resonator is placed on top of the microdisk and is side coupled to a microstripline on a dielectric substrate. To understand the details of microstrip-ring physics we start with a side-coupled microstrip-ring system on a uniform dielectric substrate.

Fig. 2.25 shows the geometry of a ring resonator with a mean radius of $R' = (R_o+R_i)/2$ and a width of $w_r = R_o - R_i$ on a dielectric substrate with a relative permittivity of $\varepsilon_s$ and a thickness $h_s$. For an isolated narrow such that $w_r/2R \leq 0.1$ isolated ring the dominant resonant modes are $TM_{m10}$ and the field components are $E_z$, $H_r$ and $H_\phi$ for these modes [37]. The resonant frequencies of these modes can be simply calculated from:

$$f_{RF,m} = m_{RF}\, c/(2\pi\, R' n_{RF,e}) \tag{2.18}$$

where $c$ is speed of light, $m_{RF}$ is a positive integer and $n_{RF,e}$ is the effective refractive index of $TM_{m10}$ mode. $n_{RF,e}$ may be calculated using the effective dielectric constant of a microstrip line given approximately by [46]:

$$\begin{aligned} n_{RF,e} &= \sqrt{\varepsilon_{eff}} \\ \varepsilon_{eff} &= \frac{\varepsilon_r + 1}{2} + \frac{\varepsilon_r - 1}{2} \times \frac{1}{\sqrt{1 + 12\frac{w}{h_s}}} \end{aligned} \tag{2.19}$$

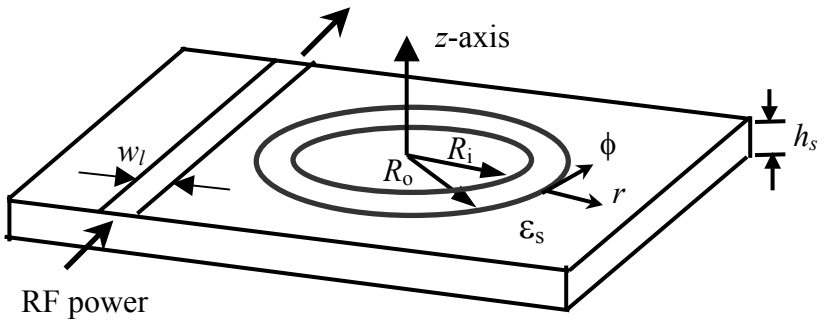


**Figure 2.25**. Geometry of microstrip ring resonator side-coupled to a microstripline on a uniform dielectric substrate.

It is also possible to use the Wheeler's effective permittivity [37]:

$$\varepsilon_{eff} = 1 + q(\varepsilon_s - 1) \tag{2.20}$$

where $q$ is called the filling factor. Experimentally it has been shown that for $\varepsilon_d$ = 9.9, $q$ is proportional to $(w/2R)^{0.09}$ and $(w/h_s)^{0.09}$ [37]. Equation (2.20) is useful for more complex cases where Equation (19) fails. In this situation, experimental results are typically used to estimate the filling factor. Fig. 2.26(a) shows the photograph of a side coupled ring resonator fabricated on RTD 6006 dielectric substrate with a $\varepsilon_s$ = 6.15, $h_s$ = 0.508 mm.

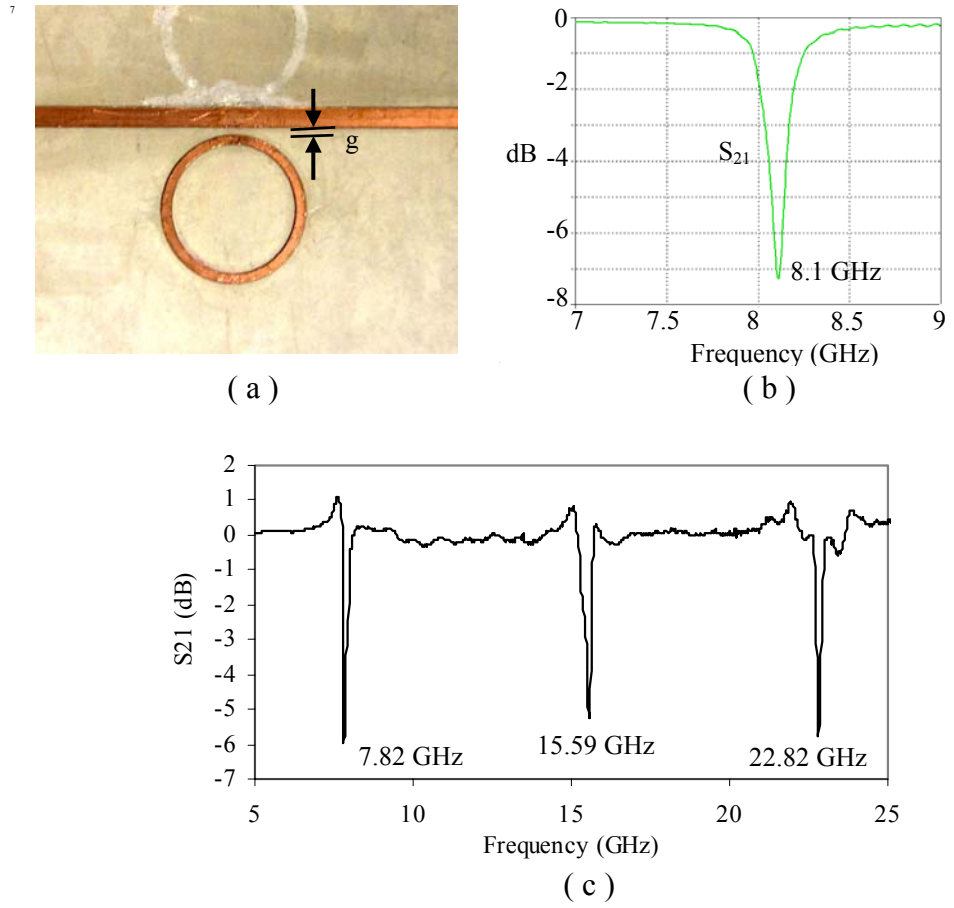


**Figure 2.26**. ( a ) Ring on uniform dielectric substrate (RTD 6006): $\varepsilon_r$ = 6.15, dielectric thickness ($h_s$ ) = 0.508 mm, microstripline width ($w_1$) = 0.8 mm, ring diameter = 6.11 mm, gap size (g) = 0.32 mm. (b) The simulated $S_{21}$ for the ring shown in (a). (c) Measured $S_{21}$ . Resonant frequencies up to the third harmonic are shown.

Fig. 2.26(b) is the simulated $S_{21}$ using CST electromagnetic simulator [2]. The fundamental resonance of the ring resonator occurs at $f_{RF}$ = 8.1 GHz. Fig. 2.26(c) shows the measured $S_{21}$ through the microstripline. The RF resonances ($TM_{110}$, $TM_{210}$, $TM_{310}$) appear as dips in the transmitted RF power spectrum. The measured fundamental resonance is about 7.82 GHz that is very close to the simulated value.

If we use equation (2.19) to calculate $\varepsilon_{eff}$ and substitute into equation (2.18) we find that $f_{RF1}$ = 7.91 GHz. This agreement validates our assumptions and the approximations in Equations (2.18) and (2.19). The slight (1%) difference between calculation and measurement is mostly due to errors in ring width and diameter measurements. Also the resonant frequency calculated using equation (2.18) is the intrinsic resonant frequency of an isolated ring. Coupling to the microstrip line changes the resonant frequency (loading effect) similar to any other loaded oscillator. When a ring resonator is strongly coupled to a microstripline (small gap sizes), the symmetry breaks due to the proximity of the microstripline to the ring and two coupling configurations are possible, depending on whether induced magnetic field or induced electric field is maximum at the resonator near the microstripline. The broken symmetry splits each mode into two modes with slightly different resonant frequencies: even and odd modes [36]. Odd modes have lower frequencies and are capacitively coupled to the line, while the even modes have higher frequencies and are magnetically coupled to the line [35]. The coupling strength depends on mode order. The different coupling mechanisms result in different loading factors and hence different frequency shifts and loaded *Q*s. Resonant

frequencies cannot be calculated using equation (2.18), although this relation may still be used to get a rough idea about the resonant frequencies. It is evident that calculating the loaded *Q*-factors and resonant frequencies as a function of geometrical parameters and mode nature is an involved task. We will explore this issue as we continue to analyze the ring resonator on a $LiNbO_3$ microdisk.

In the microdisk modulator design, the ring is placed on a $LiNbO_3$ microdisk. The role of the ring is to provide an *E*-field normal to the disk surface and localized to the disk circumference where the highly confined optical WG modes are traveling.

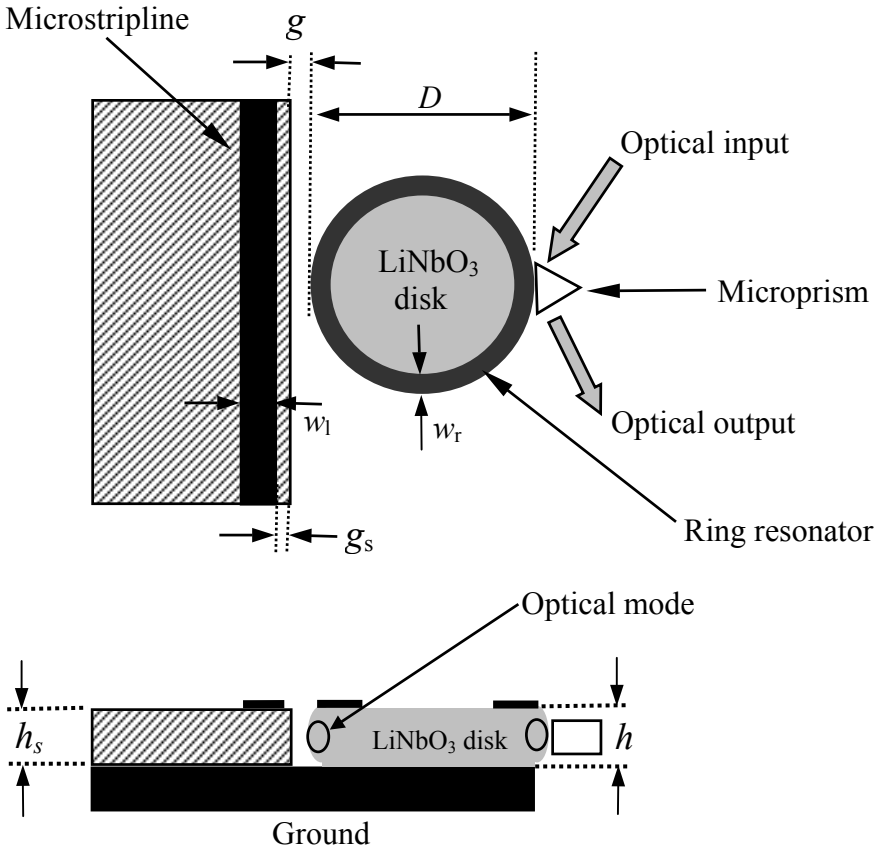


**Figure 2.27**. Geometry of ring resonator on $LiNbO_3$ side-coupled to a microstripline (top view and side view)

In our design we use a side-coupled microstripline to couple energy to a resonance of the RF ring resonator. Fig. 2.27 shows a schematic diagram of the ring, microdisk and the microstripline.

This configuration is more complicated than the side-coupled ring on a uniform substrate (in Fig. 2.25) because the ring and line are on two different high contrast dielectric materials with an air gap in between. Fig. 2.28(a) shows a typical experimental arrangement for characterizing the performance of the ring resonator on the $LiNbO_3$ microdisk.

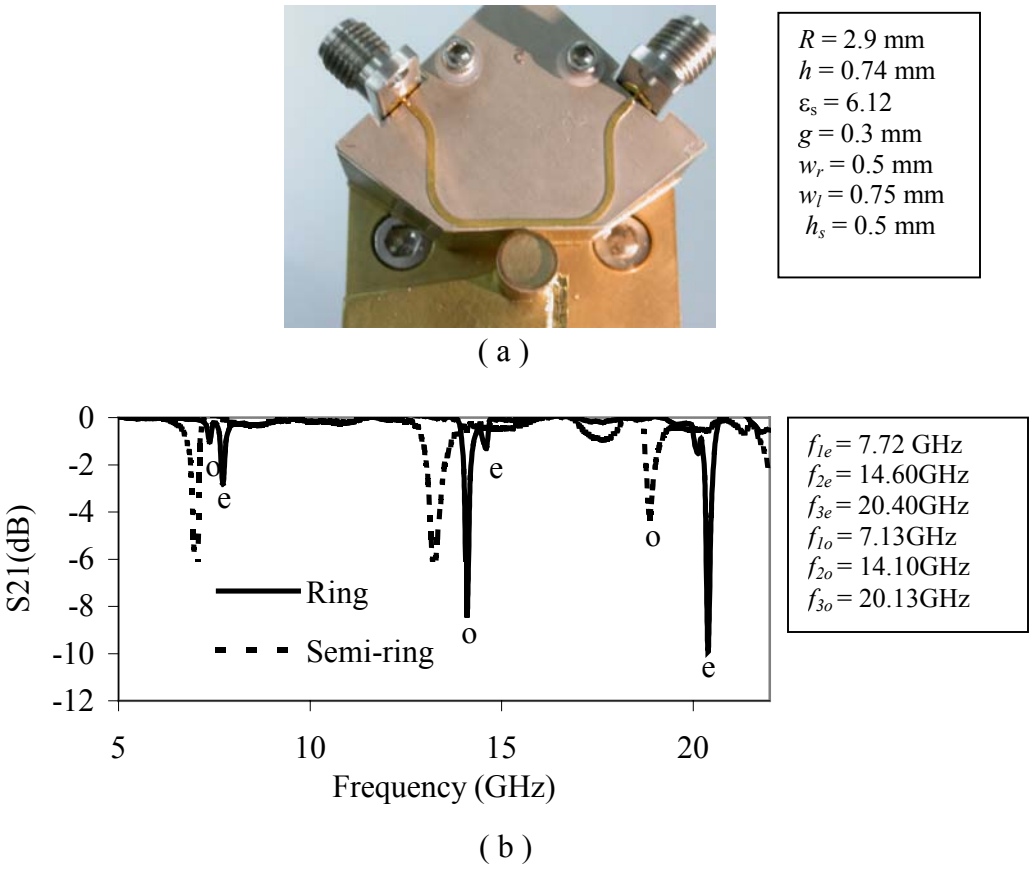


**Fig. 2.28**. (a) Photograph of the ring resonator on $LiNbO_3$ microdisk side-coupled to the microstripline. (b) $S_{21}$ measurement results for ring and semi-ring on the $LiNbO_3$ microdisk shown in (a).

We use *S*-parameter measurement ($S_{11}$ and $S_{21}$) to estimate the resonant frequency and the quality factor of the RF resonances. Fig. 2.28(b) shows the measured $S_{21}$ for the ring in Fig. 2.28(a) as well as a semi-ring on the same microdisk. The resonant dips up to the third harmonic of the ring are shown in this figure. For the ring resonator (solid line) we observe two dips (one small and one large) due to even-odd mode splitting. The coupling strength of the ring as indicated by the depth of the resonant dips is better at higher frequencies than that of the semi-ring, and the width of the resonant dips is smaller for the ring due to a better quality factor. These observations prove the validity of our argument regarding the superiority of the ring resonator especially at high frequencies. Before analyzing the electromagnetic behavior of this system we will examine simultaneous RF-optical resonance in this configuration.

As mentioned in section 1.3, an optically resonant modulator can only modulate light at RF frequencies equal to $m_o \times \Delta\nu_{FSR}$ but an efficient modulation also requires a proper spatial distribution of the oscillating *E*-field to maximize the accumulated electro-optic induced phase shift at each roundtrip. Fig. 2.29 shows the simulated resonant *E*-field distribution on a cut-plane that passes through the middle of the disk. Fig. 2.29(a) shows the 2-D *E*-field magnitude distribution and Fig. 2.29(b) shows a 3-D view of the *E*-vectors distributed around the disk. Since we want to satisfy the frequency matching condition $f_{RF,m} = m_{RF} \times \Delta\nu_{FSR}$ for low values of $m_{RF}$ ($m_{RF} < 10$), the RF wavelength, $\lambda_{RF,m} = c/(n_{e,RF} \times f_{RF,m})$, is not small enough (compared to ring circumference: $2\pi R$) for resonant traveling wave operation.

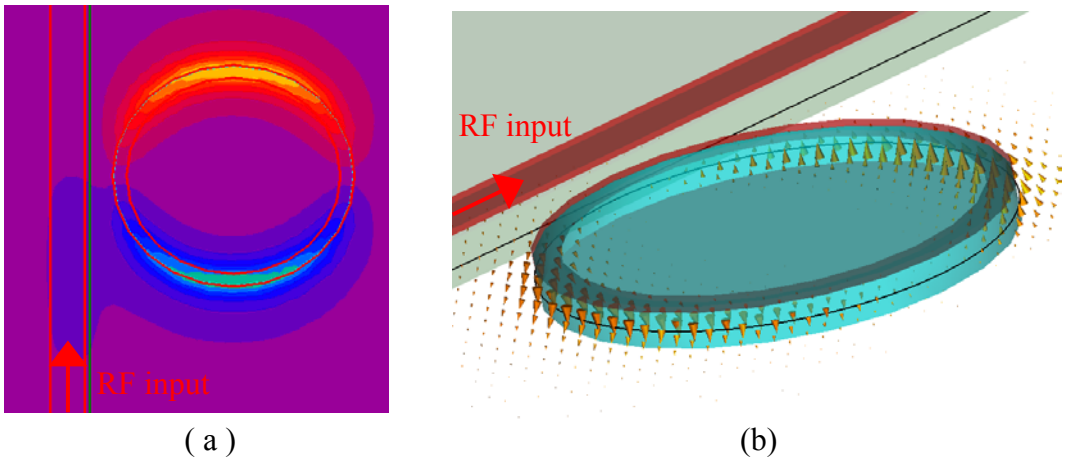


**Figure 2.29** Simulated *E*-field distribution on a cut plane passing through the middle of a $LiNbO_3$ microdisk when the fundamental resonance of the ring resonator is excited. (a) 2-D *E*-field magnitude distribution. (b) 3-D view of the *E*-vectors distributed around the disk. The *E*-vectors are plotted on a log scale.

So, similar to the semi-ring resonator, the ring resonator is a standing wave resonator and the locations of the maximum and minimum are fixed by the broken symmetry of the feed point. In Fig. 2.30 the voltage distribution along a linear standing wave resonator, that is equivalent to the ring resonator, is shown.

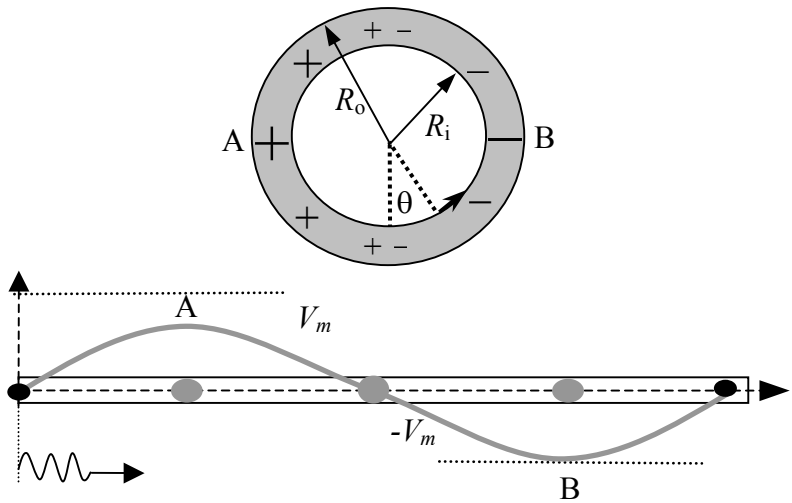


**Figure 2.30** The *E*-field distribution for the fundamental mode of the ring resonator and equivalent linear resonance.

The traveling optical wave (WG resonance) will always experience a position dependent *E*-field intensity during its round trip. A voltage oscillation on a ring resonator that is excited by a single tone at its fundamental resonant frequency ($f_{RF,1}$) can be expressed as:

$$V = V_m \cos(k_{RF} x_l)\cos(\omega_{RF} t) \tag{2.21}$$

The electro-optic induced phase shift for a photon that enters the microdisk resonator at point 'A' may be written as:

$$\varphi = \frac{2\pi x_l}{\lambda_{res}} \delta n_e = \frac{2\pi x_l}{\lambda_{res}} \xi \cos(k_{RF} x_l)\cos(\omega_{RF} t) \tag{2.22}$$

where $\xi = n_e^3 r_{33} E_{eff}/2 = (1/2)\, n_e^3 r_{33}\, \beta_{EO}/h$ (Eq. 14) and $x_l = (c/n_e)t$.

If we integrate equation (2.22) over ten optical roundtrip times ($10\tau_p$) that are also equal to the ten RF periods ($10T_{RF} = 10/f_{RF}$), then:

$$\varphi_{tot} = \frac{2\pi}{\lambda_{res}} \xi \int_0^{10T_{RF}} x_l \cos(k_{RF} x_l)\cos(\omega_{RF} t) dt \tag{2.23}$$

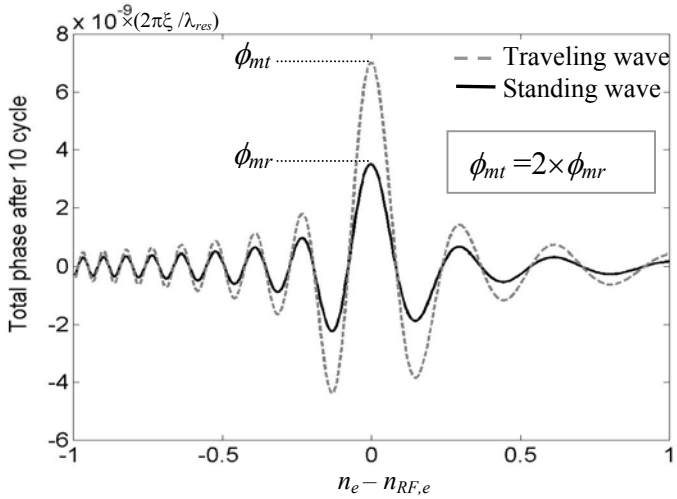


**Figure 2.31** The accumulated electro-optical phase for a photon that enters the resonator at the peak of the voltage oscillation after traveling for 10 cycles (solid line). The dashed line shows the accumulated electro-optic phase for a photon in a traveling wave modulator.

Fig. 2.31 shows the calculated value of $\phi$ against RF-optical detuning ($|n_e - n_{RF}|$).

So when $f_{RF} = \Delta\nu_{FSR}$ or $n_e = n_{RF}$, the phase shift is maximized but its magnitude is still half of the value that can be obtained in a conventional velocity matched traveling wave electro-optic phase shifter. When both optical and RF waves are traveling, their phase can be locked in such a way that the optical phase shift per unit length is written as:

$$\phi[V_{RF}(t)] = \frac{2\pi[n_e + \delta n_e(V_{RF})]}{\lambda_0} = \frac{2\pi}{\lambda_0}\left(n_e + \frac{1}{2}n_e^3 r_{33}\frac{\beta'_{EO}}{h} \times V_{RF}\right) \qquad (2.24)$$

where $\beta'_{EO}$ is the overlap factor and $h$ is the gap size between the electrodes.

For the microdisk modulator we use the refractive index change and the transfer function to calculate the optical power modulation. The modulated effective optical refractive index of TE modes in a frequency matched ($f_{RF} = \Delta\nu_{FSR}$) microdisk-microring system can be written as:

$$n_e(t) = n_{eo} + \delta n_e(t) = n_{eo} + \frac{1}{2}n_{eo}^3 r_{33}\frac{\beta_{EO}\beta_S}{h} \times V_m \cos(\omega_{RF} t) \qquad (2.25)$$

The new factor $\beta_S$ is a correction factor that accounts for the standing wave nature of voltage oscillation. As shown in Fig. 2.31 in a standing ring resonator based modulator $\beta_S = 0.5$. In equation (2.24) this factor doesn't exist because of the traveling wave nature of the RF wave.

We now turn our attention to the resonant frequencies of the microring resonator. The microdisks used in our experiments are *z*-cut (the *c*-axis is parallel to the *z*-axis and normal to the disk flat surface). The bulk dielectric constant of $LiNbO_3$ along the *c*-axis (*z* in Fig. 2.24 that is also the *E*-field direction for $TM_{m10}$ modes) is $n_{RF} = 5.1$ at frequencies between 1-50 GHz [2]. If $LiNbO_3$ is used as the substrate in a microstripline structure (Fig. 2.32(a)), the effective permittivity is reduced. For

example for a 0.4 mm thick substrate and a linewidth of 0.3 mm using equation (2.19), $\varepsilon_{eff} = 17.45$ and $n_{RF,e} = 4.18$. But a ring resonator on a $LiNbO_3$ microdisk has a cross-section similar to that shown in Fig. 2.32(b). For this configuration $\varepsilon_{eff}$ cannot be calculated by a simple formula so we use CST simulation software [2] to estimate the propagation constant and derive $n_{RF}$.

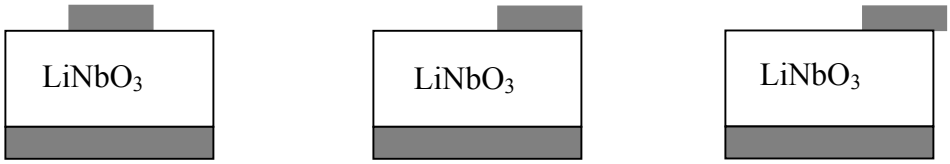


( a ) ( b ) ( c )

**Fig. 2.32**. $S_{21}$ measurement results for ring and half ring on $LiNbO_3$

For a similar substrate thickness and line width $n_{RF,e} = 3.76$, If we move the line further to the edge and create a 50 μm overhang in the air (which is equivalent to increasing the inner and outer radius of the ring), then $n_{RF}$ decreases to 3.56. This shows that by tailoring the ring/microdisk design one may reduce $n_{RF,e}$ to more closely match the optical refractive index ($n_e = 2.14$). Also the optical mode propagates at a radius almost equal to the disk radius ($R$) while the mean ring radius is $R' = (R_o+R_i)/2$. So as to satisfy the frequency matching condition ($\Delta\nu_{FSR} = f_{RF1}$), $n_{RF,e}$ should be larger than $n_e$ by a factor $R/R'$ (for a disk with a diameter of 3 mm and a ring with a width of 0.3 mm, $R/R' = 1.11$).

Another important factor that needs to be taken into account in RF frequency tuning

is that the loaded resonant frequency is larger than the value estimated by equation (2.18) due to side coupling to the microstripline. As we mentioned before, strong side-coupling results in separate degenerate even and odd modes in the microring and the loading effect is different for these modes. Taking into account the loading effect and the geometry of the resonator, one may expect that the resonant frequencies of the side-coupled ring on a dielectric disk should have the form:

$$f_{RF1} = \Delta f_L + \frac{c}{2\pi R' \sqrt{\varepsilon_{reff}}} \tag{2.26}$$

where:

$$\varepsilon_{eff} = f_\varepsilon \left( \varepsilon_r, t_s / w_r \right) \tag{2.27}$$

$$\Delta f_L = \begin{cases} f_{LE}(g) \\ f_{LO}(g) \end{cases} \tag{2.28}$$

$f_\varepsilon$, $f_{LO}$ and $f_{LE}$ are unknown functions that should be evaluated based on a particular geometry. $f_\varepsilon$ is equivalent to equation (2.19) for a regular microstrip line but it gives smaller values of effective permittivity for given values of $w$, $h$ and $\varepsilon_r$ due to the absence of dielectric on one side of the line as well as other design factors. To calculate $f_\varepsilon$ the wave equation for asymmetric microstripline should be solved. $f_{LO}$ and $f_{LE}$ are loading factors for even and odd modes as a function of the gap size ($g$) between the disk and line. These functions can be evaluated using experimental data. For example Fig. 2.33 shows resonant frequency measurement for the fundamental even mode of a ring resonator on a $LiNbO_3$ disk side-coupled to a microstripline with different coupling gap ($g$) sizes. In this experiment $g_s$ = 0.1 mm, $D$ = 3 mm, $w_r$ = 0.3 mm, $w_l$ = 0.75 mm, $h$ = 0.4mm, $h_s$ = 0.5 mm, and $\varepsilon_s$ = 6.12. The

experimental results show that tuning the gap over a wide range (600 μm) doesn't change the resonant frequency more than 200 MHz.

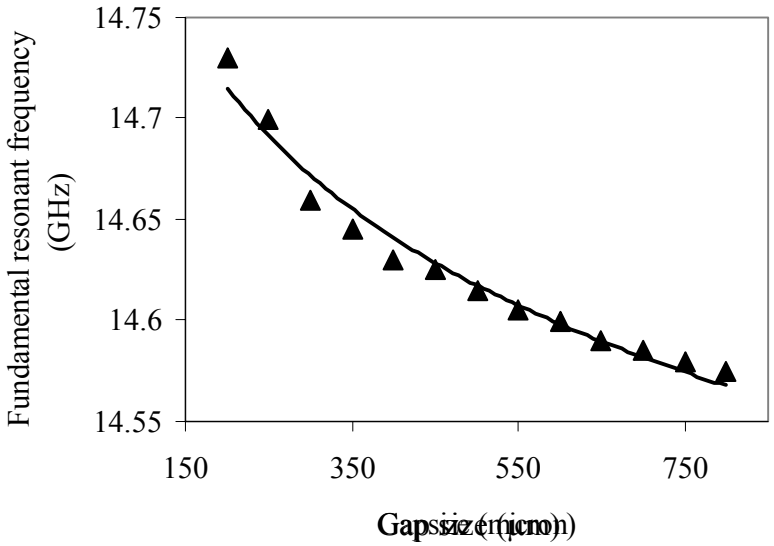


**Figure 2.33** Resonant frequency as a function of gap size for the even mode of a ring resonator ($w$ = 300 μm) on a $LiNbO_3$ microdisk with a diameter of 3 mm and a thickness of 0.4 mm. (approximated line equation: $f_{RF} = 15.292g^{-0.0073}$)

If we use equation (2.26) to estimate the fundamental resonant frequency of a ring resonator with $R_i$ = 2.75 mm, $R_o$ = 3.05 mm and $n_{RF,e}$ = 3.56 (that corresponds to the configuration shown in Fig. 2.31(c)) on a 3 mm diameter and a 0.4 mm thick $LiNbO_3$ microdisk with a $\Delta f_L$ =100 MHz then $f_{RF,1}$ = 10.14 GHz. The optical free spectral range for this disk is 14.6 GHz so that a factor of 1.44 reduction in $n_{RF,e}$ (2.07 in $\varepsilon_{eff}$) is required to achieve RF-optical frequency matching.

In our proof of principle experiment we solve this problem by fabricating the ring separately. When the ring is placed on top of the disk an effective air gap exists between the ring and $LiNbO_3$ surface due to the surface roughness of the ring and the

microdisk. This air gap reduces $\varepsilon_{eff}$. By properly choosing the ring size, gapsize, surface roughness and fine tuning the location of the ring on the disk, we were able to tune the fundamental RF resonant frequency of the ring very close to $\Delta\nu_{FSR}$. Notice that tuning the fundamental resonance doesn't guarantee $f_{RF,m} = m_{RF} \times \Delta\nu_{FSR}$ for all values of $m_{RF}$ because, as opposed to optical resonant frequencies, the RF resonant frequencies aren't exact multiples of the fundamental resonance because of different loading factors and even-odd splitting.

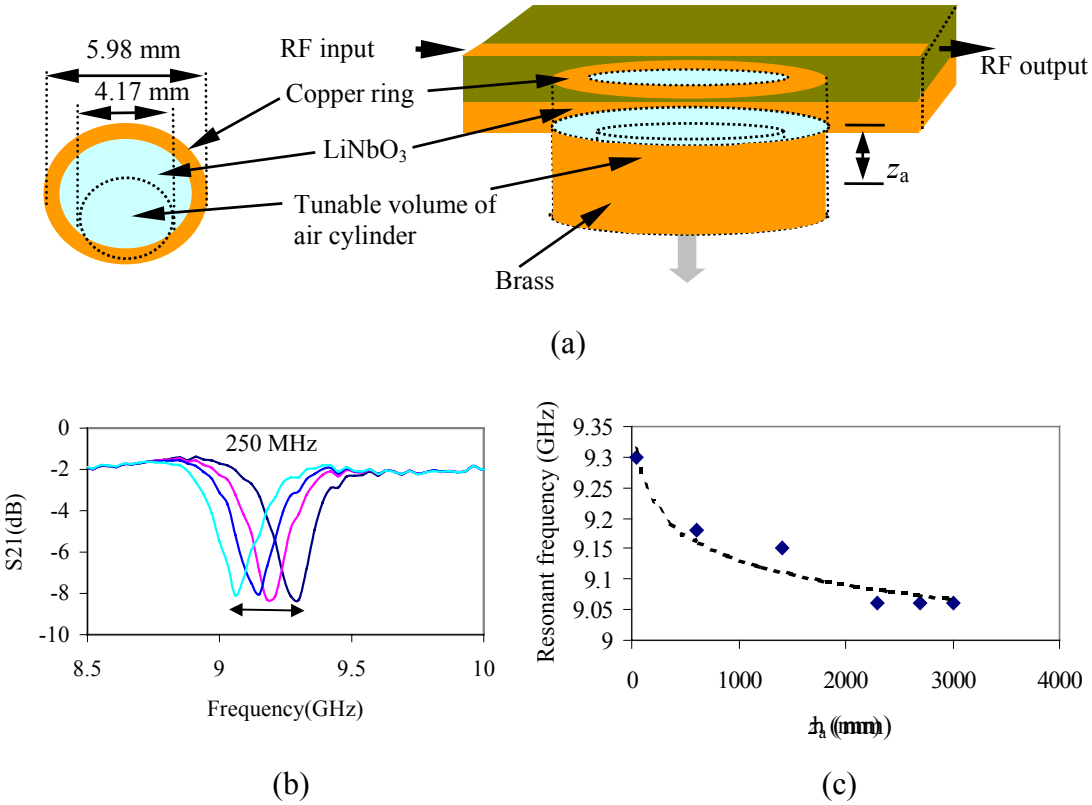


**Fig. 2.34** (a) Schematic diagram of the configuration used for tuning the RF resonant frequency. (b) Results of $S_{21}$ measurement for different volumes of air cylinder ($z_a$ is changed). (c) Resonant frequency as a function of $z_a$.

We also explored an alternate approach to RF resonant frequency tuning by changing the ground plane design. Fig. 2.34 (a) shows a schematic diagram of the new arrangement.

A tunable air cylinder beneath the disk changes the effective permittivity and consequently the resonant frequencies. In the actual experiment, a brass cylinder that can move along the $z$-axis has been used to change the air-cylinder height ($z_a$). Notice that the air cylinder is not centered. Fig. 2.34(b) shows the results of $S_{21}$ (throughput) measurements for different values of $z_a$. As may be seen, the minimum (which represents the resonant frequency) decreases as we increase $z_a$. Fig. 2.34(c) shows the resonant frequency against $z_a$. For $z_a > 3$ mm the resonant frequency changes only slightly.

This tuning method is useful for fine-tuning the RF-resonant frequency but, since the maximum tuning range is limited (about 250 MHz in this case), still other techniques should be used for RF-optical frequency matching.

### 2.5.3 Voltage gain and RF critical coupling

In addition to generating the proper voltage distribution around the disk, the RF resonator also provides voltage gain. At resonance, the amplitude of the voltage oscillation ($V_m$) on the ring is larger compared to the input RF voltage amplitude ($V_{in}$). The voltage amplitude on the ring is a function of the ring quality factor and

RF coupling coefficient. The voltage gain is defined as $G_v = V_m/V_{in}$ and it can be estimated from $S$ parameter measurements. The average stored energy ($U$) in a resonator can be expressed as:

$$Q_{RF,U} = \frac{\omega_{RF} U}{P_{loss}} \tag{2.29}$$

Where $Q_{RF,U}$ is the unloaded quality factor and $P_{loss}$ is the energy lost in the resonator per second, not withstanding coupling loss:

$$P_{loss} = P_{RF}\left(1 - |S_{11}|^2 - |S_{21}|^2\right) - P_l \tag{2.30}$$

$P_l$ is the power lost in the microstripline. The energy stored in the ring-microdisk capacitor can be expressed as a function of the voltage and geometrical parameters:

$$U = \beta_c \times \frac{1}{4} \times \frac{1}{2}\left(\varepsilon_{e,RF}\varepsilon_0 \frac{A}{h}\right)V_m^2 \tag{2.31}$$

Where $A$ is the ring area ($\pi R_o$-$\pi R_i$). The extra factor (1/4) is a result of having a time and space varying voltage distribution (we are using the RMS values of the voltage in the conventional formula for static energy storage in a capacitor). $\beta_c$ is a factor that connects the actual capacitance and the capacitance calculated assuming the ring-microdisk-ground is a parallel plate capacitor ($C = \varepsilon_r\varepsilon_0 A/d$). $\beta_c$ can be estimated either by simulation or measuring the optical modulation. The capacitance per unit length ($C'$) for a microstripline can be written as: $C' = n_{RF}/cZ_o$ ($Z_0$ is the characteristic impedance of the line and c is the speed of light). $n_{RF}$ and $Z_o$ can be calculated from simulation results and $\beta_c = C'/C$. For a 0.3 mm wide microstip on a 0.4 mm thick $LiNbO_3$ substrate, $\beta_c \approx 2.8$.

Since, in our experiments the ring resonators are hand made and mechanically tuned on the disk, $\beta_c$ should be evaluated separately for each modulator.

Using equations (2.30) and (2.31):

$$V_m = \sqrt{\frac{8hP_{loss}Q_{RF,U}}{\beta_c \omega_{RF} \varepsilon_{e,RF} \varepsilon_0 A}} \tag{2.32}$$

We can rewrite equation (2.30) in terms of the microstripline loss factor ($L_T$, $P_{out} = (1/L_T)P_{in}$):

$$P_{loss} = P_{RF}\left(1 - |S_{11}|^2 - |S_{21}|^2 - 1.5(\frac{L_T - 1}{L_T})\right) \tag{2.33}$$

The voltage gain $G_v = V_m / V_{in}$, where $V_{in}$ (input voltage amplitude) is related to the input RF power through $V_{in} = (2Z_0 P_{RF})^{0.5}$ in which $Z_o$ is the microstripline impedance. Here we have assumed that the microstripline is properly terminated with a matched impedance. Using equation (2.33) in equation (2.32):

$$G_v = \frac{V_m}{V_{in}} = \sqrt{\frac{4hP'_{loss}Q_{RF,U}}{\beta_c Z_o \omega_{RF} \varepsilon_{e,RF} \varepsilon_0 A}} \tag{2.34}$$

where $P_{loss}'$ is the loss factor given by:

$$P'_{loss} = \left(1 - |S_{11}|^2 - |S_{21}|^2 - 1.5(\frac{L_T - 1}{L_T})\right) \tag{2.35}$$

The *S*-parameters and $L_T$ can be directly measured using the network analyzer. The quality factor of a dielectric resonator that is magnetically coupled to a microstripline may be determined using the measured *S*-parameters [43]. Since the even mode of the ring resonator is also magnetically coupled to the microstripline, we can use the method described in Ref. 43 to determine the unloaded quality factor that is needed in equation (2.32). Fig. 2.35 shows the measurement points for loaded and unloaded quality factors in the reflection and transmission coefficient magnitude planes as a function of coupling factor η and the definition of various terms used.

The coupling factor is defined as $S_{11o}/S_{21o} = \eta$ where $S_{11o}$ and $S_{21o}$ are measured values of reflection and transmission at resonance.

Also η relates the various quality factors by the well-known relation [43]:

$$Q_{RF,U} = Q_{RF}(1+\eta) = \eta Q_{ext} \tag{2.36}$$

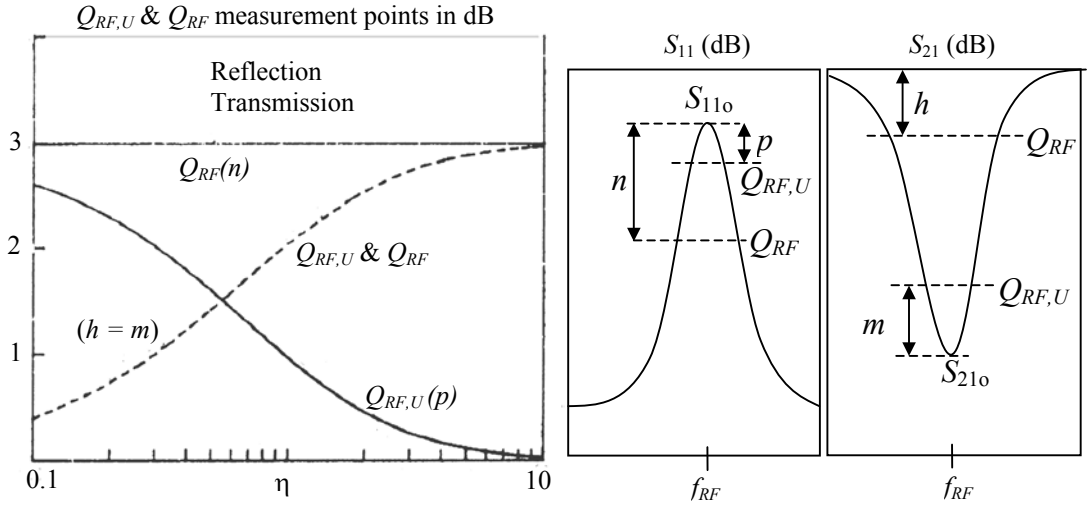


**Figure 2.35** $Q_{RF,U}$ and $Q_{RF}$ measurement points in the reflection and transmission coefficient magnitude planes as a function of coupling factor η and the definition of various terms [43].

Equation (2.34) may not be accurate enough for calculating the exact value of $V_m$ but it is very useful for evaluating the effect of different parameters on the voltage gain. When $S_{11o} = S_{21o} = 0.5$ and $\eta = 1$, the ring is critically coupled to the microstripline. In this situation the stored energy (and therefore $V_m$) is maximized. The RF coupling factor can be tuned by changing the gap size ($g$) between the microdisk and the microstripline to achieve critical coupling. We have simulated the *S*-parameters and the *E*-field intensity inside a microdisk using the CST electromagnetic simulator [(2)]. Fig. 2.36 shows the simulation results. The $LiNbO_3$ microdisk has a diameter of 5.13 mm and thickness of 0.4 mm. As may be seen when $g = 380$ μm ($\eta = 1$), the *E*-field amplitude is maximized. When $\eta > 1$ ($S_{11o} > S_{21o}$) the ring is over coupled, and

when $\eta < 1$ ($S_{11o} < S_{21o}$) it is under coupled. We can calculate $\beta_c$ using equation (2.32) and the simulation results. The average value of $\beta_c$ in this case is 2.7.

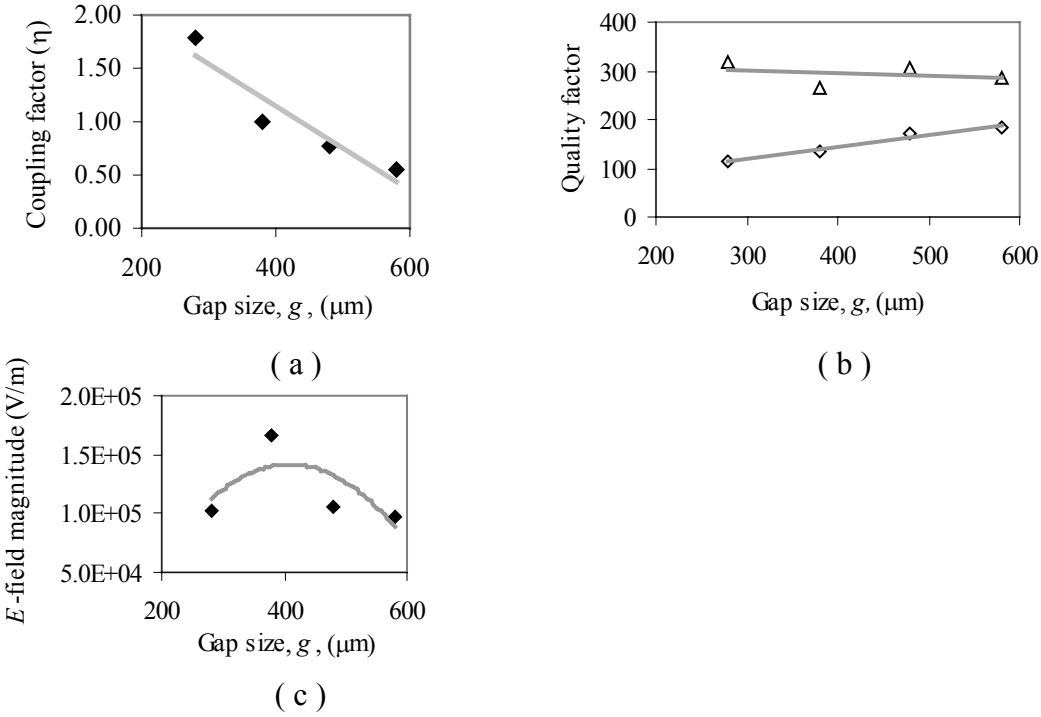


**Figure 2.36** CST simulation results for ring resonator on a $LiNbO_3$ microdisk with a diameter of 5.13 mm and a thickness of 0.4 mm. (a) The coupling factor (η) against gap size ($g$). (b) $Q_u$ and $Q_l$ against coupling factor. (c) The $E$-field oscillations amplitude against $g$.

As expected, the absolute values of resonant frequency derived from the simulation are smaller than the optical FSR and they decrease as we increase the gap size (loading effect). Since the resonant frequency also changes as a function of $g$, it is difficult to have RF-optical frequency matching and RF critical coupling simultaneously.

As mentioned in section 2.4.1, mounting the microdisk on a cylinder improves the DC-shift. The same arrangement also allows us to tune the gap size since the brass

cylinder can move relative to the microstripline. We use an experimental arrangement similar to the one shown in Fig. 2.28 to study RF coupling. Fig. 2.37(a) shows experimental results of *S*-parameter measurements on a $LiNbO_3$ structure with a diameter of 3 mm and a thickness of 0.4 mm for three different values of *g*. Fig. 2.37(b), 2.37(c) and 2.37(d) are the calculated quality factor, coupling factor and the *E*-field oscillation amplitude (calculated using equation 2.34) as a function of against the gap size. We have used the value of $\beta_c$ derived from the simulation results (Fig. 2.36).

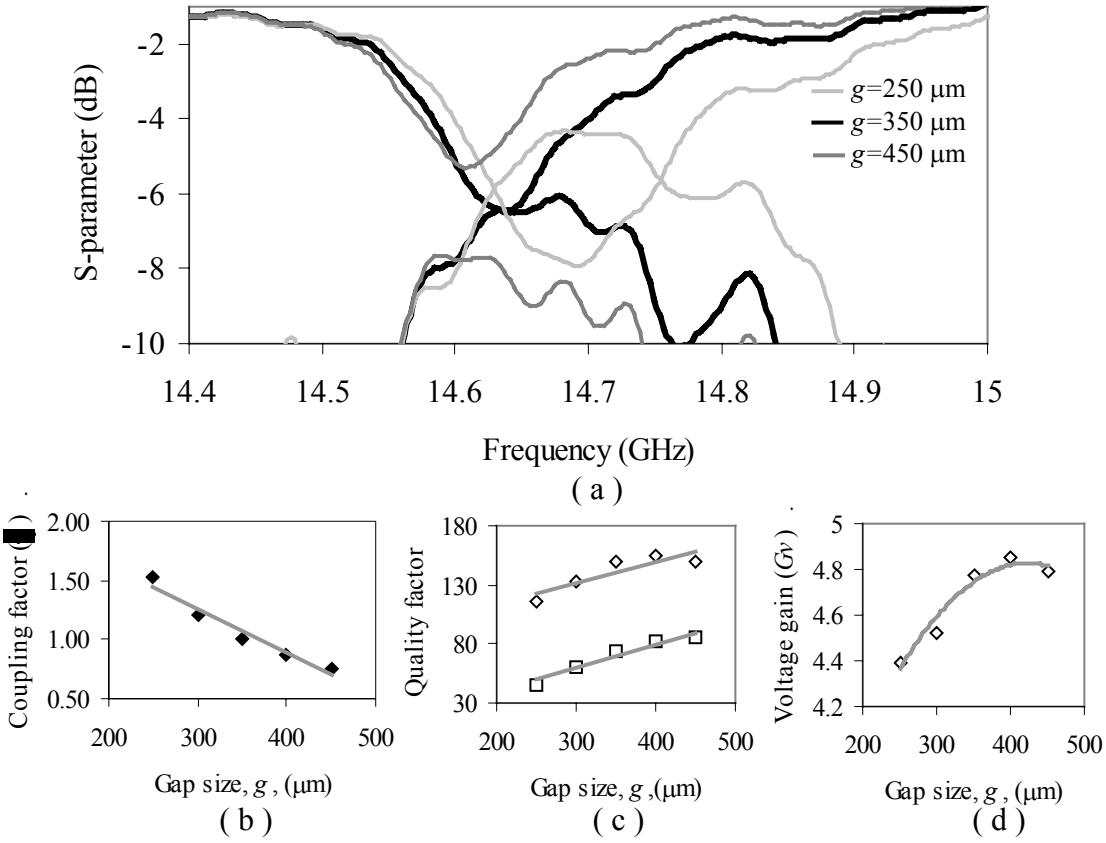


**Figure 2.37** (a) Experimental results of *S*-parameter measurements for a $LiNbO_3$ with a diameter of 3 mm and a thickness of 0.4 mm for three different values of *g*. (b,c,d) The calculated quality factor, coupling factor, and the *E*-field oscillation amplitude (calculated using Eq. 2.34) against the gap size.

In this case at a gap size of $g$ = 350 μm, the ring is critically coupled to the line. The estimated voltage gain at critical coupling condition is 4.9. We should point out that whenever $S$-parameters are expressed in dB they represent the relative transmitted and reflected power as opposed to voltage amplitude. So the critical coupling condition $S_{11o} = S_{21o} = 0.5$ becomes $S_{11o}^2 = S_{21o}^2 = -6$ dB.

If instead of matched termination, we open terminate the microstripline then, in an ideal situation the standing wave ratio would be infinite. In this case, the voltage amplitude on the line is $2V_{in}$ (instead of $V_{in}$). By properly tuning the location of the voltage maxima on the line, we can improve the voltage gain (ideally by a factor of 2). This is achievable by tuning the length of the open end.

## 2.6 Fundamental FSR modulation

Modulation in resonant optical modulators is fundamentally different from traveling wave optical modulators because in the latter case at least one of the waves (optical or microwave) is a resonance inside a microwave or optical resonator. Resonance enhances the electro-optic interaction but imposes a limitation on the frequency response. As mentioned before, in an optically resonant modulator, effective modulation only occurs within a limited bandwidth (BW) around a discreet set of frequencies defined by the optical free spectral range (FSR) and optical $Q$-factor. If the modulating RF frequency ($f_{RF}$) is very close to $\Delta\nu_{FSR}$ the behavior of the

microdisk modulator may be explained using a simple model based on the optical transfer function of an optical resonator and electro-optic modulation of the effective optical refractive index.

This section covers the theoretical and the experimental aspects of linear modulation at the fundamental frequency of the microdisk modulator.

### 2.6.1 Physics and modeling

Our previous work on $LiNbO_3$ microdisk modulators [47-48] uses general principles of resonator–coupler systems to derive the modulation response in the time domain. Although this approach is very accurate, it requires time consuming calculations because it is based on evaluating the interference of the traveling waves inside the disk after a large number of round trips around the disk (details of this calculation can be found in section 3.4 of Ref. 47). In the previous calculations the RF-resonance hasn't been treated properly because, instead of modeling the modes of the ring resonator, the modulation has been modeled based on a periodic metal-electrode structure. One possible approach to a more complete model is to use the same time-domain model of a resonator-coupler combined with RF resonance of a ring resonator. Theoretically this should result in a complete model for expressing modulator response for all harmonics ($m_o \times \Delta\nu_{FSR}$) as a function of RF quality factor,

RF coupling factor, optical quality factor, optical coupling coefficient and the geometrical parameters.

A second approach is to use the optical transfer function of the microdisk modulator (in frequency domain) with an electro-optically modulated refractive index. This approach is applicable only if $f_{RF}$ is very close to $m_o \times \Delta\nu_{FSR}$ so that we can ignore the restriction imposed on the modulation by the frequency response. We choose the second approach as it leads to a very simple model in which the role of all measurable parameters and their impact on modulator efficiency is clearly demonstrated. The main disadvantage of this simple model is the absence of bandwidth calculations. Basically we assume the bandwidth is limited by the optical-$Q$.

To analyze the modulator performance, it is helpful to review the role of different device parameters contributing to the modulation process. Fig. 2.38 is a schematic diagram of the modulator illustrating important parameters that influence modulation performance. The efficiency of electro-optic interaction between optical whispering gallery modes and the applied electric field is directly proportional to the following factors:

1) Interaction time or length. The interaction time is the photon lifetime inside the resonator $\tau_p = Q/\omega_0$ where $Q$ is the quality factor of the optical resonator.
2) $E$-field oscillation amplitude inside the mode region that can be written as: $E_m = \beta_{EO}(G_V V_{in}/h)$.

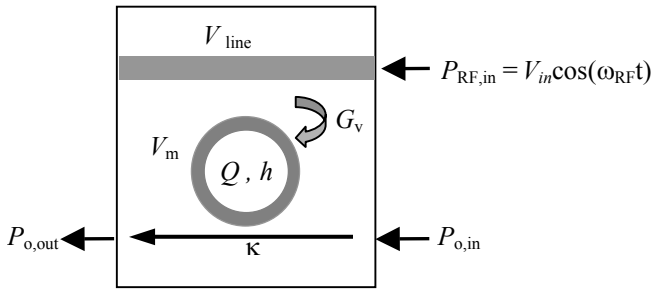


**Figure 2.38** Schematic diagram of the microdisk modulator representing the parameters involved in the modulation process.

In section 2.3.3 we mentioned that the transfer function of the microdisk optical resonator can be a series of transmission dips (equation 2.10) or a series of coupled peaks (equation. 2.16) depending on the optical coupling method and alignment. In each case the optical transfer function is expressed as a function of optical coupling factor ($\kappa$) the circulation loss factor ($a$), and microdisk refractive index for TE modes ($n_e$). So at a given wavelength ($\lambda_0$), the time variation of the optical output power ($\delta P_{o,out}$) can be written as a function of time variation of the refractive index ($\delta n_e$) (equations (25) and (34)):

$$n_e(t) = n_e + \delta n_e(t) = n_e + \frac{1}{2} n_e^3 r_{33} \frac{\beta_{EO}\beta_S}{h} \times G_v V_{in} \cos(\omega_{RF} t) \qquad (2.37)$$

So knowing $\beta_{EO}$ (from DC shift measurement), $G_v$ (from *S*-parameter measurement), the optical $Q$ (or the distributed loss factor $\alpha$) and the optical coupling factor ($\kappa$) we can calculate the modulated optical power as a function of RF input voltage amplitude ($V_{RF}$).

$$P_{o,out} = f_{EO}(V_{RF}) \qquad (2.38)$$

$f_{EO}$ is called the electro-optic transfer function of the optical resonance.

Fig. 2.39(a) shows the simulated electro-optic transfer function for an optical resonance (transmission dip) in a microdisk $LiNbO_3$ with a thickness of 0.4 mm. The laser wavelength is tuned to $\lambda_{res} + 0.25\Delta\lambda_{FWHM}$. Fig. 2.39(b) shows the simulated DC shift based on experimental results. The optical input power ($P_{o,in}$) is 50 μW, $G_v = 6$ and $Q = 3\times10^6$. The dashed and the doted lines are respectively the first ($N_1$) and the second ($N_2$) derivatives of $f_{EO}$. It is evident that an efficient linear modulation ($P_{o,out} \propto V_{RF}$) requires a small second derivative and a large first derivative.

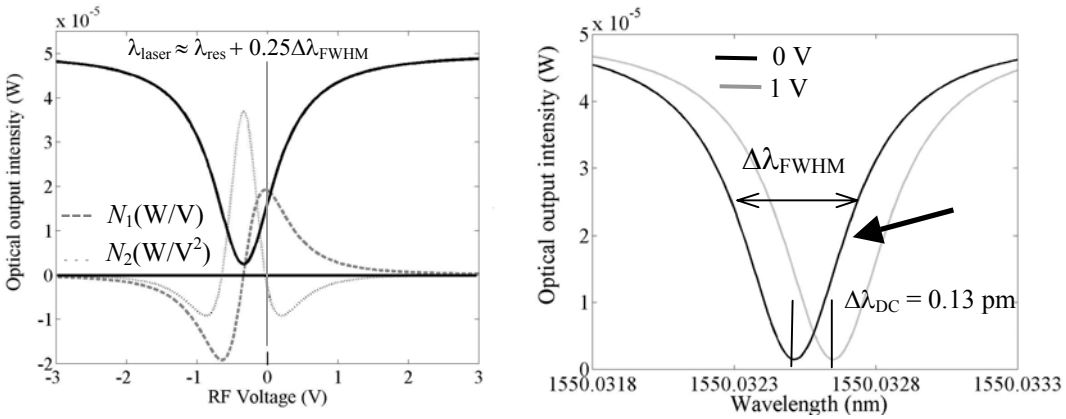


( a ) ( b )

**Figure 2.39** (a) The electro-optic transfer function of a microdisk modulator ($h$ = 0.4 mm, $\kappa = 0.1$, $\alpha = 0.0075$ cm$^{-1}$, $P_{o,in}$ = 50 μW, $G_v$ = *6*. (b) The simulated DC-shift ($\Delta\lambda_{DC}$) based on measured value.

As may be seen in Fig. 2.39(a) at $V_{RF} = 0$, $N_1$ is maximum and $N_2$ is zero. This is the optimized condition for linear modulation and is a result of proper tuning of the laser wavelength ($\lambda_{laser}$) relative to the resonant wavelength ($\lambda_{res}$). When the laser wavelength is tuned to the linear regime we may simplify the calculations further by using the first derivative:

$$P_{o,m} = 2N_1 \beta_s V_{in} \tag{2.39}$$

$P_{o,m}$ is the peak-to-peak value of the modulated optical power. Although $N_1$ can be derived from $f_{EO}$, but an easier way to estimate $N_1$ is to write it as a function of the voltage ($G_v$) gain, the DC shift, $\beta_s$, and the mode slope for the corresponding optical mode:

$$P_{o,m} = 2G_v \beta_s V_{in} \times S \times \Delta\lambda_{DC} \tag{2.40}$$

$S$ is the optical mode slope (usually measured in μW/pm) near the laser wavelength. This equation is used to calculate the modulated optical power for a known value of $G_v$ or to estimate $G_v$ based on the measured value of $P_{o,m}$.

If a coupled optical peak with a symmetric spectral profile is used for modulation, we can estimate the mode slope based on the measured optical-$Q$ in the following way:

$$Q = \lambda_{res}/\Delta\lambda_{FWHM} \;\&\; S = P_{o,max}/\Delta\lambda_{FWHM} \Rightarrow S = (Q \times P_{o,max})/\lambda_{res}$$

Then equation (2.40) can be rewritten as:

$$P_{o,m} = 2G_v \beta_s V_{in} \times (Q\, P_{o,max}/\lambda_{res}) \times \Delta\lambda_{DC} \tag{2.41}$$

Where $P_{o,max}$ is the optical output power at resonance. This equation clearly shows the role of all critical parameters in the linear modulation process (the same simplification is possible if we use a transmission dip).

### 2.6.2 Frequency response and bandwidth

The calculated optical power in equation (2.38) is independent of the modulating RF frequency.

However in practice optical and electrical responses of the microdisk and the ring resonator impose limitations on the modulation bandwidth. In section 1.3.3 the effect of the optical transfer function on the RF frequency response of an optical resonator was explained based on a simple fact: the RF side bands (194 THz $\pm f_{RF}$) generated by optical modulation must be resonant inside the microdisk resonator. As a result the optical transfer function is effectively a RF bandpass filter with pass band frequencies of bandwidth $\Delta\nu_{FWHM} = \nu_{res}/Q$ around $m_o \times \Delta\nu_{FSR}$. One way to include the frequency response into our simple model is to filter in frequency domain. We can calculate the Fourier transform of the modulated optical power from equation (2.38) and filter it through the microdisk optical transfer function ($f_o$). Then frequency dependent modulation amplitude can be derived from the inverse Fourier transform of the filtered frequency spectrum:

$$P_{out}(t, f_{RF}) = B_{opt}(f_{RF}) \times P_{o,out}(t) = \mathcal{F}^{-1}\{f_o(\omega) \times \mathcal{F}\ f_{EO}(V_{RF}(t))]\ \} \qquad (2.42)$$

The RF frequency response of the microstripline-ring system also has a frequency dependent voltage gain factor $G_v(f_{RF})$, but usually this bandwidth is larger than the optical bandwidth.

In our calculations we assume that the optical bandwidth dominates the frequency response of the system and if $\Delta\nu_{FSR} = f_{RF}$ then $B_{opt} = 1$.

### 2.6.3 Experimental results

To observe and measure the modulation performance of the $LiNbO_3$ microdisk modulator we employ the same arrangement used for studying the optical coupling and WG modes (Fig. 2.7). The only difference is that the output fiber is attached to a 10/90 single mode power splitter. 10 percent of the optical output power goes to a low-speed photo detector for monitoring the mode and the location of the laser wavelength relative to the resonant wavelength, and 90 percent is sent to a high-speed detector to measure the modulated optical power.

Fig. 2.40 shows the evolution of the microdisk optical modulator structure. Fig. 2.40(a) shows the first and the simplest setup. There is no microstrip structure and the disk is fed directly with, SMA connector. The two-prism optical coupling method has been used and the optical input lens, output fiber and microprisms were mounted on four separate *xyz* stages controlled by picomotors[(1)]. Fig. 2.40(b) shows a setup with the linear RF-resonators explained in Sec. 2.5.1 and with the same opto-mechanical arrangement but the disk is mounted on the ground-plane of the PCB board (a small part of dielectric material is removed) so the resonators can be coupled to the central microstrip feed line. Fig. 2.40(c) shows the semi-planar setup with half-ring RF resonators. We use the term semi-planar because the microprisms, microdisk and the PCB board are mounted on a common brass substrate to make the device smaller and more robust. However, the optical input and output stages are on separate mounts.

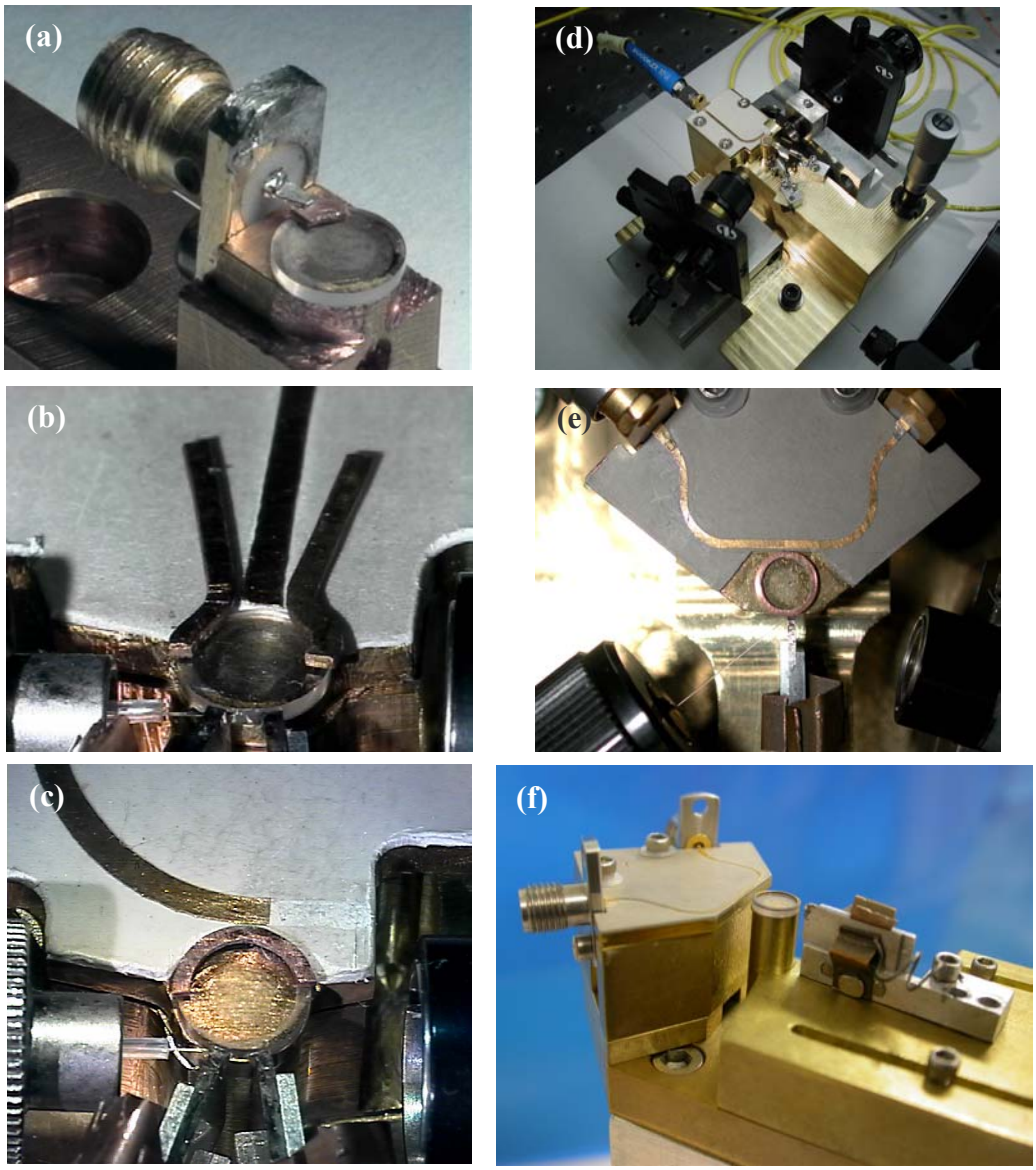


**Figure 2.40** Evolution of the $LiNbO_3$ microdisk optical modulator. (a) Direct RF feeding, non-planar, double-prism optical coupling. (b) Linear RF-resonator, non-planar, double prism optical coupling. (c) Half-ring RF-resonator, semi-planar, double-prism optical coupling. (d) Half-ring RF-resonator, planar, double-prism optical coupling. (e) Full-ring RF-resonator, semi-planar, single-prism optical coupling, RF through put. (f) Full-ring RF-resonator, semi-planar, single-prism optical coupling, RF-throughput, controlled RF coupling.

Fig. 2.40(d) shows a planar-setup in which all components are mounted on the same brass substrate. In this configuration the optical input and output are manually

controlled with two small *x-y-z* stages, there is no picomotor involved and optical alignment can be maintained for a long time. Although the planar setup is stable, due to the lack of accurate control on the input and output launch positions, it is hard to achieve high optical coupling efficiencies. The best optical coupling (15%) has been achieved with configurations (a) and (b) because of the high degree of freedom and accuracy of the mechanical motion. Fig. 2.40(e) shows the latest version of the planar setup where a single prism is used to couple in and out and there is a RF output port that allows RF throughput ($S_{21}$) measurement. Fig. 2.40(f) is designed to control RF-coupling by changing the relative height and distance between the ring resonator and the side-coupled microstrip line. The $LiNbO_3$ microdisk is mounted on a brass cylinder and it can move independently of the RF board. As explained in section 2.4.1 this semi-planar configuration increases the optical DC shift. The single prism technique is used for optical coupling and is similar to the arrangement (b) and (c).

To characterize the modulation performance of the $LiNbO_3$ microdisk modulator we measure the detected modulated voltage at different RF powers and frequencies. The detector used in our experiments has a responsivity $R$ = 280 μV/μW at 8 GHz that reduces to about 260 μV/μW around 15 GHz. A single mode tunable laser with a line width < 0.5 MHz provides the input optical power at wavelength $\lambda_o$ = 1550 nm. The wavelength is tunable within a 0.1 nm range (around center wavelengths between 1525 nm and 1575 nm) with an accuracy of 0.3 pm. By controlling the laser wavelength we can find the optimum position in the mode spectrum (largest

slope) in order to maximize the modulation. We use a RF tracking source to sweep the frequency near $f_{RF} = \Delta\nu_{FSR}$ for RF-bandwith measurements. For measuring modulation as a function of input RF power, the RF frequency is set to $f_{RF} = \Delta\nu_{FSR}$ where the modulation is maximum and the power is changed while the relative position of the laser wavelength is fixed.

The first experiment is a comparison between the ring and semi-ring performance. The disk used has a diameter of $D$ = 5.8 mm and thickness $h$ = 0.720 mm. Optical coupling in and out using the arrangement shown in Fig. 2.40(e) gives a maximum coupled power of 100 μW. The optical $Q$ is near $3\times10^{6}$ and $\Delta\nu_{FSR} \approx 7.6$ GHz (for *TE WG* modes). Fig 2.41 shows the measured $S_{21}$ through the microstripline that is coupled to a ring and semi-ring.

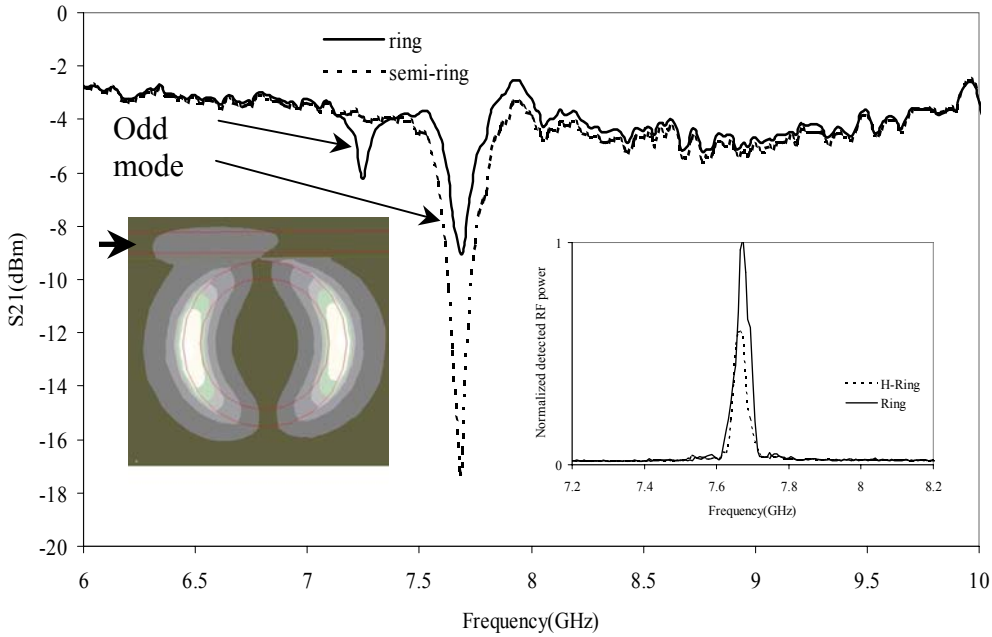


**Figure 2.41** Measured $S_{21}$ for a semi-ring and ring at fundamental resonance and the simulated even mode (left inset) field distribution on the ring. The right inset shows the detected modulated power with semi-ring and ring resonators.

As may be seen, the even mode of the ring and the fundamental resonance of the semi-ring are tuned to $\Delta\nu_{FSR}$. The left inset shows the simulated *E*-field distribution in the middle of the disk at fundamental even mode. The right inset shows the detected *RF* power from the detector showing modulation improvement replacing the semi-ring with a ring.

Fig. 2.42 is a close up photograph of the 8.7 GHz microdisk modulator in a full planar arrangement (Fig. 2.39(d)). The $LiNbO_3$ microdisk employed, has a diameter of 5.13 mm, $\Delta\nu_{FSR}$ of 8.7 GHz and a thickness of 0.4 mm.

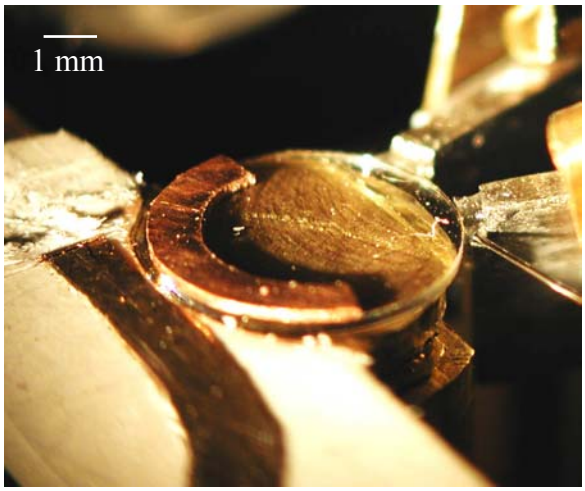


**Figure 2.42** Close up photograph of the 8.7 GHz $LiNbO_3$ microdisk modulator (Fig. 39-d).

Fig. 2.43 shows the single frequency modulation results for the microdisk modulator illustrated in Fig. 2.40. Fig. 2.43(a) shows the spectrum of the detected voltage (left). The detected modulation has a bandwidth of 90 MHz with a maximum of about 420 μV at 8.73 GHz. Fig. 2.43(b) shows the spectrum of the modulated optical resonance

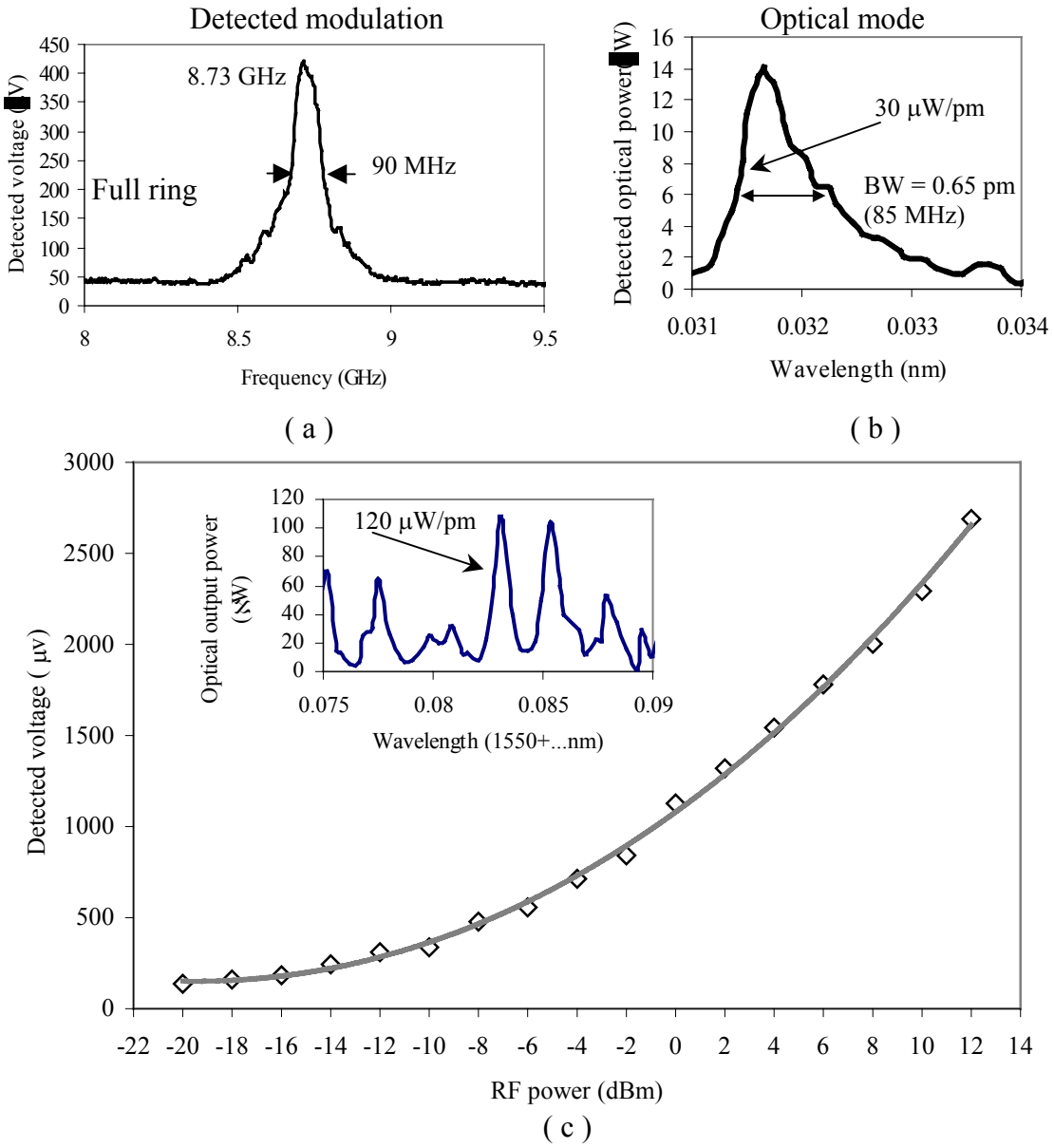


**Figure 2.43** Single frequency modulation result at $f_{RF} = \Delta\nu_{FSR} = 8.7$ GHz. The $LiNbO_3$ microdisk has a diameter of 5.13 mm and thickness of 0.4 mm. (a) Spectrum of optical detector output voltage. The detected modulation has a bandwidth of 90 MHz with a maximum of about 420 μV at 8.73 GHz. The RF-resonator is a full-ring and the input RF power is 0 dBm (1 mW). (b) Spectrum of the optical resonance. The maximum coupled optical power is about 14 μW, and the optical bandwidth is about 85 MHz (mode slope is 30 μW/pm). (c) Detected optical voltage output (at 8.7 GHz) against RF input power. In this experiment a semi-ring RF-resonator is employed. The inset is the corresponding optical mode.

The maximum coupled optical power is 14 μW and the optical bandwidth is about 85 MHz (mode slope is 30 μW/pm).

As expected, the optical modulation band width is limited by the optical *Q*. The RF-resonator in this case is a full-ring (as opposed to what is shown in the photograph) and the injected RF power is 0dBm (1 mW). Fig. 2.43(c) shows the detected voltage (at 8.7 GHz) against RF input power for the same modulator but with a semi-ring resonator. The inset is the corresponding optical mode with a slope of 120 μW/pm and maximum coupled optical power of 110 μW. As may be seen, although the optical mode slope is about 4 times bigger in Fig. 2.42(b) with 0 dBm RF power, the detected modulation is about 1100 μV that is only 2.5 times larger than the maximum detected modulation in Fig. 2.42(a) (420 μV). Since the detected voltage is proportional to modulated optical power, this again indicates that the ring resonator is modulating more efficiently then the half-ring resonator.

Fig. 2.44 shows the $S_{21}$ and optical modulation measurement results at different fundamental resonant frequencies. It is clear that when the fundamental resonance of the ring resonator is detuned from $\Delta\nu_{FSR}$ = 8.68 GHz, the *E*-field amplitude and consequently the optical modulation efficiency drop.

In section 2.6.1 we showed that the optical modulation is linearly proportional to $P_{o,max}$ (the resonant optical output power of the modulated optical mode). To test the validity of this prediction we use a variable optical attenuator between the laser and optical input to the microdisk modulator. In this way we can control $P_{o,max}$ without perturbing the laser wavelength alignment relative to the resonant wavelength.

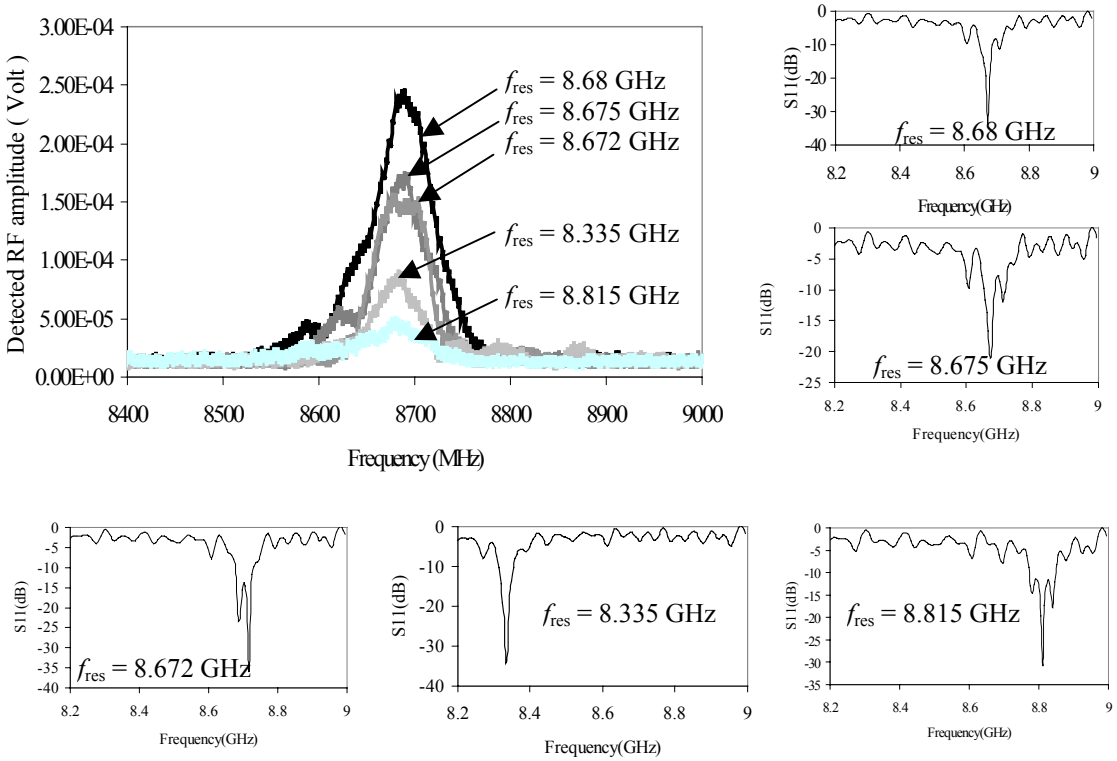


**Figure 2.44** Detected modulation at resonance and at RF frequencies detuned from resonance.

Fig. 2.45(a) shows the optical output spectrum at different optical input powers. The detected RF voltage against $P_{o,max}$ is shown in Fig. 2.45 (b). During modulation, the laser wavelength is located almost in the middle of the mode slope (dashed line). The linear behavior of $P_{o,mod}$ as a function of $P_{o,max}$ demonstrates the validity of equation (2.41).

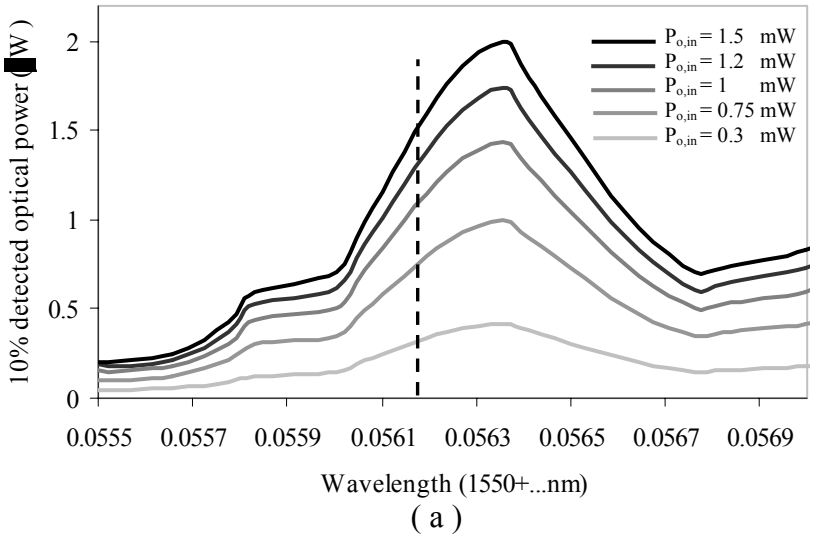


( a )

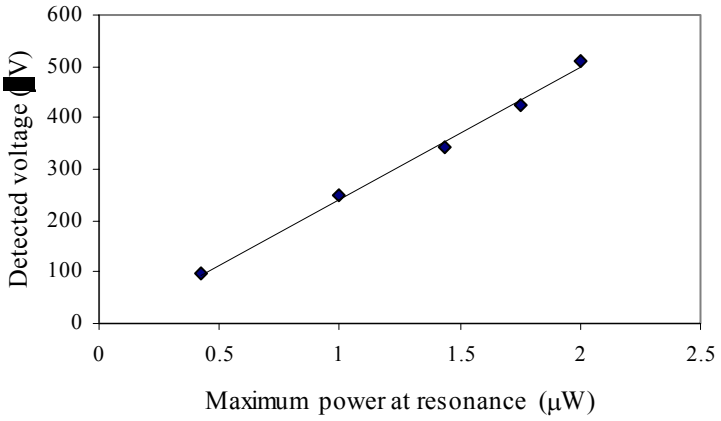


( b )

**Figure 2.45** (a) Optical output spectrum at different optical input powers. (b) Detected RF voltage against $P_{o,max}$ when the laser output is tuned to the middle of the mode slope (dashed line in (a))

High-sensitivity 14.55 GHz microdisk modulator

The microdisk modulator arrangement shown in Fig. 2.46(a) is our optimized mechanical design for a better performance. In sections 2.4.1 and 2.5.3 we showed that mounting the microdisk on a cylindrical ground plane enhances the DC-shift and adds an extra degree of freedom for controlling the RF coupling gap size, *g*. The

voltage gain provided by the critically coupled ring resonator and enhanced electric-field distribution increases the sensitivity of the microdisk modulator. The $LiNbO_3$ microdisk used in this arrangement is 400 μm thick, 3 mm in diameter and has an optical free spectral range of 14.55 GHz. The copper ring resonator has an outer diameter of 3 mm and width of 300 μm.

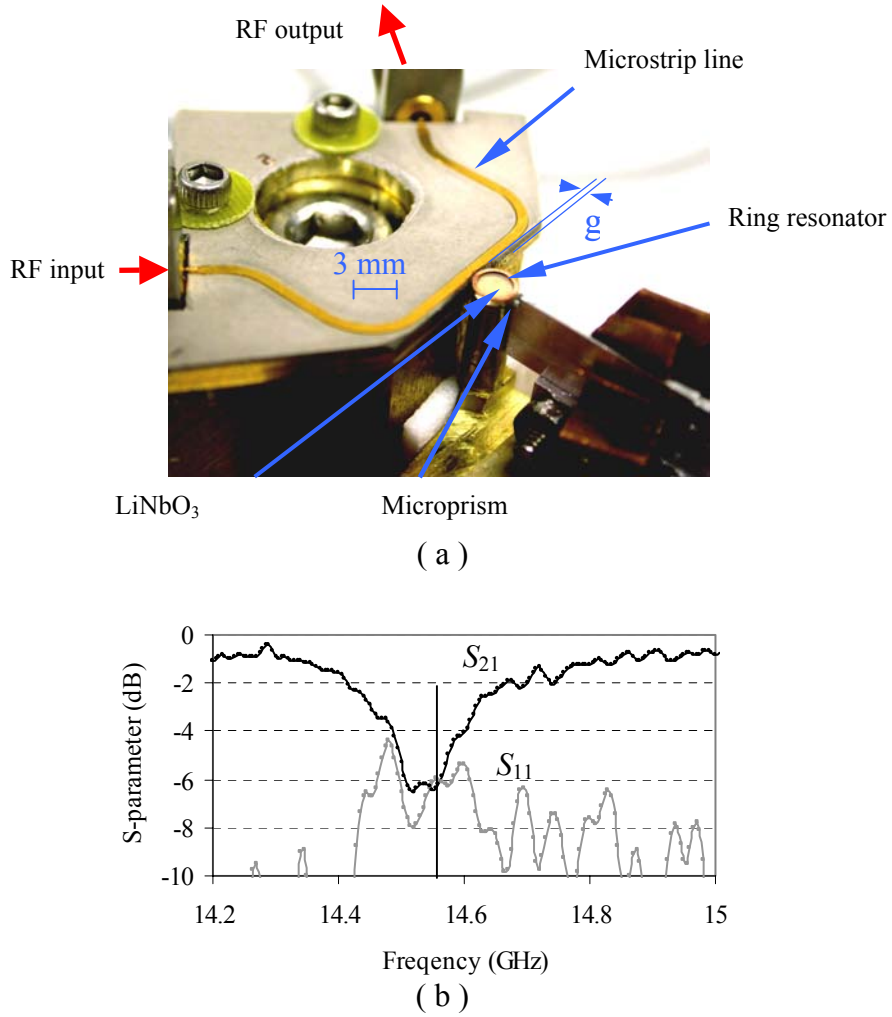


**Fig. 2.46** (a) Photograph of the microdisk modulator. (b) S-parameter measurement results for the microstrip line side coupled to the RF ring resonator

Fig. 2.46(b) shows the measured $S_{11}$ and $S_{21}$ for the microstrip line side coupled to the RF ring resonator. The RF energy stored in the ring at resonance ($f_{RF}$ = 14.6 GHz) is maximized by tuning the gap size ($g$).

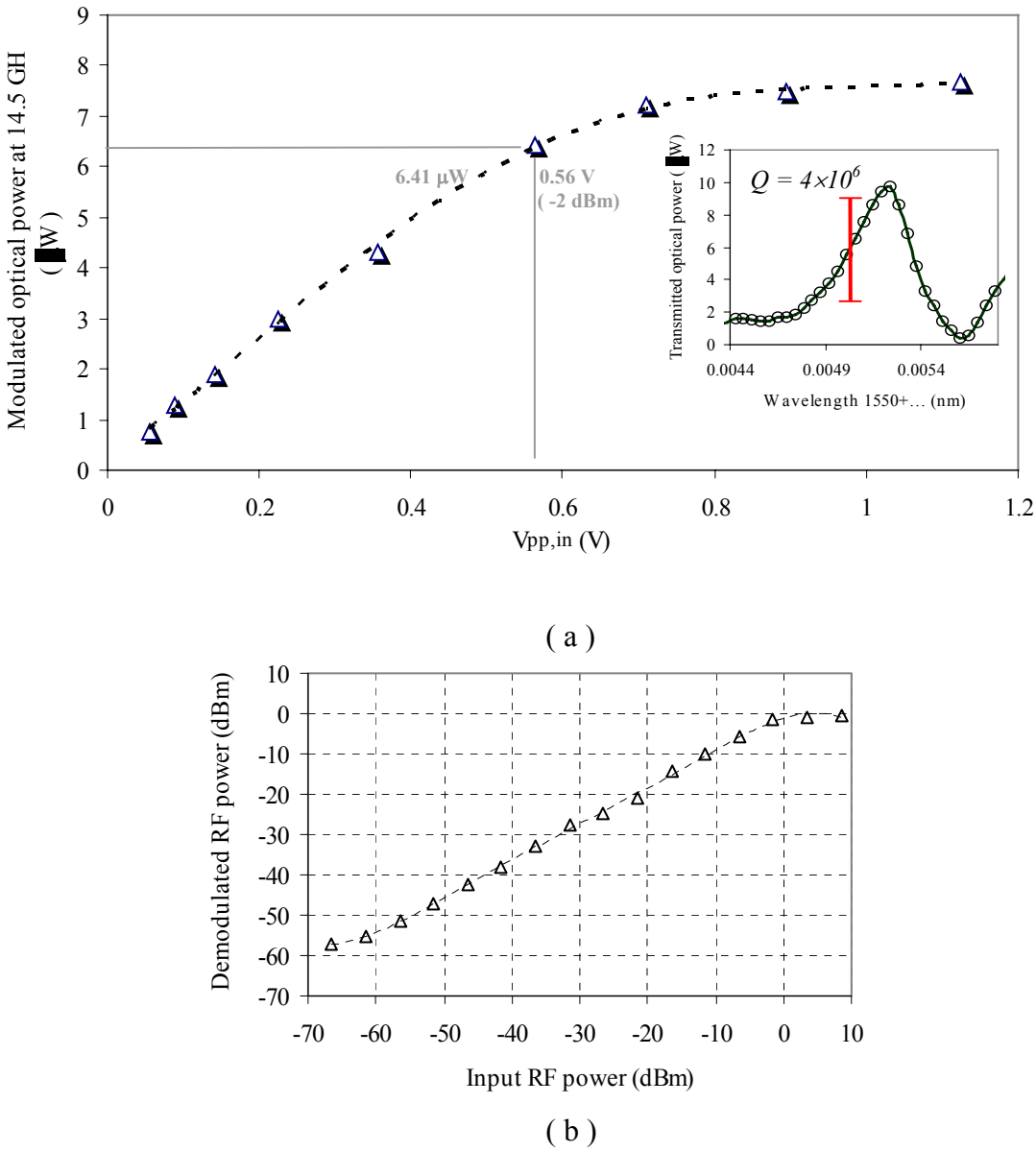


**Fig. 2.47** Linearly modulated optical intensity against peak-to-peak input voltage (and RF power). The inset shows the modulated optical mode. At $V_{pp}$ = 0.56 V, the optical power in the linear region of the optical mode is 100% modulated. (b) Demodulated RF power against input RF power.

Fig. 2.47 shows the variation of the modulated optical power against peak-to-peak voltage of the input signal. The inset shows the modulated optical mode with a $Q = 4\times10^6$. As may be seen at $V_{pp}$ = 0.56 V the linear portion of the optical mode is completely modulated. Saturation of the linearly modulated optical power with increasing $V_{pp}$ occurs because of increasing second-order harmonic generation due to nonlinear modulation. The optical intensity modulation is detected using a high-speed analog optical receiver with a responsivity of 260 μV/μW at 15 GHz. The calculated effective interacting voltage based on DC shift and detector responsivity is $V_{in}$ = 3 V at –1 dBm RF input power ($V_{pp}$ =0.56 V) RF input power representing a voltage gain of 5.3 at resonance. The voltage gain calculated based on S-parameter measurements is 5.5. Fig. 2.47(b) shows the demodulated RF power against input RF power. The modulation saturation occurs around 0 dBm received RF power.

Fig. 2.48 shows the frequency spectrum of the detected RF power at very low RF input powers. In this experiment an RF amplifier with a gain of 20 dB is used after the detector to amplify the weak detected RF power. At -67 dBm received RF power, the signal-to-noise ratio of the detected RF power is about 13 dB. Both saturation voltage and sensitivity measurement results shown in Fig. 2.47(b) and 2.48 indicate a 10 dB improvement compared to the best results reported previously for a 9 GHz $LiNbO_3$ microdisk modulator [49].

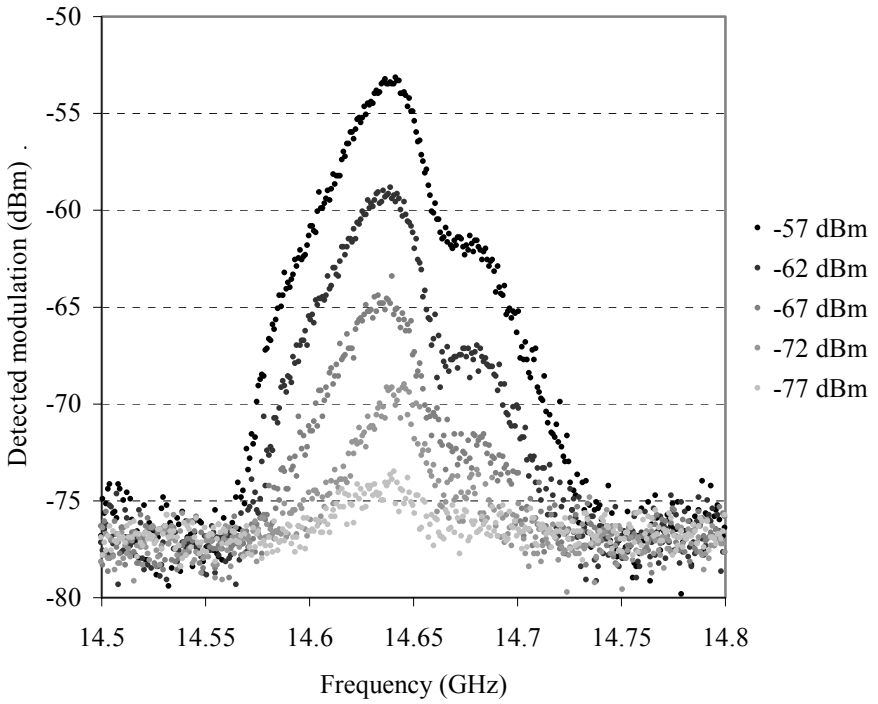


**Figure 2.48** Optical spectrum of the detected RF power at very low RF input powers.

In an additional single frequency experiment with the 14.6 GHz microdisk modulator we selected a symmetric and clean WG resonance to estimate the voltage gain ($G_v$). Fig. 2.49(a) shows the optical spectrum of the selected mode. The maximum slope ($S$) of the mode is 80 μW/pm and its line width is 0.33 pm corresponding to a bandwidth of 45 MHz and a loaded optical $Q$ of $4.7\times10^6$. Fig. 2.49(b) shows the frequency spectrum of the detected RF voltage at 0 dBm received RF power.

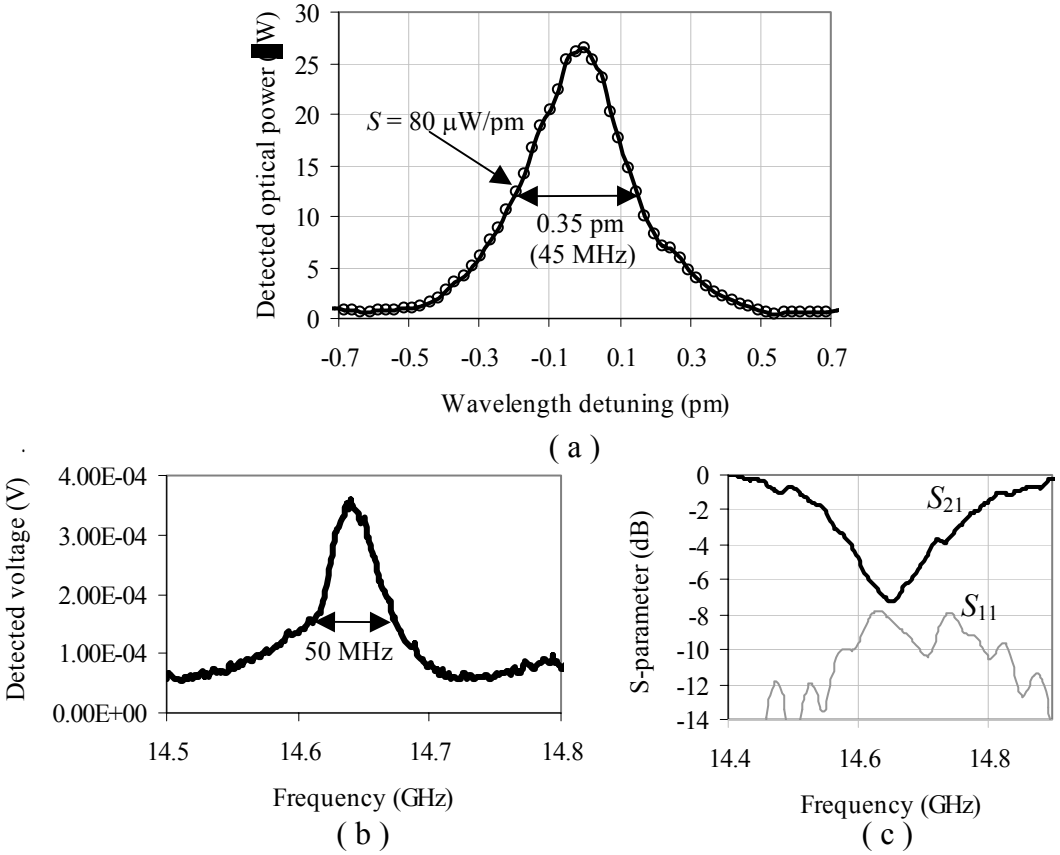


**Figure 2.49** (a) the optical spectrum of the selected WG mode. The maximum modes slope ($S$) is 80 μW/pm and its line width is 0.33 pm corresponding to a bandwidth of 45 MHz and a loaded optical $Q$ of $4.7\times10^6$. (b) Frequency spectrum of the detected RF voltage at 0 dBm received RF power. (c) Measured $S$-parameters for the microstripline side coupled to the ring resonator

The measured modulation bandwidth is 50 MHz which again validates the assumption that the modulation bandwidth is limited by the optical bandwidth. After correcting the modulated voltage and input RF power to compensate for the RF cable losses we calculated a $G_v$ = 5.12 using the measured values of $S$, $V_{in}$ and $\Delta\lambda_{dc}$ in equation (2.40). Fig. 2.49(c) shows the measured $S$-parameters for the microstripline side coupled to the ring resonator.

## 2.7 Harmonic FSR modulation

### 2.7.1 Introduction

The fundamental modulation frequency of a microdisk modulator is defined by its diameter and thus, high frequency modulation requires smaller disks. Modulation at harmonic frequencies ($m_o \times \Delta\nu_{FSR}$, $m_o$ = 2, 3,…) is an alternative way of increasing the modulation frequency of a microdisk modulator without decreasing the microdisk diameter.

The main requirement for harmonic FSR modulation is RF resonant frequency tuning. For efficient harmonic modulation at $m_o \times \Delta\nu_{FSR}$, the $m$th harmonic of the RF resonator has to be tuned to $m_o \times \Delta\nu_{FSR}$. Due to even-odd mode splitting, $f_{RF,m}$ is not exactly equal to $m_{RF} \times f_{RF,1}$.

Fig. 2.50 shows the simulated $E$-field magnitude and $E$-field vectors for even (a) and odd (b) second harmonics on a cut plane passing through the middle of a $LiNbO_3$ microdisk. The microdisk has a diameter $D$ = 5.13 mm and a thickness of $h$ = 0.4 mm.

The position of the maximum and minimum oscillation amplitudes of the even mode is rotated 90 degree relative to those of the odd mode. In principle both even and odd modes could be used for optical modulation but in most cases the resonant frequency of the even mode is $m_o \times \Delta\nu_{FSR}$ and its coupling to the microstripline are stronger.

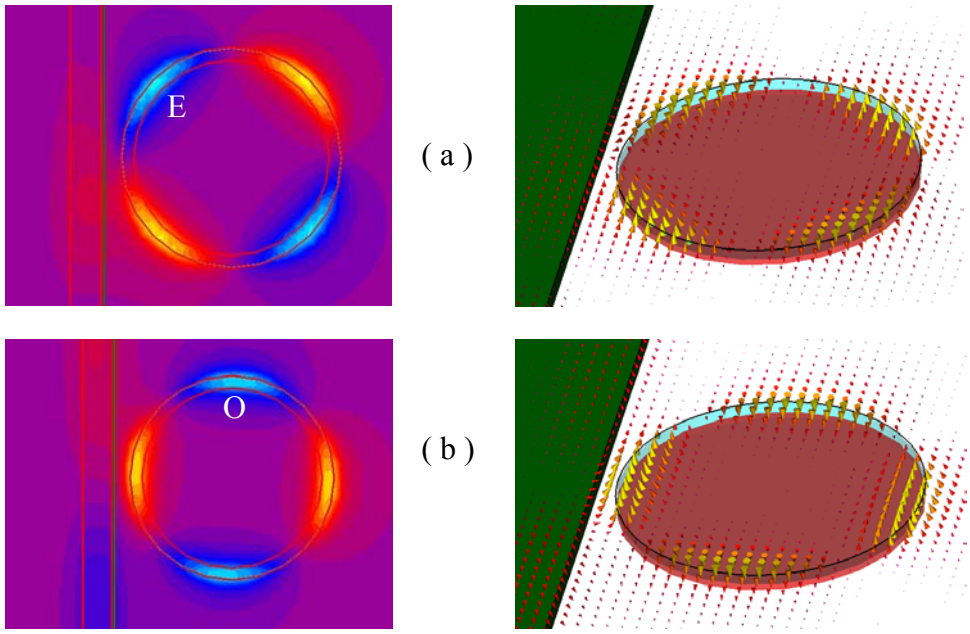


**Figure 2.50** Simulated *E*-field magnitude and *E*-field vectors on a cut plane passing through the middle of the $LiNbO_3$ microdisk for even ( a ) and odd (b) second harmonics. ($D$ = 5.13 mm, $h$ = 0.4 mm)

Fig. 2.51(a) shows the simulated *S*-parameters around the second-harmonic of a side-coupled ring resonator. Although the simulated resonant frequencies are off (for a 5.13 mm diameter $2\times\Delta\nu_{FSR}$ is 17.4 GHz) the qualitative behavior of the *E*-field inside the disk and the *S*-parameters are predicted properly.

As may be seen the even second-harmonic is critically coupled ($S_{11} = S_{21}$ = -6 dB).

Fig. 2.51(b) shows the amplitude of the *E*-field oscillation in the middle of the disk at angular positions E and O shown in Fig. 2.50. Due to critical coupling, the amplitude of the *E*-field for the even mode is larger than the odd mode oscillation amplitude. Once the RF resonant frequency of either odd or even resonance is tuned to the $m_o\times\Delta\nu_{FSR}$ (where $m_o$ is the same as the RF resonance order $m_{RF}$) the optical modulation mechanism can be treated similar to the fundamental modulation.

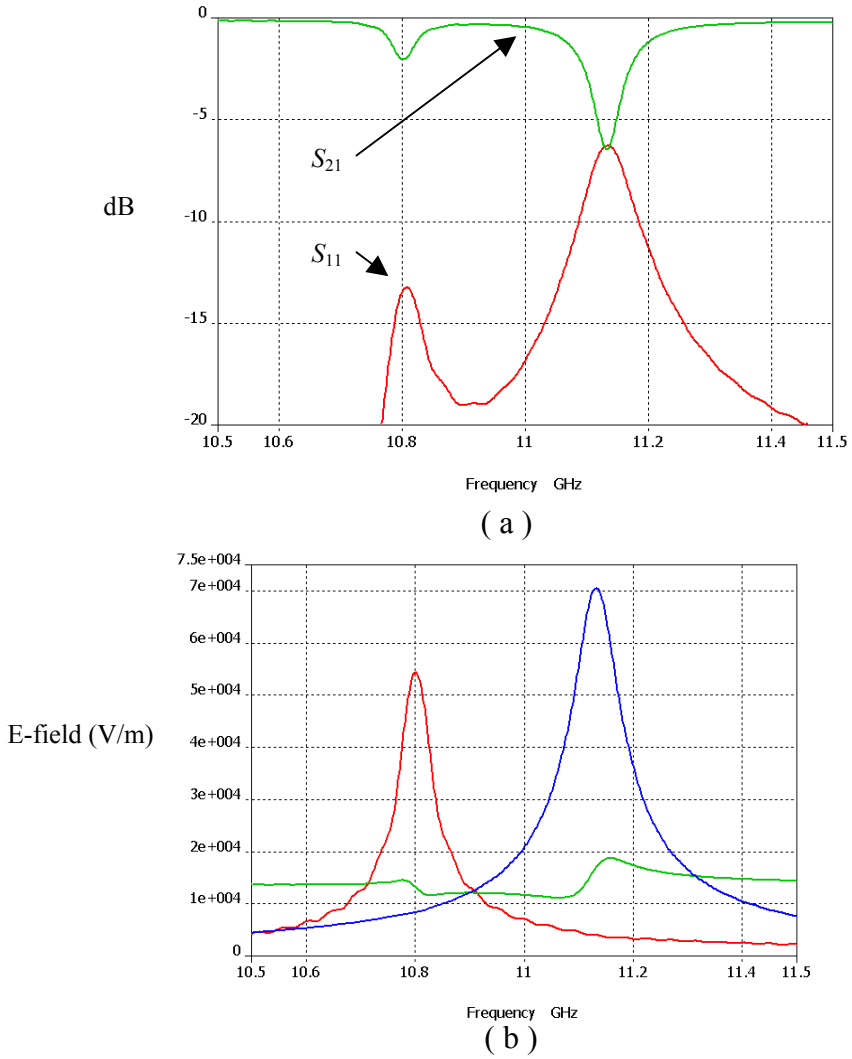


**Figure 2.51** (a) Simulated *S*-parameters around the second-harmonic of a side-coupled ring resonator. (b) The amplitude of the *E*-field oscillation in the middle of the disk at angular positions *E* and *O* shown in Fig. 2.50.

The main differences in this case are: (1) the *E*-field distribution factor $\beta_s$ is smaller due to more *E*-field variations around the microdisk. (2) $G_v$ is smaller due to frequency dependent losses of the RF components (microstripline + ring). However we can still use the same formalism with new correction factors to evaluate the modulation performance.

### 2.7.2 Experimental results

Fig. 2.52 is a photograph of the experimental arrangement used for our harmonic modulation measurements. The disk size and other parameters are the same as Fig. 2.23. Optical coupling in and out is achieved using a single prism. The laser light from a single mode tunable laser with (line width ≈ 500 MHz) is focused on the prism surface by a lens system and collected from the other side with a cleaved fiber. The optical $Q$s observed are about $3\text{-}5\times10^{6}$ and $\Delta\nu_{FSR} \approx 7.6$ GHz (for TE WG modes). A copper ring electrode ($R$ = 2.9 mm, $w_r$ = 0.5 mm) is placed on top of the disk and is side coupled to a microstrip line. Using the experimental arrangement in Fig. 2.52(a) we have modulated the laser light (wavelength $\lambda_0$ = 1550 nm) at the fundamental and second-harmonic frequencies of the ring. The optical mode used for this experiment has a $Q = 3\times10^{6}$ and maximum optical power $P_{o,max}$ = 30 μW. During modulation, the RF output port was open ended to create a standing wave on the microstrip line and increase the voltage on microstrip line. Fig. 2.52(b) shows the detected RF-power spectrum while the second-harmonic of the RF-ring resonator is tuned to $2\times\nu_{FSR}$ = 15.2 GHz. The inset is representative of throughput measurement ($S_{21}$) and shows that the fundamental at frequency 7.7 GHz and second-harmonic at frequency 15.2 GHz of ring resonator are excited. The modulation observed at 15.2 GHz is experimental proof of higher harmonic modulation using the RF-ring resonator modes. The fundamental resonance of the

ring resonator is about 100 MHz detuned relative to $\Delta\nu_{FSR}$ =7.6 GHz, which explains the weak modulation observed at 7.6 GHz.

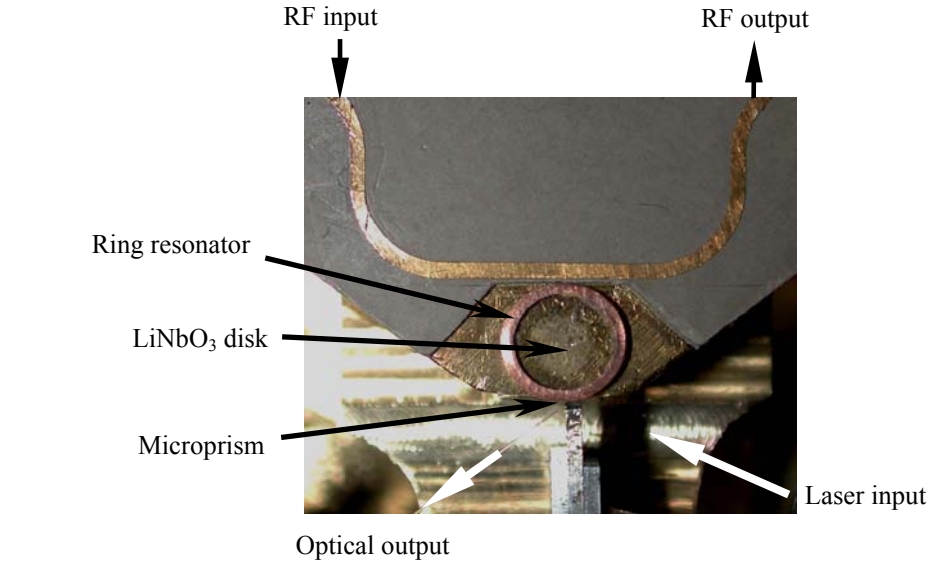


( a )

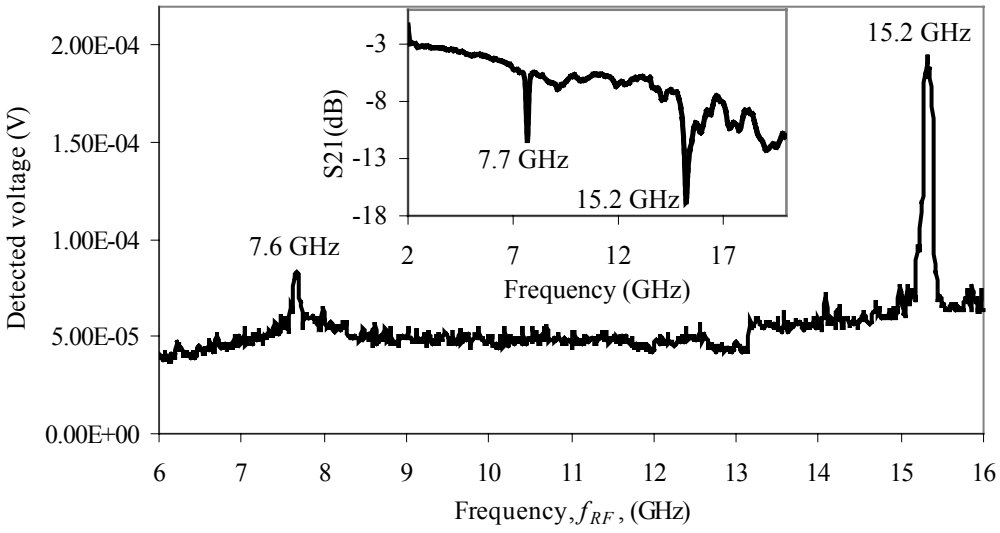


( b )

**Figure 2.52** (a) Photograph of the experimental arrangement. Disk diameter = 5.8 mm, disk thickness = 0.74 mm, FSR = 7.6 GHz. (b) Second-harmonic modulation at 2×FSR = 15.2 GHz. The inset shows the results of $S_{21}$ measurement. As may be seen the fundamental resonance of the ring is off by 100 MHz (7.7 GHz as opposed to 7.6 GHz), while the second-harmonic is exactly equal to 15.2 GHz. This explains the weak modulation observed at 7.6 GHz. (The injected RF-power to the microstrip line is 0 dBm)

Fig. 2.53 is the measured signal to noise ratio (S/N) at the fundamental ($\nu_{FSR}$ = 7.6 GHz) and the second-harmonic ($2\times\Delta\nu_{FSR}$ = 15.2 GHz). The RF-*Q* of the second-harmonic was about 80.

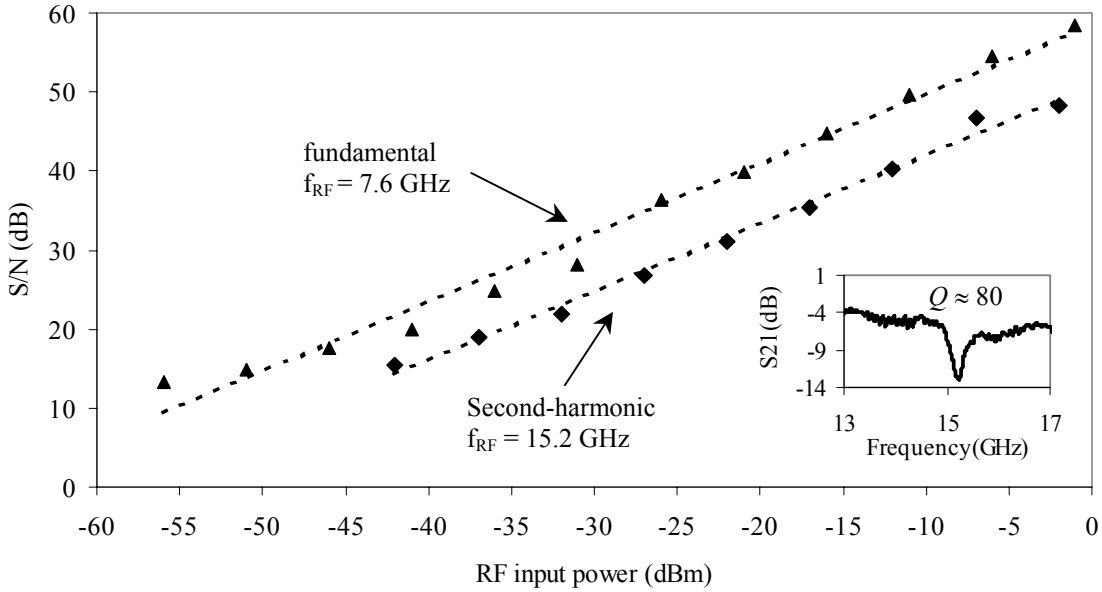


**Figure 2.53** Measured signal to noise ratio (of amplified signal) as a function of input RF power at fundamental ($f_{RF}$ = 7.6 GHz) and second-harmonic ($f_{RF}$ = 15.2 GHz) of the ring. The inset shows $S_{21}$ spectrum when the even second harmonic of the ring (f = 15.2 GHz) is excited.

To our knowledge, no result has been reported at higher harmonics previously and this is the first demonstration of efficient modulation at $2\times\Delta\nu_{FSR}$ for an electro-optic resonant modulator. A comparison between the second-harmonic modulation results with half-ring and ring resonators indicates that use of the ring electrode modulates the WG modes about 8 times better than the half-ring at $2\times\Delta\nu_{FSR}$.

Fig. 2.54 shows the third-harmonic modulation results for the 8.7 GHz microdisk modulator. Fig. 2.54(a) shows the RF frequency spectrum of the detected third harmonic modulation ($3\times\Delta\nu_{FSR}$ = 3× 8.7 GHz = 26.1 GHz).

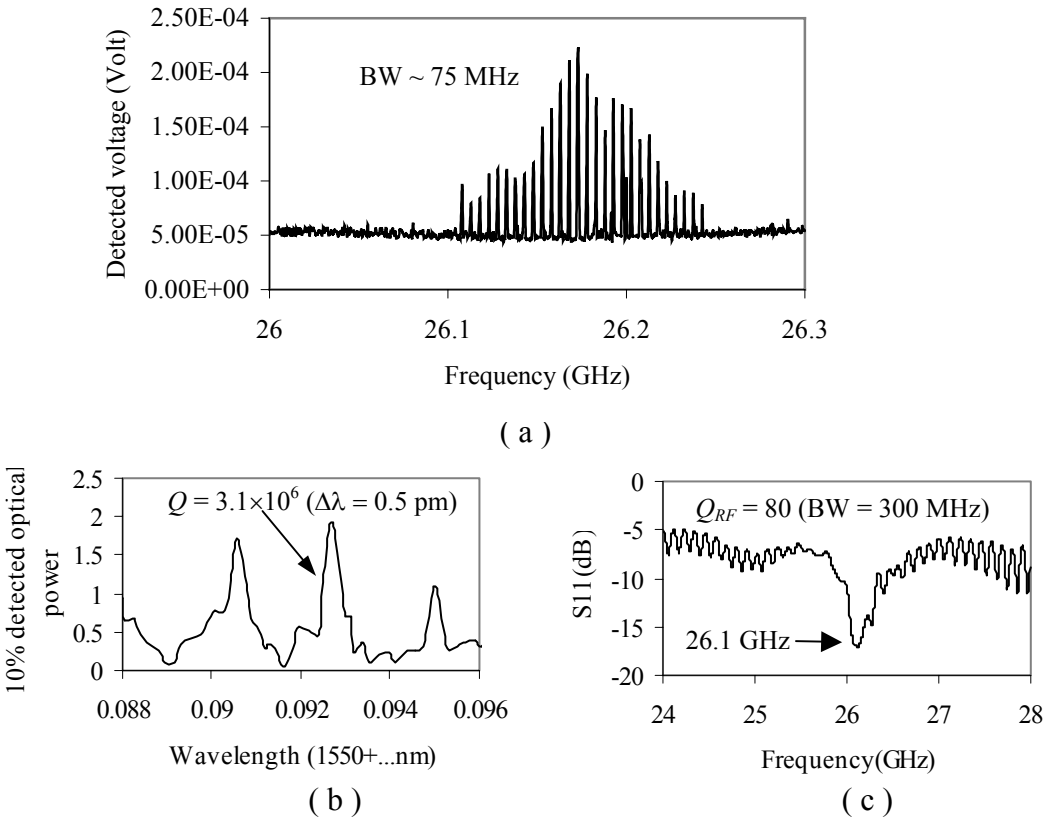


**Figure 2.54** (a) RF frequency spectrum of the detected third harmonic modulation ($3\times\Delta\nu_{FSR} = 3\times 8.7$ GHz = 26.1 GHz). (b) The spectrum of the modulated optical mode. (c) $S_{21}$ measurement result showing the 3rd resonance of the ring.

Fig. 2.54(b) shows the spectrum of the modulated optical mode with a $Q$ of $3.1\times10^6$. The $S_{21}$ spectrum result in Fig. 2.54(c) shows that the 3rd resonance of the ring resonator is tuned to $3\times\Delta\nu_{FSR}$.

## 2.8 Stabilization

In this section we describe an active stabilization circuitry designed to eliminate thermal and mechanical drift during microphotonic modulator operation. Knowing the system response to the optical mode, drift in resonant frequency can be detected by detecting a small portion of the average optical output power and measuring the power variations. Since the optical modes in the $LiNbO_3$ disk can be tuned via the electro-optic effect by applying a DC electric field, it is possible to compensate for any thermal or mechanical drifts using DC shift. In this way the laser wavelength can be locked to a specific position in the optical mode. During modulation the ring electrode is resonating at RF frequency ($f_{RF} = \Delta\nu_{FSR}$). Hence, the DC voltage should be applied in such a way that it does not influence the RF resonant mode. This has been achieved by applying the voltage via a very thin gold wire that is attached to a zero-field position on the ring. When the even mode of the ring is excited, this position is at the coupling area where the distance between the microstripline feed and the ring is minimum.

Fig. 2.55(a) shows a schematic diagram of the experimental setup. We have used a 10/90 splitter to monitor the optical output power. However, in principle, a smaller portion of the optical power can be used (around 1%) minimizing the impact on the modulated power.

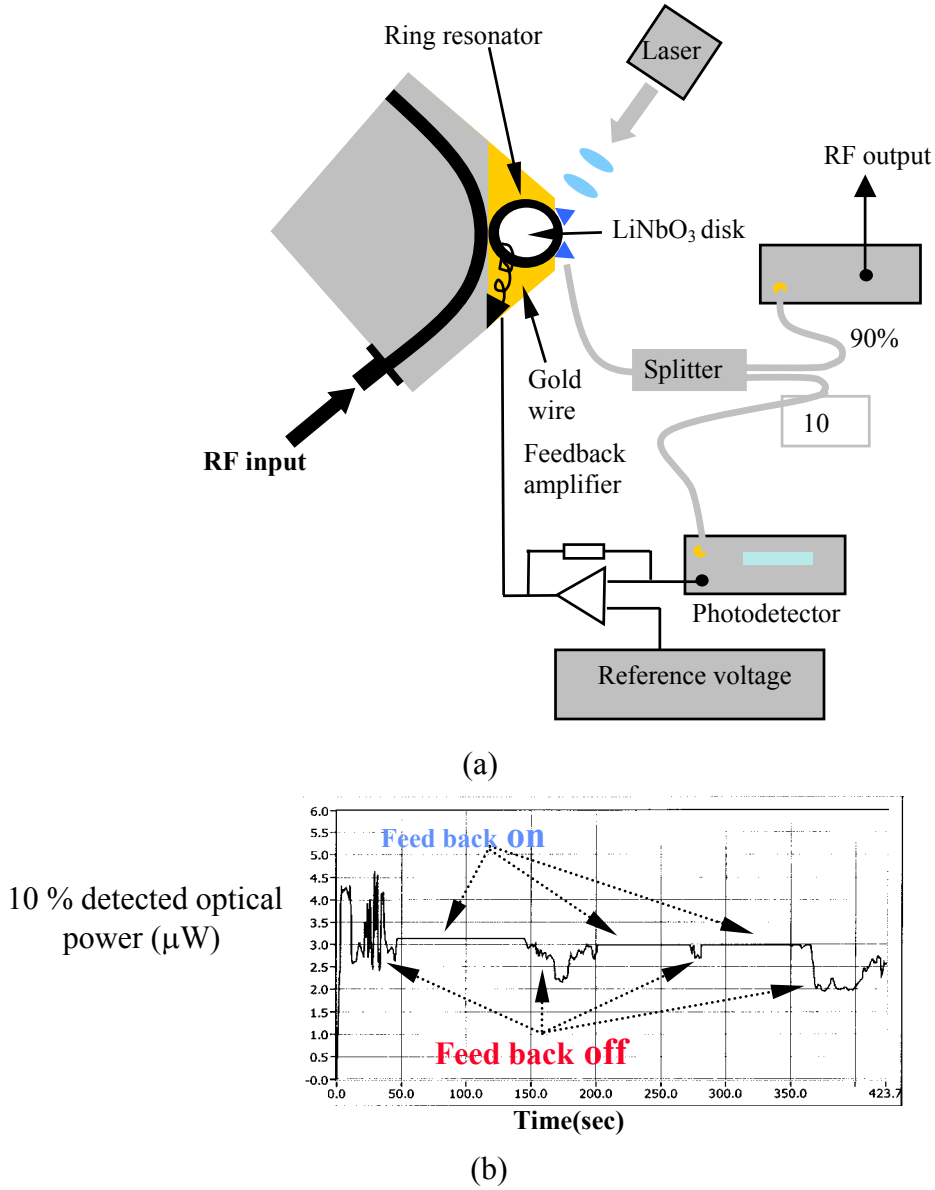


**Figure 2.55** (a) Schematic diagram showing the feedback loop arrangement. (b) Experimental results showing the effect of the feedback loop on output power fluctuations.

A differential amplifier is used to compare a reference voltage with the detected voltage and to apply an appropriate voltage on the disk. By changing the reference voltage we can lock the laser wavelength to any position on the mode. The optical peak power and the quality factor determine the slope of the mode. In our

experiments, a typical optical mode with a quality factor of $Q = 3 \times 10^6$ has a slope of about 120 μW/pm. For a disk of 5.13 mm diameter and 400 μm thickness the ring generates a DC shift of about 0.1 pm/V. So, if we choose the reference voltage in a way that the output of the differential amplifier is zero while the wavelength is tuned to the selected mode location, a 10 V peak-to-peak signal swing in amplifier output is more than enough to compensate for typical drift values. Fig. 2.55(b) shows the temporal variation of average optical power with and without the feedback loop. As may be seen, when the feedback loop is operational, the output power is very stable and the modes resonant wavelength is locked. This simple feedback circuit makes the modulator output very stable with respect to thermal and mechanical drift. This results in improved BER performance as well as improved RF-photonic link signal to noise ratio.

## 2.9 Summary

In this chapter many aspects of the microdisk modulator have been reviewed. We studied optical WG resonances in a $LiNbO_3$ microdisk resonator and optical coupling techniques for the exciting them. We investigated the theoretical and experimental aspects of the RF-ring resonator and its impact on the electro-optic interaction in a microdisk optical resonator. The DC electro-optical response of WG resonances was used to develop a simple semi-empirical method to calculate the magnitude of the

modulated optical power as a function of measurable parameters. The low-speed bistable behavior of the disk was demonstrated using a feedback loop.

The efficiency of the microdisk modulator was significantly improved by using a combination of careful opto-mechanical design, feedback stabilization, and employing the RF-ring resonator. A sensitive 14.6 GHz $LiNbO_3$ microdisk modulator was demonstrated that outperforms all previously reported devices. Comparison between experimental and theoretical calculations demonstrate the validity of the semi-empirical model. In chapter 4 this model is used to estimate the down-conversion efficiency in the novel $LiNbO_3$ microdisk photonic RF mixer.

## 2.10 References


Lithium Niobate properties

[1] R. S. Weis and T. K. Gaylord, "Lithium Niobate: Summary of physical properties and crystal structure," *Appl. Phys. A*, vol. 37, pp 191-203, 1985.

[2] W. M. Robetrtson, G. Arjavalingam, and G. V. Kopcsay, "Broadband microwave dielectric properties of $LiNbO_3$," *Electron. Lett.*, vol. 27, pp. 175-176.

[3] L. Wan, Y. Yuan, "Observation of dynamic photorefractive effect in lithium niobate waveguides," *Optics communications*, vol 73, no. 6, pp. 439-442, Nov 1989.

[4] K. K. Wong, "Properties of lithium niobate," *INSPEC*, institution of electrical engineers, 1989.

[5] A. M. Prokhov and Y. S. Kuz'minov, "Physics and chemistry of crystalline lithium niobate," The Adam Hilger series on optics and optoelectronics, 1990.

[6] M. Lee, "Dielectric constant and loss tangent in $LiNbO_3$ crystals from 90 10 147 GHz," *Appl. Phys. Lett.*, vol. 79, pp. 1342-1344, 2001.

[7] A. Mendez, A. Garcis-Cabanes, E. Diegues, and J. M. Cabrera, "Wavelength dependence of electro-optic coefficients in congruent and quasi-stoichiometric $LiNbO_3$," *Electron. Lett.*, vol. 35, pp. 498-501, 1999

[8] "RF photonic technology in optical fiber links," Edited by William S. C. Chang. Cambridge university press, 2002.

Optical coupling

[9] M. Cai, O. Painter, and K. J. Vahala, "Fiber-coupled microsphere laser," *Optics Lett.*, vol. 25, no. 19, pp.1430-1432, Oct. 2000.

[10] A. V. Chelnokov and J. M. Lourtioz, "Optimised coupling into planar waveguides with cylindrical prisms," *Electron. Lett.*, vol. 31, no. 4, pp. 269-271, Feb. 1995.

[11] J. P. Laine, B. E. Little, H. A. Haus, "Etch-Eroded fiber coupler for Whispering-Gallery mode excitation in high-Q silica microspheres," *IEEE Photon. Technol.*, vol. 11, no. 11, pp. 1429-1430, Nov. 1999.

[12] A. Yariv, "Universal relations for coupling of optical power between microresonators and dielectric waveguides," *Electron. Lett.*, vol. 36, no. 4, pp. 321-322, Feb. 2000.

[13] C. Liao, Y. D. Zhang, "Spherically tapered prism-waveguide coupler," *Appl. Optics*, vol. 24, no. 20, pp. 3315-3316, Oct. 1985.

[14] B. Little, J. P. Laine, H. A. Haus, "Analitic theory of coupling from tapered fibers and half-blocks into microsphere resonators," *J. of Lightwave Technol.*, vol. 17, no. 4, pp. 704-714, April 1999.

[15] J. -P. Laine, B. E. Little,D. R. lim, H. C. Tapalian, L. C. Kimerling, and H. A. Haus, "Microsphere resonator mode characterization by pedestal anti-resonant reflecting waveguide coupler," *IEEE Photon. Technol. Lett.*, vol. 12, no. 8, pp. 1004-1006, August 2000.

[16] V. S. Ilchenco, X. S. Yao, and L. Maleki, "Pigtailing the high-Q microsphere cavity: a simple fiber coupler for optical Whispering-Gallery modes," *Optics Lett.*, vol. 24, no. 11, pp. 723-725, June 1999.

[17] M. L. Gorodetsky and V. S. Ilchenco, "Optical microsphere resonators: optimal coupling to high-Q Whispering-Gallery modes," *J. of Opt. Soc. Am. B*, vol. 16, no. 1, pp. 147-154, Jan. 1999.

[18] R. Ulrich, "Optimum excitation of optical surface waves," *J. of Opt. Soc. Am.*, vol. 61, no. 11, pp. 1467-1476, Nov. 1971.

[19] J. Verdein, "Laser electronics," *Prentice Hall*, 1995.

Surface roughness and scattering

[20] M. L. Gorodetsky and A. D. Pryamikov, "Rayleigh scattering in high-Q microspheres," *J. of Opt. Soc. Am.*, B, vol. 17, no.6, pp. 1051-1057, June 2000.

[21] B. E. Little and J. P. Laine, S. T. Chu, "Surface-roughness-induced contradirectional coupling in ring and disk resonators," *Optics Lett.*, vol. 22, no. 1, pp. 4-6, Jan. 1997.

[22] B. Little and S. T. Chu, "Estimating surface-roughness loss and output coupling in microdisk resonators," *Optics Lett.*, vol. 21, no. 17, pp. 1390-1392, Sept. 1996.

[23] M. L. Gorodetsky, A. A. Savchenkov, and V. S. Ilchenko, "Ultimate Q of optical microsphere resonators," *Optics Lett.*, vol. 21, no. 7, pp. 453-455, April 1996.

WG modes

[24] S. Schiller and R. L. Byer, "High-resolution spectroscopy of whispering gallery modes in large dielectric spheres," *Optics Lett.*, vol. 16, no. 15, pp. 1138-1440, Aug. 1991.

[25] J. C. Knight, N. Dubreuil, V. Sandoghdar, J. Hare, V. Lefevre-Seguin, J. M. Raimond, and S. Haroche, "Maping whispering-gallery modes in microspheres with a near-field probe," *Optics Lett.*, vol. 20, no. 14, pp. 1515-1517, July 15 1995.

[26] M. L. Gorodetsky and V. S. Ilchenko, "High-Q optical whispering-gallery microresonators:precession approach for spherical mode analysis and emission patterns with prism couplers", *Optics comm.*, vol. 113, pp. 133-143, Dec. 1994.

Electro-optic bistability

[27] P. W. Smith, E. H. Turner, and P. J. Maloney, "Electro-optic nonlinear Fabry-Perot devices," *IEEE J. of Quanum Electron.*, vol. 14, no. 3, pp. 207-212, March 1978.

[28] R. S. Jameson and W. T. Lee, " Operation of an all-optical bistable device dependent upon incident and transmitted optical power," *IEEE J. of Quantum Electron.*, vol. 25, no. 2, pp. 139-143, Feb. 1989.

[29] P. W. Smith and E. H. Turner, "A bistable Fabry-Perot resonator," *Appl. Phys. Lett.*, vol. 30, no. 6, pp. 280-281, March 1977.

[30] T. Ikegami and K. Kubodera, "Nonlinear optical devices for switching applications," *Communications, 1990. ICC 90 IEEE international conference on*, vol. 3, pp. 1152-1156, Apr. 1990.

[31] P. W. Smith, E. H. Turner, and B. B. Mumford, "Nonlinear electro-optic Fabry-Perot devices using reflected-light feedback," *Optics Lett.*, vol. 2, no. 3, pp. 55-57, March 1978.

[32] K. Ogusu and S. Yamamoto, "Nonlinear Fabry-Perot resonator using thermo-optic effect", *IEEE J. of lightwave technol.*, vol. 11, no. 11, pp. 1774-1780, Nov. 1993.

RF resonator

[33] I. Wolf, and V. Tripathi, "The microstrip open-ring resonator ", *IEEE trans. on microwave theory and techniques*, vol. MTT-32, no. 1, pp. 102-107, Jan 1984.

[34] S. G. Pintzos, and R. Pregla, " A simple method for computing the resonant frequencies of microstrip ring resonators ", *IEEE trans. on microwave theory and techniques*, vol. MTT-26, no. 10, pp. 809-813, Oct 1978.

[35] S.-L. Lu, and A. M. Ferendeci, " Coupling parameters for a side-coupled ring resonator and a microstrip line ", *IEEE trans. on microwave theory and techniques*, vol. 44, no. 6, pp. 953-956, June 1996.

[36] S.-L. Lu, and A. M. Ferendeci, " Coupling modes of a ring side coupled to a microstrip line ", *Electron. Lett.*, vol. 30, no. 16, pp. 1314-1315, August 1994.

[37] Y. S. Wu, and F. J. Rosenbaum, " Mode chart for microstrip ring resonators ", *IEEE trans. on microwave theory and techniques*, Vol. MTT-21, pp. 487-489, July 1973.

[38] G. K. Gopalakrishnan, and K. Chang, " Novel excitation schemes for the microstrip ring resonator with low insertion loss", *Electron. Lett.*, vol. 30, no 2, pp. 148-149, Jan 1994.

[39] L.-H. Hseieh, and Kai. Chang, " Equivalent lumped element G,L,C, and unloaded Q's of closed- and open-loop ring resonators", *IEEE trans. on microwave theory and techniques*, vol. MTT-50, no. 2, pp 453-460, Feb 2002.

[40] G. K. Gopalakrishnan,B. W. Fairchild, C. L. Yeh, C.-S. Park, K. Chang, M. H. Weichold, and H. F. Taylor, "Experimental investigation of microwave-optoelectronic interactions in a microstrip ring resonator", *IEEE trans. on microwave theory and techniques*, vol. MTT-39, no. 12, pp. 2052-2060, Dec 1991.

[41] K. Chang, S. Martin, F. Wang, and J. L. Klein, "On the study of microstrip ring and varactor-tuned ring circuits", *IEEE trans. on microwave theory and techniques*, Vol. MTT-35, no. 12, pp. 1288-1295, Dec 1987.

[42] P. A. Bernard, and J. M. Gautray, "Measurment of dielectric constant using a microstrip ring resonator", *IEEE trans. on microwave theory and techniques*, vol. MTT-39, no 3, pp. 592-594, March 1991.

[43] A. Khanna, and Y. Garault, "Determination of loaded, unloaded, and external quality factors of a dielectric resonator coupled to a microstripline", *IEEE trans. on microwave theory and techniques*, vol. MTT-31, no 3, pp. 261-264, March 1993.

[44] K. Chang, "Microwave ring circuits and antennas", Wiley series in microwave and optical engineering, John Wiely & Sons Inc, 1996.

[45] W. C. Chew, "A broad-band annular-ring microstrip antenna," *IEEE Trans. Antennas and Prop.,* vol. AP-30, Sept 1982.

[46] D. M. Pozar, "Microwave engineering," John Wiely & Sons Inc, 1998.

$LiNbO_3$ microdisk modulator

[47] D. A. Cohen, "Lithium Niobate microphotnic modulators", Ph.D dissertation, USC May 2001. < http://www.usc.edu/alevi>

[48] D. A. Cohen, M. Hossein-Zadeh, and A. F. J. Levi, "High-Q microphotonic electro-optic modulator," *Solid-State Electronics*, vol. 45, pp.1577-1589, 2001.

[49] V. S. Ilchenko, A. A. Savchenkov, A. B. Matsko, and L. Maleki, "Sub-microwatt photonic microwave receiver", *IEEE photonics technol.*, vol 14, no. 11, Nov 2002.

---

## Technical notes

(1) Picomotor actuator from *New Focus* ..
Angular resolution < 0.6 mrad
Minimum incremental motion < 30 nm

(2) CST MICROWAVE STUDIO: electromagnetic field simulation software based on FTDT, from *Computer Simulation Technology*.

(3) *HFSS* (V8): electromagnetic field simulation software based on finite element method, from *Ansoft*.

(4) The roughness is measured by "Interferometric surface profiler" from *ADE phase shift.* The roughness parameters $S_y$ and $S_q$ are defined as:

$$\textit{Peak-Peak height : } S_y = z_{max} - z_{min}$$

$$\textit{Root MeanSquare : } S_q = [(1/N) \sum (z_i - \mu)^2]^{0.5}$$

$z_{max}$ : highest pixel in the picture
$z_{min}$ : lowest pixel in the picture
$N$ : total number of pixels (sample points)
$z_i$ : height of the $i^{th}$ pixel
$\mu$ : mean height calculated using $N$ sample points

# Chapter 3

# Microdisk modulator in RF-optical link

## 3.1 Introduction

In a RF-optical link, the data modulated RF carrier is up-converted to optical frequencies in an optical intensity modulator. Once the RF signal is up-converted to optical frequencies, it can be transmitted through optical fibers that are less lossy than conventional RF transmission lines and cables especially at mm-wave frequencies [1-5]. After transmission and distribution, the optical signal is typically down-converted to RF frequencies in a high-speed photodetector. The baseband information is then extracted from the detected RF signal by mixing with a local oscillator. Although by convention the RF carrier is referred to as the sub-carrier and the laser light (194 THz) as the carrier, in this chapter we will refer to them as the RF carrier and the optical carrier respectively. The performance of a RF-optical link that uses the microdisk modulator for optical up-conversion is an indicator of the quality of the optical modulation in a microdisk.

This chapter presents the results of employing the microdisk modulator in a 8.7 GHz RF-optical link. We also present the design and fabrication of patch antennas and

patch antenna arrays used to evaluate the performance of the modulator in a wireless RF-optical link. The noise performance of the link is simulated based on the simple model that was explained in chapter 2 as well as the conventional noise models for other optical and electronic elements in the link. Furthermore the noise calculation demonstrates the sensitivity limits and the role of different device parameters in overall signal-to-noise and bit error ratio (BER) of the link.

## 3.2 RF-optical link

Fig. 3.1(a) and (b) show the architecture of the experimental RF-optical (a) and wireless RF-optical (b) links. In this section, we will specifically discuss RF-optical links based on intensity modulation and direct detection (IM-DD). The RF carrier is modulated by the baseband signal, data or video, using a conventional RF-mixer. The output RF signal has a double-sideband suppressed carrier modulation format. A tunable DFB laser generates the optical carrier around the communication wavelength $\lambda_{laser}$ = 1550 nm ($\nu_{laser}$ = 194 THz). The intensity of the laser light is modulated by the RF signal in an optical modulator. After transmission through an optical fiber the optical signal is detected in a high-speed photodetector. The baseband information is subsequently extracted from the received RF signal by mixing with a local oscillator.

In a wireless link (Fig. 3.1(b)) the output signal of the first mixer is fed to an antenna and is transmitted through free space. On the receiver side, a second antenna feeds the received signal to the optical modulator. In both cases, depending on signal and noise levels at each stage amplifiers may be used to boost the signal power.

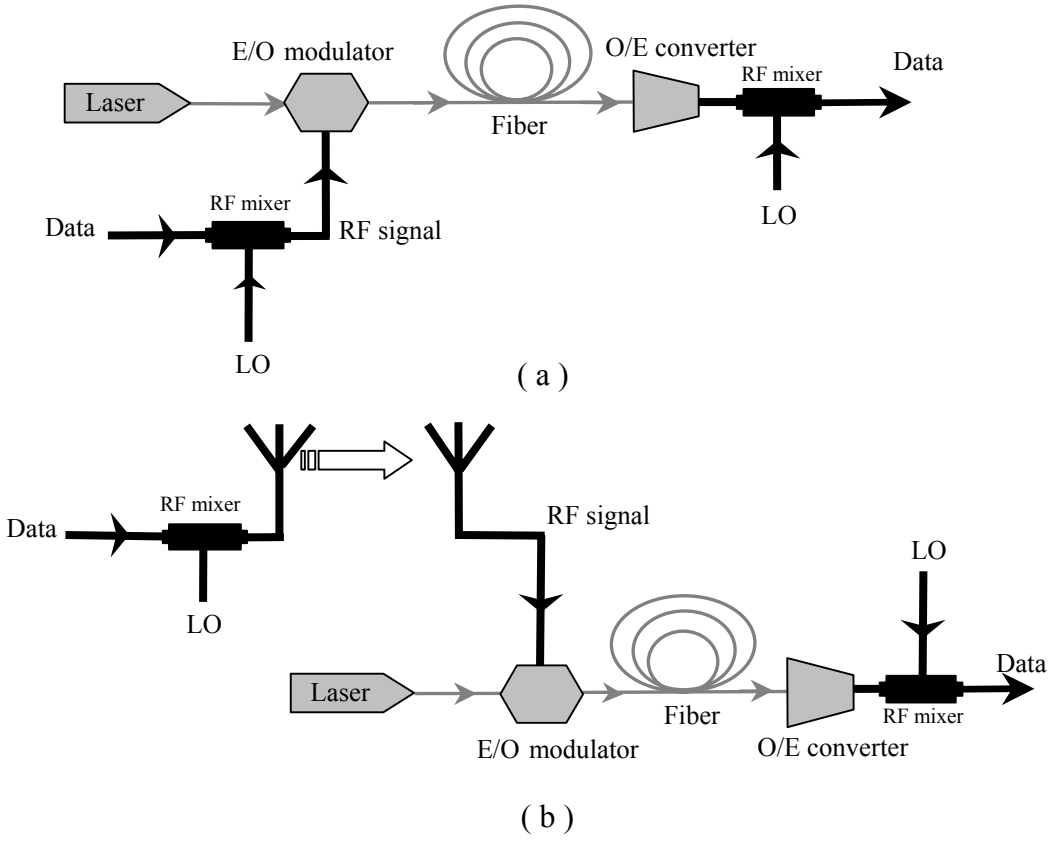


**Figure 3.1** Basic operation of wired (a) and wireless (b) RF-optical links. Depending on the signal-to-noise-ratio required at each stage, amplifiers may be used in some interfaces.

Fig. 3.2 shows the details of signal flow through a RF-optical link that employs a microdisk optical modulator. The RF carrier frequency is limited to frequencies matched to modulation frequencies of the microdisk modulator i.e. $m_o \times \Delta\nu_{FSR}$.

Fig.3.3 shows a schematic diagram of the experimental arrangement and the equipment used to build our microdisk based RF-optical links.

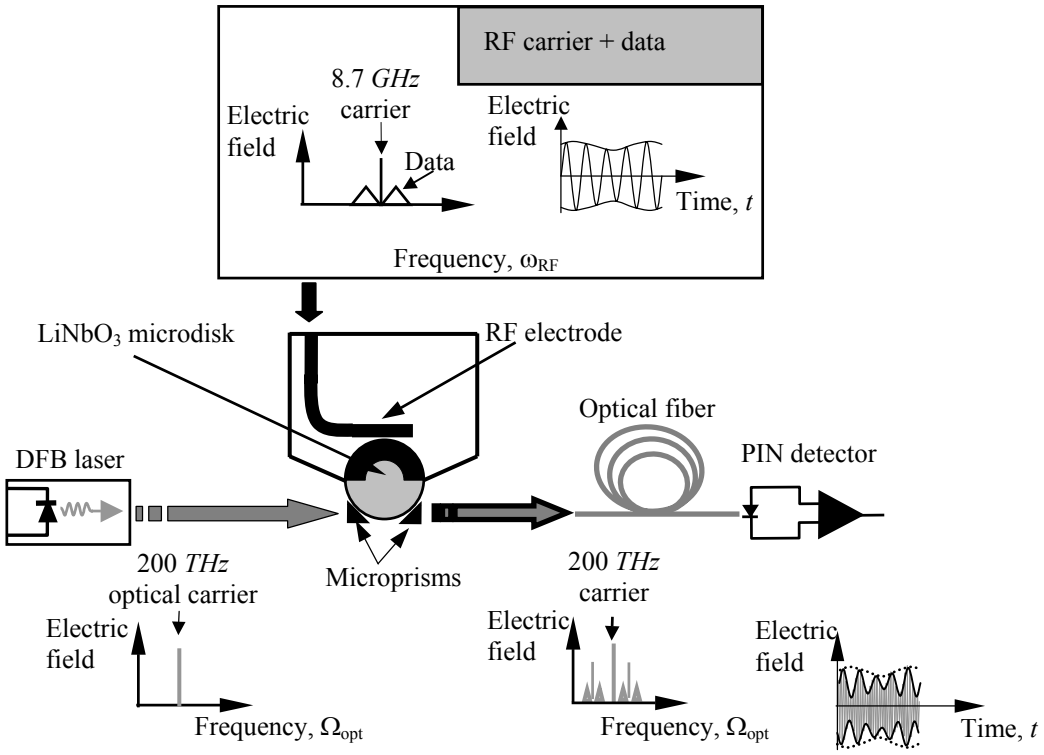


**Figure 3.2** Schematic diagram showing the signal flow in an RF-optical link that uses the microdisk optical modulator.

The microdisk employed in our modulator has a diameter of 5.13 mm, a thickness of 0.4 mm, and a FSR of 8.7 GHz for a TE polarized WG resonance. The RF resonator is a semi-ring electrode side-coupled to an open microstrip line and its fundamental resonant frequency is tuned to 8.7 GHz. The RF carrier is modulated by a data stream or video signal using a double-balanced RF-mixer [(1)]. For digital data transmission a non-return-to-zero pseudo-random bit stream (NRZ $2^7$-1 PRBS) from

a pattern generator is fed to the IF port of the RF mixer at different bit rates and for video transmission a VCR provides the baseband signal. The local oscillator signal at 8.7 GHz (power ≈ 8 dBm) is provided by a RF-synthesizer. A RF amplifier [(2)] amplifies the signal and feeds it into the microdisk optical modulator, however in the wireless case the amplified RF-signal is fed to the transmitting antenna (dashed lines) and a similar antenna directly feeds the received signal to the microdisk modulator. A single mode tunable laser provides the optical carrier at $\lambda$ = 1550 nm with a line width of less than 500 kHz. The optical output power from the microdisk is divided between two photodetectors by a single mode 10/90 optical power divider. The detector labeled as #1 is a low-speed photodetector with a bandwidth of 1 kHz. This detector that receives 10% of the optical output power monitors the location of the laser wavelength relative to the WG resonant wavelength. It may also provide the feedback voltage required for wavelength locking circuit when active stabilization is required. 90% of the modulated optical output power is transmitted through several meters of optical fiber and at the end is detected by a high-speed photodetector (#2) that is a high-speed photodetector with a bandwidth of 15 GHz [(3)].

A RF amplifier (#2) amplifies the detected signal and feeds it into a RF mixer where it is mixed with a local oscillator (LO2) to extract the baseband signal. The local oscillator signals in both the transmit and receive side are provided by the same signal generator and are phase matched. The down-converted baseband signal is amplified in a low-speed amplifier [(4)] (#3) and sent to a bit error ratio tester (BERT)

for measurement or to a TV for display. The integrity of the demodulated data is measured with the BERT and a digital oscilloscope. The laser wavelength is always tuned to one of the high-*Q* TE-resonances of the microdisk where optical modulation efficiency is maximized.

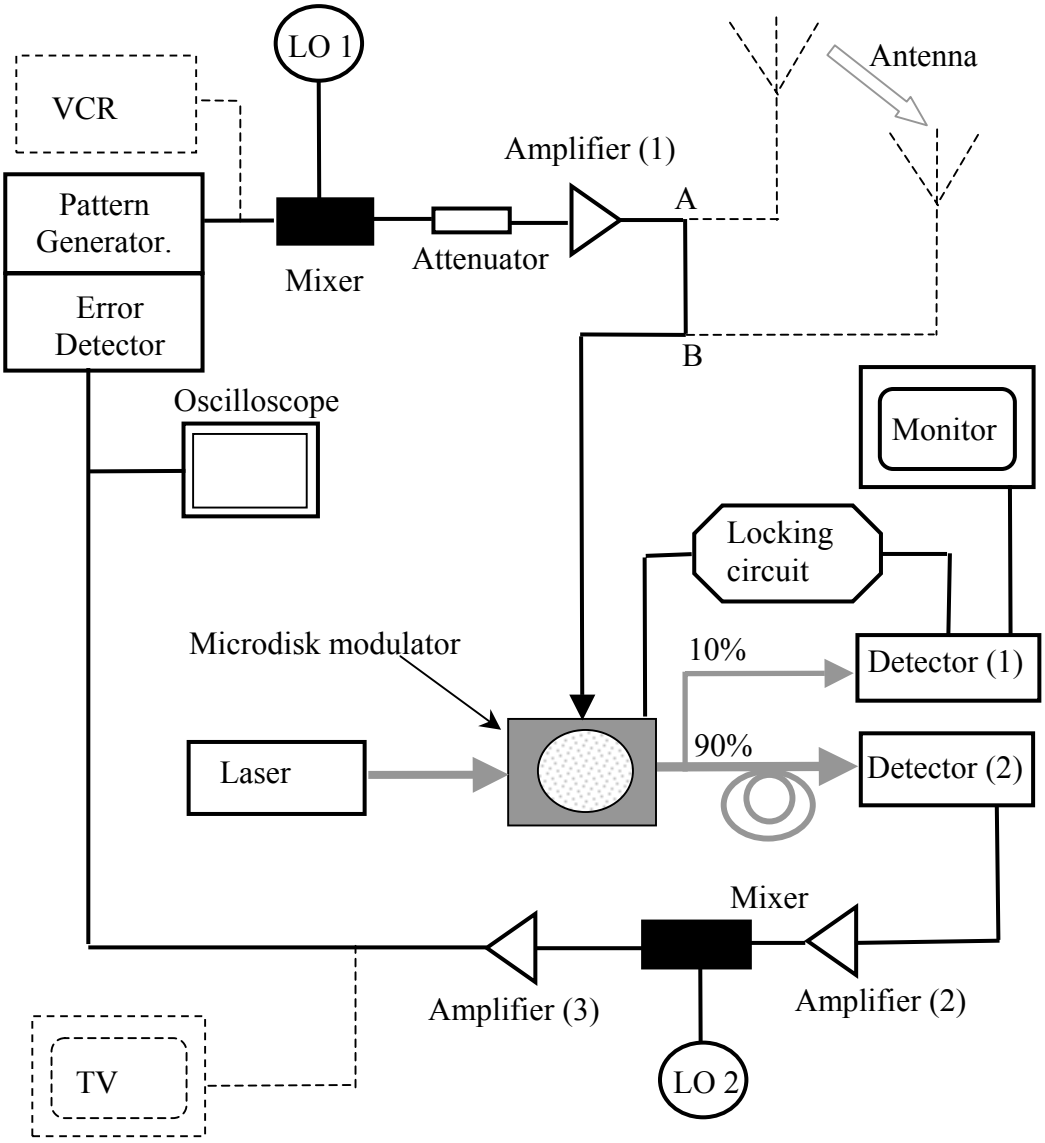


**Figure 3.3** Schematic diagram of the experimental RF-optical link designed for investigating the $LiNbO_3$ microdisk modulator performance.

The bandwidth of a typical TE-resonance is about 150 MHz, corresponding to a $Q = 3 \times 10^6$, which limits the data transmission rate to less than 150 Mb/s. As mentioned in chapter 2 the modulation bandwidth in a microdisk modulator is limited by the optical-$Q$. The RF power in all experiments is defined as the measured power within 150 MHz bandwidth centered at 8.7 GHz.

## 3.3 Video and data transmission

Fig. 3.4 shows a photograph of the 8.7 GHz microdisk modulator whose structure was described in section 2.6.3 (Fig. 39(d)). The mechanical stability of this modulator is noticeably improved by the planar design.

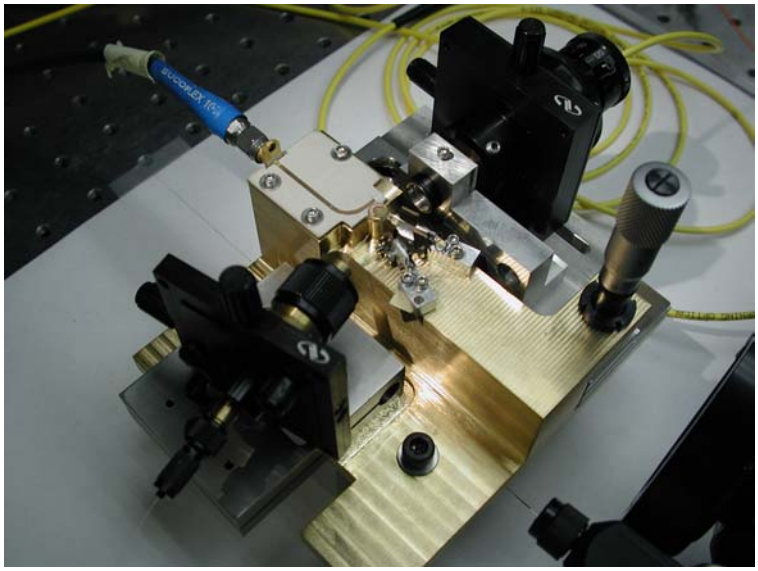

**Figure 3.4** Photograph of the 8.7 GHz $LiNbO_3$ microdisk modulator. ($D$ = 5.13 mm, $h$ = 0.4 mm)

Fig. 3.5(a) shows the measured phase-margin of the detected output at a data rate of 10 Mb/s (NRZ $2^7$ - 1 PRBS) for the indicated modulated RF-power. The inset is representative of the corresponding input and output eye-diagrams.

Fig. 3.5(b) shows the spectrum of the RF-signal before and after optical modulation.

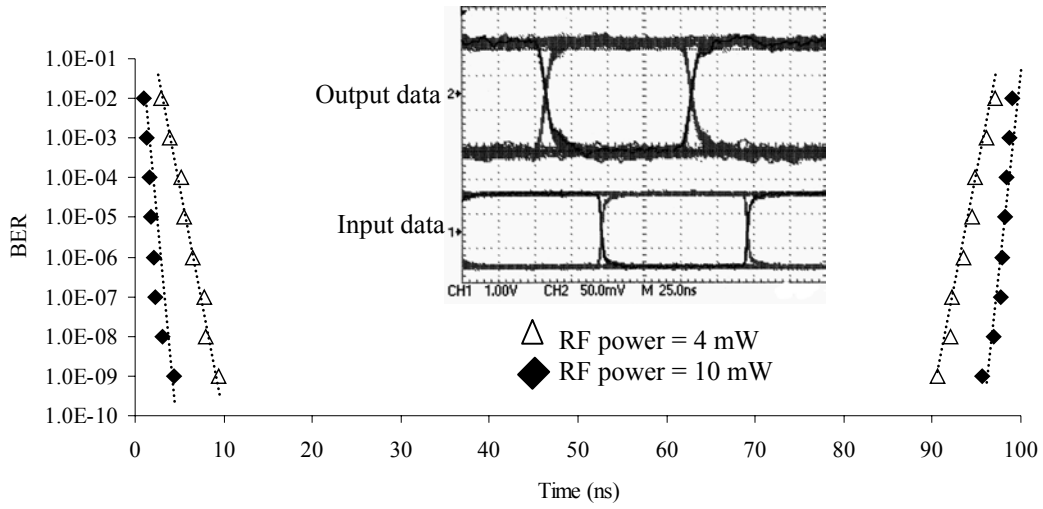


( a )

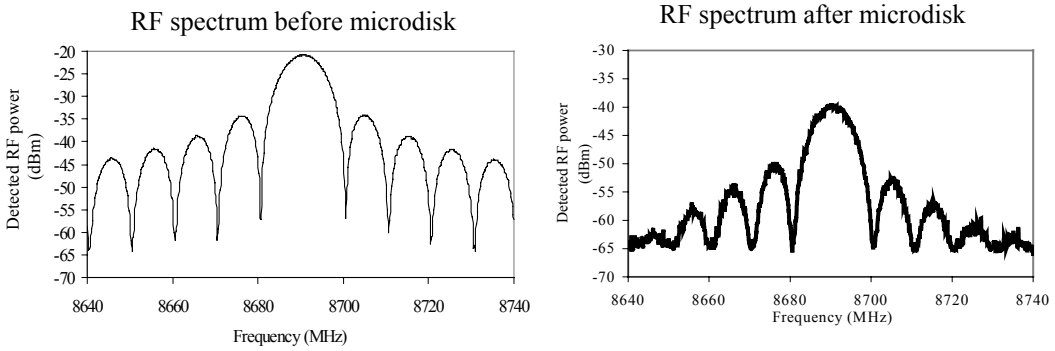


( b )

**Figure 3.5** (a) Measured phase margin of the output at 10 Mb/s (NRZ $2^7$ - 1 PRBS) for 10 mW and 2.5 mW modulating RF power. The inset shows representative input and output eye-diagrams. (b) Measured RF signal spectrum before and after microdisk modulator using 2.5 mW RF power.

Fig. 3.6 shows the measured sensitivity of BER as a function of RF power. The inset is the detected optical output power against input laser wavelength. The maximum optical output power ($P_{o,m}$) for all of these measurements is in the range 18 μW to 27 μW wherein the laser wavelength is tuned close to the maximum slope of the optical mode. Fig. 3.7 shows input and demodulated output eye-diagrams transmitted over the RF fiber-optic link at (a) 50 Mb/s and (b) 100 Mb/s NRZ $2^7$ - 1 PRBS data rates. The critical factors for high-quality data transmission are the purity and *Q*-factor of the optical mode, the magnitude of the rising or falling slope of the optical mode in the vicinity of the laser wavelength, and the optical output power from the disk.

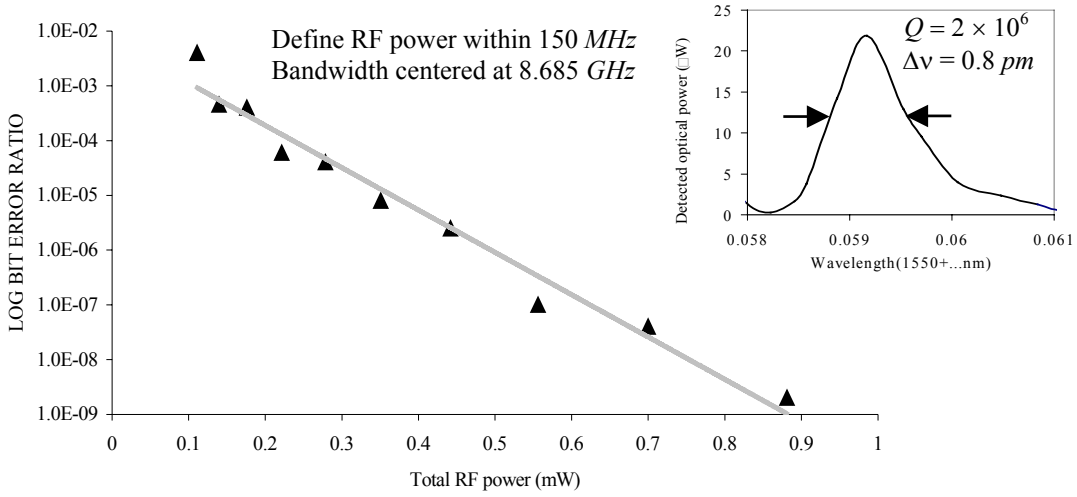


**Figure 3.6** Measured sensitivity of BER to modulating RF power (measured RF power within 150 MHz bandwidth centered at 8.685 GHz). The inset is the detected optical output power against input laser wavelength.

By tuning the laser wavelength and RF carrier frequency it is possible to optimize the modulation quality and efficiency. Due to the presence of high-*Q* (1 - 3 × $10^6$) optical modes, and the sensitivity of the modulation efficiency to the mode slope,

wavelength stability of the laser is an important issue. To ensure stable, high-quality, data transmission the wavelength stability should be less than 0.1 pm.

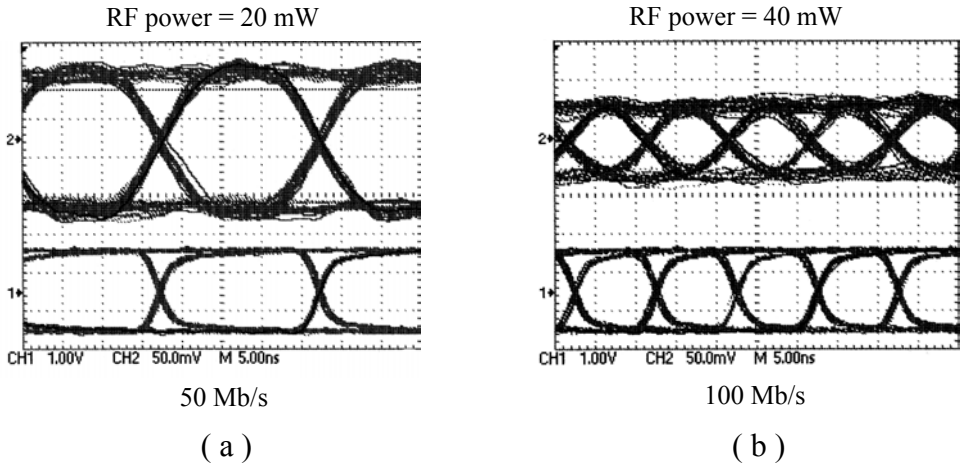


**Figure 3.7** Optical output eye-diagrams at 50 Mb/s (a) and 100 Mb/s (b) (NRZ $2^7$ - 1 PRBS). The modulating RF-power is 40 mW and 60 mW respectively.

We use the same experimental arrangement for video transmission. The demodulated video signal is amplified by a video amplifier and fed to a monitor to compare the image quality with the original version.


**Figure 3.8** Demonstration of video transmission through microdisk based RF-optical link. (a) The original image. (b) The transmitted image.

Fig. 3.8 shows the original image (left) and the transmitted image (right). The image quality hasn't been distorted and is acceptable as a proof of principle demonstration for the microdisk based RF-optical link.

## 3.4 Microstrip antenna and antenna arrays

The antenna is an important component in a wireless RF-optical link or a photonic RF receiver. Its design and performance has a strong impact on the overall link or receiver sensitivity. In this section after a brief review of patch antenna design issues, we present measurement results for planar antennas that have been designed and fabricated for microdisk based wireless links and photonic RF receivers.

### 3.4.1 Patch antenna

Microstrip resonators can be classified into two main categories depending on their length-to-width ratio. A resonator with broad strip (length ≈width) is known as a microstrip patch. When the signal frequency is in the vicinity of a resonance, a microstrip resonator radiates a relatively broad beam, broadside to the plane of the structure. A significant part of the input signal contributes to the radiation and the resonator behaves as an antenna. A patch antenna is just a rectangular resonator. The main dimensions of the patch should be near one half-guided wavelength so the

fundamental resonance of the patch can be used for coupling to radiation field. At higher harmonic radiation pattern is more complicated and the energy might be radiated to unwanted directions. Fig. 3.9(a) shows the definition of *E* and *H* radiation planes and Fig. 3.9(b) shows a typical example of the radiation patterns of a rectangular microstrip patch antenna [6].

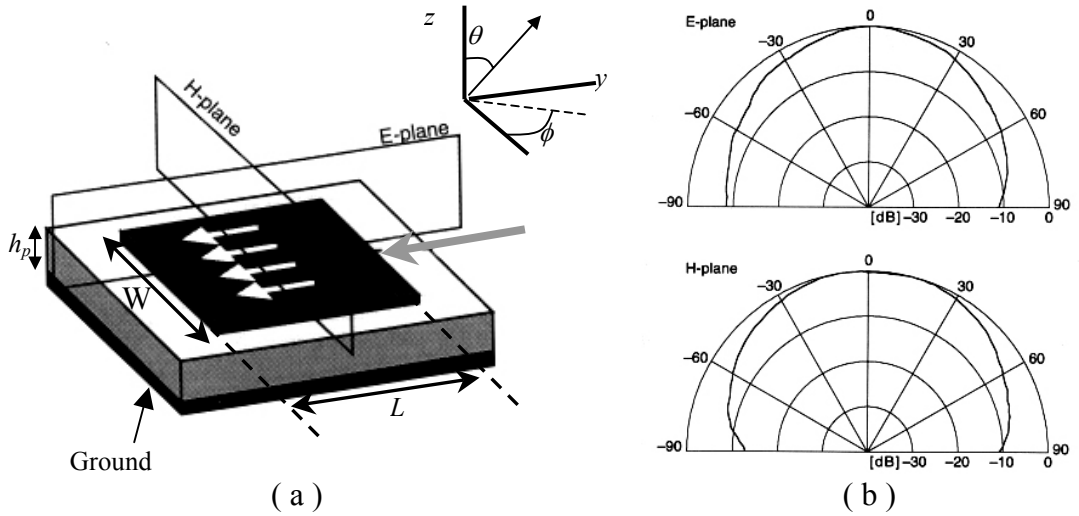


( a ) ( b )

**Figure 3.9** (a) The definition of *E*- and *H*-radiation planes. (b) A typical example of the radiation patterns of a rectangular microstrip patch antenna [1].

Typically a microstrip patch antenna has a gain within the 5-6 dB range, and exhibits a 3 dB beam width somewhere between 70 and 90 degrees. Fig. 3.10 provides a simple illustration of the operation of patch antenna in terms of an array of dipoles located at opposite edges of the patch.

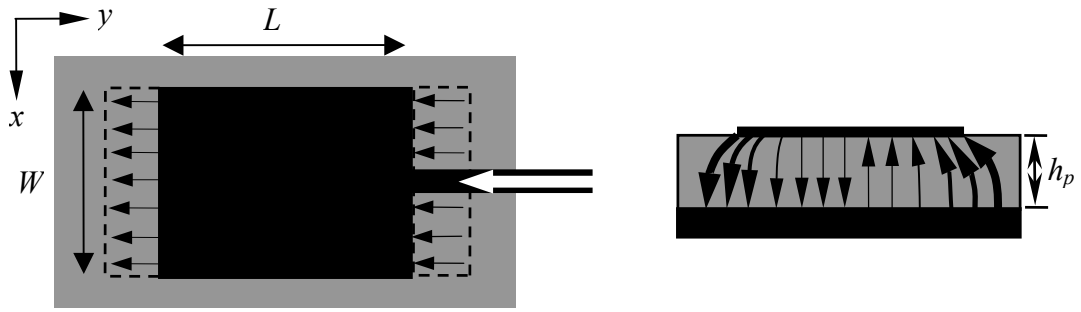


**Figure 3.10** Top view and side view of spatial distribution of *E*-field in a rectangular microstrip patch resonator showing that the *E*-field lines effectively behave like two dipole arrays.

The feed line breaks the symmetry of the patch in *y*-direction resulting in a two set of parallel dipole arrays with the same phase where in *x*-direction the dipoles are out of phase and the radiation field is canceled out. The fundamental resonant frequency of the patch ($f_r$) is determined by the dielectric constant of the substrate and the patch length *L* [2]:

$$f_r = \frac{c}{2}\frac{1}{\sqrt{\varepsilon_{re}}\left(L + 2\Delta l_{oc}\right)} \tag{3.1}$$

where $\varepsilon_{re}$ is the effective dielectric constant, *L* is the dimension of the patch parallel to dipole direction and $\Delta l_{oc}$ is the equivalent length accounting for the fringing fields at the open ends of the patch antenna. $\varepsilon_{re}$ and $\Delta l_{oc}$ can be calculated using the following equations [2]:

$$\varepsilon_{re} = \frac{\varepsilon_r + 1}{2} + \frac{\varepsilon_r - 1}{2}\left(1 + \frac{10h_p}{W}\right)^{-\frac{1}{2}} \tag{3.2}$$

$$\frac{\Delta l_{oc}}{h_p} = 0.412\frac{\left(\varepsilon_{re} + 0.3\right)\left(\frac{W}{h_p} + 0.264\right)}{\left(\varepsilon_{re} - 0.258\right)\left(\frac{W}{h_p} + 0.813\right)} \tag{3.3}$$

Where $h_p$ and $\varepsilon_r$ are the thickness and the relative dielectric constant of the dielectric substrate respectively.

Different configurations have been developed to feed a patch antenna [6-10]. Since for microphotonic receiver applications, integration of the antenna with the ring resonator is desired, we have chosen a microstrip line feed technique. The main difficulty of feeding the patch antenna is the impedance mismatch between the feeding line and the antenna. The input impedance of a patch is relatively high at the patch edge (200 Ω – 400 Ω) therefore a matching section is required between the 50 Ω microstrip line and the patch antenna. We have investigated three approaches to solve the mismatch problem: (1) tapered line coupling, (2) quarter-wave matching section and (3) inset microstrip feed.

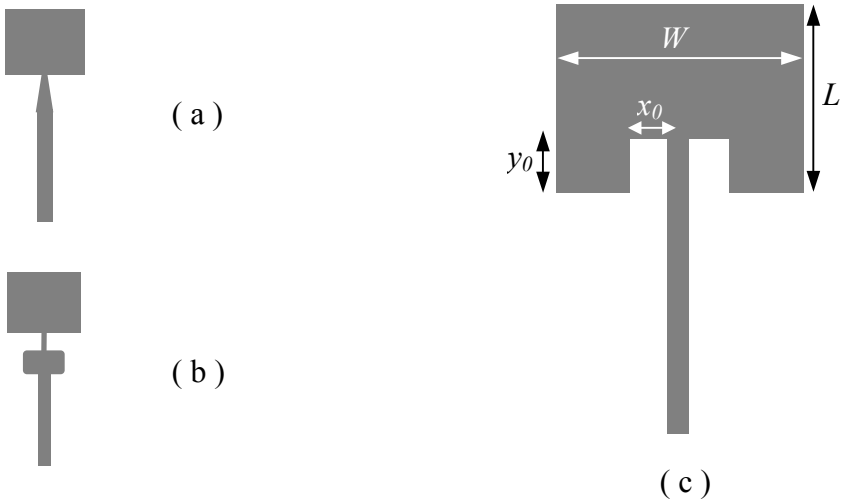


**Figure 3.11** Different techniques used for feeding the patch antenna: (a) The tapered microstrip feed. (b) Multisection impedance matching. (c) Inset microstrip feed

Fig. 3.11 shows a schematic diagram of each one of these approaches. Among them the 3rd method is much easier to implement and provides a very good impedance

matching between the feed line and the patch. The line is connected within an inset cut in the patch (see Fig. 3.11(c)). It is found experimentally that cutting such an inset does not significantly alter the resonant frequency [6]. The maximum input impedance occurs at the edge of the patch and decreases as the inset distance ($y_0$) is increased toward the center of the radiator. It has been shown that the functional behavior of the impedance is very close to $\cos^4(\pi y_0/L)$ [9]. The input impedance of a rectangular patch in the middle of the patch edge can be calculated from [7,10]:

$$Z_m = 0.5R_r\left\{\cos^2(\beta W/2)+\left[\left(\frac{Z_0}{R_r}\right)+(\beta\Delta_{loc})^2\right]\sin^2(\beta W/2)-\beta\Delta_{loc}\sin(2\beta W/2)\right\} \quad (3.4)$$

Where $\beta = (2\pi/\lambda_0\sqrt{\varepsilon_{re}})$, and $R_r$ is the radiation resistance that can be calculated from the radiation pattern, more details can be found in Ref. 7. Using equation (3.4) we can calculate the impedance at center ($Z_m$) and then find $y_0$ by solving:

$Z = 50 = Z_m\cos^4(\pi y_0/L)$. Notice that the microstrip line is 50 Ω and its width is determined by the dielectric thickness ($h_p$) and dielectric constant ($\varepsilon_r$) of the substrate.

**Single patch experimental results**

Fig. 3.12(a) shows the photograph of the fabricated patch antenna attached to a microdisk modulator. The transmit antenna is identical to the receive antenna.

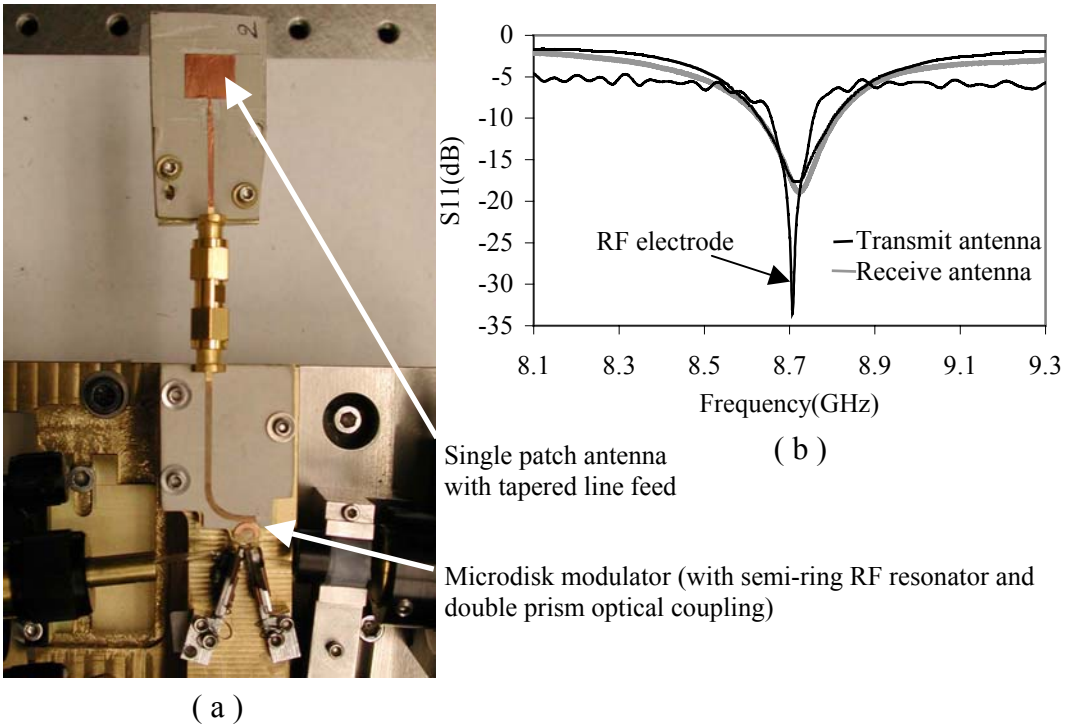


**Figure 3.12** (a) Photograph of the patch antenna (with tapered line feed) attached to microdisk modulator. (b) $S_{11}$ measurement results for receive and transmit patch antennas as well as the semi-ring resonator showing good resonant frequency matching. The antenna $Q$-factor is about 25 and the semi-ring $Q$-factor is about 70.

Since the optical FSR of the microdisk modulator is 8.7 GHz, the patch antenna resonant frequency ($f_r$) should also be 8.7 GHz. The patch antenna is fabricated on a substrate with a thickness of 0.508 mm and a dielectric constant of 2.94. Using equations 3.1-3.3 we can show that if $L$ = 10 mm the fundamental frequency of the patch is $f_r$ = 8.7 GHz. Although the width ($W$) of the patch has a miniscule effect on the resonant frequency, it affects the radiation pattern. In our design $W = L$ = 10 mm. First we use the tapered microsrtipline technique to feed the antenna. Fig. 3.12(b) shows the result of $S_{11}$ measurements for the receive antenna, transmit

antenna and the semi-ring resonator on top of microdisk. The resonant frequencies are very close (± 30 MHz) but the semi-ring has a larger $Q$.

Fig. 3.13(a) shows the same patch (same dimensions on the same substrate) but with inset line feed. Using Equation 3.4 the input impedance of the patch at the edge is $Z_m$ = 296 Ω. An inset distance ($y_0$) of 3 mm satisfies the equation 50 = $Z_m \cos^4(\pi y_0/L)$ and matches the input impedance to the 50 Ω line. Fig. 3.13(b) shows the $S_{11}$ measurement for this patch. As may be seen, the better match results in an increase in the coupling efficiency and $S_{11}$ is about 5 dB smaller at resonance.

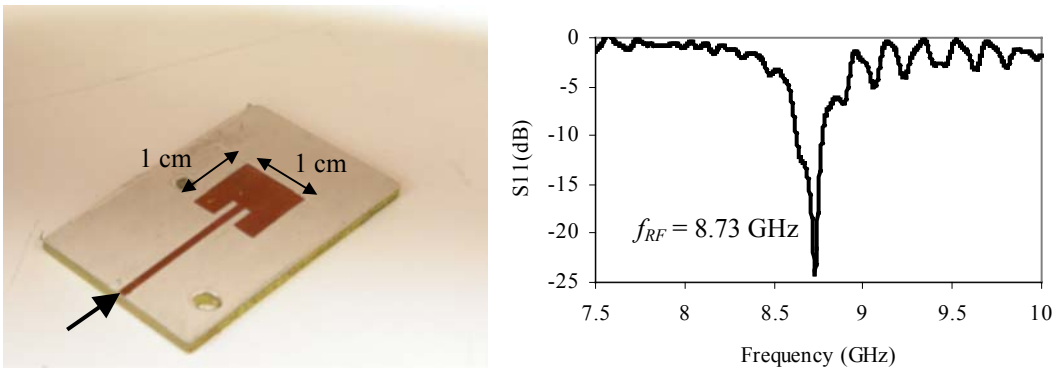


( a ) ( b )

**Figure 3.13** (a) Photograph of the single patch with inset line feed. (b) $S_{11}$ measurement result ( $Q$ = 26, $f_{RF}$ = 8.73 GHz)

### 3.4.2 Patch antenna array

As shown in Fig. 3.9, for θs within 0 - 90 degrees the radiation pattern of a single patch antenna is almost homogeneous and a large amount of the radiated

electromagnetic energy is not received by the receive antenna. If the location of the receiver is fixed for a long period of time it is reasonable to increase the efficiency of the wireless link by limiting the radiation direction so that the radiated power mainly travels toward the receive antenna. This can be achieved by employing directional antenna-arrays where the wireless gain is highly dependent on the direction. By tuning the relative phase of a series of patch antennas it is possible to eliminate the radiated power along undesired directions by means of destructive interference. It is evident that the degree of directionality is directly proportional to the number of patches employed in an array. In our first attempt we designed a four-patch antenna array. Each patch is similar to the one shown in Fig. 3.13. A microstrip power divider and phase shifter network feed the patches with the proper phase and power. Since the RF power is simultaneously distributed among all patches this feeding technique is called "corporate feeding". The patches on the left-hand side are rotated 180 degree relative to the patches on the other side, therefore the input voltage to the right side must have a $\pi$ phase shift so that all four dipoles oscillate synchronously. The spacing between the antennas is optimized for the best efficiency and directivity using CST electromagnetic simulation software [(4)]. Fig. 3.14(a) shows the photograph of the fabricated 4-patch antenna array with a resonant frequency of 8.7 GHz.

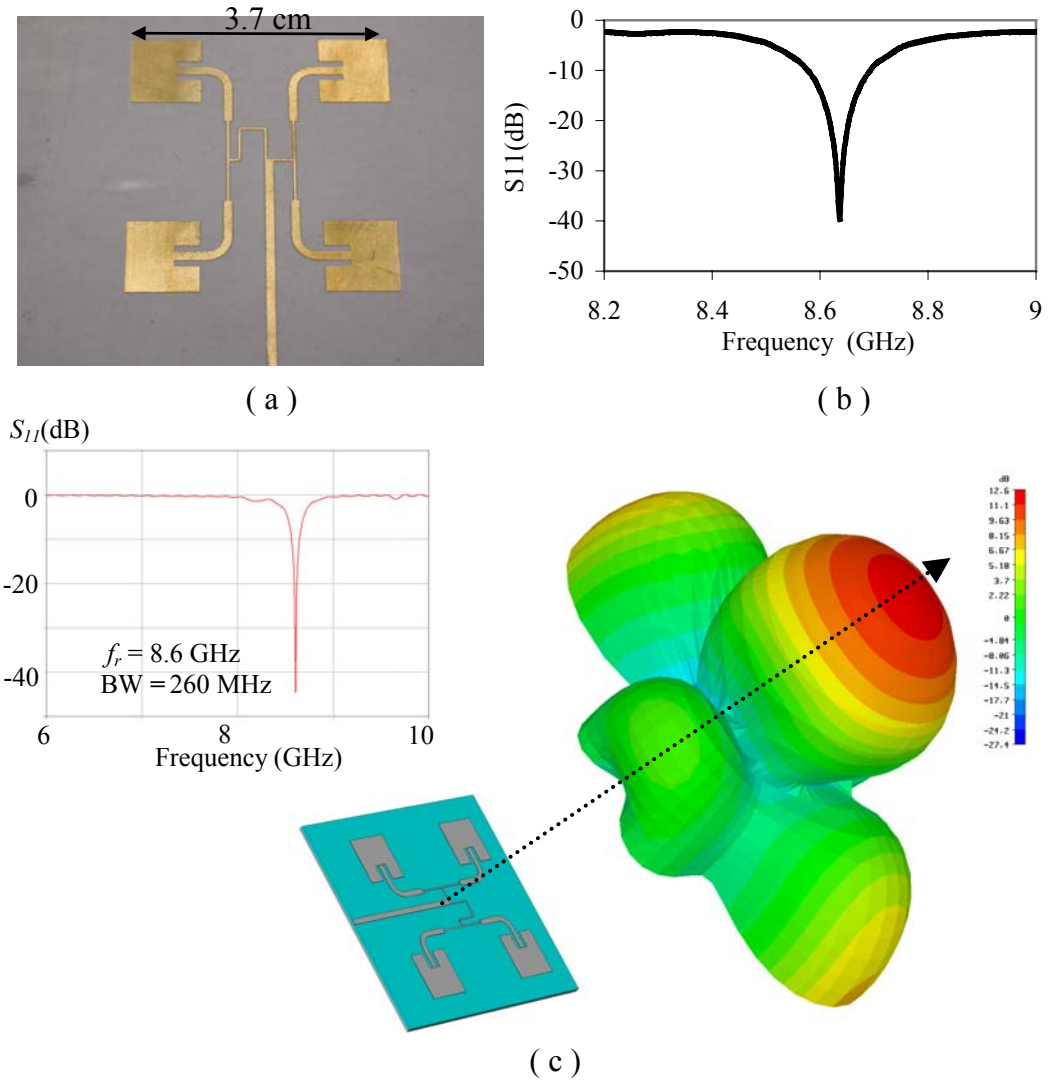


**Figure 3.14** (a) Photograph of the fabricated four-patch antenna array (made on a 0.508 mm thick dielectric substrate with ε = 2.94 and loss tangent = 0.00119). (b) $S_{11}$ measurement result showing a $Q$ of about 20 at 8.68 GHz resonant frequency. (c) Simulated $S_{11}$ and 3D radiation pattern of the four-patch antenna using CST electromagnetic simulation software.

The dielectric substrate has a thickness of 0.508 mm and a $\varepsilon_r$ of 2.94. Fig. 3.14(b) is the $S_{11}$ measurement result for this array. The antenna has a $Q$ of about 20. We have quantified the directivity and effective range of this antenna array by measuring the received RF power at different distances and directions using a similar patch antenna array for detection.

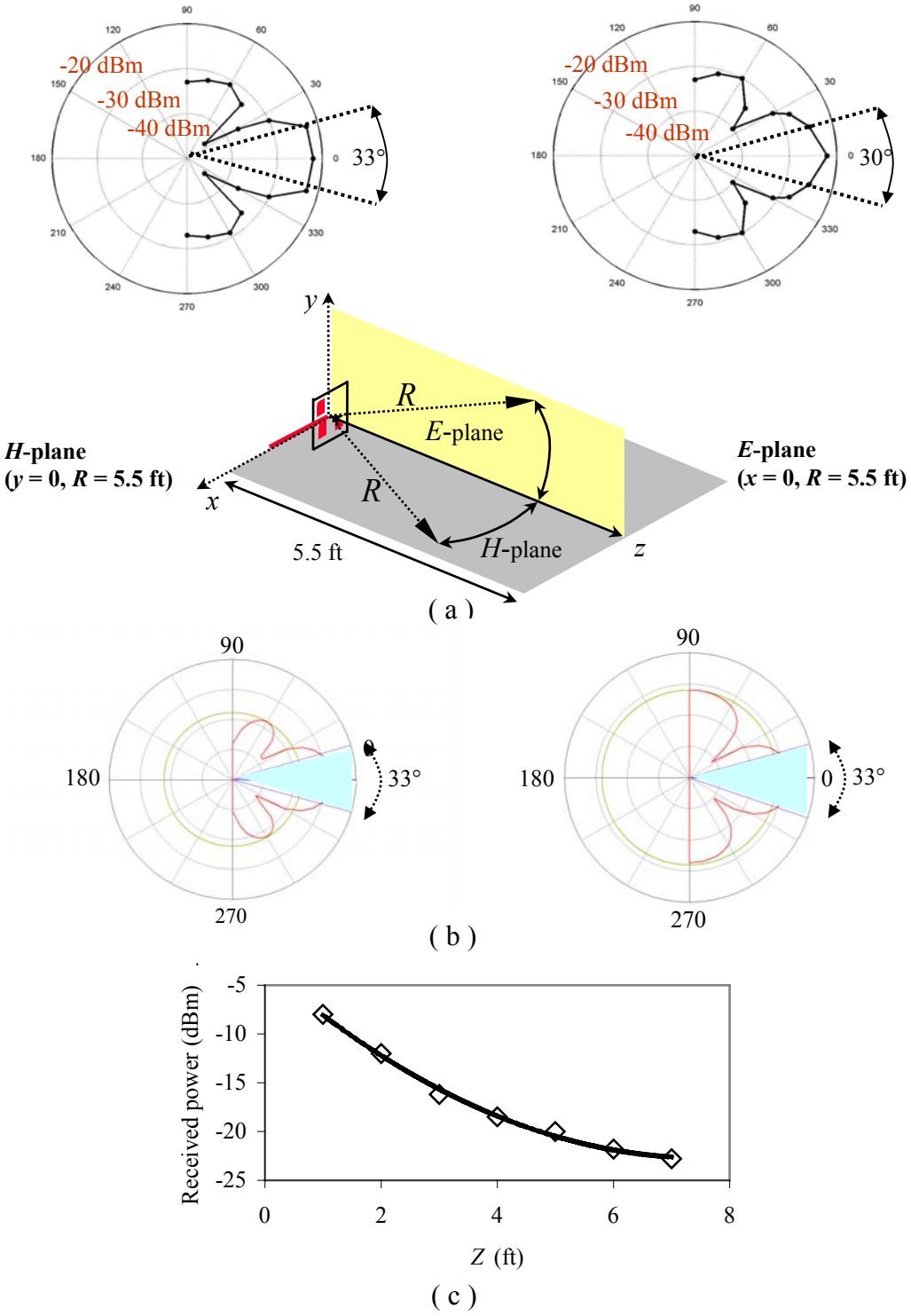


**Figure 3.15** (a) Measured radiation pattern of the 4-patch antenna array and the definition of radiation planes. (b) Simulated radiation pattern of the 4-patch antenna. (c) Received RF power as a function of the distance between receive and transmit antennae. The RF-power injected to the transmit antenna is 10 dBm and the radiation is measured along $z$-axis ($x = y = 0$).

Fig. 3.15(a) shows the measured and simulated radiation patterns of our 4-path antenna. The 3dB angular width in both planes (*E* and *H*) is about 30 degree. This corresponds to a directivity of about 36. The simulated and measured results are in very good agreement. Fig. 3.15(b) illustrates the measured received power against the distance between the transmitting and receiving antennae (*z*). The RF-power injected to the transmitting antenna is 10 dBm and the measurement is done along *z*-axis ($x = y = 0$).

As previously we mentioned, increasing the number of patches improves the directionality of the patch antenna array. In our second array design we have increased the number of patches to 10. The major difficulty with large numbers of patches is the complexity of the feeding network and the associated loss. The electromagnetic field of the feeding microstiplines can interfere with radiation fields and change the radiation pattern. In addition the power loss in the transmission lines reduces the power efficiency of the antenna. To reduce the loss and interference effects, we used a serial feeding technique to feed to the 10-patch antenna array. Fig. 3.16(a) is a photograph of a serially fed 10-patch antenna array. Fig 3.16 (b) is a schematic diagram of the antenna and simulated angular distribution of the radiated power for the main beam.

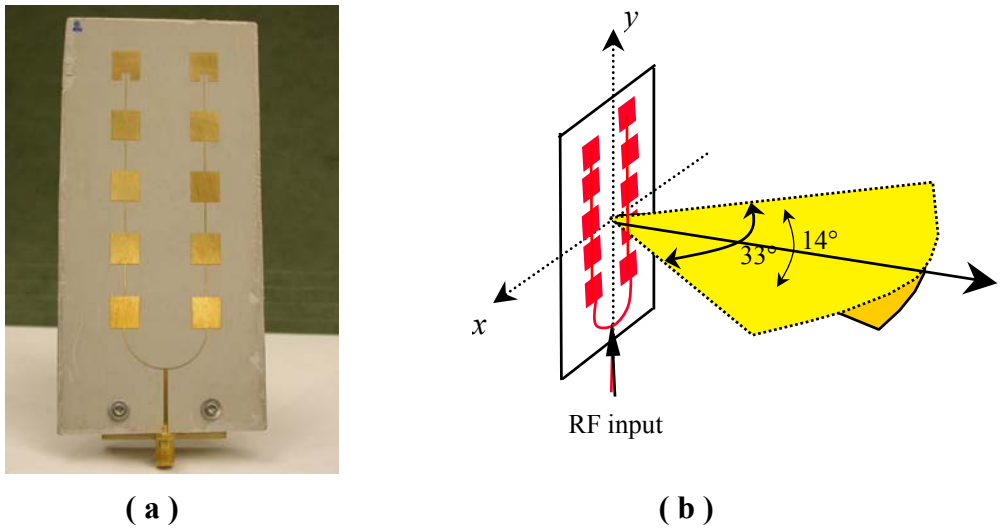


**Figure 3.16** (a) Photograph of a serially fed 10-patch antenna array. (b) Schematic diagram showing the simulated 3 dB angular width of the main radiation lobe.

Fig 3.17(a) illustrates the measured radiation pattern of the 10 patch antenna in the *E*-plane and *H*-plane. Fig 3.17(b) shows the measured RF power as a function of distance between the receive and transmit antennae when 10 dBm RF power is fed to the transmit antenna at resonant frequency.

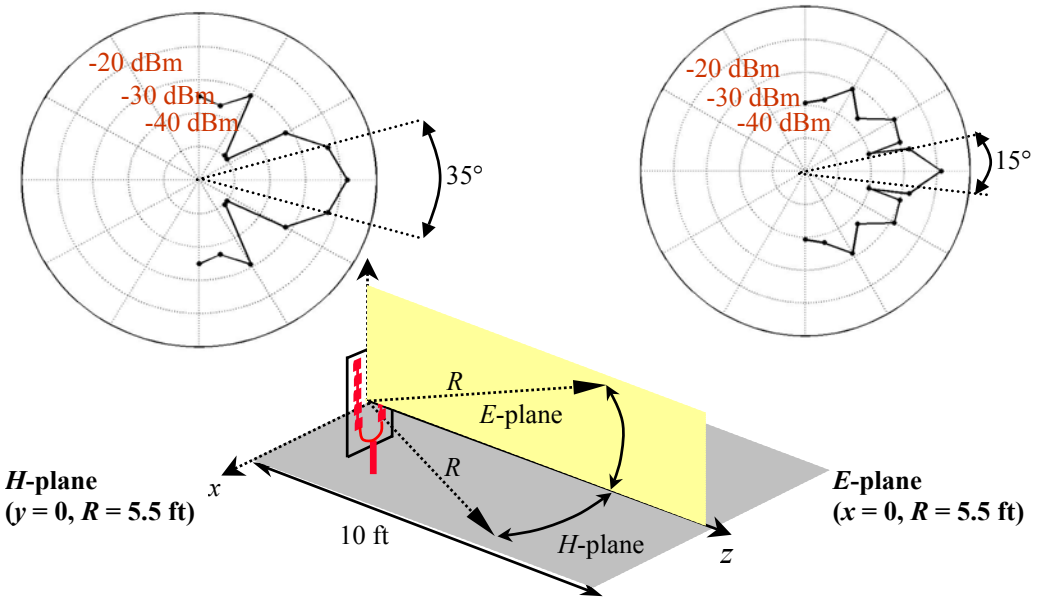


( a )

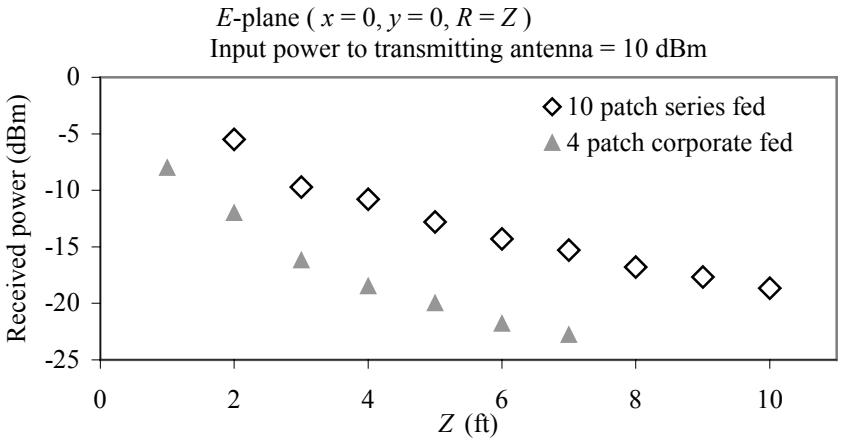


( b )

**Figure 3.17** (a) Measured radiation pattern of the 10-patch antenna array and the definition of radiation planes. (b) Received RF power as a function of the distance between receive and transmit antenna. The RF-power injected to the transmit antenna is 10 dBm and the radiation is measured along $z$-axis ($x = y = 0$).

We have also fabricated 4 and 10 patch antenna arrays with resonant frequencies around 15 GHz for the 3 mm diameter microdisk modulators.

## 3.5 Wireless video data and video transmission

Using the patch antenna and patch antenna arrays we have demonstrated the first wireless RF-optical link based on microdisk modulator. Fig. 3.18 shows the schematic and photograph of the experimental arrangement. In this experiment we have employed the single patch antenna shown in Fig. 3.12. Due to the low efficiency of the single patch, the distance between the transmit and receive antenna is about 7 inch. This experiment is a proof of principle experiment demonstrating the potential of combining the patch antenna with a microdisk modulator in a wireless optical receiver.

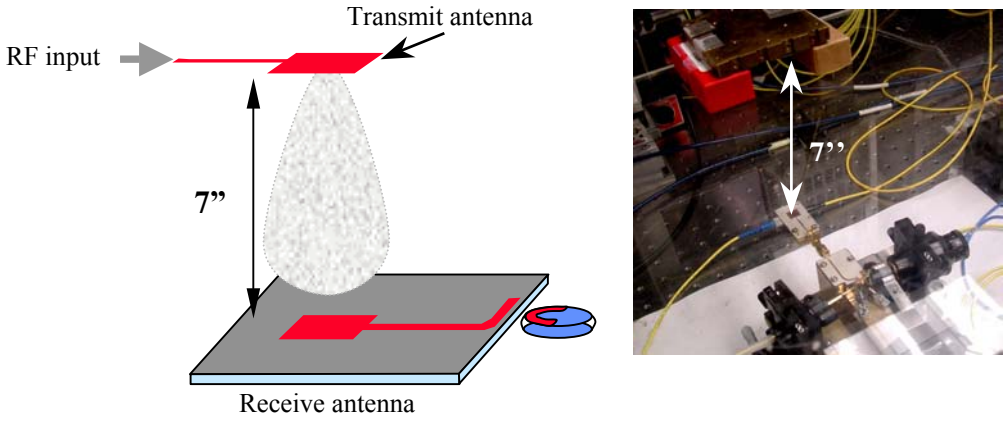


**Figure 3.18** Schematic diagram and photograph of the short wireless-optical link based on single patch and microdisk modulator.

Data and video were successfully transmitted through this wireless link though the quality was inferior to the wired link.

Fig. 3.19 (a) shows the BER measurement results at 10 Mb/s (NRZ $2^7$ - 1 PRBS) as a function of injected RF-power to the transmit antenna and Fig. 3.19(b) shows the measured eye-diagram when 18 dBm RF power is fed to the transmit antenna.

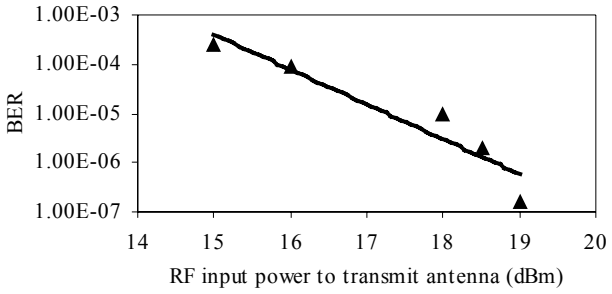


( a )

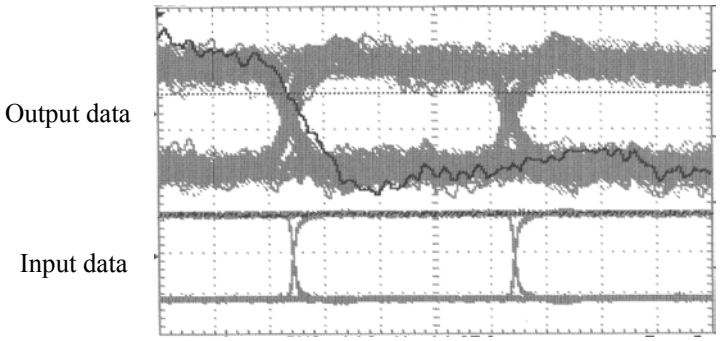


( b )

**Figure 3.19** (a) shows the BER measurement results at 10 Mb/s (NRZ $2^7$ - 1 PRBS) as a function of injected RF-power to the transmit antenna. (b) The measured eye-diagram at 18 dBm RF input power.

Fig. 3.20(a) is a schematic diagram of the wireless optical link with a 4-patch antenna. This link has been successfully tested for wireless data and video transmission over 7 ft. Fig. 3.20(b) presents the results of BER measurement, at 10 Mb/s (NRZ $2^7$ - 1 PRBS), as a function of link length.

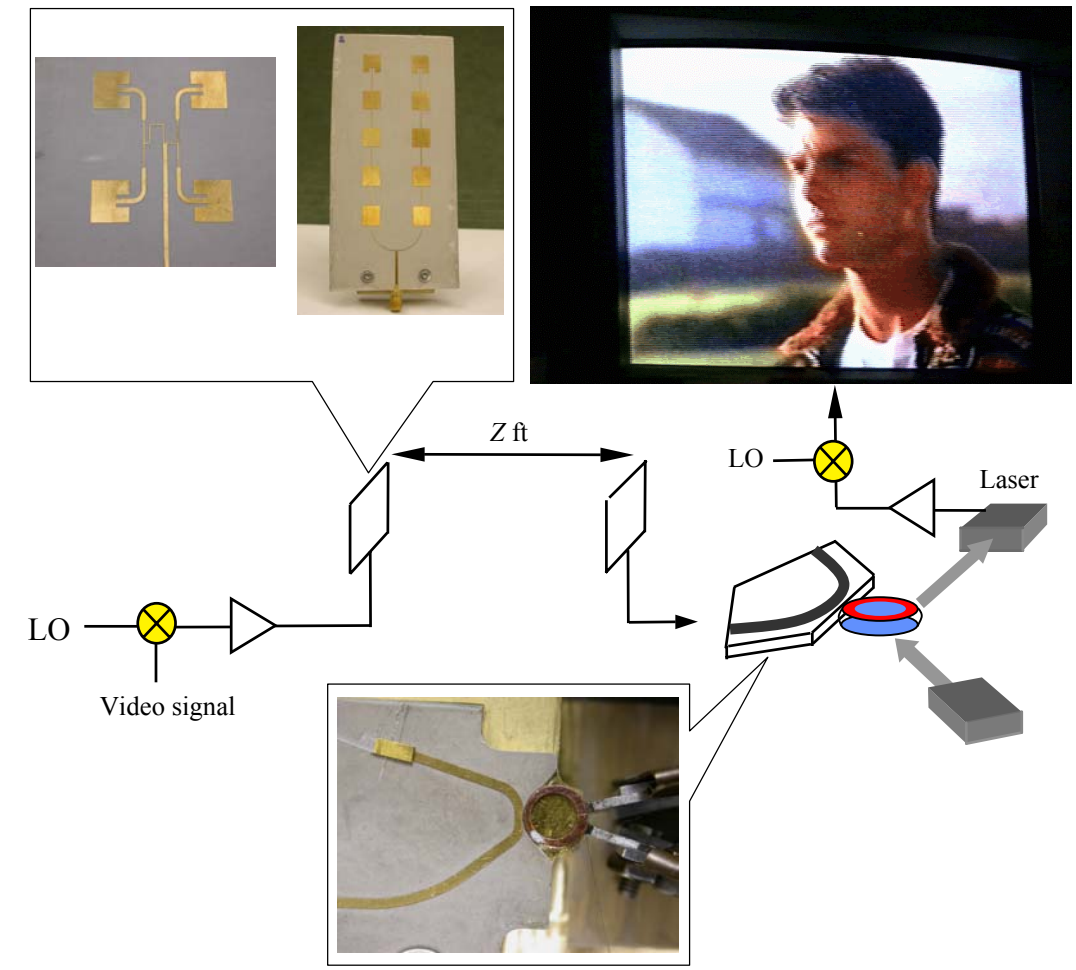


( a )

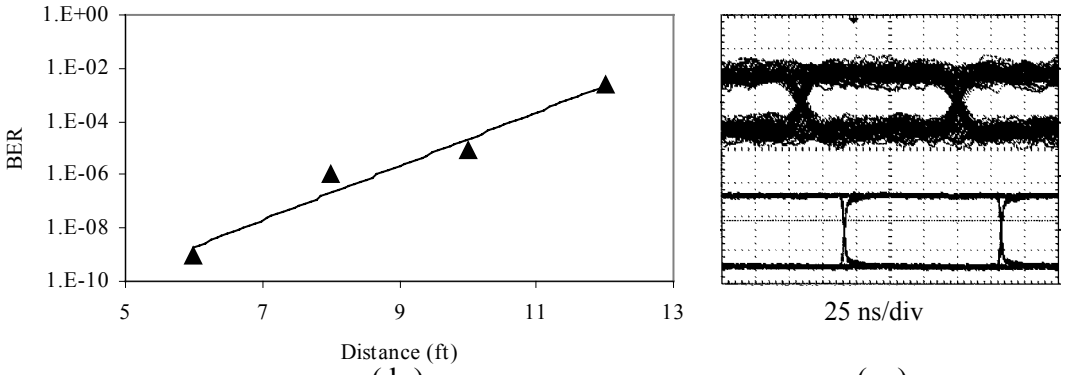


( b ) ( c )

**Figure 3.20** (a) Wireless RF-optical link using patch antenna arrays and the microdisk modulator. (b) The measured BER (at 10 Mb/s NRZ $2^7$ - 1 PRBS) as a function of the distance between two antenna (received optical power = 100 μW, injected RF power to the transmit antenna = 1W). (c) The measured eye-diagram at $z$ =10 ft. The average optical output power is about 30 μW.

Fig. 3.20(c) shows the measured eye-diagram at 10 ft. Using the patch antenna arrays we demonstrated wireless RF-optical links up to 12 ft.

## 3.6 Noise analysis

Noise in the RF-optical receiver is usually ascribed to either optical or electrical sources. The optical sources are laser relative intensity noise (RIN) and detector noise (thermal and shot noise). The electrical sources are the microstripline, RF-resonator, and amplification stages used after photodetection. Fig. 3.21(a) shows a schematic diagram of signal and noise flow in the wireless RF-optical receiver. The signal-to-noise value at each stage is calculated using standard noise equations of RF and optical devices that can be found in references 11-14. Fig. 3.21(b) presents the typical values of parameters that are required for calculating the overall signal-to-noise ratio of the RF-optical receiver, the same values as used in our simulations. After calculating the final signal-to-noise ratio, $S_d/N_d$, the equivalent BER is calculated using [12]:

$$P(e) = \frac{1}{2} erfc\left(\frac{\left(S/N\right)^{1/2}}{2\sqrt{2}}\right) \tag{3.5}$$

where $S/N = \frac{i_{sig}^2}{\overline{i_N^2}}$ is the analog signal-to-noise ratio, *P(e)* is the digital error probability and *erfc* is the complementary error function. Fig. 3.21(c) is a plot of BER against signal-to-noise ratio. We use BER and sensitivity as a measure of link performance. Our simulations show that critical parameters strongly influencing

BER are optical *Q*-factor, disk thickness, RF resonator voltage gain, and optical input amplitude fluctuations (laser RIN). The noise performance of the microdisk modulator is calculated based on the simple model explained in section 2.6.1.

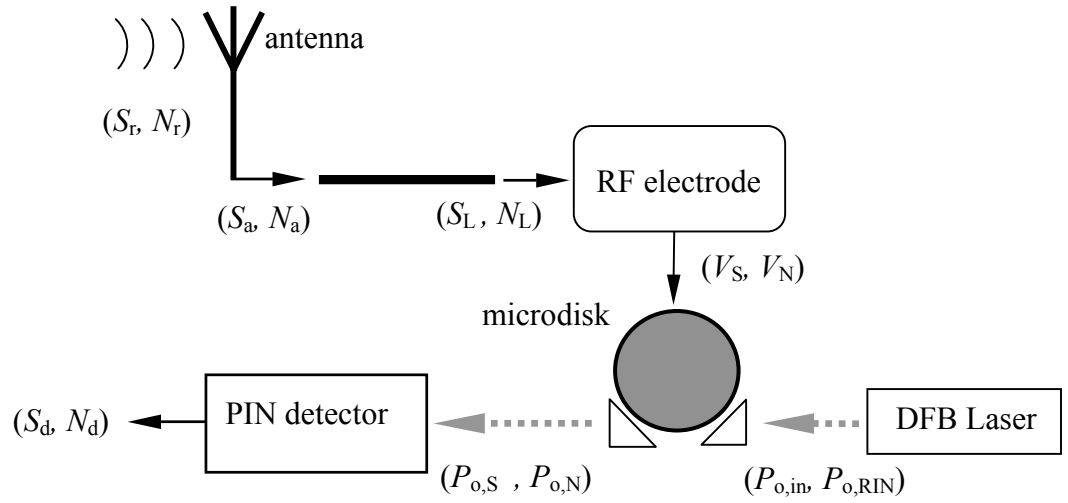


( a )

General assumptions
RIN ~ -155 *dB/Hz*
Laser output = 5 *mW*
Detector bandwidth = 100 *MHz*
Stabilized laser linewidth = 10 *kHz*
Antenna impedance ~ 50Ω
Detector *R* ~ 10 *k*Ω
Detector responsivity = 0.8 A/W
Detector amplifier noise figure = 3
Temperature = 300K
Antenna background temperature = 200K
Detector dark current = 10 nA

( b )

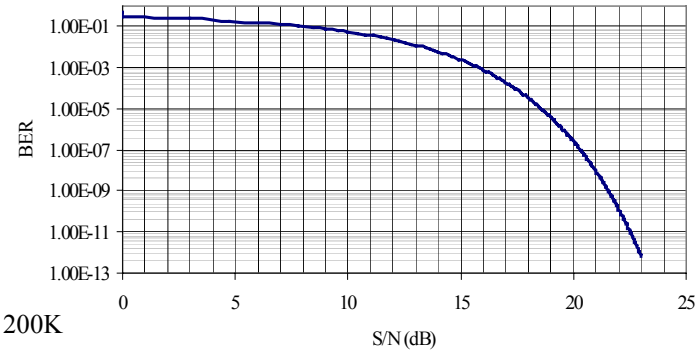


( c )

**Figure 3.21** (a) Schematic diagram of signal and noise flow in microdisk RF-wireless receiver. (b) Values of parameters required for noise calculation. (c) BER against signal-to- noise ratio [15]

As shown in Fig. 3.21(a), the received signal ($S_a$) and noise ($N_a$) power are fed to an open terminated microstripline. The signal ($S_L$) and the noise power ($N_L$) at the

coupling location (where the microstripline is coupled to the ring resonator) are related to the input values through:

$$\text{(a) } S_L = S_a/L_T \qquad \text{(b) } N_L = N_a/L_T + k_B TB(L_T\text{-}1) \tag{3.6}$$

where $L_T$ is the loss factor for the mictorstripline, $k_B$ is the Boltzman factor, and $B$ is the bandwidth. The bandwidth of the receiver is defined by the optical modulation bandwidth, which is limited by optical $Q$ ($BW \sim \nu_{laser}/Q$). The signal and noise power change throughout the microstripline due to attenuation and the thermal noise in the microstrip. Therefore the voltage amplitude of the signal and noise voltage at the coupling zone can be written as:

$$\text{(a) } V_S = 2\sqrt{2 Z_o S_L} \qquad \text{(b) } V_N = 2\sqrt{2 Z_o N_L} \tag{3.7}$$

when $Z_o$ is the characteristic impedance of the line (50 ohm). Now we can use equation (2.41) from chapter 2 to calculate the signal and noise optical power coming out of the microdisk modulator by replacing $V_{in}$ with $V_s$ and $V_N$.

$$\text{(a) } P_{o,s} = 2\beta_s \Delta\lambda_{DC} G_v (Q / \lambda_{res}) V_S \times P_{o,max}$$

$$\text{(b) } P_{o,n} = 2\beta_s \Delta\lambda_{DC} G_v (Q / \lambda_{res}) V_N \times P_{o,max} \tag{3.8}$$

If we define the optical coupling efficiency for an optical mode as $\rho = P_{o,max} / P_{o,in}$ and the electro-optical gain as $G_{EO} = 2\rho\beta_s \Delta\lambda_{DC} G_v (Q / \lambda_{res})$ :

$$\text{(a) } P_{o,s} = G_{EO} \times V_S \times P_{o,in}$$

$$\text{(b) } P_{o,n} = G_{EO} \times V_N \times P_{o,in} \tag{3.9}$$

Equations 3.9(a) and 39(b) are the signal and noise optical powers. The electro-optical gain factor ($G_{EO}$) relates the modulated optical power to the RF input voltage and input optical power. Equation 3.9(b) is not complete because the laser input

power $P_{o,in}$ has random intensity noise that contributes to the total optical power noise. The random intensity noise power can be written as:

$$P_{o,RIN} = (10^{RIN/10} \times \Delta f)^{\frac{1}{2}} P_{o,out} \tag{3.10}$$

where *RIN* is the random intensity noise (dB/Hz) and $\Delta f$ is the equivalent noise bandwidth. $P_{o,out}$ is the optical output power from the microdisk modulator at $\lambda_{laser}$. Since in most cases $P_{o,out}$ is close to $P_{o,max}$ for simplicity we assume $P_{o,out} = \rho P_{o,in}$, so the total optical noise power is:

$$P_{o,N} = [G_{EO} \times V_N + \rho (10^{RIN/10} \times \Delta f)^{\frac{1}{2}}] P_{o,in} \tag{3.11}$$

Now we should calculate the signal and noise after photodetection. The photocurrent is related to optical power through the detector responsivity ($R$) so:

$$\text{(a)} \quad \bar{i}_{OS}^2 = RP_{o,S} \qquad \text{(b)} \quad \bar{i}_{ON}^2 = RP_{o,N} \tag{3.12}$$

These are the photocurrents generated by the optical signal and noise power but there is also noise generated during the detection (shot noise and dark current noise) and the amplification process:

$$\bar{i}_N^2 = 2eB(i_p + i_d) + \frac{4k_b TBF_n}{R_L} \tag{3.13}$$

where $i_d$ is the photodetector dark current, $F$ is the amplifier noise figure, $R_L$ is the load resistance and $i_p$ is the total photocurrent generated by the received optical power. The total received optical power consists of the modulated optical power and the DC optical power that is not modulated so $i_p = R(P_{o,dc} + P_{o,S})$. The average received DC optical power ($P_{o,dc}$) may be written as $P_{o,out} - P_{o,S}/2$ . The final signal to noise ratio is calculated using equations (3.12) and (3.13):

$$\frac{S_d}{N_d} = \frac{\bar{i}_{ON}^2}{\bar{i}_N^2 + \bar{i}_{ON}^2} \tag{3.14}$$

Fig. 3.22 shows simulation results for a RF-optical-link with direct detection. The BER is calculated as a function of RF input power for different optical *Q*-factors, disk thickness, and voltage gain, $G_v$. In all cases the assumptions are 5.13 mm disk diameter, RIN = -150 dB/Hz, 15% optical coupling efficiency, 5 mW optical input power, 0.8 A/W detector responsivity, 10 nA detector dark current, 300 K temperature, 10 kΩ detector impedance, and a 3 dB detector amplifier noise-figure. Sensitivity is defined as the RF-power at which the signal-to-noise ratio is unity (SNR = 1). In Fig. 3.22(a) the effect of optical *Q*-factor on BER performance is demonstrated for $h = 400$ μm and $G_v = 2$. As may be seen, increasing optical *Q* by a factor of two improves sensitivity by a factor of eight. Fig. 3.22(b) shows the effect of reducing the disk thickness for $G_v = 2$ and $Q = 1.5 \times 10^6$. In more advanced simulations $G_v$ may be calculated as a function of RF coupling factor, the geometry of the resonator and input RF power. Fig. 3.22(c) shows the effect of increasing $G_v$ on BER performance for $Q = 1.5 \times 10^6$ and $h = 400$ μm.

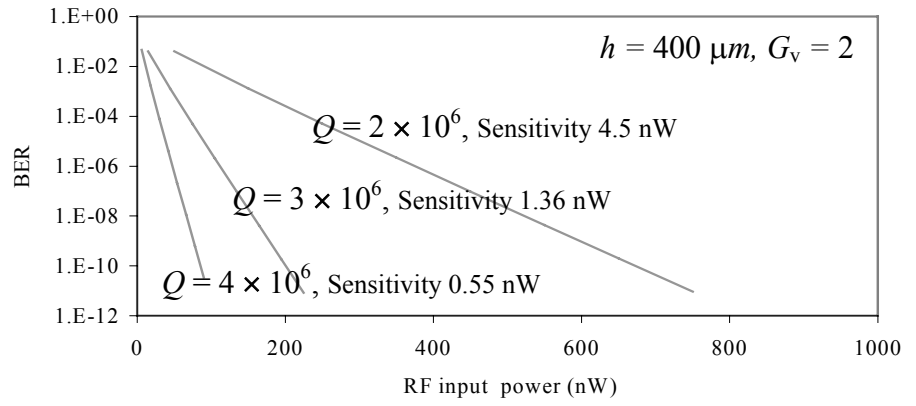


( a )

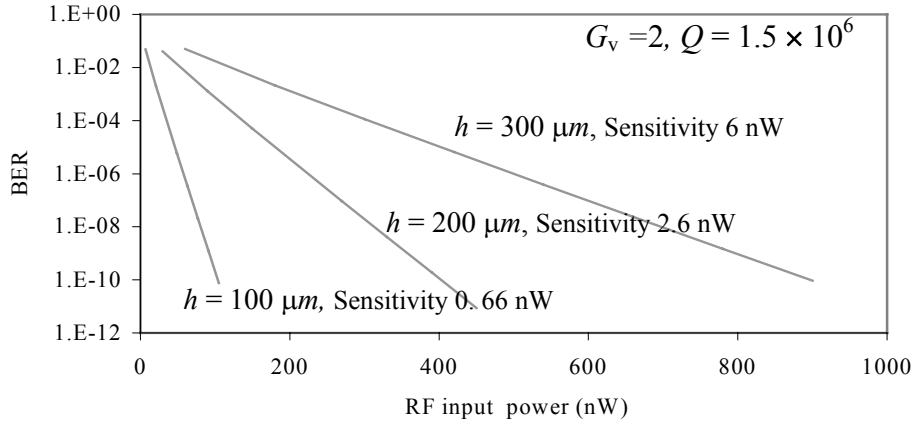


( b )

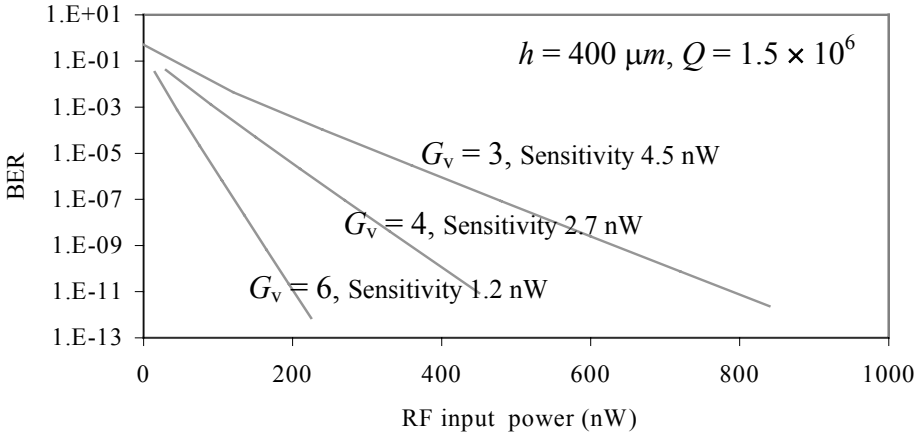


( c )

**Figure 3.22** BER calculations as a function of RF input power for different optical *Q*-factors, disk thicknesses, and voltage gain factor. In all cases optical coupling efficiency (ρ) is 15%, RIN is -150 dB/Hz, optical input power is 5 mW, detector responsivity is 0.8 A/W, detector dark current is 10 nA, temperature is 300 K, detector impedance is 10 kΩ and detector amplifier noise-figure is 3 dB. The sensitivity is defined as the RF-power at which the SNR is unity. (a) Effect of optical *Q*-factor on BER performance. (b) Effect of disk thickness on BER performance. (c) Effect of RF resonator voltage gain factor on BER performance

Calculations show nW sensitivity may be achieved by simply reducing disk thickness, increasing RF-resonator voltage gain, and reducing laser RIN. Fig. 3.23 (a) illustrates how laser RIN can influence BER. In this case $G_v = 6$, $h = 200$ μm and $Q = 2 \times 10^6$. With a value of RIN = –140 dB/Hz and $G_v = 6$ it is possible to achieve a BER around $10^{-10}$ with 200 nW RF input power.

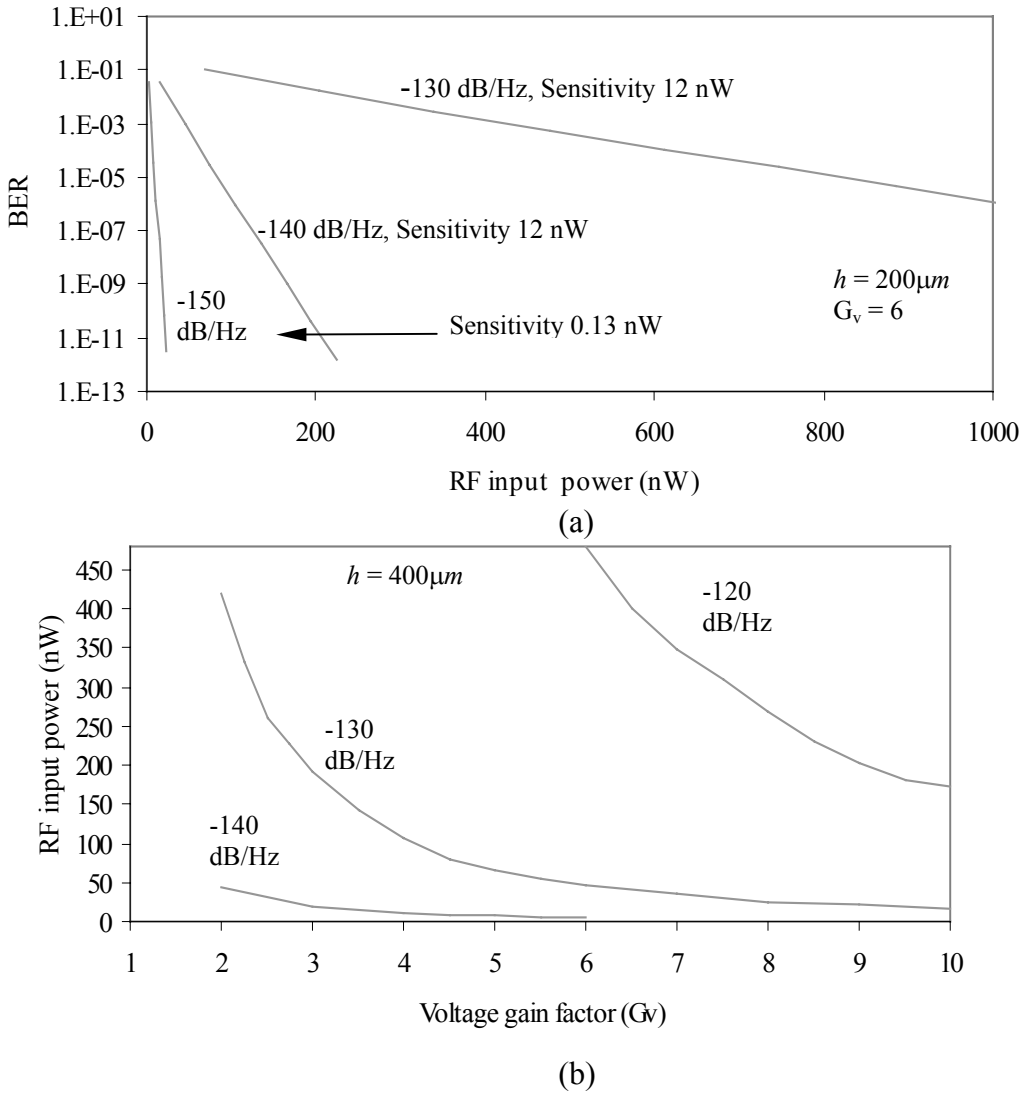


**Figure 3.23** Calculated influence of laser RIN on BER and sensitivity ($Q = 2 \times 10^6$ and other parameters are the same as in Fig. 15). (a) BER performance with different values of RIN as a function of RF input power. (b) Sensitivity with different values of RIN as a function of $G_v$.

Fig. 3.23(b) shows that the impact on the sensitivity of noise generated by laser RIN can be reduced by increasing voltage gain $G_v$ in the system. The results shown in Fig. 3.23(b) are obtained using $h = 400$ μm and $Q = 2 \times 10^6$. Increasing voltage gain by a factor of five can be equivalent to reducing RIN by 10 dB/Hz.

## 3.7 Summary

In this chapter the performance of the microdisk modulator in wired and wireless RF-optical links has been demonstrated. The experimental results show that a microdisk modulator can provide high-quality modulation up to 100 Mb/s in a RF-optical subcarrier link with an 8.7 GHz RF-carrier frequency. The modulator is able to efficiently modulate an optical carrier at $\lambda = 1550$ nm wavelength with a data modulated RF signal. By tuning the laser wavelength to a high-$Q$ optical mode 10 Mb/s NRZ $2^7 - 1$ PRBS, data was successfully transmitted through a RF fiber-optic link with a measured BER of less than $10^{-9}$.

We have shown that the microdisk modulator can directly receive signal from planar antennas. The preliminary results with home made patch antenna arrays demonstrate the potential of employing the microdisk modulator in short distance indoor wireless links. Furthermore the results of noise analysis show the impact of different link and modulator parameters on the overall signal-to-noise performance and hence BER of

the wireless RF-optical link. By optimizing these critical parameters, microdisk based optical receivers with nW sensitivity are feasible.

## 3.8 References


[1] J. Oreilly and P. Lane, "Remote delivery of video services using mm-waves and optics," *IEEE journal of lightwave technol*., vol 12, no 2, pp. 369-375, Feb. 1994.

[2] Hirata, M. Harada, K. Sato, and T. Nagtsuma, "Millimeter-wave photonic wireless link using low-cost generation and modulation techniques," *Microwave photonics international meeting*, pp. 37-40, 2002.

[3] H. Ogava, D. Polifko, and S. Banba, "Millimeter-wave fiber optic systems for personal radio communication," *IEEE Trans. on microwave theory and techniques*, vol. 40, no. 12, pp. 2285-2293 Dec. 1992

[4] D. Novak, G. H. smith, C. Lim, H. F. Liu, R. B. Waterhouse, "Optically fed millimeter-wave wireless communication," *OFC '98* technical digest, pp. 14.

[5] G. H. Smith, D. Novak, C. Lim, "A millimeter-wave full-duplex WDM/SCM fiber-radio access network," *OFC* technical digest, pp. 18.

[6] J-F Zurcher and F. E. Gadiol, "Broadband patch antennas".

[7] P. Bhartin, K. V. S. Rao, and R. S. Tomar, "Millimeter-wave microstrip and printed circuit antennas"

[8] W. S. T. Rowe and R. B. Waterhouse, "Efficient wide band printed antennas on lithium Niobate for OEICS," *IEEE trans. on antennas and Propagation*, vol. 51, no.6, pp. 1413-1415, June 2003.

[9] L. I. Basilio, M. A. Khayat, J. T. Williams, and S. A. Long, "The dependence of the input impedance on feed position of probe and microstrip line-fed patch antennas," *IEEE trans. on Antenna and propagation*, vol. 49, no. 1, pp. 45-47, Jan. 2001

[10] J. Bahl and P. Bhartia "Microstrip antennas," 1980.

[11] G. P. Agrawal, "Fiber-optic communication systems," 1997.

[12] J. M. Senior, "optical fiber communications principles and practice," Prentice-Hall series in optoelectronics, 1985.

[13] D. M. Pozar, “Microwave and RF design of wireless systems,” John Wiley and Sons, Inc. 2001

[14] L. Kazovsky, S. Benedetto, A. Willner, “Optical fiber communication systems,” Artech house publishers, 1996.

---

## Technical notes

(1) Double balanced RF mixer from *Pulsar Microwave Co.*
LO/RF 0.5- 10 GHz
IF DC-2 GHz

(2) RF amplifier manufactured by *JCA*
Frequency range: 4-8 GHz
Gain: 30 dB
Noise figure: 1.9 dB

(3) High-speed OE converter with a responsivity of 300 V/W and a bandwidth of 15 GHz. (*Agilent* 11982A)

(4) Power amplifier manufactured by *Sonoma Instruments.*
Frequency rang: 10 KHz-2.5 GHz
Gain: 20 dB

(5) CST MICROWAVE STUDIO: electromagnetic field simulation software based on FTDT, from *Computer Simulation Technology*.

# Chapter 4

# Photonic RF receiver

## 4.1 Introduction

In chapter 3 the performance of the microdisk modulator in intensity modulation direct detection (IM-DD) RF optical links was has been investigated to demonstrate the potential of employing it in RF sub-carrier fiber optic links such as LANs or fiber-feed back bone networks (section 1.1.2 and 1.1.3). In these applications, the microdisk performs linear optical intensity modulation similar to a conventional Mach-Zehnder (MZ) modulator but in a smaller volume and with less power consumption. On the receiver side, after converting the optical intensity modulation to an electric signal frequency mixing with a local oscillator in a RF mixer is used to down-convert the baseband information (video or data) from the received RF signal similar to a conventional homodyne RF receiver.

In this chapter we investigate the possibility of using the microdisk in a novel photonic RF receiver architecture without using high-speed electronic circuitry.

One of the key operations in microwave communication is frequency mixing. Several techniques have been proposed for RF mixing in the optical domain such as

nonlinear modulation in a Mach-Zehnder modulator [1-3] and nonlinear detection in a photodiode [4-6].

After a brief review of the conventional nonlinear photodetection method, we will introduce an alternative technique for self-mixing that is based on optical filtering prior to photodetection. Nonlinear optical modulation is the next technique described as a more efficient alternative to nonlinear photodetection. Previously this technique has been used in a photonic heterodyne receiver where the MZ-modulator was used as a photonic RF mixer to mix the local oscillator and the received signal [2].

Here we show that by utilizing transmitted carrier RF format combined with optical filtering prior to detection or nonlinear modulation in the modulator it is possible to down-convert the baseband signal without using a local oscillator, a RF mixer or any high speed electronic or optoelectronic devices.

## 4.2 Nonlinear photodetection

A photodiode is effectively a square-law detector for the optical $E$-field ($i_p \propto P_o \propto E^2$). Linear photodetection, used in conventional AM-DD optical links, is basically mixing the 194 THz ($\lambda$ = 1550 nm) optical carrier with the side bands 194THz $\pm \Delta\nu_b$ MHz ($\Delta\nu_b$: baseband signal) to generate the baseband photocurrent. In RF sub-carrier optical links, since the baseband signal is replaced with a data modulated RF

carrier, the photodetector output needs to be mixed with a local oscillator in order to extract the baseband data. If the photodiode operates in the nonlinear regime where $i_p \propto P_o^2$, it can function as an optical RF mixer similar to a conventional electronic diode mixer. The bias voltage on the photodiode may be used as the third terminal to mix the RF signal with a local oscillator in the optical domain. This technique has been employed in several photonic RF mixer designs for receiver and transmitter applications [4-6]. By using the transmitted RF carrier modulation format it may be possible to use this technique for passive down-conversion in RF subcarrier microwave-optical links.

**Physics of nonlinearities in photodiode**

Recently there has been an increasing amount of work concerning the nonlinearities in photodetectors (PD's) because it can be an important limiting factor in high-fidelity analog and digital communication systems [7]. The nonlinearities in PD's have been measured and modeled by numerical solutions of coupled differential equations governing the flow of carriers and distribution of the electric field along the PD.

The main nonlinear mechanisms have been identified as: (a) Space-charge fields that change the electron velocity and the diffusion constants (b) PD potential drop from current flow in the external load resistance which lowers the internal electric field. (c) Carrier trapping effect and (d) The current flow in the p-contacts [7-11]. So far all efforts have been concentrated on improving the PD design to reduce

nonlinearities in the photodetection especially at larger photocurrents. Operation at large photocurrent is desired because it increases the dynamic range and reduces the loss and noise figure in externally-modulated links [7].

Conversely for photonic RF mixing applications the question is 'How can we modify the design of a regular p-i-n photodiode to enhance the second-order nonlinearities?' The answer to this question requires a deep understanding of the physics of nonlinearities in a p-i-n photodiode. This subject has been briefly discussed in Appendix (A). We can understand the basic mechanism behind nonlinear photodetection by focusing on nonlinearity generated by the space-charge effect. The photocurrent density can be estimated as: $J_{photo} = e \times n_{photo} \times v_e$ ($e$: electron charge, $n_{photo}$: photo-generated electron density, $v_e$: electron velocity). In a standard configuration, where highly linear operation is desired, the photodiode is reverse biased in such a way that electron velocities are saturated and therefore $v$ is not a function of $n_{photo}$. By decreasing the reverse bias voltage below the threshold required for carrier velocity saturation, $v$ becomes a function of $n_{photo}$. Knowing $n_{photo}$ is proportional to incident optical power ($P_o$) and assuming $v(n_{photo}) \propto n_{photo}$ then $J_{photo} \propto P_o^2$. Experimentally it has been demonstrated that changing the reverse bias voltage from 8 Volt to 1 Volt increases the detected second-harmonic power by 20 dB [7]. Through the same mechanism second-harmonic nonlinearity increases by increasing the optical power incident to photodiode. So low-bias voltage and high photocurrent seem to be the trivial answer to our question. For a conventional p-i-n diode (the one used in [7]) at its best bias point and modulation frequency (5 GHz),

the second-harmonic power is 24.5 dB below the fundamental power, and is thus very inefficient for real applications. However the large magnitude of the linearly modulated photocurrent at RF frequencies doesn't interfere with the minuscule baseband photocurrent and can be filtered out using a low pass filter. This may result in an acceptable signal-to-noise ratio for certain applications. Ideally we need a specialized design for strengthening the nonlinear behavior.

## 4.3 Down-conversion through optical filtering

In this section we demonstrate that by tailoring the optical spectrum after modulation and prior to detection it is possible to extract the baseband information from the RF signal using only a slow-photodiode operating in the linear regime.

### 4.3.1 Introduction

Let's assume the baseband signal is a pure sinusoidal signal so the received RF voltage is written as:

$$V_{RF} = V_0\left(1 + m_I \cos(\omega_b t)\right)\cos(\omega_{RF} t) \tag{4.1}$$

where $\omega_b$ is the baseband frequency, $\omega_{RF}$ is the RF carrier frequency, $m_I$ is the RF modulation index and $V_0$ is the RF voltage amplitude. If this signal modulates the optical carrier ($\omega_{opt}$: THz regime), then the optical electric field will have the form:

$$E_{opt}(t) = E_0\left[1 + M\left(1 + m_I \cos(\omega_b t)\right)\cos(\omega_{RF} t)\right]\cos(\omega_{opt} t) \qquad (4.2)$$

where $E_0$ is the amplitude of the optical carrier and $M$ is the optical modulation index. Fig. 4.1 shows the frequency spectrum of the optical signal. In the frequency domain the optical modulation process adds two sidebands to the optical carrier where each sideband is a baseband modulated RF carrier. We call these *RF-optical* sidebands because they are RF signals up-converted to optical frequencies.

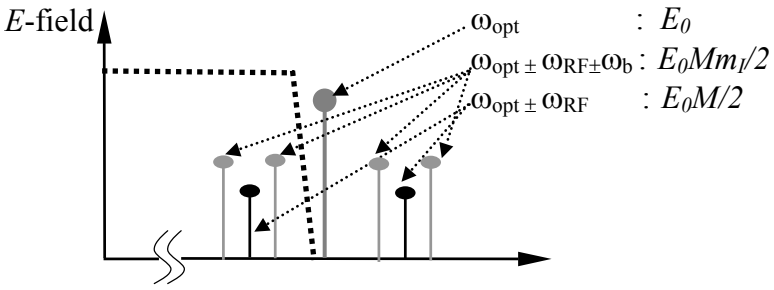


**Figure 4.1** Schematic diagram of the frequency spectrum of an optical carrier modulated with an RF signal. The RF signal is an RF sub-carrier modulated by a single-tone baseband. The amplitude of each frequency component is written as a function of optical *E*-field and the modulation indexes.

By expanding equation (4.2) we can calculate the amplitude of each frequency component as shown in Fig. 4.1. The amplitude of the RF sub-carrier (black lines) and up-converted baseband components (light gray lines) is determined by RF and optical modulation indices. If the optical carrier and the upper RF-optical sideband are filtered out the modified optical *E*-field can be written as:

$$E'_{opt}(t) = \mathrm{Re}\frac{ME_0}{2}\left[\frac{m_I}{2}\left(e^{i(\omega_{opt}-\omega_{RF}-\omega_b)} + e^{i(\omega_{opt}-\omega_{RF}+\omega_b)}\right) + e^{i(\omega_{opt}-\omega_{RF})}\right] \qquad (4.3)$$

This can be easily done using a band-pass optical filter with proper band width and role-off.

Using equation (4.3) we can calculate the spectrum of the modified optical intensity $I(t)$:

$$I(t) = \left|E'_{opt}(t)\right|^2 = \frac{M^2 E_0^{\,2}}{4}\left[1 + \frac{m_I^2}{2} + 2m_I \cos(\omega_b t) + \frac{m_I^2}{2}\cos(2\omega_b t)\right] \qquad (4.4)$$

The optical intensity spectrum consists of a DC component, the baseband frequency and its second-harmonic. So if we use a photodetector we can generate the baseband current and its second-harmonic.

Notice that using this approach we can extract the baseband information from the RF signal by means of *linear* optical modulation, optical filtering and *linear* photodetection. Also the speed of the photodetector is determined by the bandwidth of the baseband signal and not the RF carrier.

Fig. 4.2 shows a schematic diagram of the signal flow in a RF-subcarrier optical-link that uses optical filtering for optical down-conversion. The RF-carrier is modulated by the baseband signal in a regular double-balanced RF mixer which generates a double sideband suppressed carrier (DSB) modulation signal ($m_I > 2$). The mixer output is fed into a MZ modulator to modulate the optical carrier generated by a single mode DFB laser (194 THz). The modulated laser light then passes through a FBG filter that rejects the optical carrier and the upper *RF-optical* sideband. Finally, the filtered light is detected by a p-i-n detector that directly generates the baseband current. A simple explanation for down-conversion in the photodetector is based on the fact that the p-i-n photodiode is a square-law *E*-field detector, meaning the output

current is proportional to the intensity of the oscillating *E*-field of the incident optical signal. Without filtering, the photodiode is effectively mixing the optical carrier frequency with the *RF-optical* sidebands to generate the RF signals. When only one RF-optical sideband is detected, the photodiode mixes the up-converted RF-carrier with up-converted basebands and therefore generates the baseband signal.

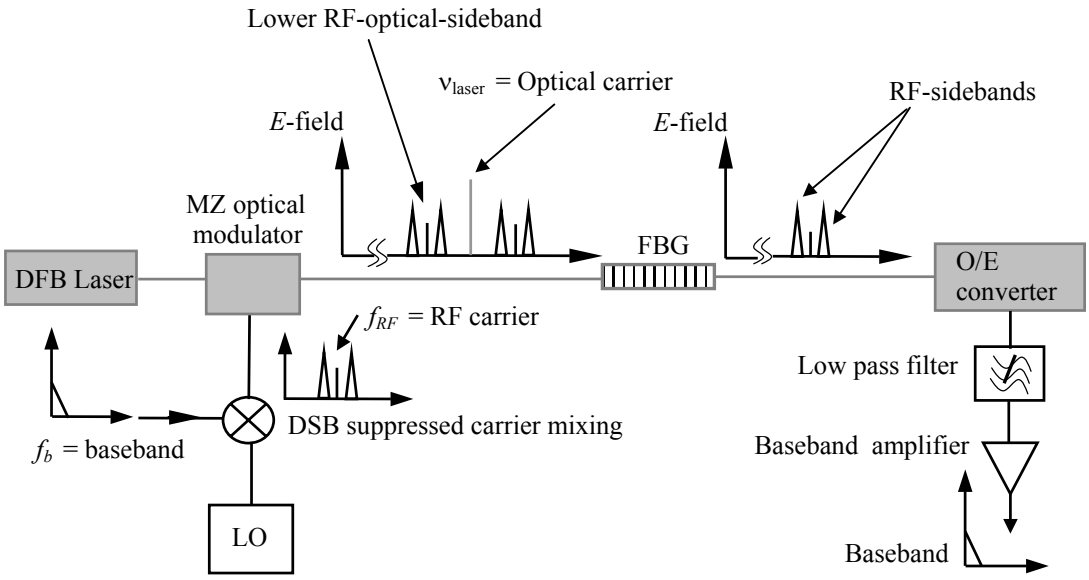


**Figure 4.2** Schematic diagram of a RF-subcarrier optical-link that uses optical filtering for optical down-conversion.

In our proof of principle experiment we use a single-frequency baseband at 100 MHz to modulate a 7.6 GHz RF-carrier. The optical filter is a custom made FBG filter with transmission characteristics shown in Fig. 4.3. The filter has a very fast role-off of about 1 dB/pm around $\lambda$ = 1553.15 nm. The photodetector is an amplified p-i-n detector with a 3 dB bandwidth of 15 GHz. A RF spectrum analyzer is used to measure the RF frequency spectrum of the photodetector output. The laser source is a tunable single mode laser with a linewidth of 20 MHz, so we can tune the

wavelength to different regions of the FBG transmission spectrum. The MZ modulator has a $V_\pi$ of 4.5 V and optical insertion loss of 5 dB. Fig. 4.4 shows: (a) the FBG transmission and the modulated optical signal spectrum, (b) The measured RF-spectrum of the photodetector output and (c) The simulated RF spectrum of the detected signal. These are shown for two different cases: (1) $\lambda_{laser}$ = 1553.16 nm where only the upper *RF-optical* sideband is rejected (2) $\lambda_{laser}$ = 1553.23 nm where the upper *RF-optical* sideband and the optical carrier are rejected.

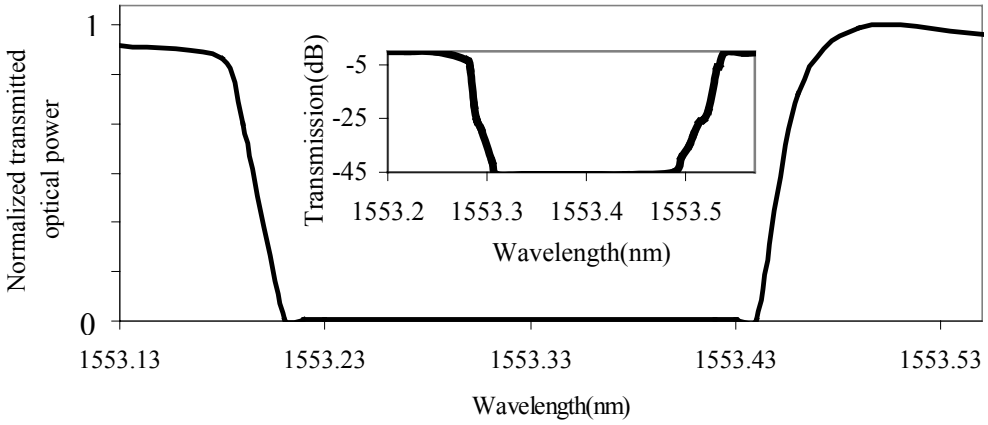


**Figure 4.3** The transmission spectrum of the Fiber Bragg Grating (FBG) employed in the optical down-conversion experiment. (Center wavelength: 1553.3 nm, Slope: 1 dB/pm, Reflection Band width: 0.26 nm)

In the first case the spectrum of the detected RF-signal is similar to the spectrum of the original RF-signal fed to the modulator and nothing is observed at baseband frequencies (no down-conversion). If the upper *RF-optical* sideband is also transmitted, only the amplitude of the detected RF signal becomes larger. In the

second case a small peak is observed at 100 MHz (baseband frequency), a large peak is observed at 200 MHz and the detected RF-signal is suppressed.

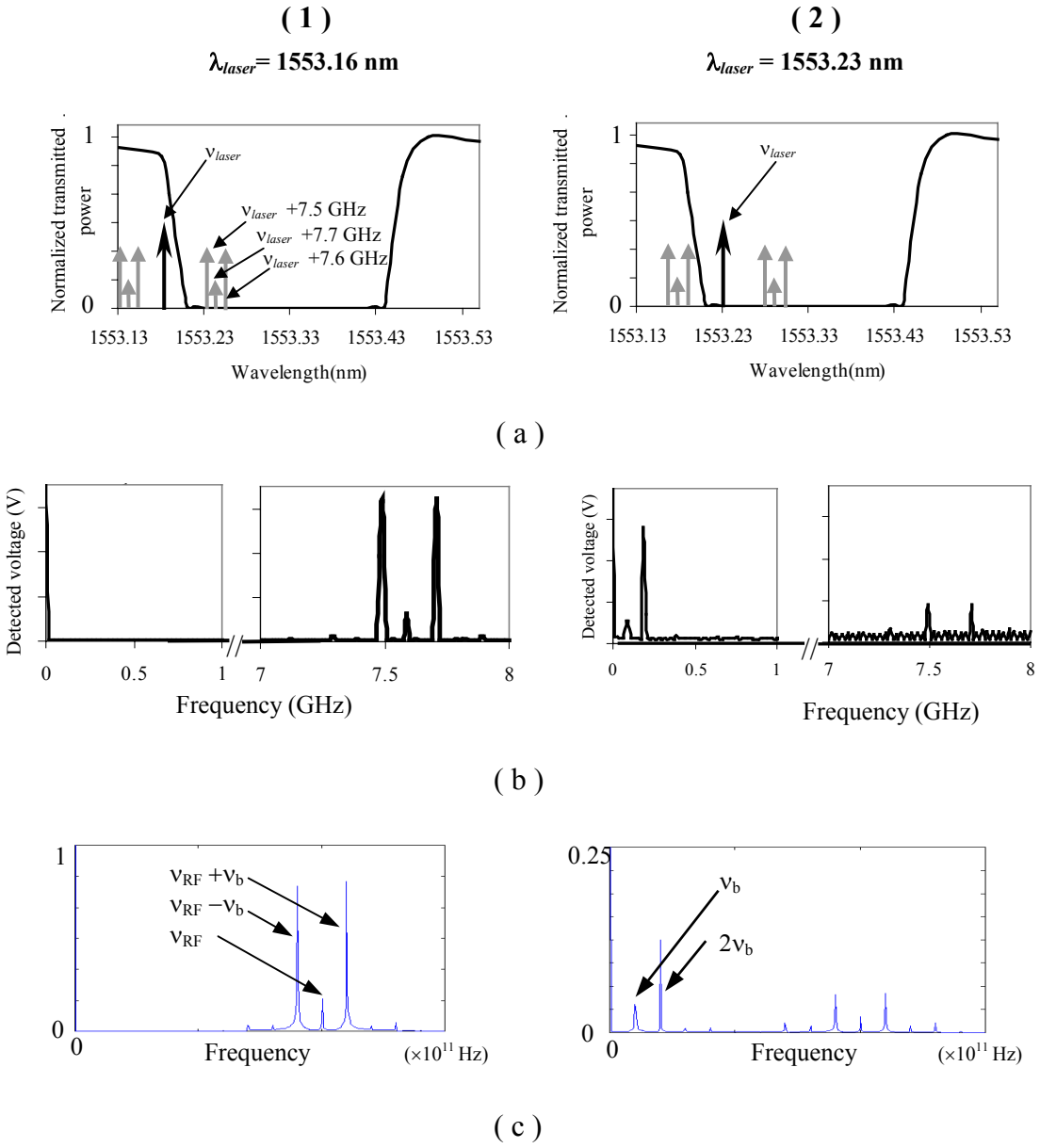


**Figure 4.4** RF down-conversion by optical filtering (a) The measured spectrum of the FBG transmission and the modulated optical signal. (b) RF-spectrum of the detected signal (c) The simulated spectrum of the detected signal. In this the simulation the RF carrier frequency is only ten times smaller than the optical frequency and the baseband signal is ten times smaller than the RF-carrier frequency, to make the FFT calculations faster.

So the signal is down-converted but there is more energy at the second-harmonic of the baseband compared to the baseband frequency. This is because the RF modulation format is a suppressed carrier and the RF carrier is about 16 dB smaller than the sidebands. So the second-harmonic of the baseband signal generated by beating between two RF-sidebands at 7600 MHz ± 100 MHz, is larger than the baseband signal generated by beating between the RF-carrier and each RF-sideband. Equation (4.4) shows that ratio between the baseband component and its second harmonic in the modified optical spectrum is $I_{\omega b}/I_{2\omega b} = 2/m_I$ so if $m_I > 2$, $I_{\omega b} < I_{2\omega b}$ and if $m_I < 2$ then $I_{\omega b} > I_{2\omega b.}$ Linearity is one of the important requirements of a RF receiver so it is evident that $I_{2\omega b}$ has to be smaller than $I_{\omega b}$.

Employing a transmitted carrier RF modulation format ($m_I < 2$) where the carrier amplitude is larger than the sideband amplitudes can solve this problem. Although sending a large amount of energy in the RF carrier frequency is inefficient for long distance communications but it may be practical for short distance indoor wireless links. In the next section we show employing transmitted carrier format can solve the linearity issue.

### 4.3.2 Self-homodyne RF down-conversion

In a conventional super-heterodyne RF receiver architecture a local oscillator (LO) and mixer are used to down-convert the signal to IF frequencies (1.2.5). Baseband

information is subsequently extracted from the IF signal in a detector/demodulator. Alternatively, in a direct–conversion (homodyne) radio receiver, baseband information is obtained by mixing the received signal and the LO without using an IF frequency [11]. In addition to such approaches, self-heterodyne techniques have been proposed to reduce the number of components as well as size, weight, and power consumption in high-carrier frequency (mm-wave), short distance applications [12].

In a self-heterodyne transmission system, the transmitter broadcasts a RF signal (carrier + sidebands) and LO so the IF signal can be down-converted by mixing the received LO and modulated RF signal in a nonlinear device called a self-mixer. The receiver power consumption, phase noise, and complexity are reduced as a result of eliminating the conventional LO and mixer. Although such an approach suffers from reduced power efficiency, it has been shown that it can lower the overall cost and complexity in mm-wave local area networks and indoor wireless transmission systems [12]. One may eliminate the down-conversion to IF frequencies in a self-heterodyne receiver, by using a transmitted carrier RF format. So the baseband signal can be directly down-converted by mixing the received carrier and sidebands in the self-mixer. We call this receiver architecture self-homodyne (self ≡ mixing the transmitted carrier and sidebands, homodyne ≡ no IF stage involved).

The concept of self-homodyne down-conversion of a transmitted carrier RF signal may be used to design a photonic RF receiver where the electronic self-mixing is replaced by photonic self-mixing using optical signal processing techniques.

Here we demonstrate baseband down-conversion from a transmitted carrier RF signal using optical filtering technique (introduced in the previous section).

**Experimental results**

In our experimental demonstration we use the arrangement shown in Fig. 4.2. In order to generate the transmitted carrier RF format we apply a DC voltage on the IF port of the double-balanced mixer so by tuning the voltage we can control $m_I$.

Similar to the previous experiment by aligning the laser wavelength (optical carrier frequency) relative to the center frequency of the FBG, we reject the optical carrier and one of the *RF-optical* sidebands. Fig. 4.5(a) shows the FBG transmission spectrum and the wavelength components of the modulated optical carrier for three different optical carrier wavelengths (lines with diamond tip). Fig. 4.5(b) shows the spectrum of the received RF signal. The RF carrier frequency is 7.6 GHz and the baseband is a 300 MHz single tone. The RF modulation format is suppressed carrier ($m_I < 2$) so the magnitude of the sidebands (8.7GHz ± 300MHz) are smaller than the carrier. We study three different cases, first the lower *RF–optical* sideband is rejected but the optical carrier is not completely suppressed (the signal shown by gray dashed in Fig 4.5 (a)). This results in the optical output intensity spectrum shown in Fig. 4.5(c). Fig. 4.5(d) shows the optical output intensity spectrum where one of the *RF-optical* sidebands and the optical carrier are completely rejected (optical spectrum shown by solid black lines in Fig. 4.5(a)).

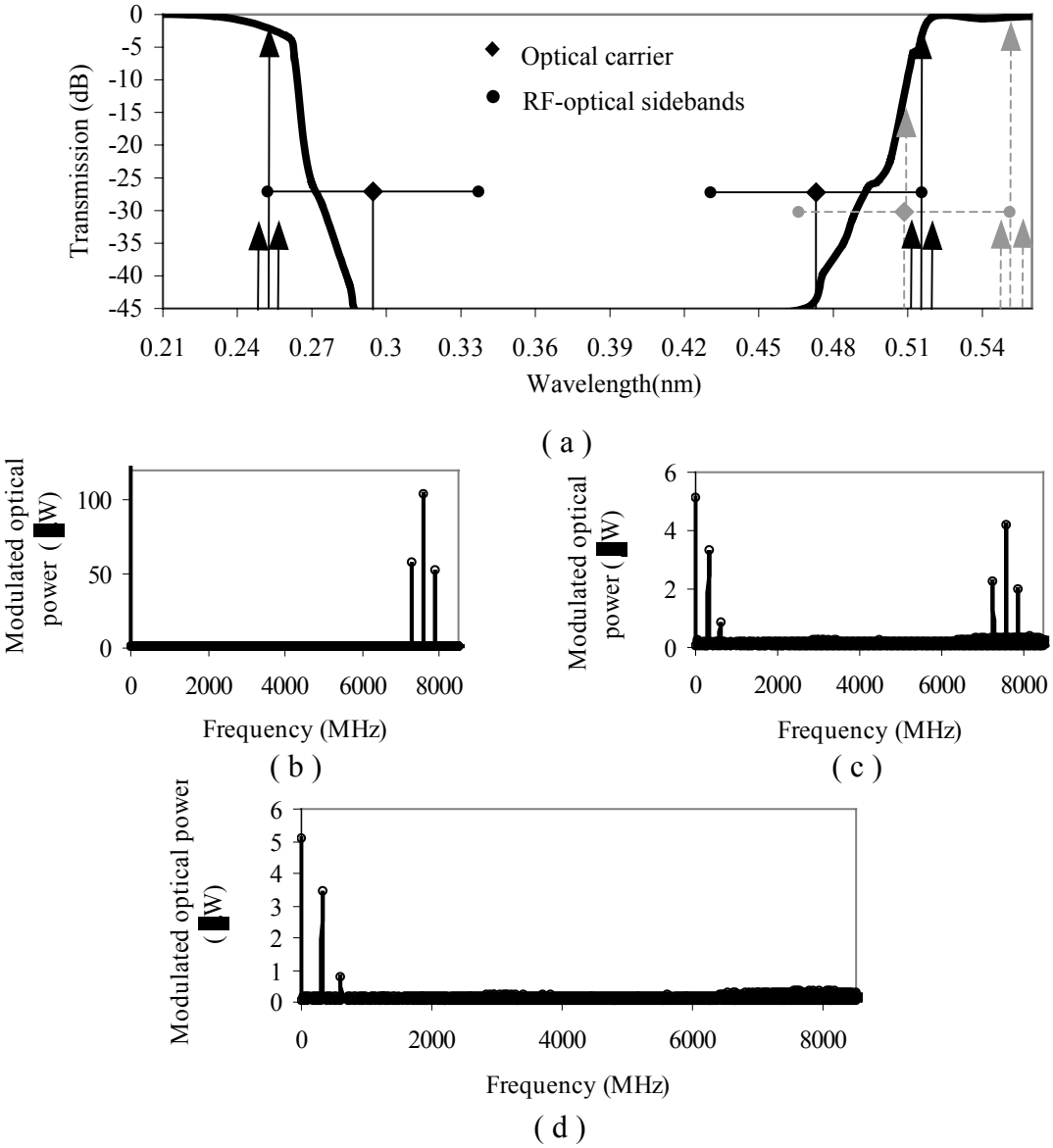


**Figure 4.5** (a) The transmission spectrum of the FBG filter and the location of the wavelength components of the modulated optical carrier. (b) Frequency spectrum of the transmitted carrier RF signal fed into the MZ modulator. (c) The spectrum of the detected signal after filtering for the optical spectrum shown by dashed gray lines in (a). (d) The spectrum of the detected signal after filtering for the optical spectrum shown by solid black lines in (a).

As we expected the down-conversion is more linear and the second-harmonic of the baseband is now suppressed relative to the baseband itself. To study the effect of the modulation index ($m_I$) on the down-conversion efficiency and linearity, we have

measured the magnitude of the down-converted signal and its second-harmonic as a function of RF modulation index. Fig. 4.6 shows the measured and calculated baseband power and its second-harmonic against $m_I$. As may be seen at $m_I = 1.2$ the magnitude of the baseband signal is maximized but the magnitude of its second-harmonic increases monotonically by in creasing $m_I$. The solid lines are calculated using equation (4.4).

Notice that highly linear down-conversion (very small second-harmonic) is accompanied by a low efficiency. At $m_I = 1$ we can have a second-harmonic suppression of 7 dB (15 dB electrical) and an efficiency close to maximum.

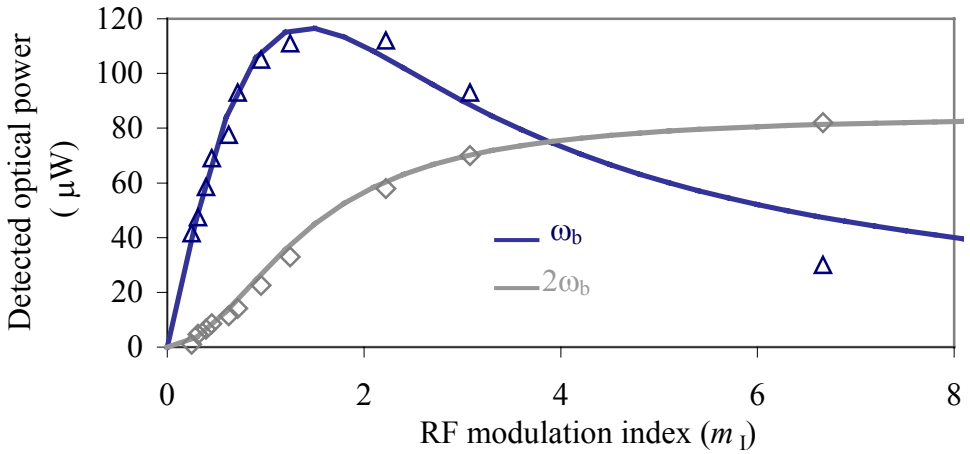


**Figure 4.6** The magnitude of the detected baseband signal (black triangles) and its second-harmonic (gray diamonds) against RF modulation index. The solid lines are the calculated using equation (4.4).

In order to evaluate the performance of this photonic down-conversion technique we replaced the 300 MHz single tone with a 10 Mb/s $2^7$-1 PRBS NRZ data stream.

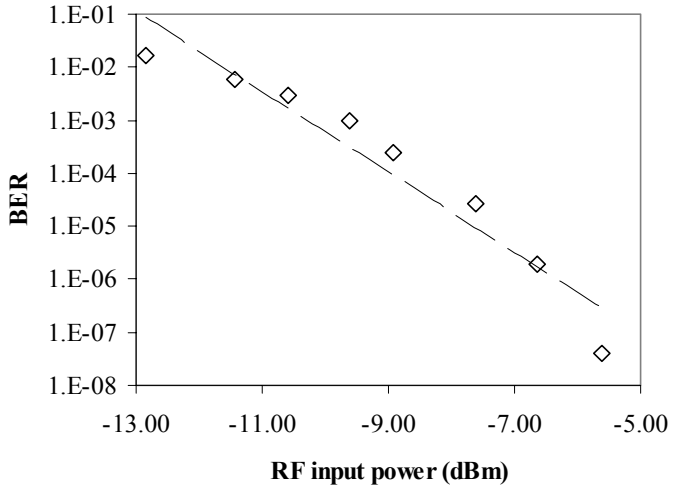


**Figure 4.7** The measured BER performance of the self-homodyne receiver that employs pre-detection optical filtering for photonic down-conversion.

We used a digital photoreceiver with a sensitivity of -41 dBm and bandwidth of 50 Mb/s to detect the down-converted signal. Fig. 4.7 shows the BER measurement results against the total received RF power. The sensitivity of the receiver can be improved by employing a MZ modulator with smaller $V_\pi$ and better insertion loss.

We repeated the same experiment using our 14.6 GHz microdisk modulator. Fig. 4.8 shows the BER measurement results of the FBG based self-homodyne receiver using the microdisk modulator.

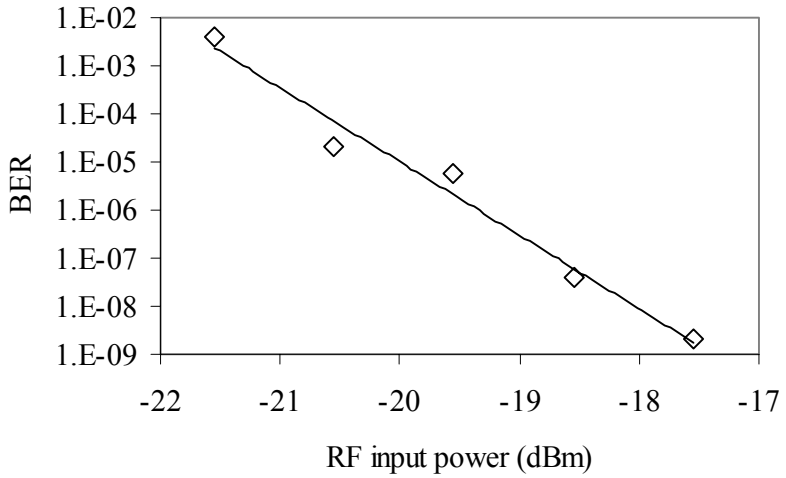


**Figure 4.8** Measured BER of the down-converted data against received RF power. The RF carrier is 14.6 GHz and the transmitted data is 10 Mb/S $2^7$-1 NRZ PRBS. The photonic down-conversion is achieved using a linear modulation in a microdisk modulator and FBG filter. The microdisk has an FSR of 14.6 GHz and a $V_{HMM}$ of 0.6 V.

The baseband signal is again a 10 Mb/s $2^7$-1 PRBS NRZ data stream while the carrier frequency is 14.6 GHz. The microdisk modulator has a $V_{HMM}$ of about 1.2 V and an optical insertion loss of 10 dB. As may be seen although we have doubled the RF carrier frequency the sensitivity of receiver is improved.

Fig. 4.9 shows the measured eye-diagrams for 10 Mb/s, 50 Mb/s and 100 Mb/s at -18 dBm received RF power.

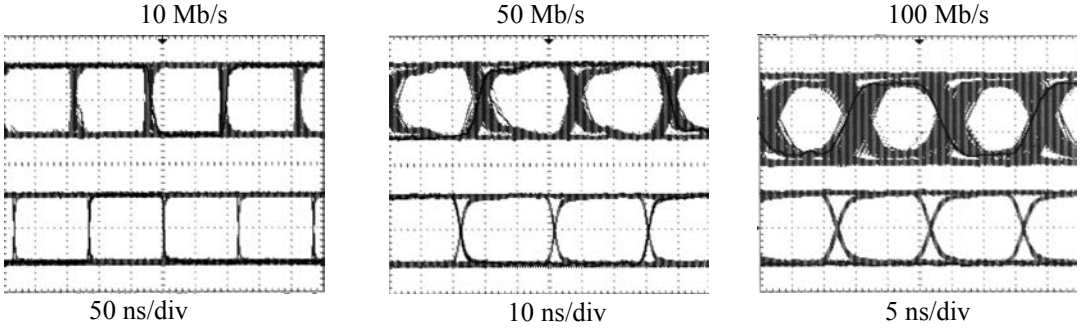


**Figure 4.9** Measured eye diagrams of the down-converted data from 14.6 GHz RF carrier using microdisk modulator and FBG

The efficiency of this down-conversion mechanism is low because a large amount of optical energy is filtered out passing through the FBG and hence does not contribute to the down-conversion process as opposed to the conventional intensity detection where almost all the available optical energy contributes to the down-conversion process. Therefore reducing the transmitted optical power at optical carrier and the upper RF-optical sideband should improve the power efficiency of this passive down-conversion process. In conclusion efficient RF down-conversion using optical filtering prior to photodetection requires both transmitted carrier RF modulation format and suppressed carrier single sideband optical modulation format.

### 4.3.3 Optical heterodyning

An alternative solution to improve the low down-converted power in the optical filtering technique is using a second laser to boost the baseband modulated optical power. In this approach the modulated optical signal is mixed with a laser that has an optical frequency equal to the up-converted RF-carrier in the lower *RF-optical* sideband. This is the optical equivalent of mixing the received RF signal with a local oscillator in conventional RF-receivers. We refer to the second laser as the optical local oscillator. So if we filter out the optical carrier frequency and the upper *RF-optical* side band, the baseband photocurrent is generated as a result of mixing the lower *RF-optical* sideband and the optical local oscillator in the photodetector. Note

that the photodetector is still working as a linear optical intensity detector and the mixing is hidden in the square-law nature of optical detection ($i_p \propto E^2$) and not in any nonlinearities in the photodiode. In effect the RF mixer and local oscillator of a conventional system are replaced with their photonic counter parts: a laser and a photodetector. Clearly the first laser and the optical modulator function as the optical up-conversion stage and play no role in the down-conversion process. We call this process optical heterodyning because the optical carrier frequency and the optical local oscillator frequency are not equal.

Fig. 4.10(a) shows a schematic diagram of the receiver architecture based on optical heterodyning and filtering. The output power of the local oscillator laser is the same power as the main laser but with a shifted wavelength $\Delta\nu = f_{RF}$ ($f_{RF}$ : the RF carrier frequency ). The optical local oscillator and the optical modulator output are combined in a 50/50 optical power combiner. Fig. 4.10(b) and (c) show the simulated output spectrum with and without optical heterodyning (mixing the second laser).

Indeed when the local optical oscillator is used the detected baseband signal becomes larger. In this case the RF signal has a transmitted carrier modulation format to show that by changing the modulation format even without the second laser we can suppress the second-harmonic of the baseband.

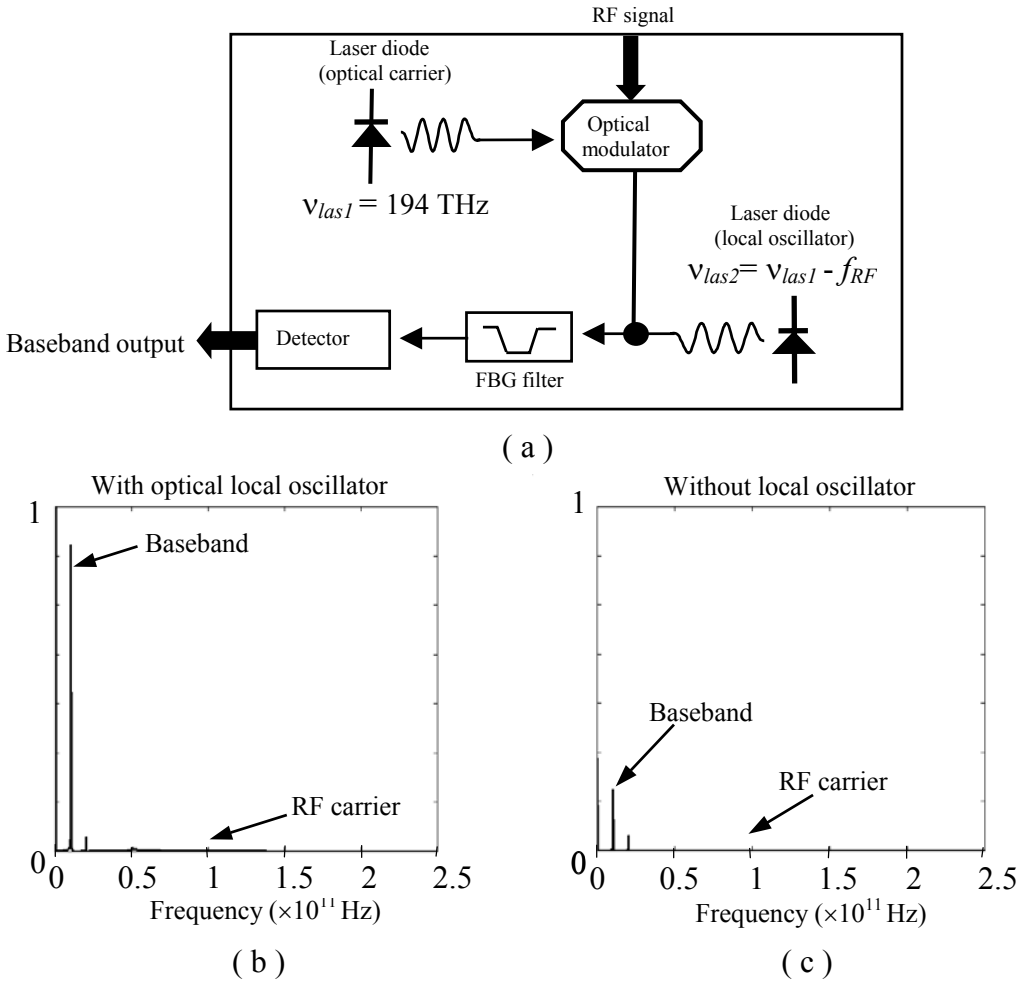


**Figure 4.10** Active down-conversion using optical filtering and local oscillator. (a) Schematic diagram of the system architecture. A second laser with the same power as the main laser but with a shifted wavelength ($\Delta\nu = f_{RF}$, $f_{RF}$: the RF carrier frequency) is combined (50/50) with the modulator output before passing through the FBG filter. (b) The simulated optical output intensity spectrum. The RF signal has a transmitted carrier modulation format (RF-carrier is not suppressed). By using the optical local oscillator the baseband signal becomes larger (by a factor of 5). In order to reduce the calculation complexity of the FFT, in this simulation the RF carrier frequency is only ten times smaller than the optical frequency and the baseband signal is ten times smaller than the RF-carrier frequency.

But when we use the optical heterodyning technique the transmitted carrier RF modulation format is no longer required and we can also use a DSC RF-modulation format. In this way the available RF power is dedicated to the efficient transmission

of data and the carrier power needed for down-conversion is provided, optically, in the receiver.

This approach seems to be very promising since it solves the problems associated with passive down-conversion using a FBG. It relaxes the restriction we had on the RF-modulation format that was limiting the application of the photonic receiver to indoor wireless systems and also it increases the efficiency of the optical down-conversion process by providing power at the proper frequency. The main difficulty of this method is the high-sensitivity of the system performance to relative power, frequency and polarization variations of the two lasers.

To address this issue we have performed a homodyne detection experiment. In this experiment the output of a single-mode laser is divided between two optical paths. 90% of the laser power is transmitted through a passive arm and 10% is modulated by digital data in a MZ modulator. All optical fibers, the splitter and the combiner are polarization maintaining (PM) to avoid fluctuations caused by random polarization rotations. Fig. 4.11(a) illustrates a schematic diagram of the experimental arrangement. The CW and the modulated signals are combined in a 50/50 optical power combiner and then mixed in a photodetector. The amplitude of the output signal is measured with an oscilloscope.

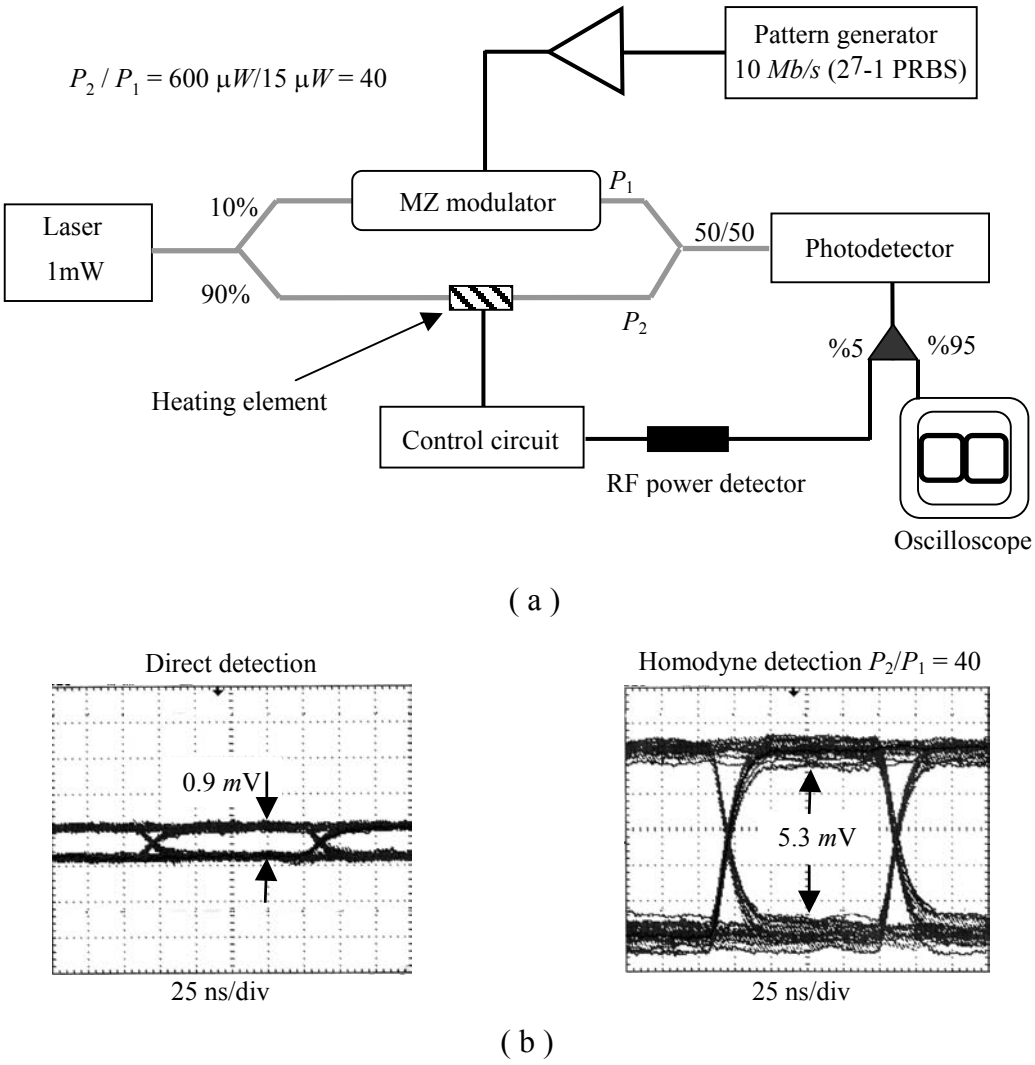


**Figure 4.11** (a) Schematic diagram of the experimental arrangement to test the feedback loop thermal phase control in a homodyne detection scheme. 90% of the laser power goes to the passive arm and 10% goes to the active arm. Due to optical insertion loss in MZ modulator $P_2/P_1$ is about 40. 5% of the detected signal is fed to a RF-power detector (that generates a voltage proportional to the received RF power). The output voltage from the power detector is used as the reference in a control circuit to drive the appropriate current through the heating element and change the phase accordingly. (b) The measured eye diagrams with and without the passive arm. Data amplitude is amplified by a factor of 5.8 that is in very good agreement with the calculated gain

Although both arms are fed by a single laser the detected data amplitude is very unstable due to relative phase fluctuations during transmission. To solve this problem we have designed a feedback loop that uses 5% of output electrical power

as a reference and controls the optical phase in CW arm accordingly to stabilize the detected data amplitude. The phase is controlled by thermal tuning of the passive arm using a thin gold wire around a small length of the fiber as the heating element. Fig. 4.11(b) shows the measured eye diagrams with and without the passive arm when the power ratio between the passive and active arm ($P_2/P_1$) is 40. Using the passive arm amplifies the detected amplitude by a factor of 5.8 as compared to a direct detection configuration. This shows very good agreement with the calculated gain of 6 (for $P_2/P_1 = 40$). This experiment demonstrates that by accurate control of relative phase fluctuation, a homodyne detection system (within a very short link) is achievable. The heterodyne system discussed earlier is similar to our homodyne experiment in the sense that they are both sensitive to relative phase of optical waves mixed in the photodiode. But in heterodyne system, the use of two lasers demands more advanced feedback loops and locking techniques must be used. The possible approaches are the electronic control of the lasers or the optical injection locking of two lasers. We should point out that in all photonic down-conversion methods based on linear or non-linear mixing in a photodetector, the detector bandwidth must be at least equal to the RF carrier frequency. In the next section we will describe a different technique for implementing a photonic self-homodyne receiver that doesn't require the optical filter.

## 4.4 Down-conversion through nonlinear optical modulation

The nonlinearities of a Mach-Zehnder modulator have been used for signal processing in some RF-photonic systems [1-3]. It has been shown a MZ modulator biased at its quadrature point can be used to mix the LO and the RF signal in optical domain and generate the IF signal.

In this section we demonstrate, both Mach-Zehnder and microdisk modulators can perform second-order nonlinear modulation when biased at their maximum or minimum transmission points. Then the combination of second-order nonlinear modulation and transmitted RF format is used to implement a photonic self-homodyne receiver.

### 4.4.1 Introduction

In a photonic self-homodyne RF-receiver we can replace the function of a single-ended diode or FET mixer in a transmitted carrier wireless link with a sensitive optical modulator that performs down-conversion in the optical domain. In this approach the nonlinear dependence of the modulator's transmitted optical power ($P_{o,out}$) on applied RF voltage ($V_{RF}$) is the source of nonlinearity in the system.

Fig. 4.12 illustrates the photonic self-homodyne RF receiver architecture. The received RF signal contains both sidebands and the center frequency (transmitted-

carrier double-sideband modulation format) and is fed to an optical modulator biased at its nonlinear operating point. The carrier and sidebands are mixed through the second-order nonlinearity ($P_{o,out} \propto V_{RF}^2$), hence the optical output intensity spectrum contains the baseband and high-frequency products around the second-harmonic of the carrier frequency. A photoreceiver with a bandwidth matched to the baseband signal generates the baseband photocurrent ($i_p$) and automatically filters out the high-frequency components.

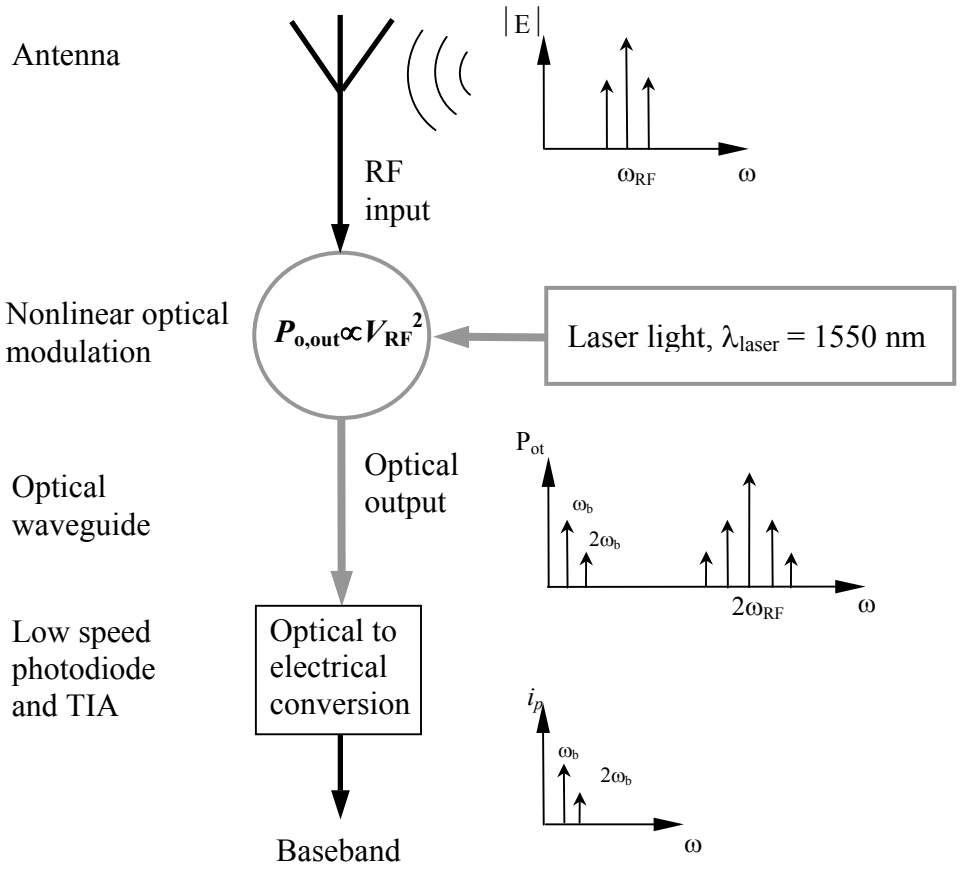


**Figure 4.12** Schematic diagram of the photonic self-homodyne RF receiver. The transmitted carrier RF signal is received by the antenna and is directly fed to a square-law optical intensity modulator. Through nonlinear optical modulation the optical output intensity spectrum contains the baseband and high frequency components that are filtered out by the response of the low-speed photodetector.

The bandwidth of all electronic circuitry used in the system is no greater than that of the baseband signal. The electro-optic transfer function of an optical intensity modulator $f_{EO}(V_{RF})$ can be expanded around $V_{RF} = 0$ to give

$$P_{o,out} = P_o^{(0)} + P_o^{(1)} + P_o^{(2)} + ... = N_0 + N_1 V_{RF} + \frac{N_2}{2} V_{RF}^2 + ... \tag{4.5}$$

Here, $N_i$ ($i > 0$) is the $i$th Taylor expansion coefficient of $P_{o,out}(V_{RF})$ at $V_{RF} = 0$ and $N_0$ is the transmitted optical power at $V_{RF} = 0$. At a fixed wavelength the magnitude of $N_i$ depends on modulator properties and the chosen bias point.

The first-order term in equation (4.5) generates linear optical intensity modulation ($P_{o,out} \propto V_{RF}$) while other terms contribute nonlinear frequency components. Usually, such nonlinearities are minimized in conventional direct detection (DD) optical communication links. If the RF voltage amplitude is small enough and the modulator is biased at its extreme transmission point (where $dP_{o,out}/dV_{RF} = 0$) the second-order term $P_o^{(2)}$ dominates the behavior of the modulator and the optical output power ($P_{o,\,out}$) dependence on voltage around $V_{RF} = 0$ will be similar to an ideal square-law mixer with:

$$P_{o,out} \approx N_0 + \frac{N_2}{2} V_{RF}^2 \tag{4.6}$$

If the baseband is a pure sinusoidal signal, the received RF voltage can be written as:

$$V_{RF} = V_0\left(1 + m_I \cos(\omega_b t)\right)\cos(\omega_{RF} t) \tag{4.7}$$

where $m_I$ is the RF modulation index, $\omega_b$ is the baseband frequency and $\omega_{RF} = 2\pi f_{RF}$ is the RF carrier frequency. The second-order term can be written as

$$P_o^{(2)} = \frac{N_2}{2} \times V_{RF}^2 = \frac{N_2}{2} V_0^2 \left(1 + m_I \cos(\omega_b t)\right)^2 \cos^2(\omega_{RF} t) \tag{4.8}$$

Expanding the right hand side of equation (4.8), one obtains a DC term equal to $(N_2V_0^2/4)(1+ m_I^2/2)$, high frequency components centered around $2\omega_{RF}$ given by

$$\frac{N_2V_0^2}{4}((1+m_I^{\,2}/2)\cos(2\omega_{RF}t)+(m_I^{\,2}/4)\cos^2(2\omega_b t)\cos(2\omega_{RF}t)+m_I\cos(\omega_b t)\cos(2\omega_{RF}t)) \tag{4.9}$$

and the two down-converted low-frequency terms at $\omega_b$ and $2\omega_b$ are given by

$$\frac{N_2V_0^2m_I^{\,2}}{8}\cos(2\omega_b t)+\frac{N_2V_0^2}{2}m_I\cos(\omega_b t) \tag{4.10}$$

The oscillation amplitude of the total second-order modulated optical power is

$$P_{o,\max}^{(2)}=(1+m_I^{\,2}+2m_I)\frac{N_2}{2}V_0^2 \tag{4.11}$$

which is just the maximum amplitude in equation (4.8). If we use a slow speed photodetector with a responsivity $R$, the optical power modulated at $\omega_b$ generates baseband photocurrent $i_{\omega b}$ that carries the received information:

$$i_{\omega_b}=R\frac{N_2V_0^2}{2}m_I\cos(\omega_b t) \tag{4.12}$$

The efficiency of this down-conversion process may be defined as the ratio between the amplitude of the optical power modulated at $\omega_b$ and $P_{o,\max}^{(2)}$. This efficiency is limited by the generation of undesired frequency components at $2\omega_b$, $2\omega_{RF}\pm 2\omega_b$, and $2\omega_{RF}\pm \omega_b$ as well as the DC component. The linearity of the down-conversion is also an important parameter in receiver operation and is defined as the ratio of the optical power amplitude modulated at $\omega_b$ and $2\omega_b$ (first and second terms in equation 4.10). Here we assume that the strength of the second-order nonlinearity dominates higher order terms in equation (4.5) so the generation of higher harmonics of the baseband ($3\omega_b$, $4\omega_b$, etc.) can be ignored.

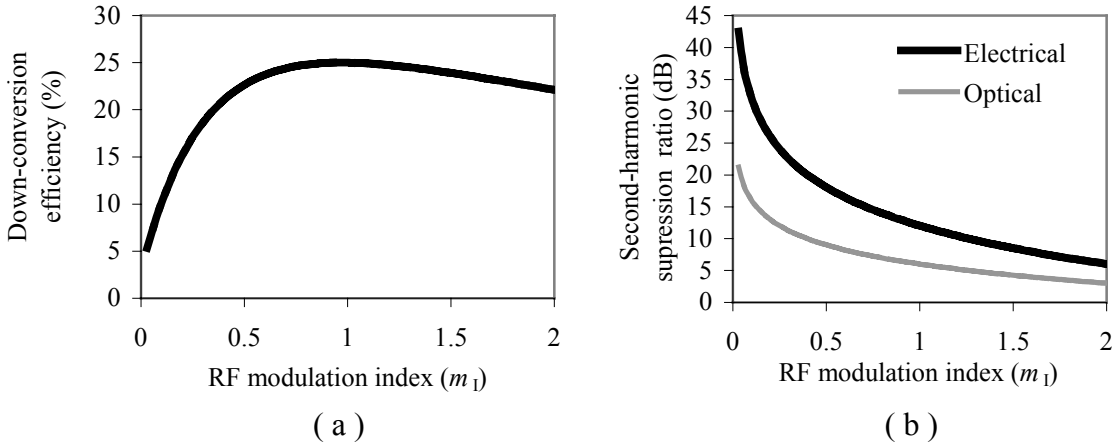


**Figure 4.13** (a) Calculated down-conversion efficiciency ($P_{o,\omega b}/P_{o,max}^{(2)}$) versus RF modulation index ($m$). (b) Second-harmonic suppression ratio against $m_I$. The electrical (after detection) and optical suppression ratios are related through $P_{e,\omega b}/P_{e,2\omega b}=(i_{\omega b}/i_{2\omega b})2\propto(P_{o,\omega b}/P_{o,2\omega b})^2$

The down-conversion efficiency and its linearity are determined by the RF modulation index ($m_I$). In Fig. 4.13 the down-conversion efficiency (a) and second-harmonic suppression ratio (b) are calculated against $m_I$.

The second-harmonic baseband term ($2\omega_b$) can be suppressed relative to the baseband ($\omega_b$) by employing a transmitted carrier RF modulation format ($m_I < 2$) and the down-conversion efficiency reaches its maximum value of 25% around $m_I = 1$. By choosing $m_I = 0.8$, an efficiency of about 25% and a second-harmonic suppression of 7 dB optical (14 dB electrical, $P_e \propto i_p^2 \propto P_{o,out}^2$) can be achieved. The sensitivity of a photonic RF receiver strongly depends on the magnitude of the second-order nonlinearity ($N_2$) in equation (4.5) and thus is determined by the modulator sensitivity and the transfer function $f_{EO}$. Given that most wireless links only require a limited bandwidth around a high frequency carrier, a microdisk resonant optical modulator is a suitable choice for this application. In chapter 2 we

showed that tuning the laser wavelength we can maximized the efficiency of linear modulation and suppressed second order nonlinearity. Conversely for down-conversion in the optical domain, large second-order nonlinearity is a requirement. This can be achieved by tuning the laser wavelength to a maximum or minimum optical transmission of a high-$Q$ whispering gallery (WG) resonance. The large value of $N_2$ at resonance in Fig. 2.38 supports our argument.

It is useful to compare a conventional electronic diode and the microdisk optical modulator as second-order mixers. In both cases the aim is to generate a current proportional to $V_{\mathrm{RF}}^2$. When the RF voltage is applied across a diode, the current may be expanded as:

$$i(V_{RF}) = i_o + V_{RF} G_d + \frac{V_{RF}^2}{2} G_d' + .... \tag{4.13}$$

where $G_\mathrm{d}$ is the dynamic conductance of the diode and the $G_\mathrm{d}' = \alpha\ G_\mathrm{d}$, ($\alpha = q/nk_BT$). If $V_{RF}$ has the same form as equation (4.7) the baseband current is:

$$i_{\omega b} = \frac{m_I}{2} G_d' V_{RF}^2 \tag{4.14}$$

This equation is equivalent to equation (4.12) for the photonic mixer where $RN_2$ in equation (4.12) is replaced by $G_\mathrm{d}'$. In order to compete with an electronic diode mixer we need large second-order nonlinearity and a very sensitive low speed photodiode. Fig. 4.14 shows the typical $P_{\mathrm{o,out}}$-$V$ and $I$-$V$ curves for a microdisk mixer and an electronic diode and also the frequency spectrum of their output current (with an input voltage similar to equation 4.7).

As opposed to the microdisk mixer, the frequency spectrum of the electronic diode contains the linear terms around $\omega_{\mathrm{RF}}$. This is because there is no pure nonlinear bias

point in the *I-V* curve of a diode while at $\lambda_{laser} = \lambda_{res}$ the microdisk has a purely nonlinear response. Since the only useful frequency component is the baseband modulated current, the amount of wasted energy, energy pumped to undesired frequencies, is larger in a diode mixer.

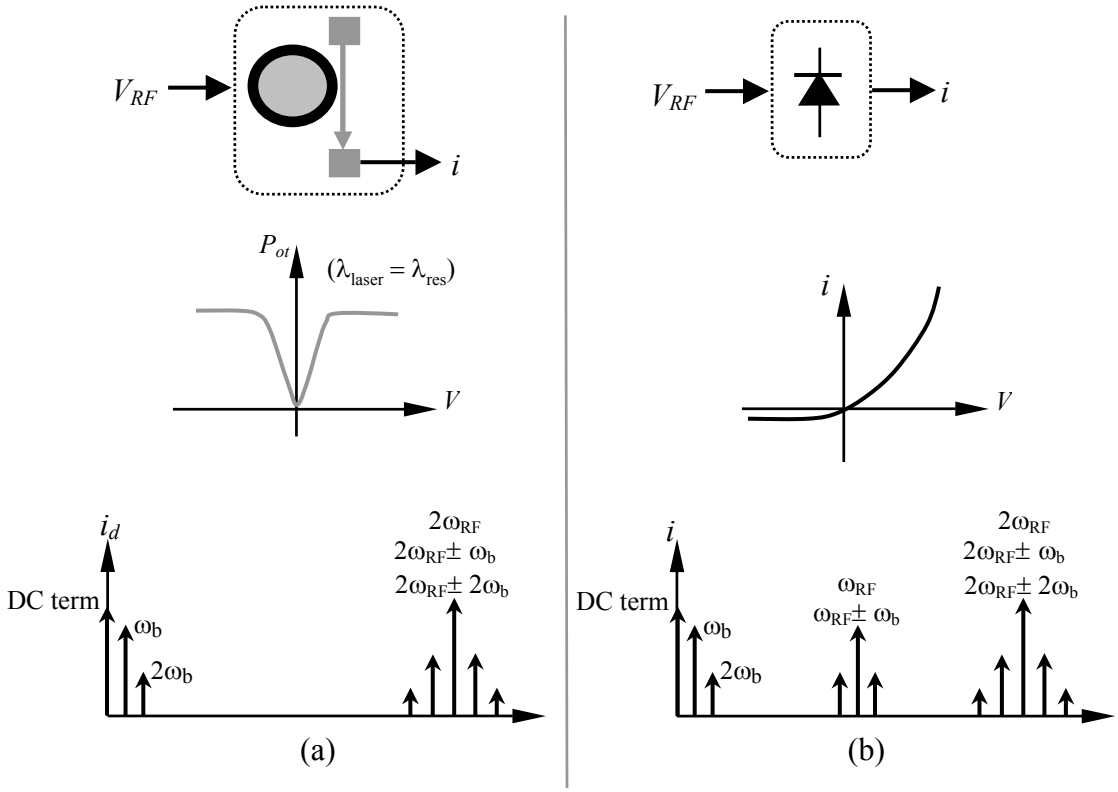


**Figure 4.14** (a) The output optical power of a microdisk modulator against the input voltage and the frequency spectrum of the photocurrent generated by the voltage in equation 4.7. (b) The current across a conventional diode against the input voltage and the frequency spectrum of the current generated by the voltage in equation 4.7.

### 4.4.2 Nonlinear optical modulation using MZ modulator

Fig. 4.15(a) shows the typical response of a MZ-modulator. The output optical power can be written as:

$$P_{o,out} = \tfrac{1}{2}[1+\cos^2(\tfrac{1}{2}\Delta\beta L)] \tag{4.15}$$

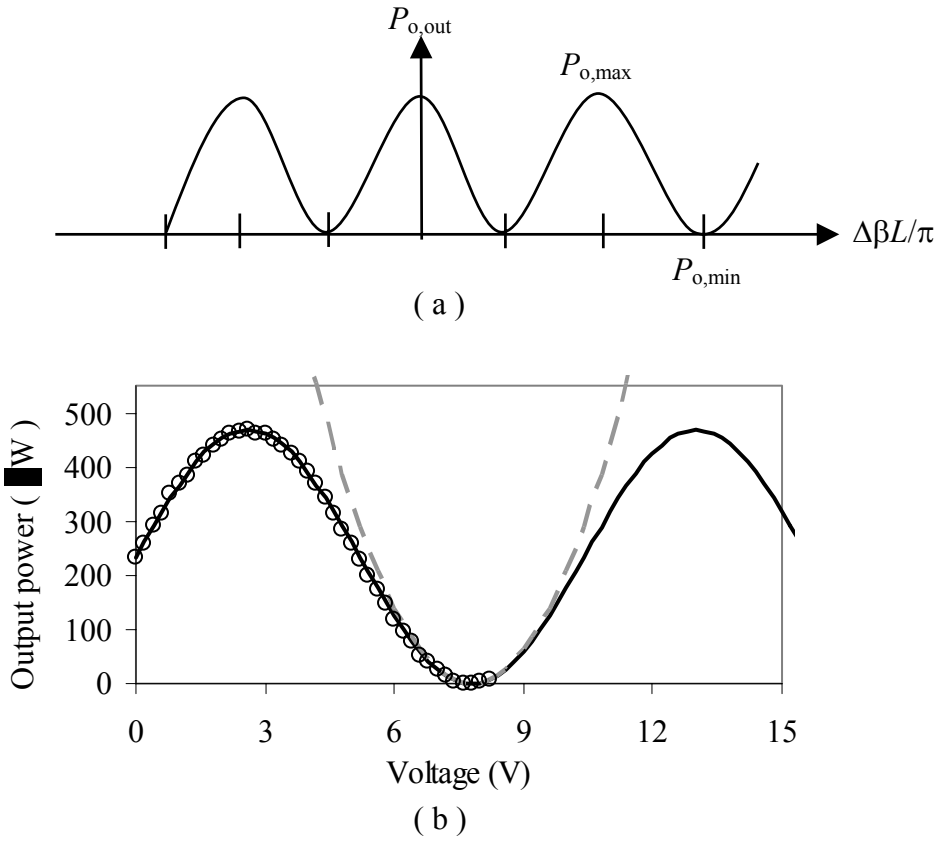


**Figure 4.15** (a) $P_{o,out}$ versus $\Delta\beta L/\pi$ characteristic of a Mach-Zehnder modulator. (b) The DC response of the MZ modulator used in our experiments. The circles are the measured data points while the solid line is the calculated response using equation 4.16 assuming $P_{o,max}$ = 468 μW, $\phi$ = 2.375 rad and $V_\pi$ = 5.2 V. The dashed curve is the parabola defined by $N_2V^2/2$ where $N_2$ is the second derivative of the equation 4.16.

$\Delta\beta$ is the propagation constant variation in the active arm created by the electro-optical effect ($2\pi\Delta n_e/\lambda \propto V_{RF}$), and $L$ is the interaction length in the active arm.

The main parameter that quantifies the modulation sensitivity of a MZ modulator is $V_\pi$ or the voltage required to create a $\pi$ optical phase shift in the active arm ($\Delta\beta L = \pi$).

When $\Delta\beta L/\pi$ is an integer number the optical output power is maximum or minimum so $dP_{o,out}/dV_{RF} = 0$ and $N_2 = d^2 P_{o,out}/dV_{RF}^2$ has its maximum value. If a MZ modulator is biased at any of these extreme transmission points it can be used as a square-law RF mixer.

We can rewrite equation (4.15) in terms of the input voltage ($V$) and the $\pi$ phase shift voltage ($V_\pi$):

$$P_{o,out} = P_{o,max}[\cos(\phi+\pi V/2V_\pi)]^2 \qquad (4.16)$$

Fig. 4.15(b) shows the DC response of the MZ modulator used in our experiments. The circles are the measured values of the optical output power as a function of the input voltage. The solid curve is generated using equation 4.16 and the proper values of $P_{o,max}$, $\phi$ and $V_\pi$ to fit the experimental data: $P_{o,max}$ = 468 μW, $\phi$ = 2.375 rad and $V_\pi$ = 5.2 V. The optical input power is 1500 μW and the optical insertion loss is 5 dB. The dashed curve is the parabola defined by $N_2V^2/2$ where $N_2$ is the second derivative of the equation 4.16. As may be seen $V < 0.25V_\pi$ can be considered as small signal regime because in this range the parabola perfectly overlaps with the actual response. So as mentioned in the previous section at this regime the MZ modulator behaves like an ideal second-order intensity modulator and the simple formulation developed for down-conversion can be used to estimate the down converted optical power.

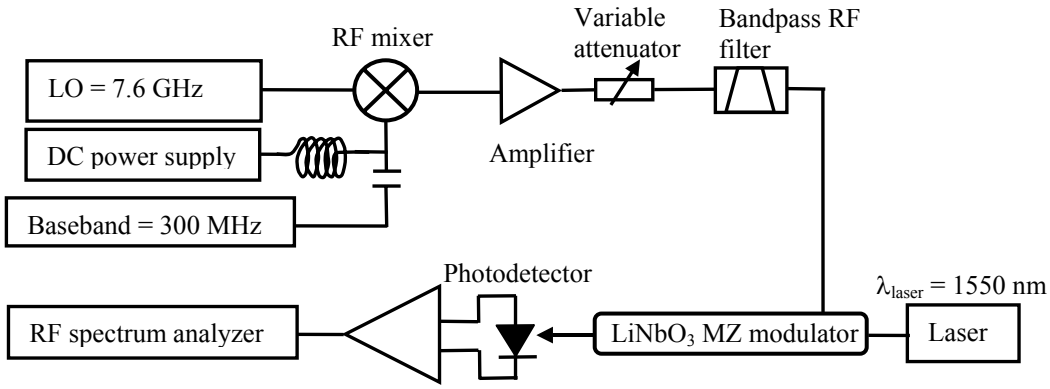


**Figure 4.16** Experimental arrangement for studying photonic down-conversion through nonlinear modulation in an MZ modulator.

In order to validate theoretical prediction of our simple model we used the experimental setup shown in Fig. 4.16. In this experiment the baseband is a 300 MHz single tone and the RF carrier frequency is 7.6 GHz. Mixing the baseband with the local oscillator in a biased RF-mixer generates the transmitted carrier RF signal (equation 4.7) where the RF modulation index can be controlled by varying the bias voltage. A band pass RF filter removes all intermodulation products at baseband and the higher harmonics of the carrier so that the output only contains the double sideband (DSB) modulated RF-carrier. The MZ modulator is biased at its minimum transmission operating point. The modulator parameters and maximum optical output power are the same as Fig. 4.15(b) and the photodetector responsivity is 270 μV/μW.

Fig. 4.17(a) shows the calculated and detected rms voltage at baseband ($V_1$) and the second-harmonic of the baseband ($V_2$) as a function of $m_1$. The calculation is based on square-law optical modulator model (equation 4.6) where $N_2$ is calculated using equation 4.16 and the measured values of MZ modulator parameters. One can

calculate the detected voltage amplitude at $\omega_b$ and $2\omega_b$ using equation 4.10 and the photodetector responsivity. Fig. 4.17(b) shows the calculated and measured rms voltage at baseband ($V_1$) and the second-harmonic of the baseband ($V_2$) as a function of the total received RF power at $m_I = 1.2$.

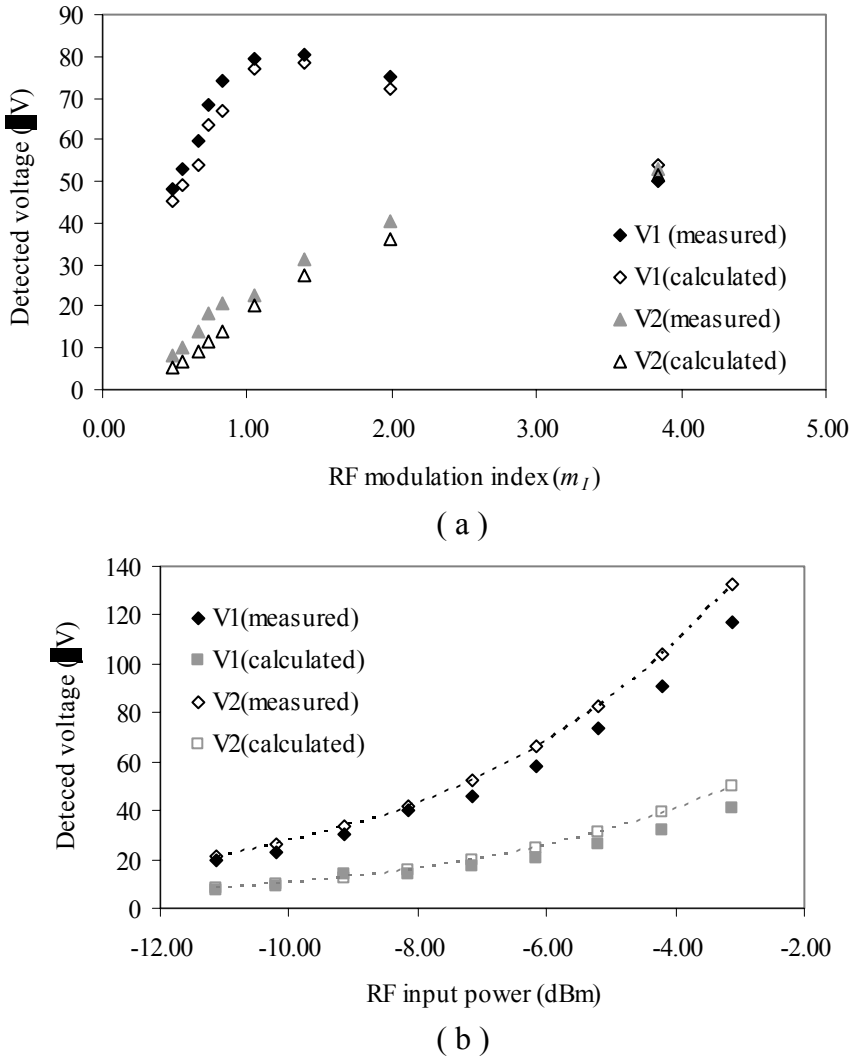


**Figure 4.17** (a) Calculated and detected rms voltage at baseband and the second-harmonic of the baseband as a function of $m_I$. The calculation is based on square-law optical modulator model. (b) Calculated and measured rms voltage at baseband and the second-harmonic of the baseband ($V_2$) as a function of the total received RF power at $m_I = 1.2$.

The received RF power is related to $m_I$ and $V_0$ through $P_{RF} = V_0^2(1+ m_I^2/2)/100$ so again we can use equation 4.10 and photodetector responsivity to calculate the detected voltage amplitude at $\omega_b$ and $2\omega_b$ as a function of $P_{RF}$.

The calculated and measured results are in good agreement showing that at small signal regime the modulator is effectively a square-law modulator

We have also demonstrated direct data down-conversion at data rates up to 100 Mb/s from a transmitted carrier RF signal (carrier frequency =7.6 GHz) by replacing the signal generator in the experimental arrangement of Fig. 4.16, with a pattern generator and the photodetector with a digital photoreceiver. The patterns are NRZ $2^7$-1 PRBS and the sensitivity of the photoreceiver is –41 dBm for a BER of $10^{-9}$.

Fig. 4.18 shows the measured eye diagrams at 10, 50 and 100 Mb/s. The respective BER results are $10^{-9}$, $10^{-6}$ and $10^{-5}$ at –10 dBm total received RF power

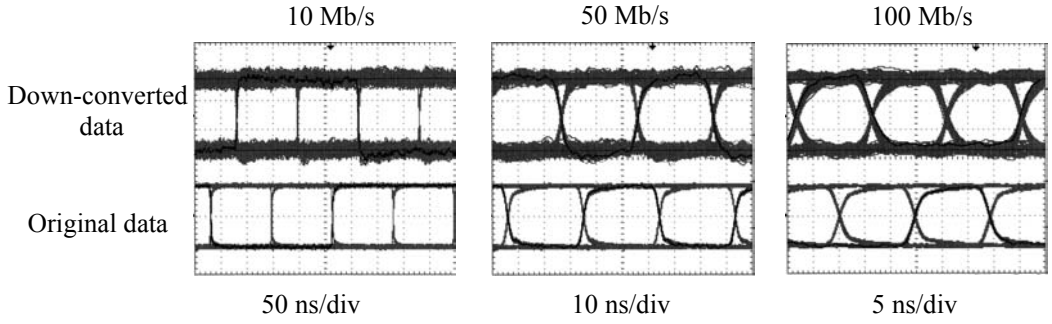


**Figure 4.18** Measured eye-diagrams at 10, 50 and 100 Mb/s (PRBS NRZ $2^7$-1). The data is down-converted from a 7.6 GHz RF carrier through nonlinear optical modulation in an MZ modulator.

### 4.4.3 Nonlinear optical modulation using microdisk modulator

In chapter 2 (2.6.1) we introduced the electro-optic transfer function $f_{EO}$ that governs the behavior of the modulator. We showed that at a given RF voltage depending on the laser input wavelength, $f_{EO}$ can be a linear or nonlinear function of input voltage. This section explores the nonlinear operation regime for RF down-conversion applications.

Fig. 4.19 shows how the location of the laser wavelength relative to the resonant wavelength can change the linearity of the optical modulation in a microdisk modulator.

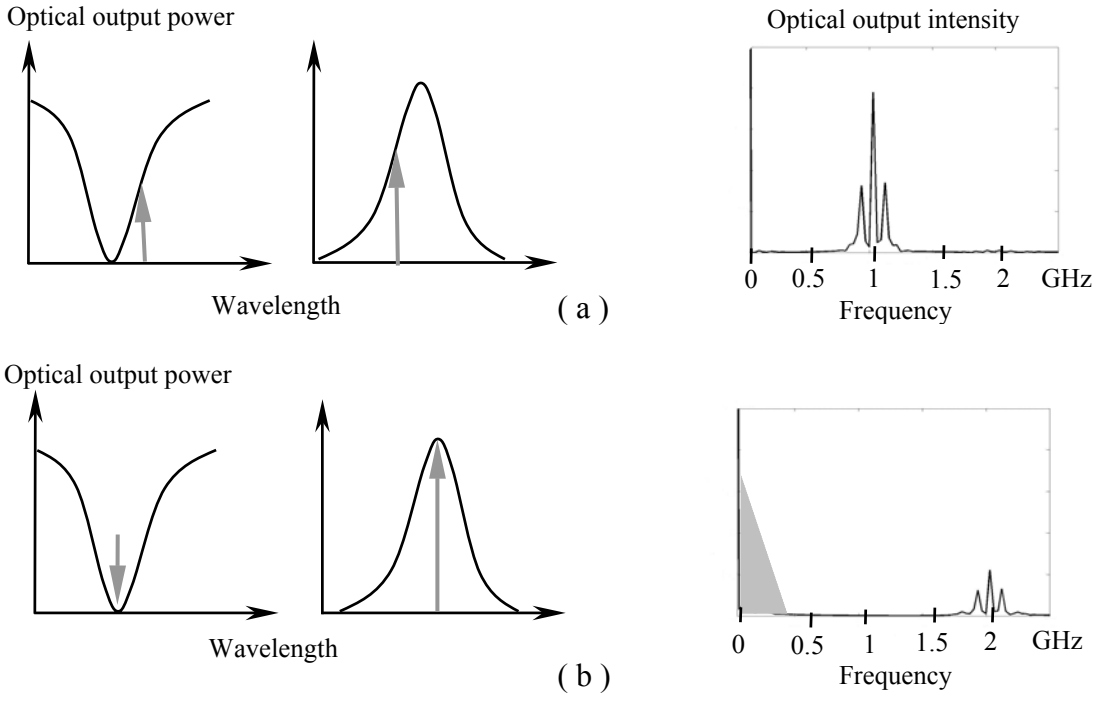


**Figure 4.19** Simulated optical output power spectrum of microdisk modulator at linear (a) and nonlinear (b) operation regime. The RF input power is a 1 GHz RF carrier modulated by a 100 MHz (single frequency) baseband signal

Two cases were simulated: (a) the laser wavelength is tuned to the middle of the mode slope where $P_{o,mod} \propto V_{RF}$ (b) the laser wavelength is tuned to a resonant wavelength where $P_{o,mod} \propto (V_{RF})^2$. The RF input voltage has a form similar to equation (4.7). The simulation clearly shows that when $\lambda_{laser} = \lambda_{res}$ the spectrum of the optical output power is similar to what is shown in Fig. 4.14(a).

To demonstrate nonlinear modulation with a microdisk electro-optic modulator, we have performed a single frequency modulation experiment. Fig. 4.17 shows the experimental results of switching between linear and nonlinear operation by changing the laser wavelength.

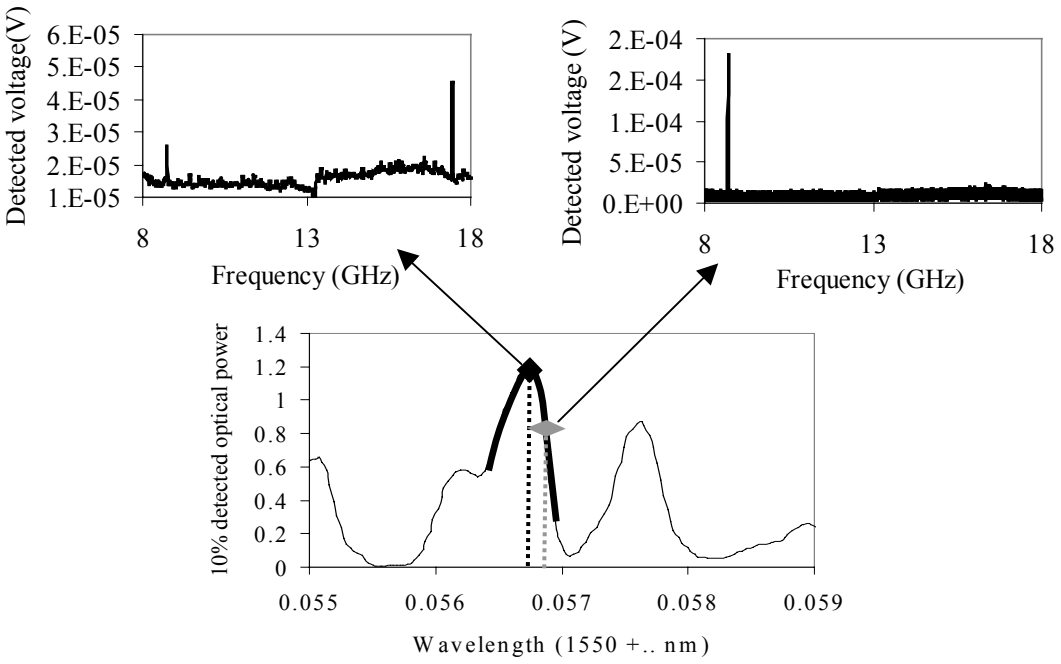


**Figure 4.20** Nonlinear modulation with microdisk modulator. The microdisk is fed by a 0 dBm single frequency RF signal ($f_{RF}$ = 8.7 GHz = optical free spectral range of the disk). When the laser wavelength is set to the middle of the optical mode slope the modulation is linear and is only observed at 8.7 GHz (right). If the laser wavelength is tuned to the WG resonant frequency, modulation becomes nonlinear and a second-harmonic of the input RF frequency (17.4 GHz) is generated while the linear component decreases (left).

When the laser wavelength is set to the middle of the optical mode slope, the modulation is linear. But if we tune the laser wavelength to the WG resonant frequency, modulation becomes nonlinear and generates the second-harmonic of input RF frequency is generated.

The calculations in section 4.4 show that for small signal RF down-conversion the critical parameter is $N_2$ or the second order derivative of the electro-optical transfer function ($f_{EO}$). Basically $N_2$ is equivalent to the mode slope ($S$) for linear modulation. In chapter 2 we calculated $f_{EO}$ for a microdisk modulator using the optical transfer function and electro-optically modulated optical refractive index. We can use the same approach to calculate $f_{EO}$ while the microdisk is biased to its extreme nonlinear operating regime ($\lambda_{laser} = \lambda_{res}$).

Fig. 4.21 shows the simulated transmitted optical output power ($P_{o,out}$) of a typical microdisk modulator as a function of wavelength and input RF voltage amplitude. In our simulation the modulator parameters are chosen to be representative of the experimental values with $Q = 3.5\times10^6$ (corresponding to $\alpha = 0.0075$ cm$^{-1}$ and $\kappa_0 = 0.095$), $h = 400$ μm, and $G_v = 6$. The optical input power is 50 μW and $\lambda_{laser} \sim 1550$ nm. The DC-shift is set to the measured value of $\Delta\lambda_{DC} = 0.13$ pm/V (corresponding to $\beta_{EO} = 0.5$) for our optimized 14.55 GHz microdisk modulator.

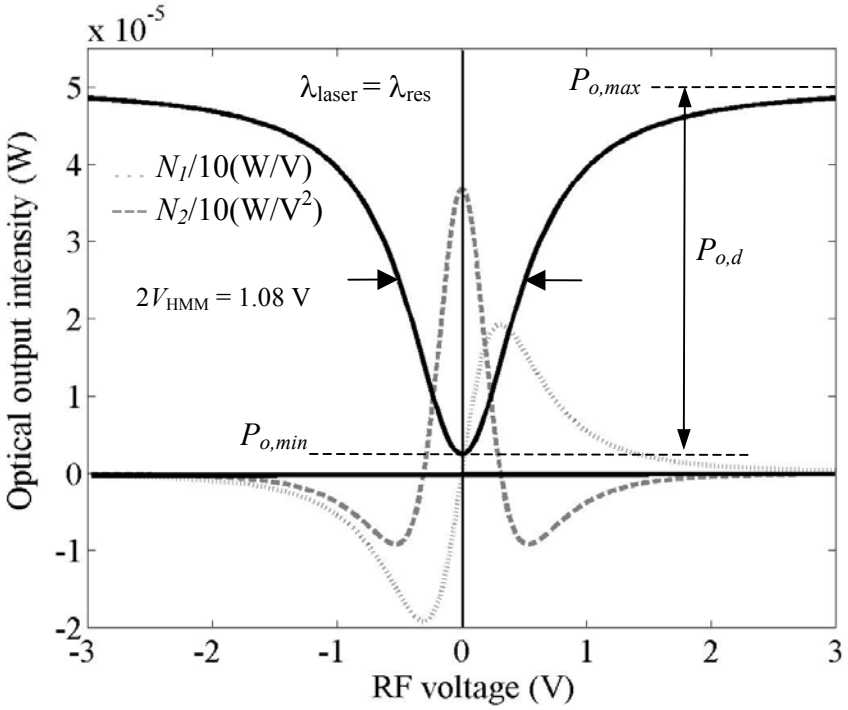


**Figure 4.21** Calculated optical output intensity of an ideal microdisk modulator as a function of RF input voltage ($G_v = 6$). The dashed and the dotted lines are generated as the first ($N_1$) and second ($N_2$) Taylor coefficients in an expansion of the optical transfer function (solid line). The laser is biased to the extreme nonlinear operating regime $\lambda_{laser} = \lambda_{res}$.

At small signal RF input powers, the simulated value of $N_2$ can be directly used in Equation (8) to calculate the down-converted baseband current as a function of input RF voltage amplitude. To define what constitutes small signal it is useful to quantify the sensitivity of the modulator by a voltage amplitude $V_{HMM}$ that modulates half of the optical mode power *(*$P_{o,d} = P_{o,max} - P_{o,min}$*)*. $V_{HMM}$ is determined by the optical *Q, h,* $r_{33}$, and $G_v$. Typically the $V_{HMM}$ for our $LiNbO_3$ microdisk modulators is between 0.4 V and 0.6 V. $N_2$ is directly proportional to $V_{HMM}$ and maximum ($P_{o,max}$). Note that if the optical coupling process is lossless, $P_{o,max}$ is equal to the optical input power ($P_{o,in}$). Fig. 4.21 shows that a $V_{HMM}$ of 0.54 V and optical input power of 50 μW result in $N_2 = 0.032$ mW/V$^2$. We have calculated the down-converted optical

power (at $\omega_b$) with two different methods. First by using the electro-optic transfer function ($f_{EO}$) and measuring the amplitude of $\omega_b$ in the Fourier transform of $P_{o,out}$ and then by substituting the estimated $N_2$ in equation (8) for different values of $G_v$. The calculation shows that if $V_{RF} < 0.25 \times V_{HMM}$ the microdisk modulator is effectively operating as a square law optical intensity modulator ($N_i \sim 0,\ i > 2$) and the baseband modulated optical power is equal to $m_I N_2 V_0/2$. Basically this means for input voltage amplitudes $|V_0| < 0.25 V_{HMM}$ the parabola defined by $N_2 V_0^2/2$ perfectly matches with $P_{o,out} = f_{EO}(V_{RF})$. This approximation provides a powerful tool for calculating the baseband current as a function of the received RF power.

Fig. 4.22(a) shows the calculated baseband modulated optical power against RF input power for a microdisk modulator with an electro-optic transfer function similar to the one shown in Fig. 4.21. If we use a PIN diode with a responsivity $R$ in series with a transimpedance amplifier the baseband voltage can be written as:

$$V_b = RZ_T \frac{N_2 V_0^2}{2} m_I \cos(\omega_b t) \tag{4.17}$$

where $Z_T$ is the transimpedance.

Fig. 4.22(b) shows the down-converted voltage amplitude and power gain ($V_b/V_o$ and $P_{\omega b}/P_{in}$) against received RF power for a microdisk photonic RF receiver with the following parameters: $R = 0.9$ (A/W), $Z_T = 700\text{K}\Omega$, $Q = 4.8\times10^6$, $V_{HMM} = 0.4$ Volt.

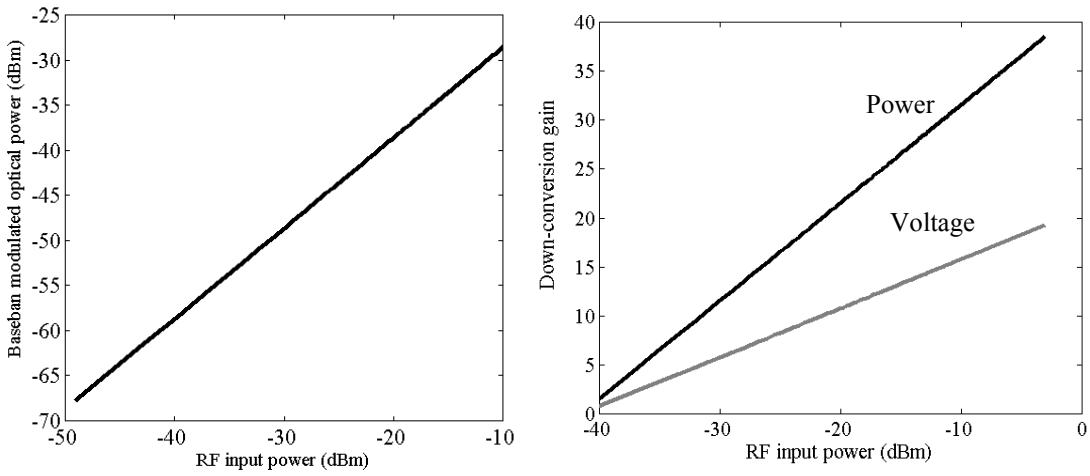


**Figure 4.22** (a) Calculated baseband modulated optical power against RF input power for a microdisk modulator with an electro-optic transfer function similar to Fig. 4.21. (b) The down-converted voltage and power gain against received RF power for a microdisk optical RF receiver ($R$ = 0.9 (A/W), $Z_T$ = 700KΩ, $Q = 4.8\times10^6$, $V_{HMM}$ =0.4 Volt)

### 4.4.4 Comparison

We have shown both MZ modulator and microdisk modulator can be used for nonlinear optical modulation and RF mixing in optical domain. Fig. 4.23(a) and (b) shows the calculated optical output power against the applied RF voltage for a MZ and a microdisk modulator respectively (solid lines). The dashed curves are the parabolas defined by $(N_2/2)V^2$. At small signal regime (defined by the dotted boxes) where $V_{RF} < 0.25V_{HMM}$ ($< 0.25V_\pi$ for MZ modulator) the parabolas perfectly match the actual response, hence the strength of the second-order nonlinear modulation can be estimated simply by calculating $N_2$. So we can use the magnitude of $N_2$ to

compare the performance of MZ and microdisk modulator as nonlinear modulators at small signal regime. The received RF signal for wireless communications is bellow –30 dBm corresponding to a voltage amplitude of less than 0.01 V. Knowing the typical value of $V_{HMM}$ is between 0.2 V and 0.6 V and typical value of $V_\pi$ is between 1 V and 5 V, our comparison is valid for all wireless applications. Fig. 4.23(c) shows the calculated value of $N_2$ versus $V_{HMM}$ and $V_\pi$ assuming the MZ has an insertion loss of 4 dB and microdisk modulator has an insertion loss of 10 dB. One may see that the state-of-the-art $LiNbO_3$ MZ modulator with a $V_\pi$ of 1 V [14] has the same nonlinear modulation efficiency as a $LiNbO_3$ microdisk modulator with a $V_{HMM}$ of about 0.4 V that can be easily made using a 200 μm $LiNbO_3$ thick microdisk.

More importantly the insertion loss of the microdisk modulator can be improved without affecting its sensitivity while in a MZ modulator generally enhanced sensitivity is accompanied by extra loss. So the 4 dB insertion loss for a MZ modulator with a $V_\pi$ of 1 V is a very optimistic assumption while the 10 dB insertion loss and $V_{HMM}$ of 0.5 V for a $LiNbO_3$ microdisk modulator is easily achievable by reducing the disk thickness to a 200 μm.

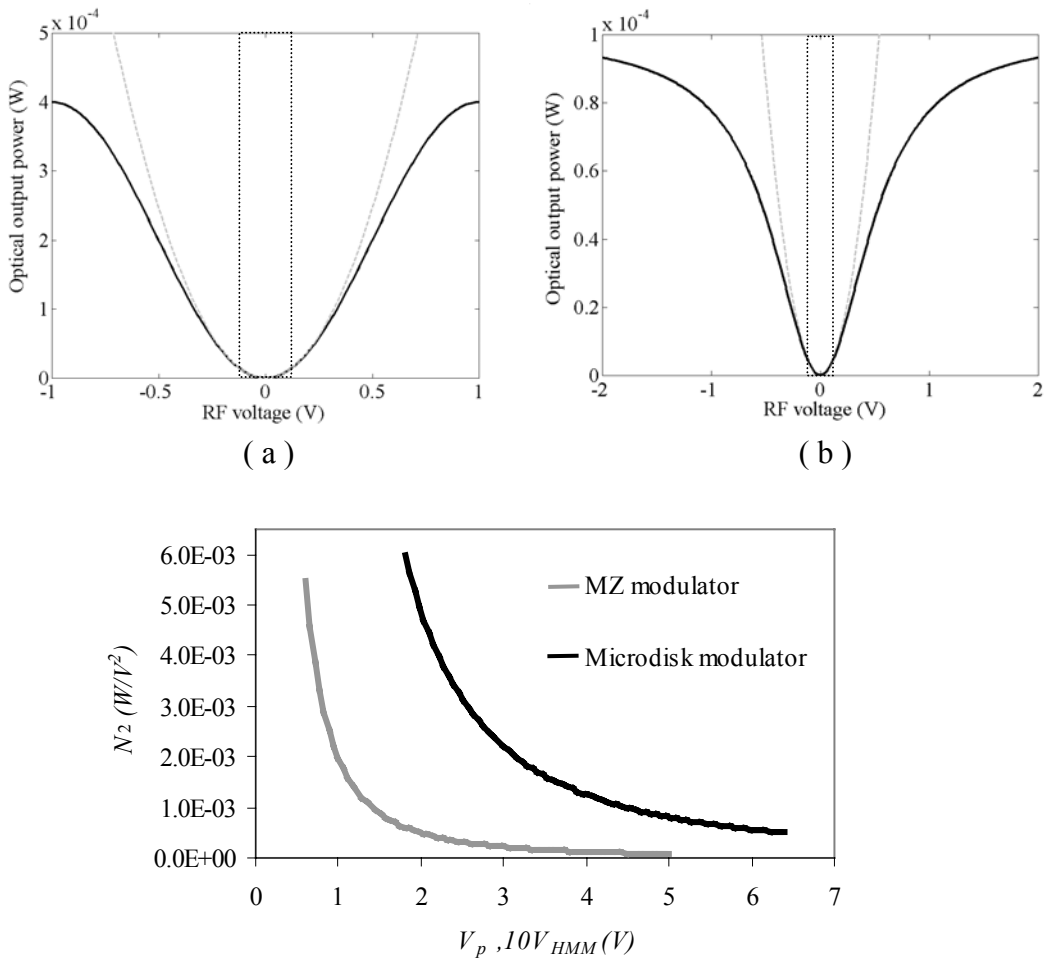


**Figure 4.23** (a) Calculated optical output power against the RF voltage for a MZ modulator with a $V_\pi$ of 1V and insertion loss of 4dB. The gray line is the approximated hyperbola $(N_2/2)V^2$. The dotted blocks shows the small signal region. (b) Calculated optical output power against RF voltage. The microdisk has a $V_{HMM}$ of 0.55 V and insertion loss of 10 dB. The optical input power is 1 mW. (c) Calculated value of $N_2$ versus $V_{HMM}$ and $V_\pi$ assuming the MZ has an insertion loss of 4 dB and microdisk modulator has an insertion loss of 10 dB

Although in most of our experiments the optical insertion loss was around 10 dB but insertion losses as low as 3 dB has been already demonstrated. Fig. 4.24 shows $N_2$ versus $V_{HMM}$ for the $LiNbO_3$ microdisk modulator in Fig 4.23(b) and for three different values of insertion losses.

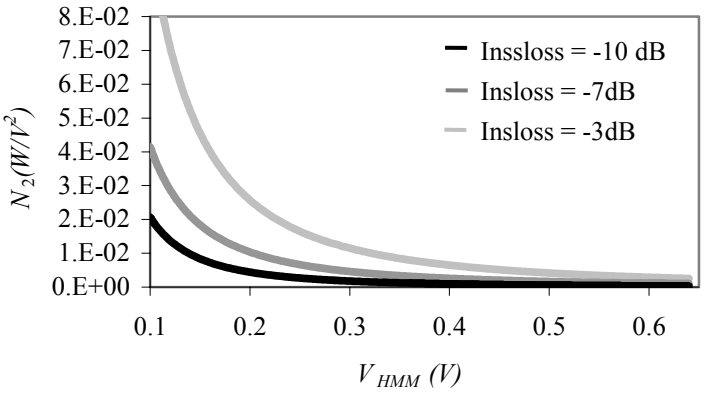


**Figure 4.24** The simulated magnitude of $N_2$ as a function of $V_{\mathrm{HMM}}$ for different values of insertion loss. The optical input power is 1 mW.

Currently a commercial 10 GHz MZ modulator has a $V_\pi$ of 4.5 V and an optical insertion loss of about 4 dB [13] resulting in a $N_2$ of $9\times10^{-5}$ W/V$^2$ at 1 mW optical input power. Our 14.6 GHz $LiNbO_3$ microdisk modulator has a $V_{\mathrm{HMM}}$ of 0.6 V and insertion loss of 10 dB. Resulting in a $N_2$ of $7\times10^{-4}$ W/V$^2$ (at 1 mW optical input power) that is 8 times larger.

## 4.5 Microdisk photonic self-homodyne RF receiver

### 4.5.1 Modeling

The calculation for the single tone baseband signal can be extended to more general baseband signals such as video and data. For an arbitrary baseband signal the received RF voltage may be written as:

$$V_{RF} = V_0\left(1 + m_I B(t)\right)\cos(\omega_{RF} t) \tag{4.18}$$

where $B(t)$ is an arbitrary baseband signal. The optical output power fed to the detector can be calculated using equation (4.7) in the electro-optic transfer function ($f_{EO}$). Given the frequency dependent photodetector responsivity ($R(\omega)$) the photocurrent can be calculated as follows:

$$P_{o,out}(\omega) = \mathcal{F}\{P_{o,out}(t)\} = \mathcal{F}\{f_{EO}(V_{RF}(t))\} \tag{4.19}$$

$$i_p(t) = \mathcal{F}^{-1}\{R(\omega) \times P_{o,out}(\omega)\} \tag{4.20}$$

We have simulated the signal flow in the photonic RF receiver to show details of the down-conversion process in both the frequency and time domain. Fig. 4.25(a) shows the modulated transfer function when the laser emission wavelength ($\lambda_{laser}$) is centered at one of the microdisk optical resonant wavelengths and the modulator is fed by the data modulated RF carrier. $\Delta\lambda_{RF}$ is the maximum shift in resonant wavelength due to the applied RF voltage (this shift is exaggerated to show the down-conversion mechanism). In the simulation, the RF carrier frequency $f_{RF}$ = 10 GHz is modulated by a 62.5 Mb/s non-return-to-zero (NRZ) data stream with a modulation index of $m$ = 0.8. Fig 4.25(b) shows the RF spectrum of the transmitted-carrier input signal and the inset shows the original data stream in a 640 ns time interval. Fig 4.35(c) shows the calculated spectrum of the optical output intensity. Nonlinear modulation generates the baseband signal and high-frequency components around 20 GHz.

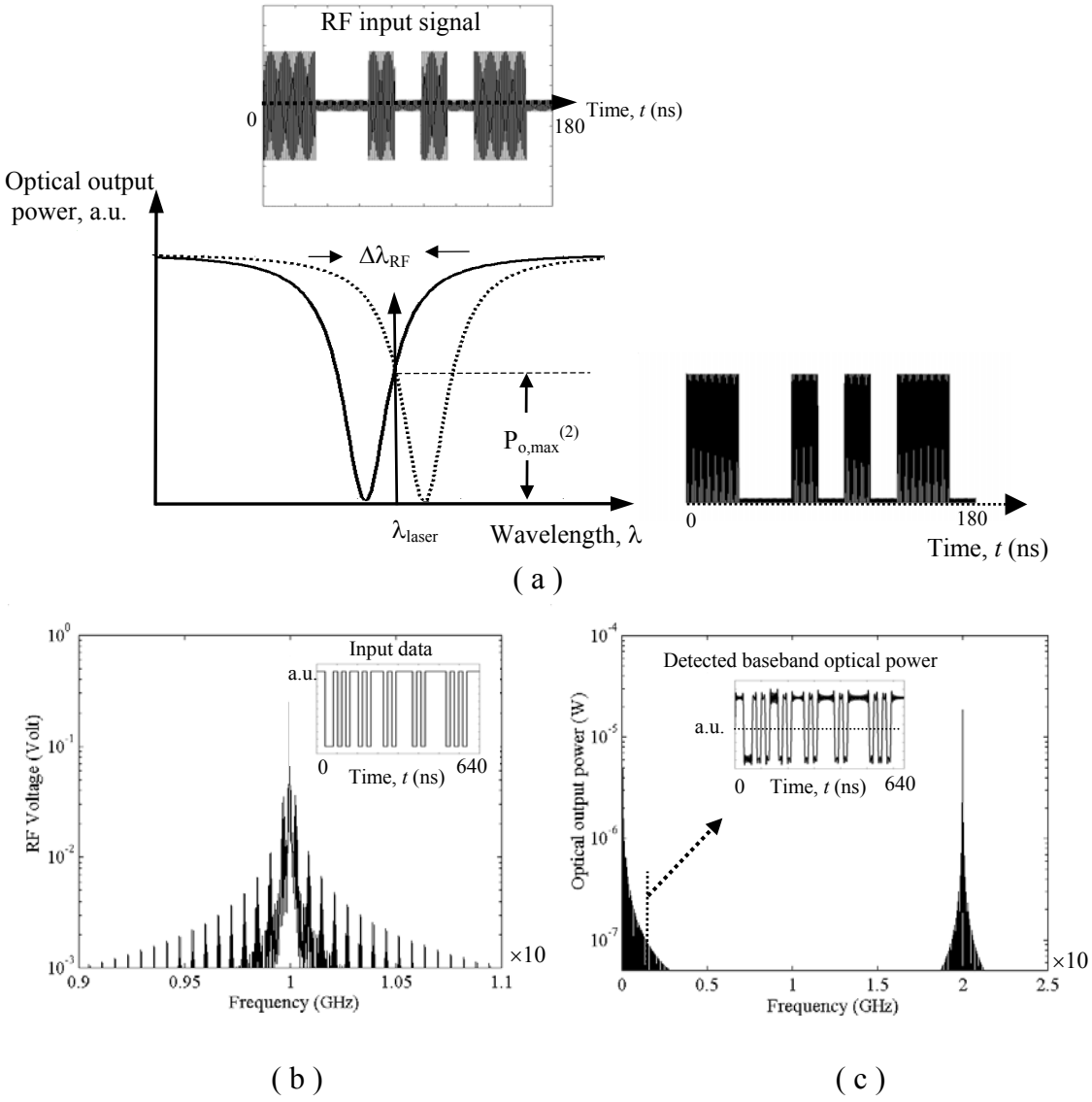


**Figure 4.25** Simulated signal flow in a self-homodyne RF receiver. (a) Modulated optical transfer function when the laser emission wavelength ($\lambda_{laser}$) is centered at one of the microdisk optical resonant wavelengths and the modulator is fed by the data modulated RF carrier. The RF carrier frequency is 10 GHz and is modulated by a 62.5 Mb/s data stream with a modulation index of $m_I$ = 0.8. The modulation amplitude is exaggerated to show the down-conversion mechanism. (b) Spectrum of the transmitted-carrier RF input signal. The inset shows the original data stream in a short time interval (640 ns). (c) Calculated spectrum of the optical output intensity. Nonlinear modulation generates the baseband signal and high-frequency components around 20 GHz. The photodetector bandwidth of 0.1 GHz (dashed line) filters out the high-frequency components and only the baseband is converted to an electric signal. The inset shows the detected data stream again in a 640 ns time interval

The photodetector bandwidth of 150 MHz (dashed line) filters out the high-frequency components and only the baseband is converted to an electric signal. The inset shows the detected data stream once again in a 640 ns time interval.

### 4.5.2 Experimental results

**Single tone down-conversion:**

In our initial experiments we used a single tone baseband signal to study the effect of RF modulation index ($m_I$) and RF power on down-conversion efficiency and its linearity. Fig. 4.26(a) and (b) are photographs of the 14.6 GHz microdisk modulator. Fig. 4.26(c) is a schematic diagram of the experimental arrangement. The modulator uses a 400 μm thick $LiNbO_3$ microdisk of 3 mm diameter and a free spectral range of $\Delta\nu_{FSR}$ = 14.6 GHz. The laser source is a tunable single mode laser with 0.05 pm wavelength resolution and a linewidth of less than 0.5 MHz. The laser wavelength is always tuned to the minimum of the chosen transmission dip to maximize the second-order nonlinear modulation strength ($N_2$). The RF signal is a 10 MHz single tone baseband signal mixed with a 14.6 GHz RF-carrier in a double-balanced RF-mixer. By DC-biasing the IF port of the mixer we can control the modulation index ($m_I$) and hence the magnitude of the transmitted power at the carrier frequency.

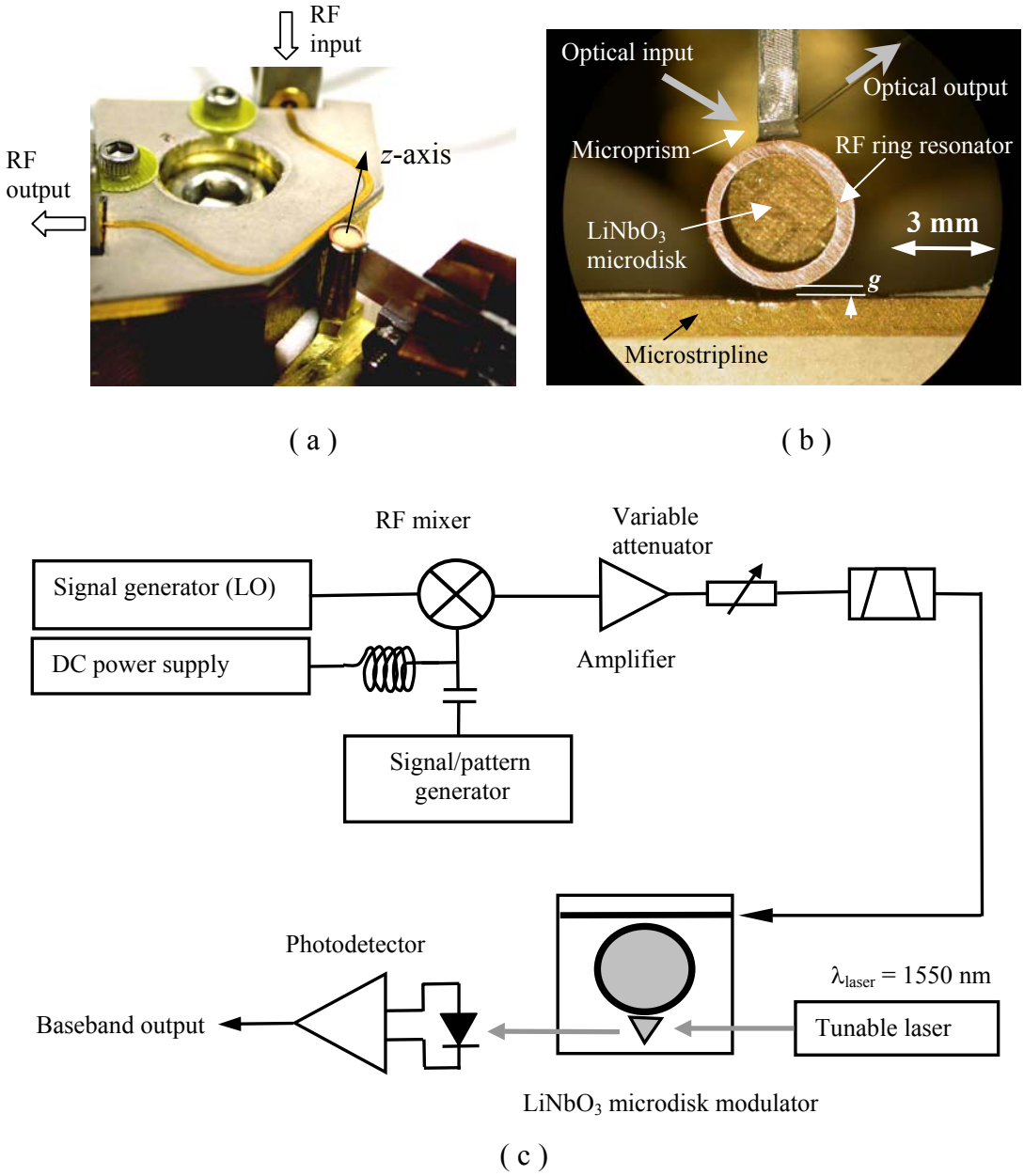


**Figure 4.26** (a) Photograph of the $LiNbO_3$ microdisk modulator. (b) A close-up view of the modulator showing the microstripline, $LiNbO_3$ microdisk, microprism, microring RF resonator and the output fiber. (c) Schematic diagram of the experimental arrangement used for photonic RF down-conversion measurements. The RF modulation index ($m_I$) is tuned using the DC bias on the mixer. The laser is a tunable single mode laser with a resolution of 0.1 pm and linewidth of less than 0.5 MHz. The RF filter eliminates any low frequency component generated due to nonlinearities in RF devices. The local oscillator frequency is 14.6 GHz that is equal to the optical free spectral range of the microdisk modulator.

The RF signal is fed to the microdisk modulator through a bandpass RF filter with 1 GHz bandwidth around 14.5 GHz, to make sure that all of the nonlinear products generated in the RF components are filtered out. The optical output is detected in an amplified photodetector with a bandwidth of 150 MHz and responsivity of 3 mV/μW.

Fig. 4.27 shows the down-converted optical power against the total RF input power when $m_1 = 0.8$. The black circles are the experimental data and the white circles and dashed line are the simulated data. The inset shows the optical resonance selected for nonlinear modulation.

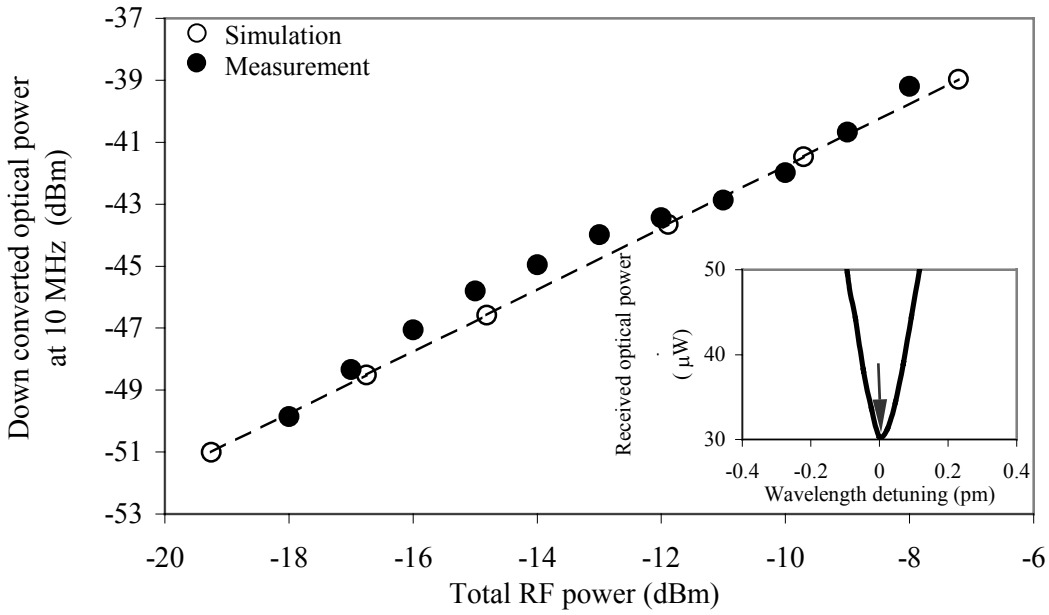


**Figure 4.27** The measured and calculated baseband modulated optical power versus total RF input power. The inset shows the optical spectrum of the WG resonance chosen for down-conversion ($Q$ = $2.7\times10^6$, $N_2 = 2.23\times10^{-2}$ mW/V$^2$).

The arrow indicates the location of the laser wavelength, $\lambda_{laser}$. The optical resonance has a $Q$ of $2.7\times10^6$ and a $N_2$ coefficient of 0.023 mW/V$^2$ ($V_{HMM} = 0.7$ V).

The simulated data in Fig. 4.28 are calculated using $m_I N_2 V_0^2/2$ and knowing that the total average RF power of a single tone modulated RF carrier (Equation 3) is given by $P_{RF} = V_0^2(1+ m_I^2/2)/100$ (this can be easily calculated by integrating the average power of the RF signal). Fig. 4.28(a) shows the variation of the down-converted optical power at 10 MHz as a function of the modulation $m$ and for three resonances with different quality factors. The modulation index is tuned to the desired values by changing the DC bias applied to the mixer.

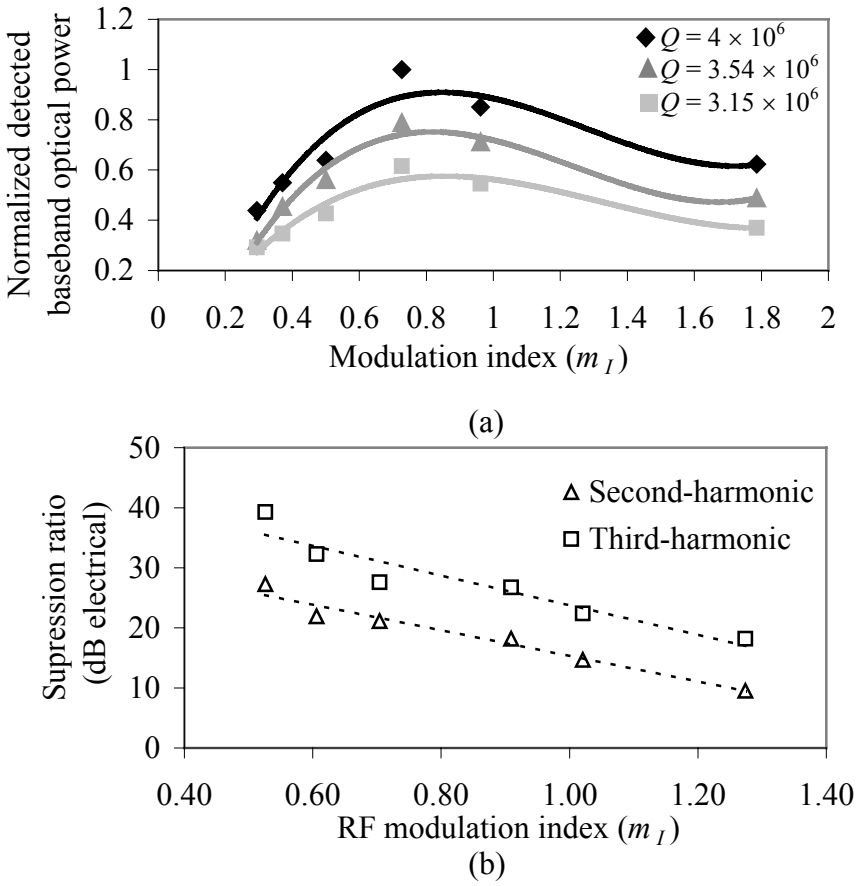


**Figure 4.28** (a) Measured baseband modulated (10 MHz) optical output power against $m$ for three optical modes with different optical quality factors. (b) Measured second and third Harmonic suppression ratios (electrical) against $m$.

The total received RF power is about -15 dBm that corresponds to $V_0$ = 0.05 V (3). Since for the optical resonance used $V_{HMM}$ is around 0.8 V, so $V_0 < 0.1\ V_{HMM}$ guarantees device operation in the small-signal regime (section III). As may be seen in Fig. 4.28(a), down-conversion efficiency is maximized around $m_I$ = 0.8, in very good agreement with the simulated curve for an ideal square law mixer.

Also, as anticipated, the amount of down-converted power increases as we increase the optical $Q$ (a larger $Q$ results in a larger $V_{HMM}$ and therefore a larger $N_2$). To evaluate the linearity of the down-conversion process we have measured the detected power at the second and third harmonic of the baseband signal (20 MHz and 30 MHz respectively).

In a perfect square law modulator the third harmonic should be absent but the chosen optical resonance lacks an ideal symmetric shape and so generates odd harmonics. Fig. 4.28(b) shows the harmonic suppression ratio against $m$. As predicted (Fig. 4.11(b)) the suppression ratio decreases as $m_I$ increases. At $m_I$ = 0.8 the second-harmonic suppression ratio is about 17 dB (electrical).

**Down-conversion of digital data**

To demonstrate data transmission we use the arrangement in Fig. 4.26(c) but replace the signal generator with a NRZ pattern generator and the photodetector with a digital photoreceiver. The photoreceiver has a –3 dB frequency bandwidth of 120 MHz and a sensitivity of –34.5 dBm. Fig. 4.29(a) shows the measured frequency spectrum of the input RF signal and the down-converted signal after detection. The

carrier frequency is 14.62 GHz and the baseband data is a 10 Mb/s NRZ $2^7$-1 pseudo-random bit stream (PRBS). Fig. 4.29(b) shows the measured bit error ratio (BER) against the total RF input power.

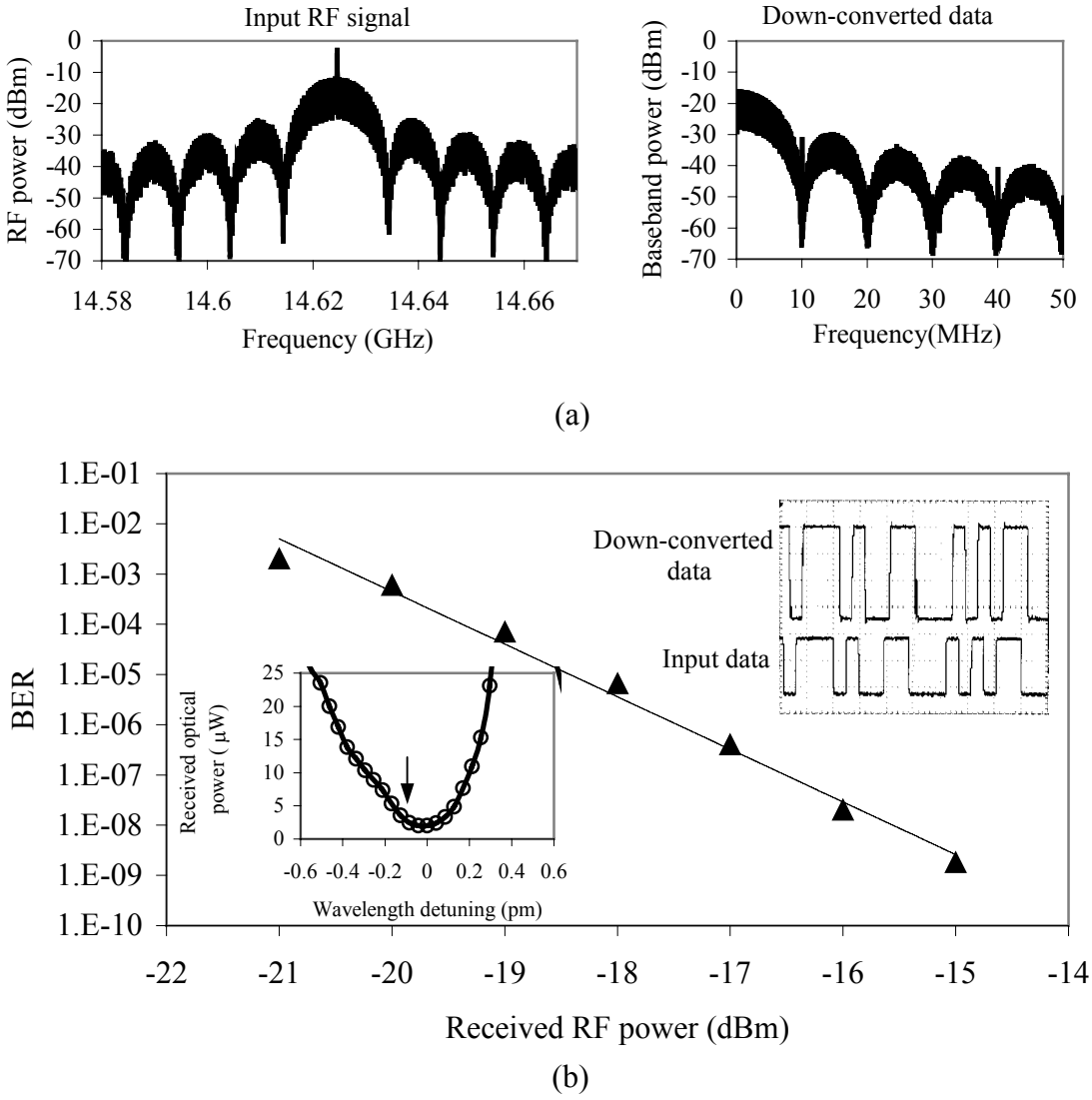


**Figure 4.29** Measurement results of photonic data down-conversion in $LiNbO_3$ microdisk modulator. (a) The frequency spectrum of the input RF signal and down-converted signal. The RF carrier frequency is 14.6 GHz and it is modulated by a 10 Mb/s $2^7$-1 NRZ PRBS bit stream. (b) The BER sensitivity of the photonic RF receiver. The RF power is the measured RF power within 10 MHz bandwidth centered around 14.6 GHz. The right inset shows the input and detected data in time domain. The left inset shows the optical spectrum of the selected WG resonance.

The received RF power is defined as the measured RF power within 10 MHz bandwidth centered around 14.6 GHz. The left inset shows the spectrum of the optical resonance with $Q = 2\times10^6$. The inset on the right shows the input and down-converted data in the time domain.

In Fig. 4.30 the measured eye diagrams at 10 Mb/s, 50 Mb/s and 100 Mb/s are shown. The received RF power is –15 dBm. The maximum data rate is limited by the optical $Q$ to approximately 100 Mb/s. We note that the down-conversion efficiency can be increased by reducing the disk thickness ($h$) and employing a high-$Q$ RF ring resonator (both these factors lead to a larger $N_2$ coefficient).

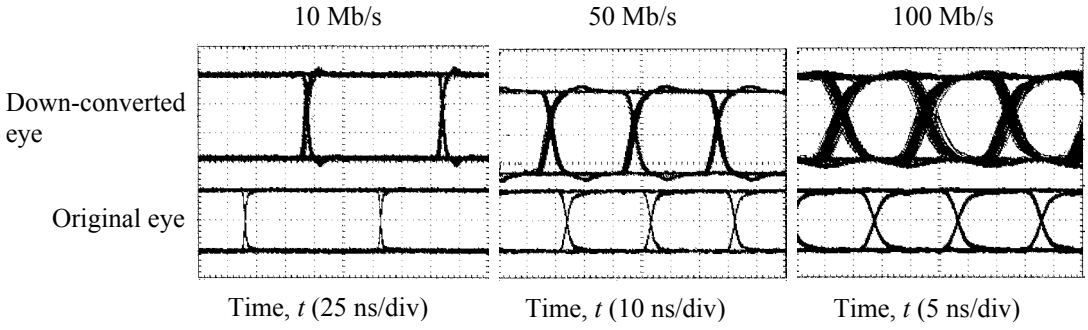


**Figure 4.30** Measured eye diagrams at 10 Mb/s, 50 Mb/s and 100 Mb/s (received RF power = -15 dBm).

### 4.5.3 Noise in microdisk photonic self-homodyne RF receiver

A precise analysis of the noise performance of the photonic self-homodyne RF receiver is a very difficult task due to the variety of noise sources in the system. Here we just want to identify these noise sources and derive a simple analytic

expression for the overall signal to noise ratio of the receiver as function of the device parameters.

Fig. 4.31 is a schematic diagram of the signal and noise flow in the receiver.

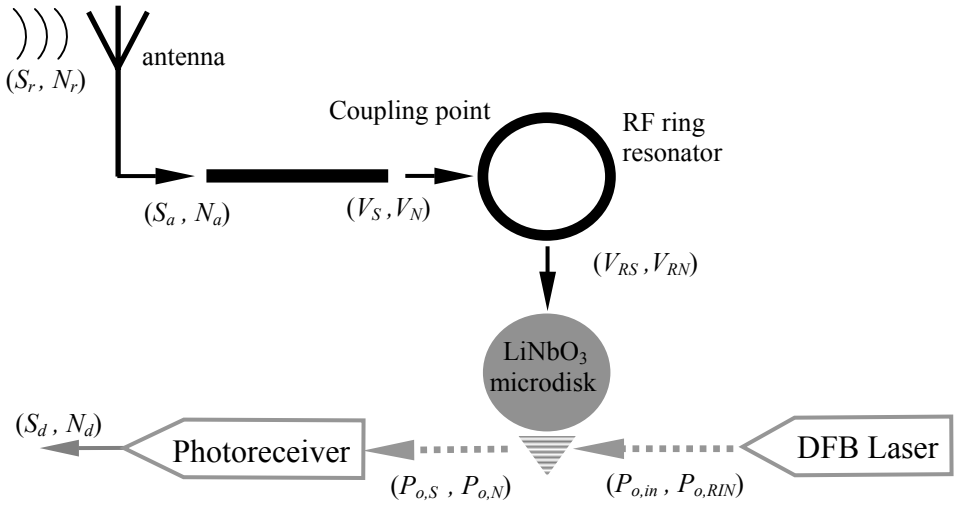


**Figure 4.31** Schematic diagram showing the signal and noise flow in the photonic self-homodyne receiver

For simplicity we assume that the baseband signal is a single tone with the frequency $\omega_b$. The received signal ($S_a$) and noise ($N_a$) power from the antenna are fed to an open terminated microstripline. The microstripline attenuates the signal and adds some thermal noise. The voltage amplitude of the signal and noise at the coupling zone can be written as:

$$\text{(a)}\quad V_S = 2\sqrt{2Z_0 S_a / L_T} \qquad \text{(b)}\quad V_N = 2\sqrt{2Z_0[N_a / L_T + k_B TB(L_T - 1)]} \quad (4.21)$$

where $L_T$ is the loss factor for the mictorstripline, $k_B$ is the Boltzman factor and $B$ is the bandwidth defined by the optical modulation bandwidth, which is limited by optical $Q$ ($BW \sim \nu_{laser}/Q$).

Since the fundamental resonance of the RF ring resonator has a voltage gain $G_v$, the amplitude of the voltage oscillation on the ring resonator is $V_{RS} = G_v V_S$ while the amplitude of the voltage noise induced on the ring resonator is not necessary $G_v V_N$ because the noise isn't coherent and can not build a resonant field on the resonator similar to a coherent signal. So we assume that the induced noise on the ring resonator is related to the noise on the microstripline with unknown coefficient $G_{VN}$. The ring resonator also adds extra thermal noise to the signal due to its resistance and temperature. Since the temperature of the ring resonator is a function of RF input power, one may expect that the thermal noise power is proportional to $V_S^2$ so the total voltage noise across the microdisk is:

$$V_{RN} = G_{VN} V_N + \sqrt{4 R_{ring} k_B B T(V_S^2)} \tag{4.22}$$

where $R_{ring}$ is the resistance of the ring resonator and $T(V_S^2)$ is the ring temperature as a function of RF power at the coupling point.

Now we need to calculate the optical output power modulated at baseband frequency $\omega_b$ and the output optical noise within the bandwidth between DC and $\omega_b$ that is approximately the same as $B$. The baseband modulated optical power can be easily calculated $P_{o,S} = \frac{N_2}{2} m_I V_{RF}^2$ using while the calculation of the output optical noise is much more difficult. The baseband optical output noise power consists of three major components: (1) $P_{o,RIN}$: Laser RIN, (2) $P_{o,mix}$: The optical noise generated as a result of electro-optical mixing of the resonator voltage noise around RF carrier frequency ($V_{RN}$) and the RF signal frequency components, and (3) $P_{o,bb}$: The optical

noise generated by the resonator voltage noise ($V_{RN}$) at frequencies smaller than $\omega_b$ (baseband frequencies).

The first component can be easily calculated using equation 2.10 and replacing $P_{o,out}$ with $P_{o,S}$ :

$$P_{o,RIN} = (10^{RIN/10} \times \Delta f)^{\frac{1}{2}} P_{o,S} \tag{4.23}$$

The second component is more complex since it involves down-conversion and mixing. If we add a single frequency noise component to the RF signal, the RF voltage at the coupling point will have the following form:

$$V'_{RF} = V_S\left(1 + m_I \cos(\omega_b t)\right)\cos(\omega_{RF} t) + V_{RN} \cos(\omega_N t + \varphi_N) \tag{4.24}$$

where $\omega_N$ is an arbitrary frequency within a bandwidth $B$ around $\omega_{RF}$. Now knowing $P_{o,out} = N_2 V^2_{RF}/2$ (equation 4.6), we can derive all the noisy baseband frequency terms by calculating $(V'_{RF})^2$. If we just keep the first order noise terms it can be shown that only three mixed terms will have frequencies smaller than $B$:

(a) $V_N V_S \cos(\omega_{RF} t - \omega_N t - \varphi_N)$

(b) $\frac{m_I V_N V_S}{2} \cos(\omega_b t + \omega_{RF} t - \omega_N t - \varphi_N)$

(c) $\frac{m_I V_N V_S}{2} \cos(\omega_b t - \omega_{RF} t + \omega_N t + \varphi_N)$ (4.25)

So if the we have a uniform noise distribution within a bandwidth $B$ round $\omega_{RF}$ then the total optical intensity noise amplitude can be written as the summation of the optical intensity modulation generated by each one of these terms multiplied by the bandwidth:

$$P_{o,mix} = B V_o V_N (1 + m_I) \frac{N_2}{2} \tag{4.26}$$

The third optical noise component is the linear modulation generated by the second term in equation 4.22 and can be approximated using equation 2.8(b) but with $G_v = 1$ (since the voltage gain doesn't amplifies the thermal noise):

$$P_{o,bb} = 2\beta_s \Delta\lambda_{DC} P_{o,\max} (Q/\lambda_{res}) \sqrt{4R_{ring} k_B BT(V_S^2)} \tag{4.27}$$

Now we can use the detector responsivity to calculate the signal and noise currents:

$$\text{(a) } \bar{i}_{OS}^2 = RP_{o,S} \qquad \text{(b) } \bar{i}_{ON}^2 = R(P_{o,RIN} + P_{o,mix} + P_{o,bb}) \tag{4.28}$$

Equation 4.28(b) is the photocurrent generated by the optical noise power but the photodetector also adds the shot noise and dark current noise to the total photocurrent. The total noise current generated in photodetector is given by equation 2.13:

$$\bar{i}_N^2 = 2eB(i_p + i_d) + \frac{4k_b TBF_n}{R_L}$$

here $i_p = R(P_{o,S} + P^{(2)}_{o,\max})$ where $P^{(2)}_{o,\max}$ can be derived using equation 4.11.

So the final signal-to-noise-ratio may be written as:

$$\frac{S_d}{N_d} = \frac{\bar{i}_{OS}^2}{\bar{i}_N^2 + \bar{i}_{ON}^2} = \frac{RP_{o,S}}{\bar{i}_N^2 + R(P_{o,RIN} + P_{o,mix} + P_{o,bb})} \tag{4.29}$$

The equivalent BER may be calculated using equation 3.5.

## 4.6 Summary

Four possible approaches for all-optical down-conversion from a RF signal have been presented: nonlinear photodetection, optical filtering prior to detection,

combination of optical filtering and optical heterodyning, and nonlinear optical modulation.

Preliminary simulations and experimental results shows that by improving the sensitivity of the microdisk modulator each one of these approaches has the potential to take over the task of direct optical down-conversion and eliminate the local oscillator and RF-mixer in conventional electronic wireless receivers for short-distance communication. The limitation on distance is due to a transmitted carrier modulation format that is required for self-homodyne down-conversion. The main challenge here is to choose the best approach and to improve it to a level that can compete with electronic receivers by providing lower power consumption in a smaller volume.

Our photonic self-homodyne architecture combines direct-conversion, self-heterodyning, and microdisk modulator technology to directly extract baseband information from the received signal by the self-mixing of the transmitted carrier and the sidebands in the optical domain. We have shown that the second-order nonlinearity in the transfer function of a $LiNbO_3$ microdisk optical modulator when biased at its minimum transmission point may be used to realize the self-mixing process. Since the optical output power is baseband modulated, the optical-to-electrical conversion is performed in a photoreceiver with a bandwidth limited to that of the baseband.

Receiver operation is demonstrated experimentally by demodulating digital data from a 14.6 GHz RF carrier frequency. The microdisk modulator and the photonic

self-homodyne architecture have the potential to be incorporated into a photonic integrated circuit by using alternative electro-optic materials (such as polymers and compound semiconductors). Reducing the disk diameter will extend the carrier frequency into the mm-wave regime so that this receiver architecture has the potential to be used in future indoor mm-wave wireless systems.

## 4.7 References


[1] J. Marti, V. Polo, F. Ramos, and J. M. Fuster, "Single Mach-Zehnder modulator electro-optical harmonic mixer for broadband microwave/millimeter-wave applications," *Wireless personal communications*, vol. 15, no. 1, Oct. 2000.

[2] G. K. Gopalakrishnan, W. K. Burns, and Catherine H. Bulmer, "Microwave-optical mixing in $LiNbO_3$ modulators," *IEEE Trans. Microwave Theory and Tech.*, vol. 41, pp. 2383-2391, Dec 1993.

[3] A. Narasimba, and E. Yablonovitch, "Code-selective frequency shifting by RF photonic mixing in a dual-electrode Mach-Zehnder modulator," *Electron. Lett.*, vol. 39, pp. 619-620, April 2003.

[4] J. K. Piotrowski, B. A. Galwas, S. A. Malyshev, and V. F. Andrievski, "Investigation of InGaAs P-I-N photodiode for optical-microwave mixing process," *Micriowave and radar*, 1998. MIKON'98, 12th international conference, pp. 171-175

[5] M. Tsuchiya, T. Hoshida, "Nonlinear photodetection scheme and its system applications to fiber-optic millimeter-wave wireless down-links," *IEEE Trans. On Microwave theory and techniques*, vol. 47, pp.1342, 1999.

[6] T. Hoshida, Tsuchiya, "Broad-band millimeter-wave up-conversion by nonlinear photodetection using a waveguide p-i-n photodiode," *IEEE Photon. Technol. Lett*., vol 10, pp.860, 1998.

[7] K.J. Williams, R.D.Esman, and M. Degenais, "Nonlinearities in p-i-n microwave photodetectors," *J. Lightwave Technol.*, vol 14, p.84, 1996.

[8] R.R.Hayes and D.L.Persechini, "Nonlinearity of p-i-n photodetectors," *IEEE Photon. Technol. Lett*., vol. 5, pp. 70, 1993.

[9] M. Dentan and B. de Cremous, "Numerical simulation of the nonlinear response of a p-i-n photodiode under high illumination," *J. Lightwave Technol.* vol. 8, pp.1137, 1990.

[10] K.J.Williams, R. D. Esman and M. Dagenais, "Effects of high space-charge fields on the response of the microwave photodetectors," *IEEE Photon. Technol. Lett.*, vol. 6, pp.639, 1994.

[11] A. A. Abidi, "Direct-conversion radio transceivers for digital communications," *IEEE J. Solid-State Circuits*, vol. 30, pp 1399-1410, Dec 1995.

[12] Y. Shoji, K. Hamaguchi, H. Ogawa, "Millimeter-wave remote self-heterodyne system for extremely stable and low cost broad-band signal transmission", *IEEE Trans. Microwave. Theory and Tech,* vol. 50, pp1458-1468, June 2002.

[13] www.fcsi.fujitsu.com/products/LWCharacteristicsTables/linb03.htm

[14] M. Sugiyama, M. Doi, S. Taniguchi, T. Nakazawa, and H. Onaka, "Low-drive voltage $LiNbO_3$ 40-Gb/s modulator", *IEEE Leos news letter*, vol. 17, no. 1, pp. 12-13, Feb 2003.

# Chapter 5

# Conclusion and future work

## 5.1 Introduction

In the previous chapter the key aspects of a self-homodyne photonic RF receiver based on $LiNbO_3$ microdisk modulator technology was described. The proof-of-principle experiments and analytical studies show the feasibility of employing this type of receiver in indoor wireless links or short distance fiber-feed backbone networks.

In this final chapter we explore future research challenges toward building a practical photonic RF wireless link. We start with the receiver side and show that by adding extra features to our design and employing alternative electro-optic materials, a fully integrated RF-photonic receiver with adequate sensitivity is possible. Next we review the state-of-the-art in RF/mm-wave generation using optical heterodyning. We discuss the possibility of building a photonic RF-mm wave transmitter that, when combined with our receiver design, can result in an all-optical wireless link. In principle the carrier frequency of this link can be extended to the mm-wave domain without any major complication because the signal processing is performed at optical frequencies.

## 5.2 Self-homodyne photonic RF receiver

In Chapter 4 we proposed two different techniques for direct down-conversion of the baseband information from a transmitted carrier RF signal in the optical domain:

1) Modifying the spectrum of the modulated optical carrier prior to detection.
2) Nonlinear optical modulation.

We refer to these techniques as DOF (down-conversion through optical filtering) and DNOM (down-conversion through nonlinear optical modulation) respectively. A self-homodyne photonic RF receiver can employ either one of these techniques to eliminate the high-speed electronic circuitry from the receiver side.

The efficiency of both techniques depends on the sensitivity of the optical modulator and the photoreceiver. Although both a traveling wave MZ modulator and a resonant microdisk modulator can be used for linear or nonlinear optical modulation in the photonic receiver, we showed that in both situations $LiNbO_3$ microdisk outperforms the MZ modulators.

The DOF technique requires a very sensitive linear optical modulator and a band-stop optical filter while the DNOM technique only requires a very sensitive second-order nonlinear optical modulator. On the other hand the DNOM technique is more sensitive to wavelength fluctuations as well as thermal and mechanical perturbations. This may be explained by observing the behavior of the first and second derivatives of the electro-optic transfer function of the microdisk. As may be seen in Fig. 4.21, $N_2$ is more sensitive to the bias point than $N_1$. For the modulator simulated in Fig.

4.21 $N_2$ is 5 times more sensitive to the difference between the resonant wavelength and the laser wavelength compared to $N_1$. Since the down-conversion efficiency of DOF and DNOM techniques directly depends on $N_1$ and $N_2$ respectively, therefore DOF is more stable.

Another difference between the two techniques is the amount of DC optical power received by the photoreceiver that affects the detector shot noise. In DOF the laser wavelength is biased to the middle of the optical resonance so given the small magnitude of the received RF power a relatively large amount of optical output power is not modulated. This DC optical power cannot be filtered out without affecting the baseband modulated optical power. Assuming the total modulated optical power is $0.01P_{o,max}$ and the laser wavelength is biased at $0.25P_{o,max}$, the DC optical power is 25 times larger than the total modulated optical power.

In DNOM technique part of the down-converted optical power is DC and since the photodetector speed is limited by the baseband, the up-converted optical power (around $2\omega_{RF}$) is also seen as DC optical power by the photodetector. If the optical resonance is critically coupled, these are the only DC components in the optical power spectrum. As shown in the previous chapter at $m_I$ = 0.8, 25% of the nonlinearly modulated optical power is baseband modulated so the DC optical power received by the detector is about 75% of the total modulated optical power. In conclusion the shot noise in DNOM case is about 25 times smaller than in the DOF case. As explained in Section 4.5.3 a detailed analysis of the noise performance of the photonic receiver is quite complicated therefore depending on what mechanism

dominates the signal-to-noise ratio of DNOM technique may or may not be larger than that of DOF.

In the next section we address the potential modifications that can solve some of the problems associated with these techniques and improve the over all sensitivity of the receiver.

## 5.3 Microdisk photonic receiver: potential improvements

Regardless of the chosen photonic down-conversion technique the performance of the photonic self-homodyne RF receiver is determined by three major factors (1) Power and wavelength stability of the laser. (2) Sensitivity and stability of the microdisk modulator. (3) Responsivity and noise performance of the photoreceiver.

The laser performance is independent of the other components and directly affects the signal-to-noise ratio of the down-converted signal. It is trivial that the laser source in a photonic receiver should have very low RIN, narrow linewidth and very stable wavelength. Although for a given sensitivity, improvement of the modulator and receiver reduces some of the constraints on laser performance, here our goal is to reach the best sensitivity using a commercial high-quality laser. For this reason we will only address the possible improvements in the second and third issues mentioned above.

### 5.3.1 Microdisk modulator

As shown in Chapter 2 the sensitivity of the microdisk modulator is mainly determined by the optical quality factor and the intensity of the modulating *E*-field. The unloaded optical-*Q* is limited by the surface quality of the $LiNbO_3$ microdisk and the presence of the external particles on the sidewall. So a high quality polishing and a clean surface can improve the optical-*Q*. Recently advanced polishing techniques have been developed that can result in optical-*Q*s as high as $10^{10}$ [1]. But we should keep in mind that the required bandwidth puts a fundamental limitation on the *Q* (Fig. 1.10). So ideally we want to reach the bandwidth-limited regime, where the required bandwidth limits the *Q*, as opposed to surface-quality limited case. Optical coupling is also an important issue that affects the loaded optical-*Q* of the resonator as well as the unidirectional nature of the WG resonance. An ideal optical coupling mechanism should be lossless and have a negligible perturbing effect on the optical resonance.

The intensity of the modulating *E*-field inside the microdisk is proportional to the voltage gain factor ($G_v$) of the ring resonator and increases as the microdisk thickness ($h$) decreases.

The voltage gain factor can be improved by employing high quality RF-ring resonators but it will be limited by the RF loss in the ring and $LiNbO_3$ as well as the radiation losses. The simulation and experimental results show that by optimizing the surface quality of the ring resonator loaded RF-*Q*s of larger than 100 are

achievable. The thinnest $LiNbO_3$ microdisk modulator reported so far has a thickness of 150 μm [2] but given the WG mode size and the possibility of fabricating toroidal $LiNbO_3$ microresonators, a thickness of 50 μm seems feasible. Reducing the microdisk thickness from 400 μm (the standard microdisk thickness used in most of our experiments) to 50 μm can increase the *E*-field intensity by a factor of 8. As we mentioned in Chapter 4, the sensitivity of the microdisk modulator is adequately expressed in terms of $V_{HMM}$. Fig. 5.1 shows the simulated value of $V_{HMM}$ as a function of $G_v$, $Q$ and $h$ using the microdisk electro-optic transfer function ($f_{EO}$).

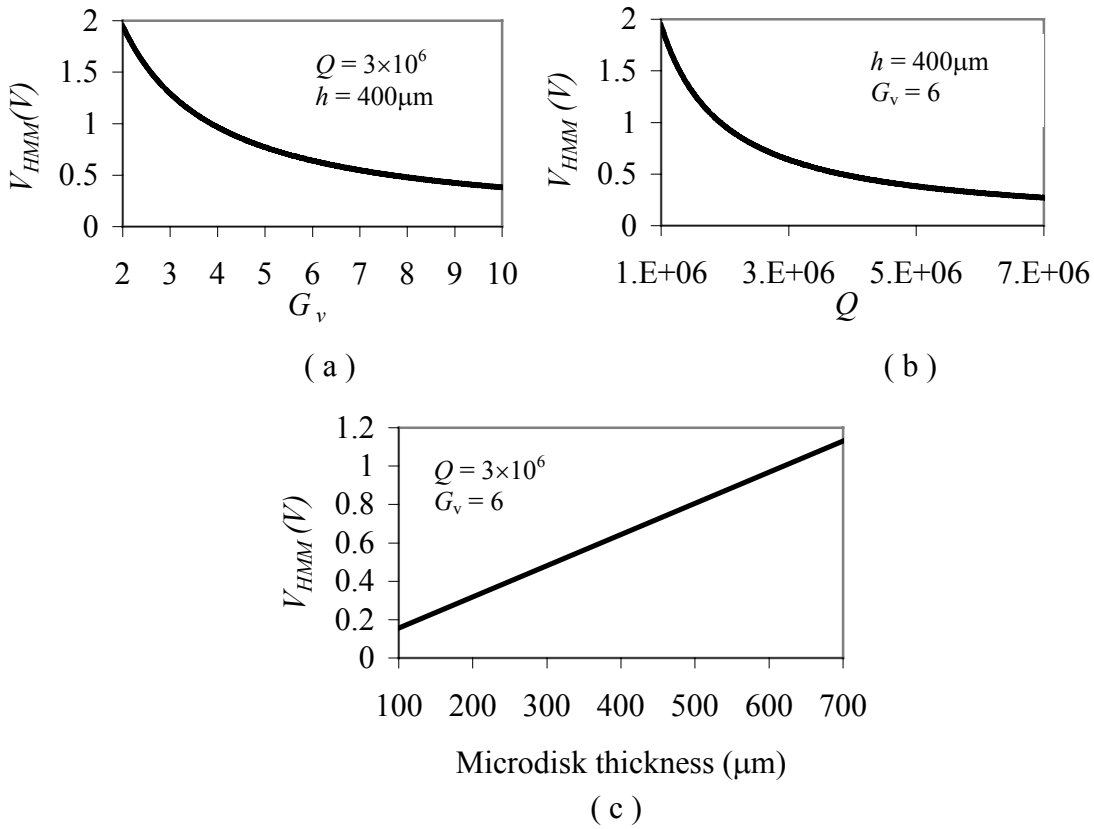


**Figure 5.1** Simulated value of $V_{HMM}$ as a function of (a) $G_v$ , (b) $Q$ and (c) $h$ using the electro-optic transfer function ($f_{EO}$).

Stability is one of the most important issues of the microdisk modulator that requires special attention. The linear or nonlinear modulation efficiency of the microdisk is very sensitive to the location of the laser wavelength relative to the resonant wavelength of the WG mode. The high quality factor of the WG modes makes the modulator extremely susceptible to thermal and mechanical fluctuations as well as the laser wavelength shift. In Chapter 2 we explained how applying a DC voltage on the ring resonator might be used to control the WG resonant wavelength through a feedback loop. The proof-of-concept experiment with a very basic feedback circuit shows that one can lock the laser wavelength to a specific location of the WG slope. This was achieved by comparing the photodetector output with a reference voltage and changing the DC bias voltage accordingly. A feedback loop that can guarantee steady sate operation over a long period of time requires a more sophisticated circuit design. As shown in Fig. 5.2 depending on desired operation regime of the microdisk modulator, the laser wavelength can be locked to different offset wavelengths relative to $\lambda_{res}$. In the case of nonlinear modulation, where the laser wavelength should be locked to $\lambda_{res}$ (zero offset), the feed back loop should be able to determine the sign of the slope because deviation from $\lambda_{res}$ to both directions generates the same amount of variation in optical output power. This will increase the complexity of the control circuit compared to what is shown in Fig. 2.55.

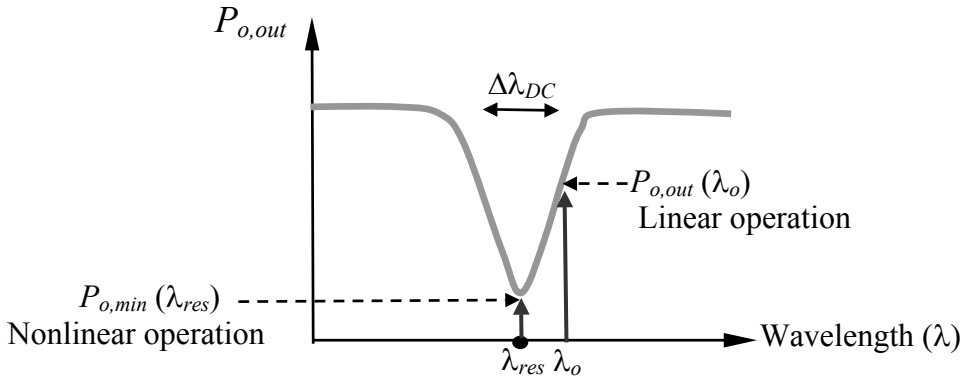


**Figure 5.2** Relative alignment of the laser wavelength and WG resonant wavelength for linear and nonlinear modulation.

We can summarize the future challenges toward a more sensitive and stable microdisk modulator as follows:

1) Improved optical coupling.
2) Fabrication of very thin microdisks with high quality sidewalls.
3) High quality microring resonators.
4) Feed back circuit for wavelength locking.

### 5.3.2 Photoreceiver

The final step in the photonic self-homodyne RF receiver is the detection of baseband modulated optical power with a slow-speed photoreceiver. The sensitivity and noise performance of the photoreceiver directly contributes to the overall sensitivity of the receiver. The minimum detectable optical power for a

photoreceiver is limited by the photodiode responsivity and the transimpedance of the amplifier. State-of-the-art photodetectors can detect optical signals as small as -50 dBm [3]. As we mentioned in Chapter 3 the shot noise in the photodetector is equal to $2eB(I_p+I_d)$. $I_p$ is the total amount of the total photocurrent (generated by the baseband modulated optical power and the DC optical power). We can write the mean square value of the noise photocurrents as:

$$\overline{i_N}^2 = 2eB[I_p + R(P_{o,ac} + P_{o,dc})] \tag{5.1}$$

where $P_{o,dc}$ and $P_{o,ac}$ are the received DC and AC optical powers respectively. As mentioned before, if we use DNM down-conversion technique, due to low speed response of the photodetector the high-frequency components in the frequency spectrum of the optical output power (around $2f_{RF}$) do not contribute in the AC photocurrent. But these components can still generate shot noise. Therefore $P_{o,dc}$ is the sum of $P_{o,min}$, the DC optical power and the modulated optical power at frequencies around $2f_{RF}$ (both generated through nonlinear modulation). For a critically coupled WG mode $P_{o,min}$ is zero but the DC and high-frequency components generated through mixing are always present. Although the DC component cannot be eliminated, a band pass optical filter with a bandwidth less than $4f_{RF}$ can eliminate the high frequency optical components around 194 THz $\pm$ $2f_{RF}$ and cancel modulated optical power at $2f_{RF}$. Fig. 5.3 demonstrates the frequency domain signal flow in the presence of the optical filter.

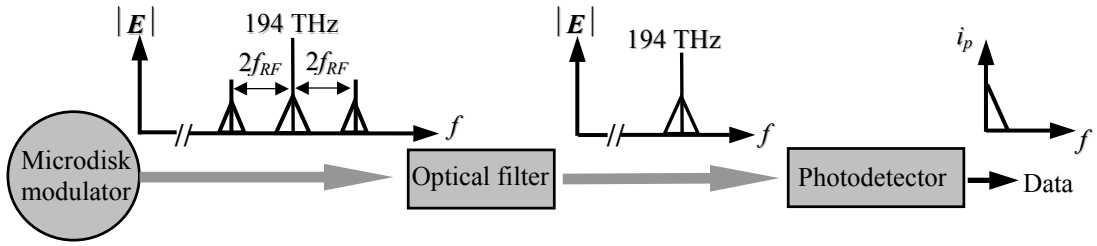


**Figure 5.3** Schematic diagram of frequency signal flow in the photonic RF receiver in the presence of the optical filter.

In conclusion, if DNOM technique is used, employing a high sensitivity photoreceiver and post modulation optical filtering can increase the sensitivity of the photonic self-homodyne RF receiver. In DOF technique there is no high-frequency component in the optical intensity spectrum and filtering cann't remove the large DC component so the only possible modification is to enhance the performance of the photoreceiver.

### 5.3.3 Integration and final design

Fig. 5.4 shows the block diagrams of the microdisk photonic self-homodyne RF receiver based on DNOM technique (a) and DOF technique (b).

Here we summarize the desired specifications of each stage:

*Laser*: The laser should be a DFB laser with a very narrow linewidth and low *RIN*. Although a larger laser power results in a more efficient down-conversion but due to

the small mode volume of WG resonances a high power density can cause thermal and nonlinear instabilities.

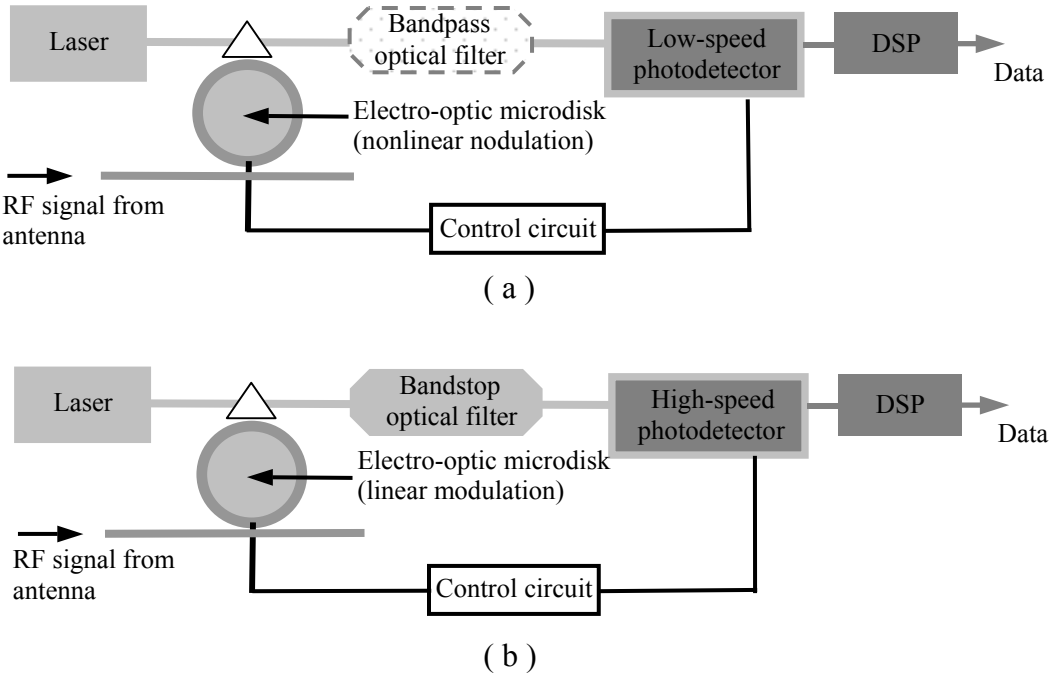


**Figure 5.4** Schematic diagram of two microdisk photonic self-homodyne RF receiver architectures: (a) DNOM, where the microdisk is biased at nonlinear modulation regime and (b) DOF where the microdisk is biased at linear operating regime.

The power threshold at which the modulator becomes unstable depends on the absorption and nonlinear characteristics of the electro-optic material used to fabricate the microdisk.

*Optical waveguides*: Low loss optical waveguides with the potential for integration with other photonic components is desired.

*Optical filter*: If we use DNOM technique, a bandpass optical filter with a bandwidth of less than $4f_{RF}$ helps the shot noise reduction (Fig. 5.5(a)). For DOF technique a band-stop filter with a bandwidth larger than $f_{RF}$ is a requirement for photonic down-

conversion (Fig. 5.5(b)). In both cases the filter role-off is determined by the RF carrier frequency ($f_{RF}$) and the bandwidth of the baseband signal.

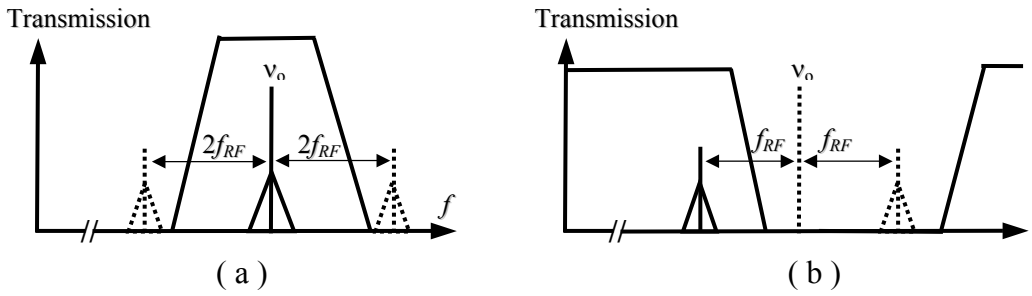


**Figure 5.5** (a) Band pass filter in a DNOM photonic RF receiver decreases the shot noise by eliminating the high frequency components. (b) Band stop filter in a DOF photonic RF receiver eliminates the optical carrier and one of the RF-optical sidebands.

Recently multipole ring resonator based filter have been demonstrated with a very low loss and narrow passbands [3]. The role off of these filters can be increased by increasing the number of ring resonators (poles). Fig. 5.6(a) shows a photograph of a three-pole ring resonator filter and Fig. 5.6(b) shows the spectral response of multipole filters up to 6 poles [3].

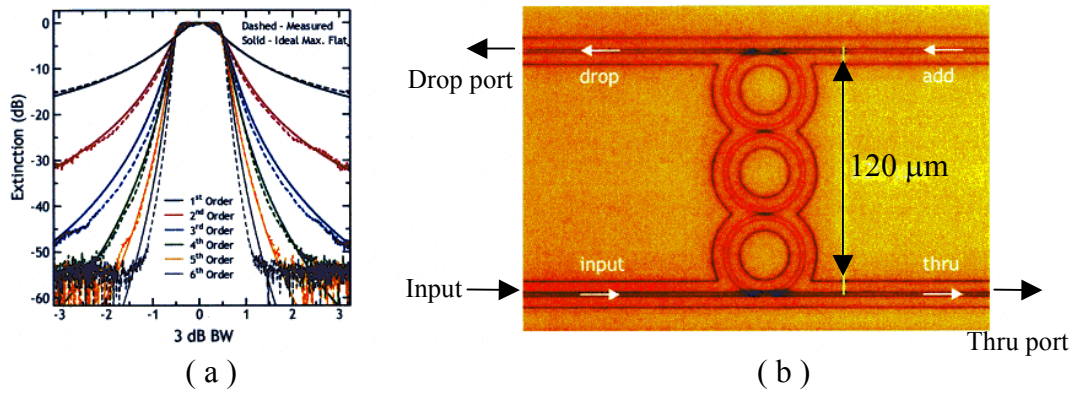


**Figure 5.6** (a) Spectral response of optical filters with different number of ring resonator. (b) The multi ring resonator bandpass optical filter fabricated on *hydex* material system [3]

The microring based filter can be used in both DNOM and DOF photonic receiver architecture because its thru port is a banstop filter and its drop port is a bandpass filter. Since these filters are fabricated on a new optical material called *hydex* the main challenge is the integration of the filter with other photonic and electronics components in the receiver.

**Integration**

Due to versatility of the material and techniques used for fabricating different components in a photonic RF receiver, currently the most feasible approach for building an integrated system is hybrid integration on a silicon bench. Various silicon micromachining techniques that are originally developed for IC industry and MEMS devices can be employed to build features such as V-grooves and steps for mounting the photonic components. Fig. 5.7(a) shows schematic diagram an integrated $LiNbO_3$ microdisk photonic receiver based on hybrid integration technique. The $LiNbO_3$ microdisk, laser and the detector are mounted on pedestals with the proper height. The miniature ball lenses are aligned in a V-groove while the microprism is etched off the silicon substrate. Since silicon has a refractive index larger than $LiNbO_3$ ($3.5 > 2.14$) it can be used for evanescent optical coupling to the microdisk. Potentially the electronic circuitry including the signal processing and the control circuit can be fabricated directly on the silicon substrate. Hybrid integration of optical and electronic elements on silicon bench is the subject of current research [20].

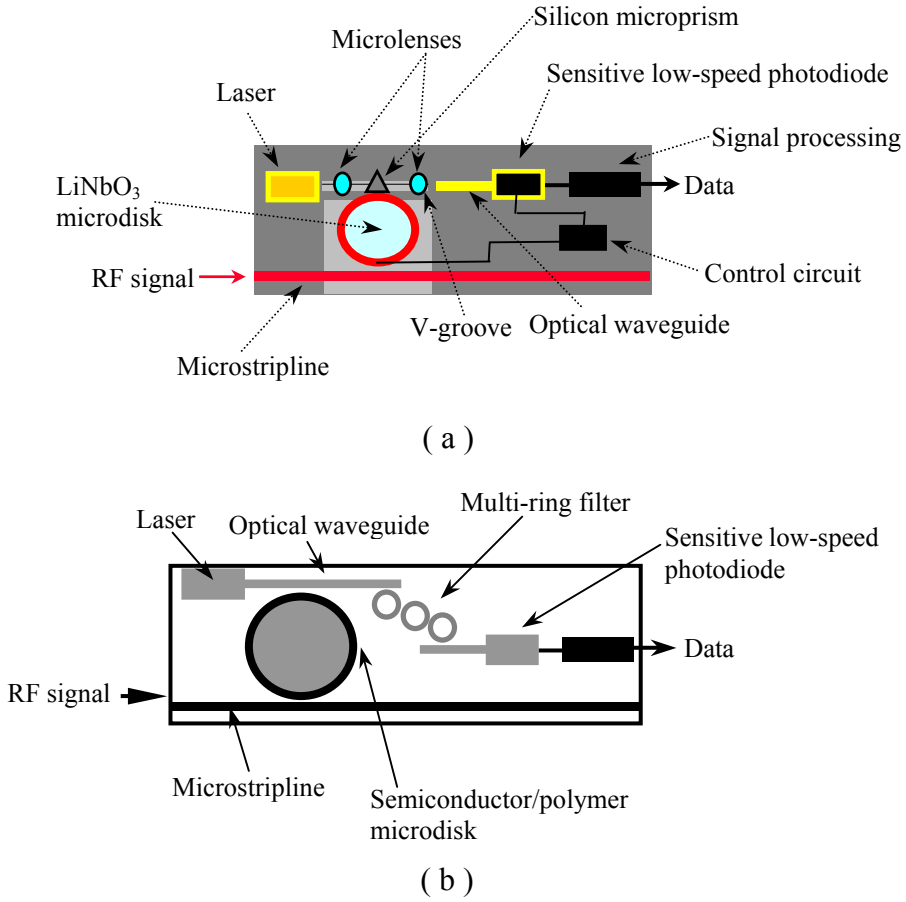


**Figure 5.7** (a) Hybrid integration of a $LiNbO_3$ microdisk photonic RF receiver on a silicon bench. (b) Monolithic integration of a semiconductor microdisk photonic RF receiver based on compound semiconductor material system.

In the future a monolithic fabrication process may be developed to build a fully integrated photonic receiver. For example lasers, detectors, waveguides, microring filters and also microdisk modulator have been already made based on compound semiconductor technology so in principle one may design a process sequence that allows monolithic integration of all these elements on the same substrate (Fig. 5.7(b)).

**Sensitivity**

In order to clarify the benefits of using photonic technology in wireless receiver design here we make a crude comparison between a photonic receiver and an electronic receiver. A state-of-the-art 60 GHz superhetrodyne electronic receiver with a sensitivity of 10 μW (-20 dBm), consumes about 400 mW power [20]. This receiver is built based on 0.15 μm N-AlGaAs/InGaAs HJFET MMIC technology and has a volume of 900 $mm^3$. The receiver consists of a low-noise amplifier (LNA), mixer and Local oscillator (LO). The local oscillator employs a dielectric resonator oscillator (DRO) that is co-integrated with a single-stage wide-band amplifier.

Fig. 5.8 is the schematic diagram of a 60 GHz photonic self-homodyne receiver indicating the specification of each section and estimated power consumption.

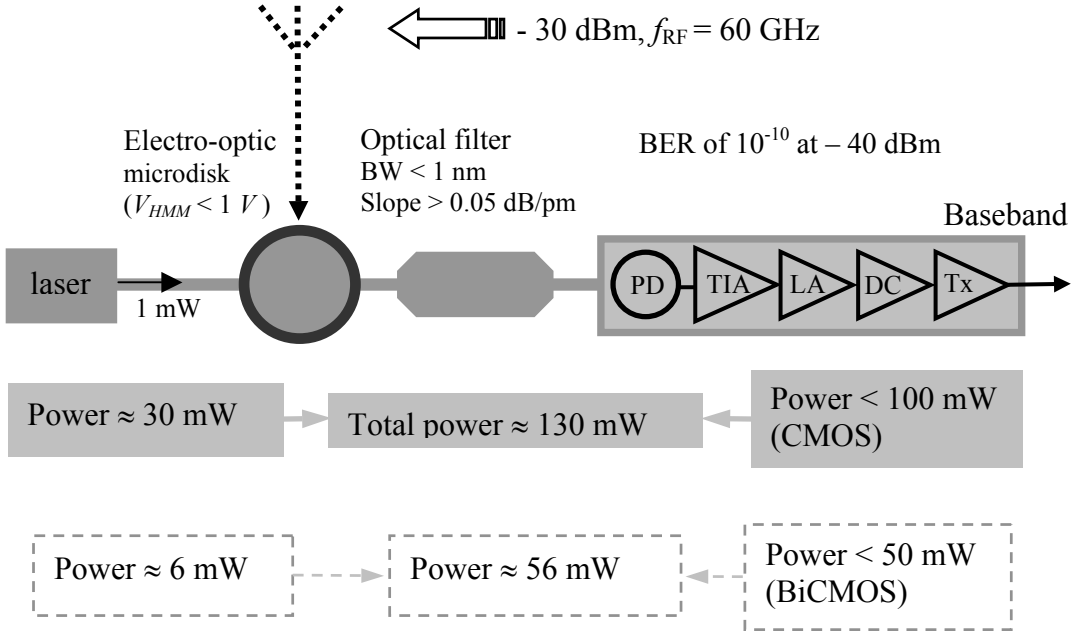


**Figure 5.8** Estimated power consumption using commercially available technology (gray blocks), and costume design technology (dotted line).

Using a low cost laser source (about 3% power efficiency) and digital photoreceiver (based on CMOS technology) the estimated power consumption for a sensitivity of -30 dBm is about 130 mW. If we replace the laser with a more efficient laser (20%) and employ a low power photoreceiver based on BiCMOS technology the total power consumption is reduce to 56 mW. So photonic self-homodyne architecture can improve the receiver sensitivity by a factor of 10 while reducing the power consumption by a factor of 4 compared to an electronic receiver.

Beside low power consumption and better sensitivity the photonic receiver will benefit from the reduced size and complexity as well as low cost fabrication due to the absence of high-speed electronic components.

The estimated value of photonic receiver sensitivity (-30 dB) is based on the current $LiNbO_3$ microdisk modulator technology, commercially available photoreceivers and a moderate input optical power (1 mW). It is very useful to explore the sensitivity limit of the receiver in the absence of current limitations on device technology.

In Chapter 4 it has been shown that the efficiency of down-conversion in a photonic mixer is directly proportional to $N_2$. For a microdisk modulator $N_2$ is determined by the maximum optical output power ($P_{o,max}$) and $V_{HMM}$. Since $P_{o,max}$ = optical insertion loss $\times$ $P_{o,in}$ , Optical insertion loss, optical input power and $V_{HMM}$ are the determining factors for the down-conversion efficiency of the microdisk photonic mixer.

So the overall sensitivity of the self-homodyne microdisk receiver is a function of all of the above-mentioned parameters plus the sensitivity of the digital photoreceiver.

If the sensitivity of the digital photoreceiver and the wireless RF receiver are defined based on the same bit error ratio (BER), we can estimate the overall sensitive of the microdisk photonic self-homodyne receiver using the formalism developed in Chapter 4. In this case the total RF input power that results in a baseband modulated optical power equal to the sensitivity of the digital photoreceiver is the minimum received power or sensitivity of the wireless receiver. This definition is equivalent to equation 1.6 for the sensitivity of photonic RF receiver discussed in section 1.5.

Here we assume a single frequency baseband and an optimized RF modulation index of $m_I = 0.8$. Fig. 5.9(a) shows the calculated receiver sensitivity against $V_{HMM}$ f1or 3 different values of optical insertion loss. The optical input power ($P_{o,in}$) is 1 mW and the sensitivity of the photoreceiver is -40 dBm. Fig. 5.9(b) shows the calculated receiver sensitivity against optical input power ($P_{o,in}$) for two microdisk modulators with $V_{HMM}$ of 0.45 V and 0.1 V. Again the sensitivity of the digital photoreceiver is -40 dBm. Fig.5.9(c) shows the calculated receiver sensitivity against sensitivity of the digital photoreceiver. The optical input power ($P_{o,in}$) is 1 mW and $V_{HMM}$ is 0.1 V. As may be seen a combination of low insertion loss (< 3dB), sensitive digital photoreceiver (<-65 dB) and efficient photonic mixing ($V_{HMM}$ < 0.2 V) results in a dramatic improvement in wireless receiver sensitivity (< -70 dBm).

With this sensitivity the microdisk photonic wireless receiver may be employed in high frequency carrier links such as LMDS[2]. For example EtherAir [3] that is a transceiver for LMDS has a sensitivity of –72 dBm at 26 GHz carrier frequency and –70 dBm at 38 GHz carrier frequency.

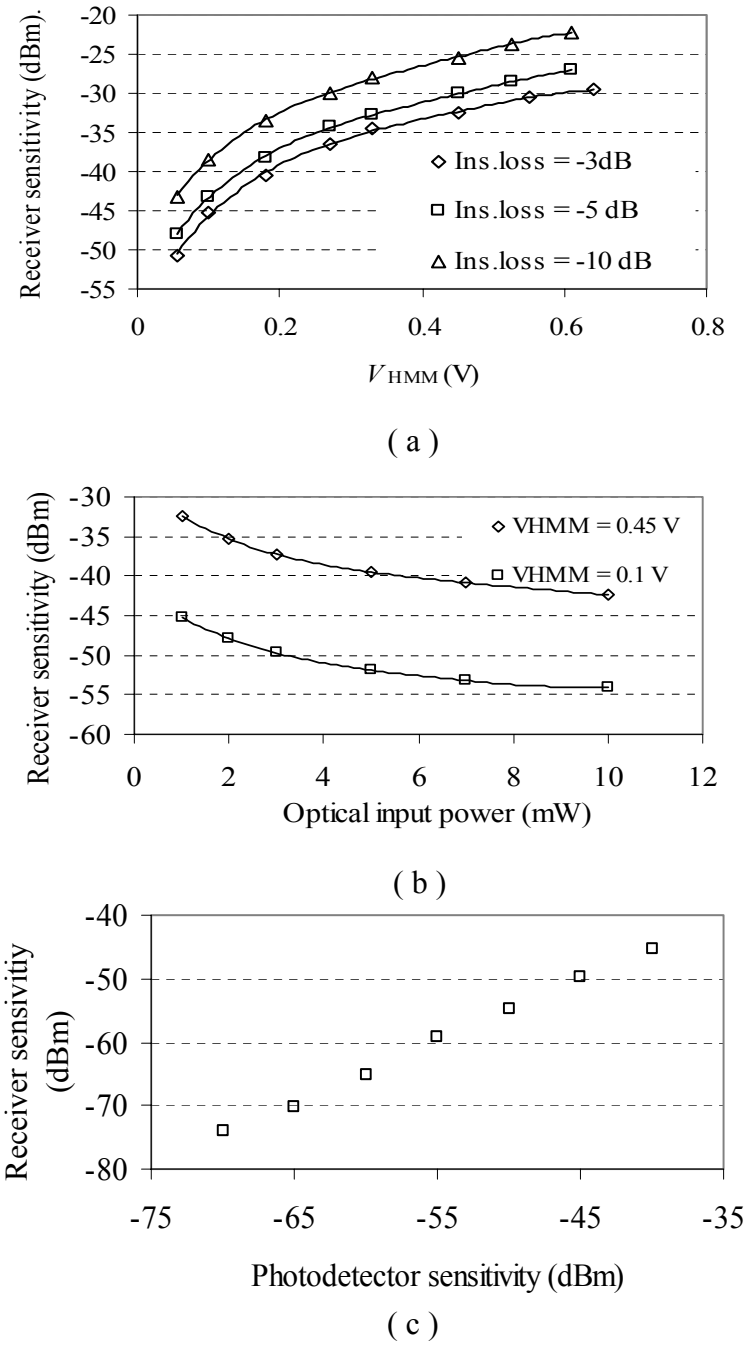


**Fig. 5.9** (a) Calculated receiver sensitivity against $V_{HMM}$ for 3 different values of optical insertion loss (-10dB, -5 dB and -10 dB). The optical input power ($P_{o,in}$) is 1 mW and the sensitivity of the photoreceiver is -40 dBm. (b) Calculated receiver sensitivity against optical input power ($P_{o,in}$) for two microdisk modulators with $V_{HMM}$ of 0.45 V and 0.1 V. The insertion loss is –3 dB. Again the sensitivity of the digital photoreceiver is -40 dBm. (c) Calculated receiver sensitivity against sensitivity of the digital photoreceiver for an optical input power ($P_{o,in}$) of 1 mW, insertion loss of –3 dB and $V_{HMM}$ of 0.1 V.

We should mention these estimations are all for a DNM based photonic receiver. If we use DOF technique for photonic down-conversion we may achieve very high sensitivity by means of optical heterodyning (see section 4.3.3). In this approach heterodyne generation of the RF carrier in the receiver enhances the signal-to-noise ratio and may also relax the restriction of using transmitted carrier format.

## 5.4 Alternative electro-optic materials

Although, based on its electro-optic and mechanical properties $LiNbO_3$ seems to be an excellent material for micro resonator fabrication, but it suffers from incompatibility with the standard integrated optic fabrication processes. The sidewalls of $LiNbO_3$ microdisk are mechanically polished and $LiNbO_3$ cannot be grown and etched on a semiconductor substrate. Investigating the alternative material systems that can provide the same functionality may result in a fully integrated photonic receiver with higher sensitivity. The important parameters that have to be considered in selecting a material system for photonic receiver applications are:

1) Electro-optic activity.
2) RF and optical loss.
3) Optical and RF refractive index.
4) Compatibility with the standard integrated fabrication process.

### 5.4.1 Electro-optic polymers

Electro-optic polymers are special polymers that if their molecules are aligned by applying an *E*-field (poling), they can have large electro-optic coefficient. Recently These materials have been used to fabricate numerous electro-optical devices including electro-optic modulators [4-6].

There has been significant advances in the synthesis of molecules with large optical nonlinearity that has been sterically designed to prevent the large dipole-dipole interactions between the molecules during electric field poling. One of the most promising of these is a ring-locked phenyltetraene bridged chromophore [4], which has been labeled CLD by chemists. The electro-optic molecule needs a host polymer that is thermally stable and also has small optical loss at the wavelength of interest. For example amorphous polycarbonate (APC) has been identified as a promising host material for CLD and the electro-optic polymer is labeled as APC/CLD. The measured electro-optic coefficient ($r_{33}$) of this material is about 90 pm/V at a wavelength of 1060 nm that corresponds to $r_{33}$ of 65 pm/V and 55 pm/V at 1300 nm and 1550 nm respectively [4]. At 1550 nm the measured value of propagation loss in a ridge waveguide fabricated from APC/CLD polymer is about 1.7 dB/cm for TM polarized mode and 1.65 dB/cm for TE polarized mode. Although APC/LCD material is difficult to process using standard photolithography, it has been shown that by adding some additional stages to the standard processing sequence high quality polymer structures can be created. APC/CLD has a refractive

index of 1.6 at 1550 nm and its microwave refractive index is about 1.5 [5]. APC/CLD has been used to monolithically fabricate a polymer micro-ring modulator with a $Q$ of $1.3\times10^5$ on a silicon substrate [5]. This device has been fabricated monolithically on a silicon substrate. The long-term thermal and photo stability of the polymer devices is a serious system issue. Currently the polymer devices have to be packaged in an inert atmosphere to maintain their electro-optical properties.

Research on various aspects of polymer electro-optic devices continues and with further improvement of the polymer electro-optic materials may become a very good candidates for monolithic fabrication of a self-homodyne receiver on a small chip. Electro-optic microdisk and optical waveguides are the only parts of the photonic receiver that can be fabricated based on polymer materials. This may raise difficulties for the monolithic fabrication process because the laser, the detector and the electronic circuitry are fabricated based on semiconductor materials. Some of the critical technologies required for the monolithic integration of polymer electrooptic modulators and VLSI circuitry has been discussed in [6].

### 5.4.2 Semiconductors

Semiconductor materials offer the obvious advantage of monolithic integration of active/passive photonic and electronic devices. Semiconductor photonic is a very mature field and it is as old as laser itself. The main disadvantages of using the

semiconductor materials in electro-optic devices is the fact that the field effect electro-optic mechanisms are weak in semiconductors and other electro-optic mechanisms are accompanied with loss and are wavelength sensitive.

**Compound semiconductors**

Various waveguide structures and optoelectronic devices and circuits have been fabricated based on compound semiconductors [7-14].

The compound semiconductor materials commonly used in optoelectronics are GaAs and InP as substrate and alloys, which can be lattice, matched to these substrates GaAlAs for GaAs and GaInAsP or InGaAlAs for InP. These materials are zincblend type semiconductors and belong to $\bar{4}3m$ symmetry group so their linear electro-optic tensor has only 3 nonzero equal elements that are equal ($r_{41} = r_{52} = r_{63}$). For GaAs $r_{41}$ = 1.43 pm/V that is much smaller than that of the $LiNbO_3$ or electro-optic polymers. But unlike polymers and electro-optic crystals, linear electro-optic effect (Pokels effect) is not the only mechanism for electro-optic activity in semiconductor materials. The subject of electro-optic activity in bulk and heterostructure semiconductor materials is very complicated and has been under investigation for many years [7,8].

The electro-optic mechanisms in compound semiconductors can be summarized as:

1) Pokels effect
2) Kerr effect
3) Franz-Keldysh effect (electrorefractive effect)

4) Quantum confined Franz-Keldysh effect
5) Quantum confined Stark effect
6) Wannier-Stark localization
7) Plasma effect
8) Band-filling effect

These electro-optic effects can be divided into two main categories: carrier and field effects. Also since the quantum confined effects as well as Wannier-Stark effect are exclusively observed in quantum-well structures, electro-optic semiconductor devices can be designed either based on quantum-wells or depletion edge translation. We should mention that except the first two effects that directly change the refractive index, the other effects change the absorption coefficient that is related to refractive index change through Kramers-Kroning dispersion relation. So the electo-optic effects in the semiconductors are mainly accompanied with a change of loss and also they are highly sensitive to the wavelength due to sensitivity of the absorption processes to wavelength. These properties are disadvantageous for designing electro-optic devices based on semiconductors especially resonant devices. For example if the absorption and refractive index change simultaneously in a resonant modulator (such a s microdisk), the spectral profile of resonant mode changes during modulation that can cause problem in both linear and nonlinear modulation performance. So ideally absorption related electrooptic mechanisms should be avoided as much as possible in the semiconductor modulators. Unfortunately even the field effect mechanisms such as Franz-Keldysh effect or quantum confined stark

effect that have beneficial effect on the highly efficient refractive index change degrade the performance, wavelength insensitivity and optical insertion loss.

Recently a microdisk modulator with a bandwidth of 8 GHz and sub-volt drive voltage has been demonstrated [14]. The electrooptic mechanism employed in this device is depletion width translation in a pn-based junction based on InGaAs. The microdisk has a *Q* of 8500 the bandwidth is limited by the capacitance of the device.

It has been shown that depletion-edge-translation lightwave modulators work based on two electric field related and two carrier-related effects: linear electrooptic, electrorefractive (Franz-Keldysh), plasma and band filling. The sum of the refractive index variations produced by each one of these effects, taking into account the waveguide geometry, accounts quantitatively for the experimental phase shifts measured in the devices [7]. Fig. 5.10 shows the voltage dependence of the effective refractive index variation and the corresponding phase shift for a *N-AlGaAs/n-GaAs/P-AlGaAs* waveguide modulator with length of 800 μm at $\lambda = 1.06$ μm. Lines correspond to the theoretical calculations [7]. The dots are the experimental data for TE mode and triangles for TM mode. As may be seen the summation of LEO, ER, PL and BF effect (indicated by total (TE) and total (TM)) is in good agreement with the experimental data. The fastest Mach-Zehnder semiconductor optical modulator reported is a 40 Gb/S InP Mach-Zehnder modulator with a $V_\pi = 2.2$ V [9]. This modulator uses a n-i-n heterostructure on a InP substrate. The length of the active arm is 3 mm. In this modulator, the optical modulation is achieved due to Pockels effect.

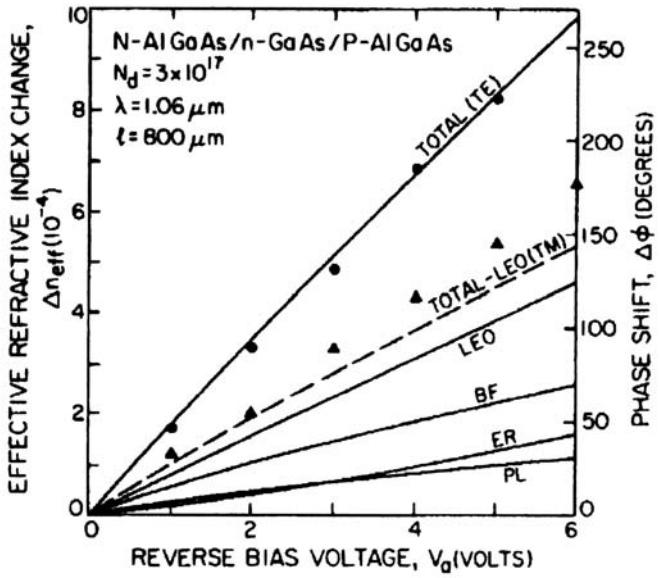


**Figure 5.10** The voltage dependence of the effective refractive index variation and the corresponding phase shift for a N-AlGaAs/n-GaAs/P-AlGaAs waveguide modulator with length of 800 μm at λ = 1.06 μm [7]. Lines correspond to the theoretical calculations. The dots are the experimental data for TE mode and triangles for TM mode

Neither the Franz-Keldysh effect nor the quantum confined Stark effect (QCSE) plays any part in the operation of this modulator. An extintion ratio of 20 dB was obtained for $V_\pi$ voltage of 2.2 at a wavelength of 1550 nm. Between 1530 and 1570 nm, the extintion ratio was still maintained at 13 dB in a fixed voltage swing of 2 V. This modulator can be directly employed in a 30 GHz photonic self-homodyne receiver.

**Silicon**

Silicon photonic is a relatively young field of research and it is attractive because most of the current electronic integrated circuits are silicon based therefore silicon processing is a very mature technology and is capable of fabrication very small and complicated features and structures. Since photonic devices still need the electronic

circuitry for control and processing, it is very useful to have the ability of manufacturing both electronic and photonic devices on the same platform.

Sources and detectors in silicon have not been reported with sufficient efficiency to make them commercially viable as yet, but this is a current active research topic [15-19]. One significant technological issue is associated with the possibility of optical phase and amplitude modulation in silicon.

Pockels effect cannot be observed in silicon owing to centro-symmetric nature of the crystal structure. Refractive index change is possible via Kerr effect, Franz-Keldysh effect and free carrier injection. Although it is widely accepted that free carrier injection (free carrier plasma dispersion effect) is the most efficient of these, this mechanism is not a fast modulation mechanism when compared to field-effect mechanisms.

Fig. 5.11 shows the calculated refractive index change generated by Kerr effect (a) and Franz-Keldysh (b) effect in silicon [19]. Recently a silicon-based modulator has been reported that overcomes the speed limitation due to slow carrier generation and/or recombination process, by using a metal-oxide-semiconductor (MOS) capacitor [17].

This modulator has a bandwidth of 1 GHz and a low speed $V_\pi$ of 12V for a 8mm device and its fabrication process in compatible with conventional CMOS processing. So its efficiency and speed is very low compared to current modulators fabricated based on $LiNbO_3$ or even compound semiconductors.

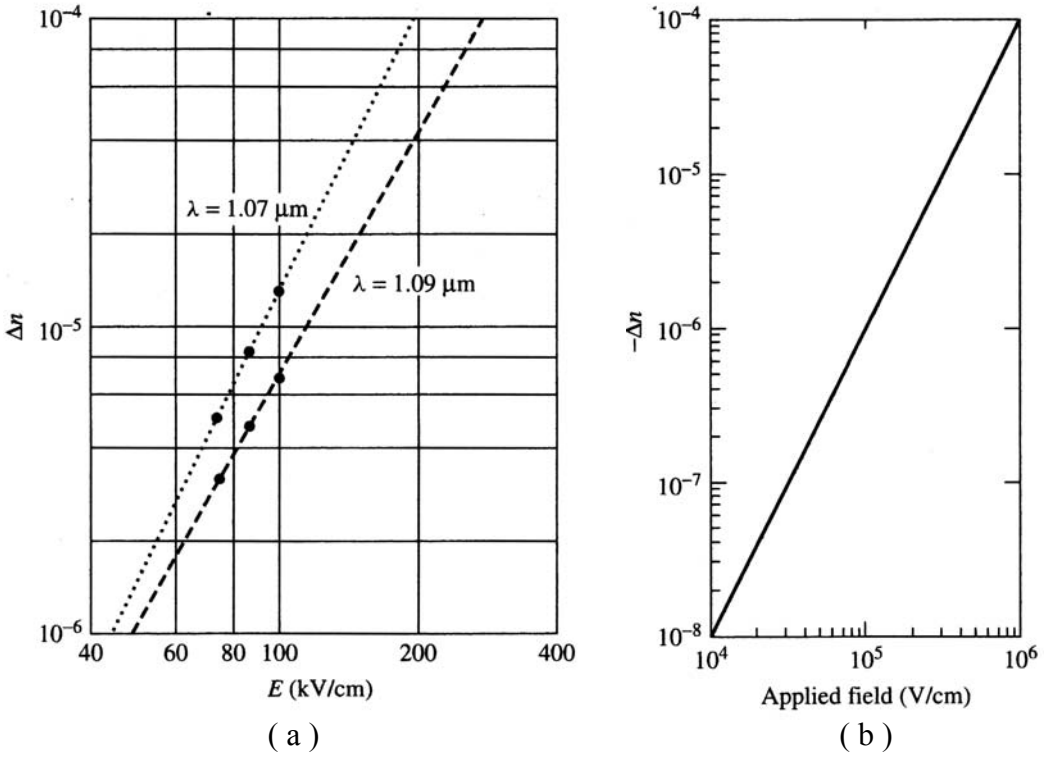


**Figure 5.11** Calculated refractive index change generated by Kerr (a) and Franz-Keldysh effect in silicon [19].

Silicon still has a long way to go before it can be considered as a candidate electro-optic material for microwave-photonic applications.

### 5.4.3 SBN

Strontium Barium Niobate is a well-known photorefractive material that has a high electro-optical coefficient and fast response time. SBN crystals come in a variety of Strontium/Barium atomic combinations. The 60% / 40% ratio, or SBN:60, is well

suited for fabricating microdisk modulators because of its relatively high Curie temperature (75 C). At an optical wavelength of $\lambda$ = 633 nm, SBN 60 has an extraordinary refractive index $n_e$ of 2.2817 and $n_o$ of 2.3103. We estimate $n_e$ = 2.28 at $\lambda$ = 1550 nm by measuring the FSR of a 3 mm diameter SBN:60 microdisk. SBN:60 has a $r_{33}$ of 235 pm/V which is about 8 times larger than that of $LiNbO_3$. So a SBN:60 microdisk modulator has a DC-shift 8 times larger than a $LiNbO_3$ microdisk with the same size.

The main difficulty of using SBN in a resonant microdisk modulator is the RF-optical frequency matching. The value of the relative permittivity for SBN:60 differs greatly from that of $LiNbO_3$ along the optical axis. The measured value for $LiNbO_3$ is $\varepsilon_r$ = 26, which contrasts with $\varepsilon_r$ = 880, the listed value for SBN:60 [20]. In Chapter 2 we showed that even for $LiNbO_3$, matching the effective RF refractive index with the optical refractive index is a very challenging task. So it is evident that simultaneous RF-optical resonance in a SBN microdisk requires major modifications in the RF ring design.

To address this issue we made a 3 mm diameter SBN:60 microdisk optical resonator with a thickness of 300 $\mu$m was studied. Similar to a $LiNbO_3$ microdisk modulator, diamond microprism was used to couple laser light into and out of the microdisk. WG modes at 1550 nm with $Q$ factors in the order of $10^6$ to $5\times10^6$ have been measured for this microdisk [30]. To achieve RF resonance we used a regular ring resonator on top of the microdisk that was slightly elevated from the microdisk surface using very thin gold wires to create an air gap underneath the ring. By

controlling the size of the air gap between the ring and the microdisk surface we were able to match the RF resonant frequency with the optical FSR frequency (13.5 GHz) and observe optical modulation [30]. This proof of concept experiment demonstrates that further modification of the ring resonator may result in a resonant electro-optic microdisk modulator that is, in principle, 8 times more sensitive than an identical $LiNbO_3$ microdisk modulator.

## 5.5 mm-wave photonic transceiver

Pushing carrier frequency in the wireless links to mm-wave frequencies is major challenge for the transmitter design as well as the receiver. Electronic devices lose their efficiency and transmission lines become extremely lossy at these frequencies. Photonic generation of millimeter and sub-millimeter wave signal is a promising technique because it provides several advantages; such as extremely wideband afforded by the characteristics of optical components, and can use low-loss fibers for transmission of very high-frequency signals.

A photonic local oscillator is based on mixing two optical signals separated by the required local oscillator frequency in a high-speed photodiode that its bandwidth is at least equal to the oscillator frequency [25]. So narrow line high power tunable lasers and high-speed photodetectors are the key elements in a photonic mm-wave oscillator. Fortunately tunable high-power lasers with linewidths of less than 1 GHz

are commercially available. But conventional p-i-n photodiodes lose their efficiency at frequencies above 60 GHz. To address this issue two novel photodiode designs have been proposed: 1) Traveling-wave photodetectors (TWPD) [22] and 2) Unitraveling-carrier photodiode (UTC-PD) [23]. So far unitraveling-carrier photodiode has offered the highest output power and speed compared to other technologies. The primary feature of the UTC-PD is that only electrons are the active carriers. This is of great benefit to high-speed and high-output operations. In addition, in the UTC-PD structure, the depletion layer thickness can be designed independently from the neutral absorption layer thickness. Therefore, the carrier transit time can be reduced by narrowing absorption layer thickness without decreasing the CR charging time [23].

Recently a compact UTC-PD module with a WR-8 rectangular waveguide output port for operation in the F-band (90-140 GHz) has been demonstrated [26]. This module generates 17 mW mm-wave power at 120 GHz with a 3 dB of 55 GHz. Fig. 5.12(a) shows a photograph of the module and Fig. 5.12(b) is micrograph of the transformer connecting the UTC-PD and the rectangular waveguide.

Fig. 5.12(c) shows the relationship between the measured mm-wave output power and input optical power at 120 GHz for several bias voltages. The UTC-PD has been also used for sub-millimeter wave generation up to 800 GHz [29]. In this case the sub-millimeter wave emitter uses a log-periodic antenna and a unit-traveling carrier photodiode that have been monolithically fabricated on A InP substrate.

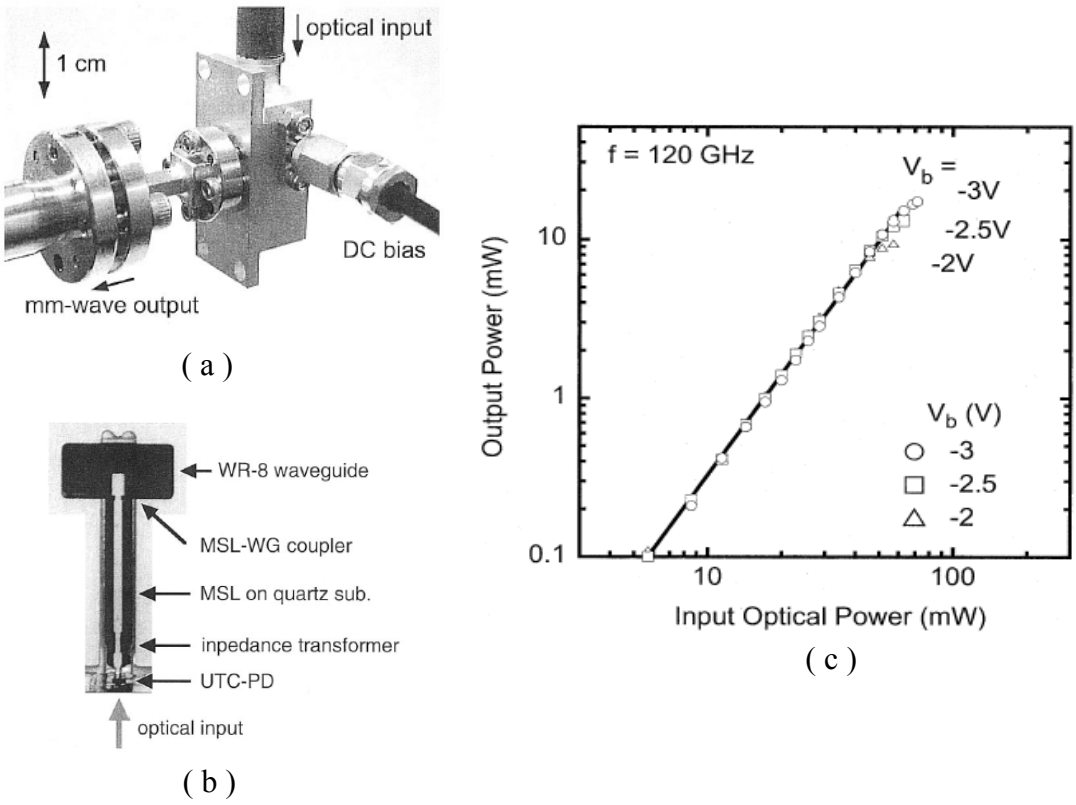


**Figure 5.12** (a) Photograph of the waveguide-output and the rectangular waveguide. of the photonic 120GHz oscillator [26]. (b) Micrograph of the transformer connecting the UTC-PD and the rectangular waveguide. (c) Relationship between the measured mm-wave output power and input optical power at 120 GHz for several bias voltages [26].

The log-periodic antenna has the features of frequency-independent real impedance from 150 GHz to 2.4 THz. The radiation from the antenna is collimated using a silicon lens. Fig. 5.13 shows a schematic diagram of a mm-wave emitter that employs a UTC-PD, a log-periodic antenna and two lasers that are fabricated on the same substrate. Although this structure seems too idealistic, given the current advancement in semiconductor processing and laser fabrication it may not be too far from reality.

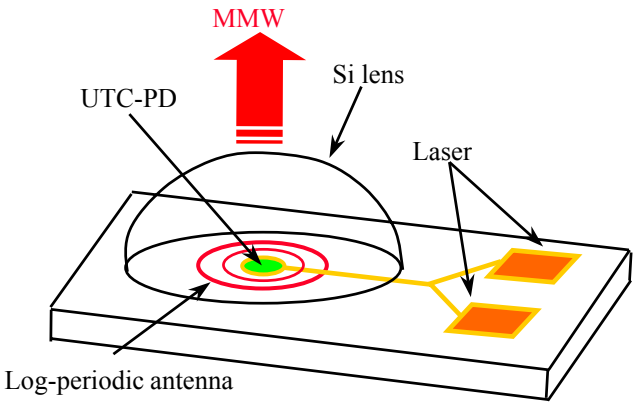


**Figure 5.13** Schematic diagram of a photonic mm-wave transmitter.

So employing UTC-PD and photonic mixing technique can open a new horizon in high-frequency LO generation for wireless applications. A combination of photonic microwave generation and photonic wireless receiver can result in a photonic wireless link where microwave is only used to transmit the signal and signal processing is performed in optical domain. An example of a mm-wave wireless link that uses mm-wave photonic techniques has been recently demonstrated [28]. The carrier frequency of this link is 120 GHz. The photonic transmitter consists of a 120 GHz mm-wave generator, and optical modulator, and a UTC-PD photonic emitter. On the receiver side a mm-wave detector (Schottky Barrier diode) is used as receiver that also demodulates the signal by means of envelop detection. Finally an E/O converter converts the demodulated signal back into the original optical signal and output it to an optical fiber.

Fig. 5.14 is the schematic diagram of the photonic wireless link demonstrated by employing UTC-PD [28]

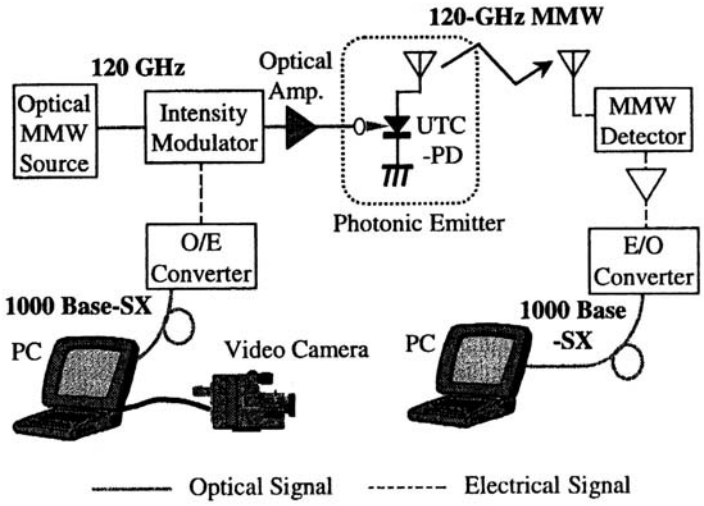


**Figure 5.14** Schematic of the photonic wireless link.[28]

The idea of a photonic wireless link can be implemented using the microdisk photonic self-homodyne receiver. Basically we just need to replace the electronic transmitter with its photonic counterpart.

Fig. 5.15 shows how the photomixing technique may be used to generate the transmitted carrier RF signal. Two lasers generate optical carriers ($\nu_2$ and $\nu_1$) with an offset frequency equal to the RF carrier frequency ($f_{RF} = \nu_2 - \nu_1$). The intensity of one of the optical carriers ($\nu_2$) is intensity modulated (in a MZ or microdisk modulator) with the baseband frequency ($f_b$) and then the both optical carriers are combined and mixed in a photodetector that generates the RF signal. Since one of the carriers was already data modulated the resulting RF signal is also data modulated. By proper adjustment of the power ratio between the optical carriers ($P_1/P_2$) and the modulation depth it is possible to generate any desired RF modulation index ($m_I$).

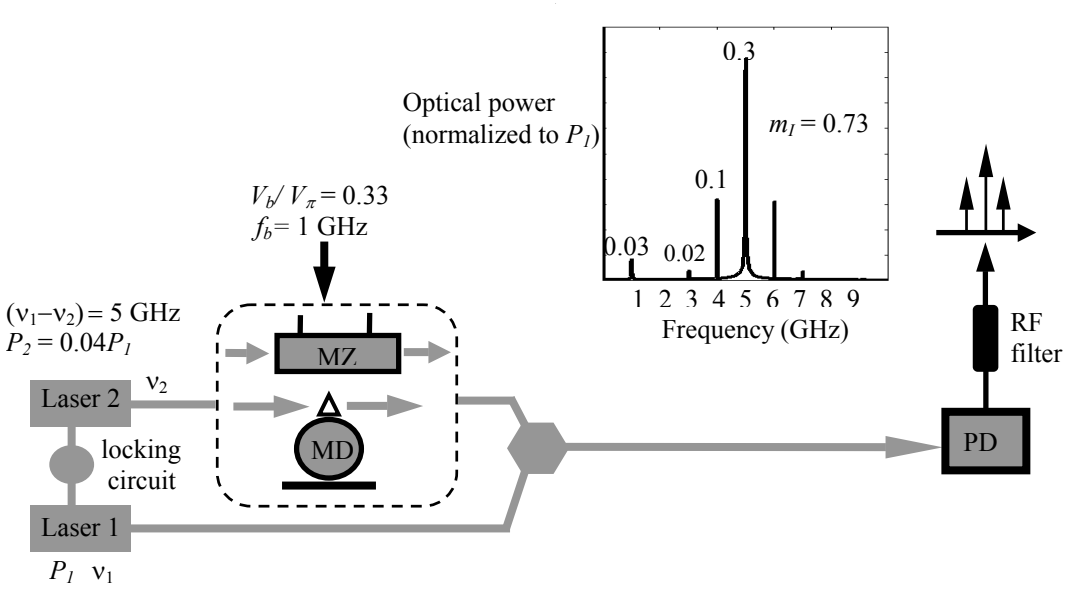


**Figure 5.15** Photonic generation of the transmitted carrier signal by means of optical modulation and photomixing.

Let's assume that the baseband frequency is 1 GHz and we want to generate a transmitted carrier RF signal with a carrier frequency of 5 GHz and $m_I = 0.7$. The simulation results show that if $P_2 = 0.04P_1$ and the optical modulation depth is 0.33 the optical intensity spectrum of the resulting signal is similar to a transmitted carrier RF signal with $m_I = 0.7$ and $f_{RF} = 5$ GHz. The main challenge in the photonic transmitter design is frequency locking of the two lasers. This can be done using optical frequency locked loop (OFLL) or optical phased-locked loop (OFLL) [27]. A detailed description of frequency locking methods and desired specifications of the laser sources is beyond the scope of this thesis. Here we just demonstrated that implementation of a photonic self-homodyne wireless link based on microdisk receiver and photomixing technique is a feasible task.

## 5.6 Summary

By improving the key components of the proposed photonic self-homodyne architectures, a stable, low power and small volume photonic receiver can be realized. Employing alternative electro-optic materials such as compound semiconductors may result in a fully integrated photonic receiver that is less complex than its electronic counterparts and consumes less power.

Using the high-speed and high efficiency offered by uni-traveling carrier photodiodes, we can generate the transmitted carrier RF/mm-wave signal photonically and implement a photonic wireless link.

## 5.7 References


[1] A. A. Savchencov, "Ultrahigh-Q crystalline optical whispering gallery mode resonators," *IEEE LEOS summer topicals meeting on WGM microcavities*, TuC1.2, 2004.

[2] V. S. Ilchenko, A. A. Savchenkov, A. B. Matsko, and L. Maleki, "Sub-microwatt photonic microwave receiver", *IEEE Photonics Technol.*, vol 14, no. 11, pp. 1602-1604, Nov 2002.

[3] Little optics (http://www.littleoptics.com)

[4] M-C Oh, H. Zhang, A. Szep, V. Chuyanov, and W. H. Steier, C. Zhang, L. Dalton, H. Erlig, B. Tsap, H. R. Fetterman, "Electro-optic polymer modulators for 1.55 μm wavelength using phenyltetraene bridged chromophore in polycarbonate," *Applied Phys Lett.*, vol. 76, no. 24, pp. 3525-3527, June 2000.

[5] P. Rabiei, W. H. Steier, C. Zhang, and L. R. Dalton, "Polymer micro-ring filters and modulators," *J. of Lightwave Technol.*, vol. 20, no. 11, pp.1968-1975, Nov. 2002.

[6] S. Kalluri, M. Ziari, A. Chen, V. Chuyanov, W. H. Steier, D. Chen, B. Jalali, H. Fetterman, and L. R. Dalton, "Monolithic integration of waveguide polymer electro-optic modulators on VLSI circuitry," *IEEE photon. Technol lett.*, vol. 8, no.5, pp. 644-646, May 1996.

[7] J. G. Mendoza-Alvarez, L. A. Coldren, A. Alping, R. H. Yan, T. Hausken, K. Lee, and K. Pedrotti, "Analysis of depletion edge translation lightwave modulators," *J. of Lightwave Technol.*, vol. 6, no. 6, pp.793-808, June 1988.

[8] K. Wakita, "Semiconductor optical modulators," *Kluwer academic publishers*, 1998.

[9] K. Tsuzuki, T. Ishibashi, T. Ito, S. Oku, Y. Shibata, R. Iga, Y. Kondo, and Y. Tohmori, "40Gb/s n-I-n InP Mach-Zehnder modulator with a π voltage of 2.2 V," *Electron. Lett.*, vol. 39, no. 20, pp. 1464-1466, Oct 2003.

[10] M. Feterman, C.-P Chao, and S. R. Forrest, "Fabrication and analysis of high-contrast InGaAsP-InP Mach-Zehnder modulators for use at 1.55-μm wavelength," *IEEE photon. Technol lett.*, vol. 8, no.1, pp. 69-71, Jan 1996.

[11] R. G. Walker, "High-speed III-V semiconductor intensity modulators," *IEEE J. of Quantum Electron.*, vol 27, no. 3, pp. 654-666, March 1991.

[12] N. Shaw, W. J. Stewart, J. Heaton, and D. R. Wight, "Optical slow-wave resonant modulation in electro-optic GaAs/AlGaAs modulators," *Electron. Lett.*, vol. 35, no. 18, pp. 1557-1558, Sept 1999.

[13] Kostadin Djordjev; Seung June Choi, Sang Jun Choi, and P. Daniel Dapkus, "Active semiconductor microdisk devices", *IEEE J. of Lightwave Technology*, vol. 20, no.1, January 2002, pp.105-113.

[14] T. Sadagopan, S. J. Choi, S. J. Choi, and P. D. Dapkus, "High-speed, low-voltage modulation in circular WGM microresonator," *IEEE/LEOS, summer topical meetings*, 2004, MC2-3.

[15] B. Jalali, S. Yegnanarayanan, T. Yoon, T. Yoshimoto, I. Redina, and F. Coppinger, "Advances in silicon-on-insulator optoelectronics,' *IEEEI.J. of selected topics in quantum electron.*, vol. 4, no. 6, pp. 938-947, Nov 1998.

[16] B. Jalali, L. Naval, and A.F.J Levi, "Si-based receivers for optical data links," *J. of lightwave technology*, vol. 12, no. 6, pp. 930-934, June 1994.

[17] A. Liu, R. Jones, L. Liao, D. Samara-Rubio, D. Rubin, O. Cohen, R. Nicolaesu, and M. Paniccla, "A high-speed silicon optical modulator based on a metal-oxide-semiconductor capacitor," *Nature*, vol. 427, Feb 2004, pp. 615-618.

[18] C. A. Barrios, U. R. Almeida, R. R. Panepucci, B.S. Schmidt, and M. Lipson, "Compact silicon tunable Fabry-Perot resonator with low power consumption," *IEEE Photonic Technol. Lett.,* vol. 16, no. 2, pp. 56-508, Feb. 2004

[19] G. T. Reed and A. P. Knights, "Silicon photonics an introduction," Wiley, 2004.

[20] T. Takashi, S. Higashiyama, H. Takemori, and Koizmi, "A silicon optical bench incorporating a tantalum-nitride thin-film resistor," *J. of Micromech. And Microeng.*, vol. 14, pp. 283-289, 2004.

[21] K. Ohata, T. Inoue, M. Funabashi, A. Inoue, Y. Takimoto, T. Kuwabara, S. Shinozaki, K. Maryhashi, K. Hosaya, and H. Nagai, "Sixty-GHz-Band ultra-miniature monolithic T/R modules for multimedia wireless communication systems", IEEE trans. on microwave theory and tech., vol. 11, no. 12, pp. 2354-2360, Dec. 1996.

[22] A. Stohr, A. Malcoci, A. Sauerwald, I. C. Mayorga, R. Gusten, and D. S. Jager, "Ultra wide-band traveling-wave photodetectors for photonic local oscillators," *J. of Lightwave Technol.*, vol. 21, no. 12, pp.3062-3070, Dec 2003.

[23] H. Ito, T. Furuta, S. Kodama and T. Ishibashi, "InP/InGaAs uni-travelling-carrier photodiode with 310 GHz," *Electron. Lett.*, vol. 36, no. 21, pp. 1809-1810, Oct 2000.

[24] Y. Muramoto, Y. Hirota, K. Yoshino, H. Ito, and T. Ishibashi, "Uni-travelling-carrier photodiode module with bandwidth of 80 GHz," *Electron. Lett.*, vol. 39, no. 25, Dec 2003.

[25] P. G. Huggard, B. N. Ellison, P. Shen, N. J. Gomes, P. A. Davies, W. Shillue, A. Vaccari, and J.M. Payne, "Generation of millimeter and sub-millimetre waves by photomixing un 1.55 μm wavelength photodiode," *J. Lightwave Technol*., vol. 21, no. 12, pp. 3062-3070, Dec. 2003.

[26] H. Ito, T. Ito, Y. Muramoto, T. Furuta, and T. Ishibashi, "Rectangular waveguide output unitraveling-carrier module for high-power photonic millimeter-wave generation in the F-band," *J. Lightwave Technol*., vol. 21, no. 12, pp. 3456-3462, Dec. 2003.

[27] J. O' Reily and P. Lane, "Remote deliver of video services using mm-waves and optics," *J. Lightwave Technol*., vol. 12, no. 2, pp. 369-375, Feb. 1994.

[28] A. Hirata, M. Harada, and T. Nagatsuma, "120-GHz wireless link using photonic techniques for generation, modulation, and emission of millimeter-wave signals," *J. Lightwave Technol*., vol. 21, pp. 2145-2153, Oct. 2003.

[29] A. Hirata, T. Nagatsuma, R. Yano, H. Ito, T. Furuta, Y. Hirota, T. Ishibashi, H. Matsuo, A. Ueda, T. Noguchi, Y. Sekimoto, M. Ishiguro, and S. Matsuura, "Output power measurement of photonic millimeter-wave and sub-millimetter wave emitter at 100-800 GHz," *Electron Lett.*, vol 38, no. 15, pp. 798-800, July 2002.

[30] Unpublished data, Experiment done by Fernando Harriague, *Advanced Network Technology Lab, USC*.

---

## Technical notes

(1) PINFET optical receiver from Laser Diode Incorporated (www.lasrdiode.com)
LDPF 0012 (Bandwidth 12 MHz, Sensitivity –53 dBm)
LDPF 0024 (Bandwidth 24 MHz, Sensitivity –50 dBm)

(2) LMDS (Local Multipoint Distribution Service) is a fixed wireless technology that operates in the 26 – 32 GHz band and offers line-of-sight coverage over distances up to 3-5 Klm.

(3) EtherAir 1500: is a digital radio system made by Ceragon networks that supports wireless fast Ethernet applications for the ISP carrier, corporate access and campus environments. This system operates in the 18,23,26,28 and 38 GHz frequency bands with a bandwidth of 155 Mbps. (www.ceragon.com).

# Glossary

| | |
|---|---|
| $a$ | Optical circulation factor in the microdisk |
| $c$ | Speed of light |
| $D$ | Microdisk diameter |
| $e$ | Electron charge |
| $E_{in}$ | Input $E$-field |
| $E_t$ | transmitted $E$-field |
| $f_{RF,m}$ | $m$th resonant frequency of the RF ring resonator |
| $f_{RF}$ | RF carrier frequency |
| $f_r$ | Resonant frequency of the patch antenna (single and array) |
| $f_{EO}$ | Electro-optic transfer function of the microdisk resonator |
| $f_o$ | Optical transfer function of the microdisk resonator (frequency domain) |
| $G_{eo}$ | Electro-optic gain factor |
| $G_{RF,OB}$ | Baseband modulated optical power at 1 W received RF power |
| $G_{tot}$ | Total gain in the wireless photonic receiver |
| $g$ | Gap size between the ring resonator and the microstripline |
| $g_o$ | Evanescent optical coupling gap size |
| $h$ | Microdisk thickness |
| $h_s$ | Dielectric substrate thickness (microstripline) |
| $h_p$ | Dielectric substrate thickness (patch antenna) |
| $i_p$ | Total output photocurrent generated in the photodetector |
| $i_{\omega b}$ | Baseband photocurrent |
| $i_{2\omega b}$ | Photocurrent at the second-harmonic of the baseband signal |
| $i_d$ | Dark current of the photodetector |
| $i_{o,S}$ | Signal photocurrent |
| $i_{o,N}$ | Noise photocurrent |
| $J_{photo}$ | Photocurrent density |
| $k$ | Wave vector of the optical WG resonance |
| $k_B$ | Boltzman factor |
| $l$ | Polar WG mode order |
| $L_T$ | Transmission line loss factor |
| $L_{eff}$ | Average length that photon travels before escaping from the resonator |
| $m$ | Azimuthal WG mode order |
| $m_o$ | Optical modulation order |
| $m_R$ | RF resonance order |
| $m_I$ | RF modulation index |
| M | Optical modulation index |
| $n$ | Optical refractive index (general) |
| $n_o$ | Ordinary bulk optical refractive index of $LiNbO_3$ (zero electric field) |
| $n_e$ | Extraordinary bulk optical refractive index |
| $n_e'$ | Electro-optically modulated extraordinary bulk optical refractive index |
| $n_{RF}$ | RF refractive index |
| $n_{RF,e}$ | Effective RF refractive index |

| | |
|---|---|
| $n_{photo}$ | Density of photo-generated electrons |
| $N_a$ | Received noise power |
| $E_{eff}$ | Effective electric field intensity |
| $P_{o,RIN}$ | Laser RIN power |
| $P_{o,out}$ | Output (transmitted) optical power |
| $P_{o,min}$ | Minimum optical power of a WG resonance |
| $P_{o,max}$ | Maximum optical power of a WG resonance |
| $P_{o,in}$ | Optical input power |
| $P_{o,mod}$ | Modulated optical power |
| $P_{o,d}$ | Available optical power in a dip |
| $P_{o,b}$ | Baseband modulated optical power |
| $P_b$ | Down-converted baseband power (electrical) |
| $P_{o,\omega b}$ | Optical power modulated at $\omega_b$ |
| $P_{o,2\omega b}$ | Optical power modulated at $2\omega_b$ |
| $P_{e,\omega b}$ | Electrical power modulated at $\omega_b$ |
| $P_{e,2\omega b}$ | Electrical power modulated at $2\omega_b$ |
| $P_{o,s}$ | Instantaneous signal optical power |
| $P_{o,n}$ | Instantaneous noise optical power |
| $P_{o,S}$ | Total signal optical power |
| $P_{o,N}$ | Total noise optical power |
| $P_{o,dc}$ | DC optical power |
| $P_{o,t}$ | Transmitted optical power |
| $P_{o,mix}$ | Down-converted optical noise power |
| $P_{obb}$ | Optical noise power in baseband regime |
| $P_{RF}$ | RF input power (received RF power) |
| $q$ | Radial WG mode order |
| $Q$ | Loaded optical quality factor of a WG resonance |
| $Q_u$ | Unloaded optical quality factor of a WG resonance |
| $Q_{RF,U}$ | Unloaded RF quality factor of a WG resonance |
| $Q_{RF}$ | loaded RF quality factor of a WG resonance |
| $R$ | Photodetector responsivity |
| $R_o$ | Outer radius of the RF ring resonator |
| $R_i$ | Inner radius of the RF ring resonator |
| $R_{ring}$ | Resistance of the ring resonator |
| $S_a$ | Received signal power |
| $S_d$ | Sensitivity of the digital photoreceiver |
| $\boldsymbol{t}$ | Optical transmission coefficient |
| $t$ | Time |
| $T_{RF}$ | RF period |
| $V$ | DC voltage across the microdisk |
| $V_{fb}$ | Feedback voltage (peak-to-peak) |
| $V_{RF}$ | Input RF voltage to the microdisk modulator |
| $V'_{RF}$ | Noisy input RF voltage to the microdisk modulator |
| $V_m$ | Amplitude of the voltage oscillation on the ring resonator |

| | |
|---|---|
| $V_{in}$, $V_0$ | Amplitude of the input RF voltage ($V_{RF}$) |
| $V_{RN}$ | Noise voltage on the ring resonator |
| $V_{RS}$ | Signal voltage on the ring resonator |
| $V_N$ | Amplitude |
| $V_S$ | Amplitude |
| $w_l$ | Width of the microstripline |
| $w_r$ | Width of the RF ring resonator |
| $z_a$ | The height of air cylinder for tuning the RF resonant frequency |
| $Z_m$ | Impedance of a rectangular patch in the middle |
| $\alpha$ | Distributed optical loss factor for WG modes (absorption+scattering) |
| $\beta_{EO}$ | Electro-optic correction factor (microdisk modulator) |
| $\beta'_{EO}$ | Electro-optic correction factor (MZ modulator) |
| $\beta_c$ | Ring capacitance correction factor |
| $\beta_s$ | *E*-field oscillation correction factor |
| $\beta_{qlm}$ | Wave vector of the WG mode |
| $\kappa$ | Optical coupling factor |
| $\delta$ | Optical skin depth |
| $\delta\theta_{FWHM}$ | Angular full width half max of the WG resonance |
| $\delta r_{FWHM}$ | Radial full width half max of the WG resonance |
| $\Delta\nu_{FSR}$ | Optical free spectral range frequency |
| $\Delta\nu_{FWHM}$ | Full width half max frequency of the WG resonance |
| $\Delta\lambda_{FWHM}$ | Full width half max wavelength of the WG resonance |
| $\Delta\lambda_{DC}$ | DC shift |
| $\Delta l_{oc}$ | Effective length of the patch antenna |
| $\lambda_{laser}$ | Laser wavelength |
| $\nu_{laser}$ | Laser frequency |
| $\lambda_{RF}$ | RF wavelength |
| $\lambda_{res}$ | Resonant wavelength of WG resonance |
| $\nu_{res}$ | Frequency of WG resonance (general) |
| $\nu_{l\,q}$ | Frequency of WG resonance |
| $v_e$ | Electron velocity |
| $v_m$ | *m*th resonant frequency of an optical resonator |
| $\rho$ | Optical coupling efficiency |
| $\tau_p$ | Photon lifetime in the microdisk resonator |
| $\tau_{RT}$ | Photon roundtrip time in the microdisk resonator |
| $\omega_{RF}$ | RF angular frequency |
| $\omega_b$ | Baseband angular frequency |
| $\varepsilon_{re}$ | Effective dielectric constant |
| $\varepsilon_r$ | Dielectric constant (relative permittivity) |
| $\varepsilon_s$ | relative permittivity of the microstripline substrate |
| $\varepsilon_{e,RF}$ | RF permittivity along *c*-axis |

# Appendix A

## Bibliography


Abeles, J. H., "Resonant enhanced modulator development," DARPA/MTO R-FLICs program: Kickoff meeting, August 2000.

Armani, D. K., Kippenberg, T. J., Spillane, S. M., and Vahala, K. J., "Ultra-high-*Q* microcavity on a chip," *Nature*, vol. 421, pp. 925-928, Feb. 2003.

Agrawal, G. P., "Fiber-optic communication systems", 1997.

Abidi, A. , "Direct-conversion radio transceivers for digital communications," *IEEE J. Solid-State Circuits*, vol. 30, pp 1399-1410, Dec 1995.

Bernard, P. A., and Gautray, J. M., "Measurment of dielectric constant using a microstrip ring resonator," *IEEE Trans. on Microwave Theory and Tech.*, vol. MTT-39, no 3, pp 592-594, March 1991.

Bahl, J., and Bhartia, P., "Microstrip antennas", 1980.

Basilio, L. I., Khayat, M. A., Williams, J. T., and Long, S. A., "The dependence of the input impedance on feed position of probe and microstrip line-fed patch antennas," *IEEE trans. on Antenna and propagation*, vol. 49, no. 1, pp. 45-47, Jan. 2001

Bhartin, P., Rao, K. V. S., and Tomar, R. s., "Millimeter-wave microstrip and printed circuit antennas"

Barrios, C. A., Almeida, U. R., Panepucci, R. R., Schmidt, B. S., and Lipson, M., "Compact silicon tunable Fabry-Perot resonator with low power consumption," *IEEE Photonic Technol. Lett.,* vol. 16, no. 2, pp. 56-508, Feb. 2004

Cohen, D. A., Hossein-Zadeh, M., and Levi, A. F. J., "Microphotonic modulator for microwave receiver," *Electron. Lett.*, vol. 37, no.5, pp 300-301, 2001.

Cohen, D. A., "Lithium Niobate microdisk modulators", PhD dissertation, USC 2001, (www.usc.edu/alevi)

Chang, W. S. C., "RF photonic technology in optical fiber links" Cambridge university press, 2002.

Chang, K., Martin, S., Wang, S. and Klein, J. L., "On the study of microstrip ring and varactor-tuned ring circuits," *IEEE Trans. on Microwave Theory and Tech.*, vol. MTT-35, no 12, pp 1288-1295, Dec 1987.

Cohen, D. A., Hossein-Zadeh, M., and Levi, A. F. J., "High-Q microphotonic electro-optic modulator," *Solid-State Electronics*, vol. 45, pp.1577-1589, 2001.

Chen, D., Bhattacharya, D., Udupa, A., Tsap, B., Fetterman, H. R., Chen, A., Lee, S., Chen, J., Steier, W. H., Wang, F., Dalton, L. R., "High-frequency polymer modulators with integrated finline transitions and low $V_{\pi,}$" *IEEE Photonics Lett.*, vol. 11, no. 1, pp.54-56, Jan. 1999.

Chang, K., "Microwave ring circuits and antennas," Wiley series in microwave and optical engineering, John Wiely & Sons Inc, 1996.

Cai, M., Hunziker, G., and Vahala, K., "Fiber-optic add-drop device based on a silica microsphere-whispering gallery mode system," *IEEE Photon. Technol. Lett.*, vol. 11, pp. 686-687, 1999.

Cai, M., Painter, O., and Vahala, K. J., "Fiber-coupled microsphere laser", *Optics Lett.*, vol. 25, no. 19, pp 1430-1432, Oct. 2000.

Cai, M., Hedekvist, P. O., Bhardwaj, A., and Vahala, K., "5-Gbit/s BER performance on an all fiber-optic add/drop device based on a taper–resonator–taper structure', *IEEE Photon. Tech. Lett.*, vol. 12, no. 9, pp. 1177-1187, 2000.

Choi, S. J., Yang, Q., Peng, Z., Choi, S. –J., and Dapkus, P. D., "High-*Q* buried heterostructure microring resonator," *IEEE/LEOS, summer topical meetings*, 2004, CTHF1.

Chelnokov, A. V., and Lourtioz, J. M., "Optimised coupling into planar waveguides with cylindrical prisms", *Electron. Lett.*, vol. 31, no. 4, pp 269-271, Feb. 1995.

Chew, W. C., "A broad-band annular-ring microstrip antenna", *IEEE Trans. Antennas and Prop.,* vol. AP-30, Sept 1982.

Djordjev, K., Choi, S.-J., Choi, S.-J., and Dapkus, P. D., "High-*Q* vertically-coupled InP microdisk resonators", *IEEE Photonics Technology Letters*, vol.14, no.3, March 2002, pp.331-333.

Djordjev, K., Choi, S. J., Choi, S. J., and Dapkus, P. D., "Active semiconductor microdisk devices", *IEEE Journal of Lightwave Technol*, vol.20, no.1, January 2002, pp.105-113.

Djordjev, K., Choi, S. –J., Choi, S. –J., Dapkus, P. D., "Novel active switching components," 28th European Conference on Optical Communication (ECOC 2002), September 2002, Monday - paper 2.3.5

Dentan, M., and De Cremous, B., "Numerical simulation of the nonlinear response of a p-i-n photodiode under high illumination," *J. Lightwave Technol.* vol. 8, pp.1137, 1990.

Fetterman, M., Chao, C.-P., and Forrest, S. R., "Fabrication and analysis of high-contrast InGaAsP-InP Mach-Zehnder modulators for use at 1.55-μm wavelength," *IEEE Photonics Technol. Lett.*, vol. 8, no. 1, Jan. 1996.

Feterman, M., Chao, C. –P., and Forrest, S. R., "Fabrication and analysis of high-contrast InGaAsP-InP Mach-Zehnder modulators for use at 1.55-μm wavelength," *IEEE photon. Technol lett.*, vol. 8, no.1, pp. 69-71, Jan 1996.

Gallagher, T. F., Tran, N. H., and Watjen, J. P., "Principles of a resonant cavity optical modulator," *Appl. Optics Lett.*, vol. 25, no. 4, pp 510-514, Feb 1986.

Gopalakrishnan, G. K., and Burns, W. K., "Performance and modeling of resonantly enhanced $LiNbO_3$ modulators for low-loss analog fiber-optic links," *IEEE Trans. on Microwave Theory and Tech*, vol. 42, no. 12, pp 2650-2656, 1994.

Guan, X., Hajimiri, A., "A 24-GHz CMOS Front-End," *IEEE J. Solid-State Circuits*, vol.39, pp. 368-373, Feb 2004.

Gopinath, A., "Maximum Q-factor of microstrip resonators", *IEEE Trans. on Microwave Theory and Techniques*, vol. 29, no. 2, pp 946-952, 1981.

Gopalakrishnan, G. K., and Chang, .K, "Novel excitation schemes for the microstrip ring resonator with low insertion loss," *Elect. Lett*., vol. 30, no 2, pp 148-149, Jan 1994.

Gorodetsky, M. L., Savchenkov, A. A., and Ilchenko, V. S., "Ultimate *Q* of optical microsphere resonators", *Optics Lett.*, vol. 21, no. 7, pp 453-455, April 1996.

Gorodetsky, M. L., and Ilchenco, V. S., "Optical microsphere resonators: optimal coupling to high-*Q* Whispering-Gallery modes," *J. of Opt. Soc. Am. B*, vol. 16, no. 1, pp 147-154, Jan. 1999.

Gopalakrishnan, G. K., Fairchild, B. W., Yeh, C. L., Park, C. –L., Chang, K., Weichold, M. H., and Taylor, H. F., "Experimental investigation of microwave-

optoelectronic interactions in a microstrip ring resonator," *IEEE Trans. on Microwave Theory and Tech.*, vol. MTT-39, no 12, pp 2052-2060, Dec 1991.

Gordon, E. I., and Rigden, J. D., "The Fabry-Perot electo-optic modulator," The *Bell system technical journal*, pp 155-179, Jan. 1963.

Gheorma, I. L., and Osgood, R. M., "The fundamental limitations of optical resonator based high-speed EO modulators," *IEEE Photon. Technol.*, vol. 14, no. 14, pp.795-797, June 2002.

Gorodetsky, M. L., and Pryamikov, A. D.,"Rayleigh scattering in high-Q microspheres", *J. of Opt. Soc. Am*., B, vol. 17, no.6, pp 1051-1057, June 2000.

Gorodetsky, M. L., and Ilchenko, V. S.,"High-Q optical whispering-gallery microresonators:precession approach for spherical mode analysis and emission patterns with prism couplers", *Optics comm.*, vol. 113, pp 133-143, Dec. 1994.

Gopalakrishnan, G. K., Burns, W. K., and Bulmer, c. h., "Microwave-optical mixing in $LiNbO_3$ modulators," *IEEE Trans. Microwave Theory and Tech.*, vol. 41, pp. 2383-2391, Dec 1993.

Hedekvist, P. O., Olsson, B.-E., and Wiberg, A., "Microwave harmonic frequency generation utilizing the properties of an optical phase modulator," *J. Lightwave Technol*., vol. 22, pp. 882-886, March 2004.

Hirata, A., Harada, M., and Nagatsuma, T., "120-GHz wireless link using photonic techniques for generation, modulation, and emission of millimeter-wave signals," *J. Lightwave Technol*., vol. 21, pp. 2145-2153, Oct. 2003.

Huang, J. J., Chung, T., Lerttamrab, M., Chuang, S. L., and Feng, M., "1.55-μm asymmetric Fabry-Perot modulator (AFPM) for high-speed applications", *IEEE Photon. Technol*., vol. 14, no. 12, pp.1689-1691, Dec 2002.

Hossein-Zadeh, M., and Levi, A. F. J., "Mb/s data transmission over a RF fiber-Optic link using a $LiNbO_3$ microdisk optical modulator", *Solid-State Electronics*, vol. 46, pp 2173-2178, 2002.

Hossein-Zadeh, M., and Levi, A. F. J., "A new electrode design for microdisk optical modulator," *CLEO* 2003 technical digest.

Hryniewicz, J. V., Absil, P. P., Little, B. E., Wilson, R. A., and Ho, P. –H., "Higher order filter response in coupled microring resonators," *IEEE Photonics Technol. Lett*., vol. 12, no. 3, pp. 320-322, March. 2000.

Hseieh, L. –H., and Chang, K., " Equivalent lumped element G,L,C, and unloaded Q's of closed- and open-loop ring resonators", *IEEE Trans. on Microwave Theory and Tech.*, vol. MTT-50, no 2, pp 453-460, Feb 2002.

Hoshida, T., Suchiya, T., "Broad-band millimeter-wave up-conversion by nonlinear photodetection using a waveguide p-i-n photodiode," *IEEE Photon. Technol. Lett*., vol 10, pp.860, 1998.

Hayes, R. R., and Persechini, D. L., "Nonlinearity of p-i-n photodetectors," *IEEE Photon. Technol. Lett*., vol. 5, pp. 70, 1993.

Huggard, P. G., Ellison, B. N.,Shen, P., Gomes, N. J., Davies, P. A., Shillue, W., Vaccari, A., and Payne, J. M., "Generation of millimeter and sub-millimetre waves by photomixing un 1.55 μm wavelength photodiode," *J. Lightwave Technol*., vol. 21, no. 12, pp. 3062-3070, Dec. 2003.

Hirata, A., Harada, M. and Nagatsuma, T., "120-GHz wireless link using photonic techniques for generation, modulation, and emission of millimeter-wave signals," *J. Lightwave Technol*., vol. 21, pp. 2145-2153, Oct. 2003.

Hirata, A., Nagatsuma, T., Yano, R., Ito, H., Furuta, T., Hirota, Y., Ishibashi, T., Matsuo, H.,Ueda, A., Noguchi, T., Sekimoto, Y., Ishiguro, M. and Matsuura, S., "Output power measurement of photonic millimeter-wave and sub-millimetter wave emitter at 100-800 GHz," *Electron Lett.*, vol 38, no. 15, pp. 798-800, July 2002.

Ito, H.,Ito, T.,Muramoto, Y.,Furuta, T., and Ishibashi, T., "Rectangular waveguide output unitraveling-carrier module for high-power photonic millimeter-wave generation in the F-band," *J. Lightwave Technol*., vol. 21, no. 12, pp. 3456-3462, Dec. 2003.

Ilchenko, V. S., Savchenkov, A. A., Matsko, A. B., and Maleki, L. "Sub-microwatt photonic microwave receiver", *IEEE Photonics Technol.*, vol 14, no. 11, Nov 2002.

Itoh, T., "Analysis of microstrip resonators", *IEEE Trans. on Microwave Theory and Techniques*, vol. 22, no. 11, pp 946-952, 1974.

Ilchenko, V. S., Yao, X. S., and Maleki, L., "Pigtailing the high-*Q* microsphere cavity: a simple fiber coupler for optical whispering-gallery modes," *Opt. Lett*., vol. 24, pp. 723-725, 1999.

Ikegami, T., and Kubodera, K., "Nonlinear optical devices for switching applications", *Communications, 1990. ICC 90 IEEE international conference on*, vol. 3, pp 1152-1156, Apr. 1990.

Ilchenko, V.S., Savchenkov,A. A., Matsko, A.B., and Maleki, L. "Sub-microwatt photonic microwave receiver", *IEEE Photonics Technol*., vol 14, no. 11, Nov 2002.

Ito, H., Furuta, T., Kodama, S., and Ishibashi, T., "InP/InGaAs uni-travelling-carrier photodiode with 310 GHz," *Electron. Lett.*, vol. 36, no. 21, pp. 1809-1810, Oct 2000.

Ito, H., Ito, T., Muramoto, Y., Furuta, T., and Ishibashi, T., "Rectangular waveguide output unitraveling-carrier module for high-power photonic millimeter-wave generation in the F-band," *J. Lightwave Technol*., vol. 21, no. 12, pp. 3456-3462, Dec. 2003.

Jameson, R. S., and Lee, W. T., " Operation of an all-optical bistable device dependent upon incident and transmitted optical power", *IEEE J. of quantum electron.*, vol. 25, no. 2, pp 139-143, Feb. 1989.

Jalali, B., Yegnanarayanan, S., Yoon, T., Yoshimoto, T., Redina, I., and Coppinger, F., "Advances in silicon-on-insulator optoelectronics,' *IEEEI.J. of selected topics in quantum electron.*, vol. 4, no. 6, pp. 938-947, Nov 1998.

Jalali, B., Naval, L., and Levi, A. F. J., "Si-based receivers for optical data links," *J. of lightwave technology*, vol. 12, no. 6, pp. 930-934, June 1994.

Kwakernaak, M. H., Leopre, A. N., Mohseni, An, H., Shellenbarger, Z. A., Abeles, J. H., Rommel, S. L., and Adesida, I., "Eletrco-refractive low loss MMI-coupled ring resonators," *CLEO 2003* technical digest.

Krahenbuhl, R., and Howerton, M. M., "Investigations on short-path-length high-speed optical modulators in $LiNbO_3$ with resonant-type electrodes," *J. Lightwave Technol.*, vol. 19, no. 9, pp.1287-1297, Sep. 2001.

Kawanishi, T., Oikawa, S., Higuma, K., Matsuo, Y., and Izutsu, M., "$LiNbO_3$ resonant-type optical modulator with double-stub structure," *Electron. Lett.*, vol. 37, no. 20, pp.1244-1246, Sep. 2001.

Kawanishi, T., Oikawa, S., Higuma, K., Matsuo, Y., and Izutsu, M., "Low-driving-voltage band-operation $LiNbO_3$ modulator with lightwave reflection and double-stub structure," *Electron. Lett.*, vol. 38, no. 20, pp.1204-1205, Sep. 2002.

Kojucharow, K., Kaluzni, H., and Nowak, W., "A wireless LAN at 60 GHz-novel system design and transmission experiments", *Microwave symposium digest, IEEE MTT-S international*, vol. 3, pp. 1513-1516, 1998.

Knight, J. C., Dubreuil, N., Sandoghdar, V., Hare, J., Lefevre-Seguin, V., Raimond, J. M., and Haroche, S., "Maping whispering-gallery modes in microspheres with a near-field probe", *Optics Lett.*, vol. 20, no. 14, pp 1515-1517, July 15 1995.

Khanna, A., and Garault, Y., "Determination of loaded, unloaded, and external quality factors of a dielectric resonator coupled to a microstripline", *IEEEb Trans. on Microwave Ttheory and Techniques*, vol. MTT-31, no 3, pp 261-264, March 1993.

Kazovsky, L., Benedetto, S., Willner, A., "Optical fiber communication systems", Artech house publishers, 1996.

Kalluri, S., Ziari, M., Chen, A., Chuyanov, V., Steier, W. H., Chen, D., Jalali, B., Fetterman, H., and Dalton, L. R., "Monolithic integration of waveguide polymer electro-optic modulators on VLSI circuitry," *IEEE photon. Technol lett.*, vol. 8, no.5, pp. 644-646, May 1996.

Lee, S. S., Garner, S. M., Chuyanov, V., Zhang, H., Steier, W. H., Wang, F., Dalton, L., Udupa, A. H., and Fetterman, H. R., "Optical intensity modulator based on a novel electro-optic polymer incorporating a high $\mu\beta$ chromophore" *IEEE J. of Quant. Electro.*, vol. 36, no. 5, pp. 527-532, May 2000.

Lee, M., "Dielectric constant and loss tangent in $LiNbO_3$ crystals from 90 10 147 GHz," *Appl. Phys. Lett.*, vol. 79, pp. 1342-1344, 2001.

Laine, J. P., Little, B. E., Haus, H. A., "Etch-Eroded fiber coupler for Whispering-Gallery mode excitation in high-Q silica microspheres", *IEEE Photon. Technol.*, vol. 11, no. 11, pp 1429-1430, Nov. 1999.

Lu, S. –L., and Ferendeci, A. M., "Coupling modes of a ring side coupled to a microstrip line," *Electtron. Lett.*, vol. 30, no. 16, pp 1314-1315, August 1994.

Little, B. E., Laine, J. P., and Haus, H. A., "Analytic theory of coupling from tapered fibers and half-blocks into microsphere resonators," *IEEE J. Lightwave Technol*., no. 17, pp. 704-715, 1999

Little, B. E., Laine, J. P., Lim, D. R., Haus, H. A., Kimerling, L. C., and Chu, S. T., "Pedestal anitresonant reglecting waveguides for robust coupling to microsphere resonators and for microphotonic circuits," *Optics Letters*, vol. 25, no. 1, pp. 152-153, 2000.

Little, B. E., Foresi, J. S., Steinmeyer, G., Thoen, E. R., Chu, S. T., Haus, H. A., Ippen, E. P., Kimerling, L. C., and Greene, W., "Ultra-compact Si-$SiO_2$ microring

resonator optical channel droppingfilters," *IEEE Photonics Technol. Lett*., vol. 10, no. 4, pp.549-551, April 1998.

Little, B. E., Chu, S. T., Haus, H. A., Foresi, J., and Lain, J. –P., "Microring resonator channel droping filters," *IEEE J. Lightwave Technol.*, vol. 15, no. 6,pp. 998-1005, June 1997.

Little, B., Laine, J. P., Haus, H. A., "Analitic theory of coupling from tapered fibers and half-blocks into microsphere resonators", *J. of Lightwave Technol.*, vol. 17, no. 4, pp 704-714, April 1999.

Levi, A. F. J., McCall, S. L., Pearton, S. J., and Logan, R. A., "Room temperature operation of submicrometre radius disk laser," *Electron. Lett*., vol. 29, pp. 1666-1667, 1993.

Liao, C., Zhang, y. D., "Spherically tapered prism-waveguide coupler", *Appl. Optics*, vol. 24, no. 20, pp 3315-3316, Oct. 1985.

Laine, J. –P.,Little, Lim, D. R., Tapalian, H. C., Kimerling, L. C., and Haus, H. A., "Microsphere resonator mode characterization by pedestal anti-resonant reflecting waveguide coupler", *IEEE Photon. Technol. Lett.*, vol. 12, no. 8, pp 1004-1006, August 2000.

Little, B. E., and Laine, J. P., Chu, S. T.,"Surface-roughness-induced contradirectional coupling in ring and disk resonators", *Optics Lett.*, vol. 22, no. 1, pp 4-6, Jan. 1997.

Little, B. and Chu, S. T., "Estimating surface-roughness loss and output coupling in microdisk resonators", *Optics Lett.*, vol. 21, no. 17, pp 1390-1392, Sept. 1996.

Lu, S. –L., and A. M. Ferendeci, " Coupling parameters for a side-coupled ring resonator and a microstrip line ", *IEEE Trans. on Microwave Theory and Tech.*, vol. 44, no. 6, pp 953-956, June 1996.

Liu, A., Jones, R., Liao, L., Samara-Rubio, D., Rubin, D., Cohen, O., Nicolaesu, R., and Paniccla, M., "A high-speed silicon optical modulator based on a metal-oxide-semiconductor capacitor," *Nature*, vol. 427, Feb 2004, pp. 615-618.

Maleki, L., Savchenkov, A., Ilchencho, V., Handley, T., and Matsko, A., "Novel photonic filter and receiver based on Whispering Gallery mode", *Microwave-photonics conf* ???

Mitomi, O., Noguchi, K., and Miyazawa, H., "Broadband and low driving-voltage $LiNbO_3$ optical modulators", *IEE Proc.-optoelectron*., vol. 145, no. 6, pp. 360-364, Dec 1998.

McCall, S. L., Levi, A. F. J., Slusher, R. E., Pearton, S. J., and Logan, R. A., "Whispering mode microdisk lasers," *Appl. Phys. Lett.,* vol. 60, pp. 289-291, 1992.

Mendez, A., Garcis-Cabanes, A., Diegues, e., and Cabrera, J. M., "Wavelength dependence of electro-optic coefficients in congruent and quasi-stoichiometric $LiNbO_3$," *Electron. Lett.*, Vol. 35, pp. 498-501, 1999

Marti, J., Polo, V., Ramos, F., and Fuster, J. M., "Single Mach-Zehnder modulator electro-optical harmonic mixer for broadband microwave/millimeter-wave applications," *Wireless personal communications*, vol. 15, no. 1, Oct. 2000.

Mendoza-Alvarez, J. G., Coldren, L. A., Alping, A., Yan, R. H., Hausken, T., Lee, K., and Pedrotti, K., "Analysis of depletion edge translation lightwave modulators," *J. of Lightwave Technol.*, vol. 6, no. 6, pp.793-808, June 1988.

Muramoto, Y., Hirota, Y., Yoshino, K., Ito, H. and Ishibashi, T. "Uni-travelling-carrier photodiode module with bandwidth of 80 GHz," *Electron. Lett.*, vol. 39, no. 25, Dec 2003.

Nakazawa, T., "Low drive voltage and broad-band $LiNbO_3$ modulator", *Microwave photonics*, international conference, pp. 45-48, 2002.

Noguchi, K.,Mitomi, O., and Miyazawa, H., "Millimeter-wave Ti:$LiNbO_3$ optical modulators", *J. of Lightwave Technol.*, vol. 16, no. 4, pp. 615-619, April 1998.

Novak, D., Smith, G. H., Lim, C., Liu, H. F., Waterhouse, R. B., "Optically fed millimeter-wave wireless communication," *OFC* '98 technical digest, pp. 14.

Narasimba, A., and Yablonovitch, E., "Code-selective frequency shifting by RF photonic mixing in a dual-electrode Mach-Zehnder modulator," *Electron. Lett.*, vol. 39, pp. 619-620, April 2003.

Ogava, H., Polifko, D., and Banba, S., "Milimeter-wave fiber optic systems for personal radio communication," *IEEE Trans. on Microwave Theory and Techniques*, vol. 40, no. 12, pp. 2285-2293 Dec. 1992.

Oreilly, J., and Lane, P., "Remote delivery of video services using mm-waves and optics," *IEEE J. of Lightwave Technol*., vol 12, no 2, pp. 369-375, Feb. 1994.

Ohata, K., Inoue, T., Funabashi, M., Inoue, A., Takimoto, Y., Kuwabara, T., Shinozaki, S., Maryhashi, K., Hosaya, K., and Nagai, H., "Sixty-GHz-Band ultra-miniature monolithic T/R modules for multimedia wireless communication systems", *IEEE Trans. on Microwave Theory and Tech.*, vol. 11, no. 12, pp. 2354-2360, Dec. 1996.

Ogusu, K. and Yamamoto, S., "Nonlinear Fabry-Perot resonator using thermo-optic effect", *IEEE J. of lightwave technol.*, vol. 11, no. 11, pp 1774-1780, Nov. 1993.

Oh, M-C., Zhang, H., Szep, A., Chuyanov, V., and Steier, W. H., Zhang, C., Dalton, L.,Erlig, H., Tsap, B., Fetterman, H. R., "Electro-optic polymer modulators for 1.55 μm wavelength using phenyltetraene bridged chromophore in polycarbonate," *Applied Phys Lett.*, vol. 76, no. 24, pp. 3525-3527, June 2000.

Ohata, K., Inoue, T., Funabashi, M., Inoue, A., Takimoto, Y., Kuwabara, T., Shinozaki, S., Maryhashi, K., Hosaya, K., and Nagai, H., "Sixty-GHz-Band ultra-miniature monolithic T/R modules for multimedia wireless communication systems", IEEE trans. on microwave theory and tech., vol. 11, no. 12, pp. 2354-2360, Dec. 1996.

O' Reily, J., and Lane, P., "Remote deliver of video services using mm-waves and optics," *J. Lightwave Technol*., vol. 12, no. 2, pp. 369-375, Feb. 1994.

Pozar, D. M., "Microwave and RF design of wireless systems," John Wiley & Sons, Inc., 2001.

Pozar, D. M., "Microwave engineering," John Wiely & Sons Inc, 1998.

Park, J., Wang, Y., and Itoh, T., "A microwave communication link with self-heterodyne direct down-conversion and system predistortion", *IEEE Trans. on Microwave Theory and Tech.*, vol. 50, no. 12, pp. 3059-3063. Dec. 2002.

Prokhov, A. M., and Kuz'minov, Y. S., "Physics and chemistry of crystalline lithium niobate," The Adam Hilger series on optics and optoelectronics, 1990.

Pintzos, s. G., and Pregla, R., " A simple method for computing the resonant frequencies of microstrip ring resonators ", *IEEE Trans. on Microwave Theory and Tech.*, vol. MTT-26, no. 10, pp 809-813, Oct 1978.

Piotrowski, J. K., Galwas, B. A., Malyshev, S. A., and Andrievski, V. F., "Investigation of InGaAs P-I-N photodiode for optical-microwave mixing process," *Micriowave and radar*, 1998. MIKON'98, 12th international conference, pp. 171-175

Reynolds, S.,Floyd, B., Pfeiffer, H., Zwick, T., "60 GHz transceiver circuits in SiGe bipolar technology," *ISSCC* 2004, session 24, pp. 442.

Rabbiei, P., Steier, W., Zhang, C., Wang, C. –G., Lee, H. J., Turner, E. H., and Maloney, P. J., "Polymer micro-ring modulator with 1 THz FSR," *CLEO 2002* technical digest.

Rabiei, P., Steier, W. H., Zhang, C., and Dalton, L. R., "Polymer micro-ring filters and modulators," *IEEE J. of Lightwave Technol*., vol. 20, no. 11, pp 1968-1974, Nov. 2002.

Reynolds, S. K., Floyd, B., Beukema, T., Zwick, T., Pfeiffer, U., and Ainspan, H., "A direct-conversion receiver IC for WCDMA mobile systems," *IEEE J. Solid-State Circuits*, vol.38, pp. 1555-1560, Sept 2003.

Robetrtson, W. M., Arjavalingam, G., and Kopcsay, G. V., "Broadband microwave dielectric properties of $LiNbO_3$," *Electron. Lett.*, vol. 27, pp. 175-176

Rowe, W. S. T., and Waterhouse, R. B., "Efficient wide band printed antennas on lithium Niobate for OEICS", *IEEE trans. on antennas and Propagation*, vol. 51, no.6, pp. 1413-1415, June 2003.

Reed, G. T., and Knights, A. P., "Silicon photonics an introduction," Wiley, 2004.

Sugiyama, M., Doi, M., Taniguchi, S., Nakazawa, T., and Onaka, H., "Low-drive voltage $LiNbO_3$ 40-Gb/s modulator", *IEEE LEOS news letter*, vol. 17, no. 1, pp. 12-13, Feb 2003.

Shoji, Y., Hamaguchi, K., and Ogawa, H., "Millimeter-wave remote self-heterodyne system for extremely stable and low-cost broad-band signal transmission", *IEEE Trans. On Microwave Theory and Tech*., vol. 50, no. 6, June 2002.

Smith, G. H., Novak, D., Lim, C., "A millimeter-wave full-duplex WDM/SCM fiber-radio access network," *OFC* technical digest, pp. 18.

Sadagopan, T., Choi, S. J., Choi, S. J., and Dapkus, P. D., "High-speed, low-voltage modulation in circular WGM microresonator," *IEEE/LEOS, summer topical meetings*, 2004, MC2-3.

Shaw, N., Stewart, W. J., Heaton, J. and Whight, D. R., "Optical slow-wave resonant modulation in electro-optic GaAs/AlGaAs modulators," *Electron. Lett*., vol. 35, no. 18, pp 1557-1558, Sep. 1987.

Schiller, S., and Byer, R. L., "High-resolution spectroscopy of whispering gallery modes in large dielectric spheres", *Optics Lett.*, vol. 16, no. 15, pp 1138-1440, Aug. 1991.

Smith, P. W., Turner, E. H., and Maloney, P. J., "Electro-optic nonlinear Fabry-Perot devices", *IEEE J. of quanum electron.*, vol. 14, no. 3, pp 207-212, March 1978.

Smith, P. W., and Turner, E. H., "A bistable Fabry-Perot resonator", *Appl. Phys. Lett.*, vol. 30, no. 6, pp 280-281, March 1977.

Smith, P. w., Turner, E. H.,and Mumford, B. B., "Nonlinear electro-optic Fabry-Perot devices using reflected-light feedback", *Optics Lett.*, vol. 2, no. 3, pp 55-57, March 1978.

Senior, J. M., "optical fiber communications principles and practice", Prentice-Hall series in optoelectronics, 1985.

Shoji, Y., Hamaguchi, K., Ogawa, H., "Millimeter-wave remote self-heterodyne system for extremely stable and low cost broad-band signal transmission", *IEEE Trans. Microwave. Theory and Tech,* vol. 50, pp1458-1468, June 2002.

Savchencov, A. A., "Ultrahigh-Q crystalline optical whispering gallery mode resonators," *IEEE LEOS summer topicals meeting on WGM microcavities*, TuC1.2, 2004.

Shaw, N., Stewart, W. J., Heaton, J., and Wight, D. R., "Optical slow-wave resonant modulation in electro-optic GaAs/AlGaAs modulators," *Electron. Lett.*, vol. 35, no. 18, pp. 1557-1558, Sept 1999.

Stohr, A., Malcoci, A., Sauerwald, A., Mayorga, I. C., Gusten, R., and Jager, D. S., "Ultra wide-band traveling-wave photodetectors for photonic local oscillators," *J. of Lightwave Technol.*, vol. 21, no. 12, pp.3062-3070, Dec 2003.

Tsuzuki, K., Ishibashi, T., Ito, T., Oku, S., Shibata, Y., Iga, R., Kondo, Y., and Tohmori, Y., "40 Gb/s *n-i-n* InP Mach-Zehnder modulator with a π voltage of 2.2 V," *Electron. Lett*., vol. 39, no. 20, pp. 1464-1466, Oct. 2003.

Thiyagarajan, S. M. K., Levi, A. F. J., Lin, C. K., Kim, I., Dapkus, P. D., and Pearton,S. J., "Continuous room-temperature operation of optically pumped InGaAs/InGaAsP microdisk lasers," *Electron. Lett.,* vol. 34, pp. 2333-2334, 1998.

Tsuchiya, M., Hoshida, T., "Nonlinear photodetection scheme and its system applications to fiber-optic millimeter-wave wireless down-links," *IEEE Trans. On Microwave theory and techniques*, vol. 47, pp.1342, 1999.

Tsuzuki, K., Ishibashi, T., Ito, T., Oku, Shibata,Y., Iga, R., Kondo, Y., and Tohmori, Y.,"40Gb/s n-I-n InP Mach-Zehnder modulator with a π voltage of 2.2 V," *Electron. Lett.*, vol. 39, no. 20, Oct 2003.

Takashi, T., Higashiyama, S., Takemori, H., and Koizmi, "A silicon optical bench incorporating a tantalum-nitride thin-film resistor," *J. of Micromech. And Microeng.*, vol. 14, pp. 283-289, 2004.

Ulrich, R., "Optimum excitation of optical surface waves", *J. of Opt. Soc. Am.*, vol. 61, no. 11, pp 1467-1476, Nov. 1971.

Visagathilagar, Y. S., Mitchel, A., and Waterhouse, R. B., "Fabry-Perot type resonantly enhanced Mach-Zehnder modulator," *Microwave Photonics*, MWP '99. International Topical Meeting on, vol.1, pp 17-20, 1999.

Vidal, B., Polo, V.,Corral, J. L., and Marti, J., "Efficient architecture for WDM photonic microwave filters," *IEEE Photon. Technol. Lett.*, vol. 16, pp. 257-259, Jan. 2004.

Verdein, J., "Laser electronics," *Prentice Hall* , 1995.

Wu, Y. S., and Rosenbaum, F. j., "Mode chart for microstrip ring resonators," *IEEE trans. on microwave theory and techniques*, vol. MTT-21, pp 487-489, July 1973.

Walker, R. G., "High-speed III-V semiconductor intensity modulators," *IEEE J. of Quantum Electron.*, vol. 27, no. 3, March 91.

Wolf, I., and Tripathi, V., "The microstrip open-ring resonator," *IEEE Trans. on Microwave Theory and Tech.*, vol. MTT-32, no. 1, pp 102-107, Jan 1984.

Wooten, E. L., Kissa, K. M., Yan, A. Y., Murphy, E. J., Lafaw, D. A.,Hallemeir, P. F.,Mack, D., Attanasio, D. V., Fritz, D. J., McBrien, G. J., and Bossi, D. E., "A review of Lithium Niobate modulators for fiber-optic communications systems", *IEEE J. of selected topics in Quant. Electron.*, vol. 6, no. 1, pp. 69-82, Jan-Feb 2000.

Weis, R. S., and Gaylord, T. K., "Lithium Niobate: Summary of physical properties and crystal structure," *Appl. Phys. A*, vol. 37, pp 191-203, 1985.

Wan, L., Yuan, Y., "Observation of dynamic photorefractive effect in lithium niobate waveguides," *Optics communications*, vol 73, no. 6, pp. 439-442, Nov 1989.

Wong, K. K., "Properties of lithium niobate," *INSPEC*, institution of electrical engineers, 1989.

Williams, K. J., Esman, R. D. and Dagenais, M., "Effects of high space-charge fields on the response of the microwave photodetectors," *IEEE Photon. Technol. Lett.*, vol. 6, pp.639, 1994.

Williams, K. J., Esman, R. D., and Degenais, M., "Nonlinearities in p-i-n microwave photodetectors," *J. Lightwave Technol.*, vol 14, p.84, 1996.

Wakita, K., "Semiconductor optical modulators," *Kluwer academic publishers*, 1998.

Walker, R. G., "High-speed III-V semiconductor intensity modulators," *IEEE J. of Quantum Electron.*, vol 27, no. 3, pp. 654-666, March 1991.

Yariv, A., "Universal relations for coupling of optical power between microresonators and dielectric waveguides", *Electron. Lett.*, vol. 36, no. 4, pp 321-322, Feb. 2000.

Zurcher, J. _F., and Gadiol, F. E., "Broadband patch antennas".